The XMM-BCS galaxy cluster survey

Róbert Šuhada

München 2011

The XMM-BCS galaxy cluster survey

Róbert Šuhada

Dissertation
an der Fakultät für Physik
der Ludwig–Maximilians–Universität
München

vorgelegt von
Róbert Šuhada
aus Košice, Slowakei

München, den 25. März 2011

Contents

List of Figures

List of Tables

Zusammenfassung

Wir erleben eine einzigartige Epoche in der Geschichte der Erforschung von Galaxienhaufen. Wir haben nun Fenster zum Universum über das gesamte elektromagnetische Spektrum, die uns sich ergänzende Ansätze für die Erkennung und Studien von Galaxienhaufen bieten. Fast vierzig Jahre nach der theoretischen Voraussage haben die ersten großen Radioteleskope begonnen den Himmel, auf der Suche nach massereichen Haufen zu untersuchen, die durch den Sunyaev-Zel'dovich Effekt (SZE) mit ihrem heißen Gas auf dem kosmischen Mikrowellen-Hintergrund als "Schatten" sichtbar werden. Im Röntgenlicht kann dieses heiße Plasma auch direkt beobachtet werden. Optische und Infrarot-Teleskope ermöglichen uns, die Galaxienpopulation von Haufen zu studieren und durch den Gravitationslinseneffekt auch die beherrschende unsichtbare Komponente - die dunkle Materie zu erforschen.

Das Aufkommen der Multi-Wellenlängen Himmelsdurchmusterungen bringt auch die Notwendigkeit mit sich, einzelne Methoden zur Identifizierung von Galaxienhaufen zu vergleichen und untereinander zu kalibrieren. Dies ist auch das Hauptziel dieser Arbeit, die im Rahmen des XMM-*Newton* - Blanco Cosmology Survey (XMM-BCS) Projekts durchgeführt wird. Dieses Projekt ist eine koordinierte Multi-Wellenlängen-Himmelsdurchmusterung in einer 14 Quadratgrad Testregion. Im optischen Band ist sie abgedeckt durch den Blanco Cosmology Survey, im mittleren Infraroten durch Beobachtungen mit dem *Spitzer*-Weltraumteleskop und im Röntgenlicht mit XMM-*Newton*. Diese Region wurde auch von beiden SZE Durchmusterungsinstrumenten gescannt: das South Pole Telescope (SPT) und das Atacama Cosmology Telescope (ACT).

Im ersten Teil der Arbeit beschreibe ich die Analyse der 6 Quadratgrad Kernregion der Röntgen-Himmelsdurchmusterung. Ein Haufenkatalog mit 46 Galaxienhaufen ist von den erfassten ausgedehnten Quellen konstruiert worden. Diese Haufen sind als signifikante Galaxienüberdichten in den optischen Daten bestätigt und ihre photometrische Rotverschiebungen gemessen. Ich gebe die physikalischen Parameter der Haufen abgeleitet aus ihrer Röntgen-Leuchtkraft an und führe einen ersten Vergleich mit optischen Himmelsdurchmusterungen durch. Der Haufen-Katalog wird für den direkten Vergleich mit optischen/mittleren infraroten Katalogen nützlich sein, um die Anwahlfunktionen der Himmelsdurchmusterungen zu untersuchen, für Stacking-Analysen des SZE Signals und nach der Ergänzung von detektierten Haufen aus der Ausweitung des Röntgenfeldes auch für kosmologische Analysen.

Diese Ausweitung auf 14 Quadratgrad ist die erste wissenschaftliche Nutzung der neuen XMM-*Newton* Mosaik-Modus Beobachtungen. Ich habe eine Datenanalyse-Pipeline für diese neue XMM-*Newton* Betriebsart entwickelt und berichte hier über die Entdeckung von zwei

Galaxienhaufen, SPT-CL J2332-5358 und SPT-CL J2342-5411, im Röntgenlicht. Diese Haufen wurden auch unabhängig durch ihr SZE Signal mit dem SPT und im optischen Band in den BCS Daten erfasst. Sie sind damit die ersten Haufen, die unter Durchmusterungsbedingungen von allen drei großen Haufenidentifikazionsmethoden detektiert wurden. Diese Arbeit zeigt auch das Potenzial der Mosaik-Modus Beobachtungen große Himmelsbereiche effektiv abdecken zu können und massereiche Haufen bis zu Rotverschiebungen ~ 1 auch mit kurzen Beobachtungszeiten erfassen zu können.

Der letzte Teil der Arbeit ist ein Beispiel für Multi-Wellenlängen-Analysen von Galaxienhaufen mit hohen Rotverschiebungen ($z > 1$) im Rahmen des XMM-*Newton* Distant Cluster-Projekts. Mit der Entdeckung und dem Studium dieser hochrotverschobenen Galaxienhaufen beginnen wir, zum ersten Mal zu sehen, wie sich die heute komplett passive Population von Galaxien in Haufen bildet und wie bei den hohen Rotverschiebungen diese Galaxien immernoch deutliche Anzeichen von Sternbildung zeigen.

Abstract

We are experiencing a unique epoch in the history of galaxy cluster studies. We have now open windows across the whole electromagnetic spectrum which offer us complementary approaches for cluster detection and analyses. Almost forty years after its theoretical prediction, first large radio telescopes started to scan the sky looking for massive clusters as "shadows" in the cosmic microwave background imprinted there by their hot gas content via the Sunyaev-Zel'dovich effect (SZE). In X-rays this hot plasma can be observed also directly. Optical and infrared telescopes give us a view on the galaxy population of clusters and through gravitational lensing also on its dominant, invisible component - the dark matter.

The advent of multi-wavelength cluster surveys brings also the necessity to compare and cross-calibrate each cluster detection approach. This is the main aim of this work carried out in the framework of the XMM-*Newton*-Blanco Cosmology Survey project (XMM-BCS). This project is a coordinated multi-wavelength survey in a 14 deg^2 test region covered in the optical band by the Blanco Cosmology Survey, in the mid-infrared by the *Spitzer* Space Telescope and in X-rays by XMM-*Newton*. This area is also part of the sky scanned by both SZE survey instruments: the South Pole Telescope (SPT) and the Atacama Cosmology Telescope (ACT).

In the first part of the thesis I describe the analysis of the initial 6 deg^2 core of the X-ray survey field. From the detected extended sources a cluster catalog comprising 46 objects is constructed. These cluster candidates are confirmed as significant galaxy overdensities in the optical data, their photometric redshifts are measured and for a subsample confirmed with spectroscopic measurements. I provide physical parameters of the clusters derived from X-ray luminosity and carry out a first comparison with optical studies. The cluster catalog will be useful for direct cross-comparison with optical/mid-infrared catalogs, for the investigation of the survey selection functions, stacking analysis of the SZE signal and for cosmological analyses after combing with clusters detected in the extension of the survey.

The extension of the survey to 14 deg^2 is a first scientific utilization of the novel XMM-*Newton* mosaic mode observations. I have developed a data analysis pipeline for this operation mode and report on the discovery of two galaxy clusters, SPT-CL J2332-5358 and SPT-CL J2342-5411, in X-rays. The clusters were also independently detected through their SZE signal by the SPT and in the optical band in the BCS data. They are thus the first clusters detected under survey conditions by all major cluster search approaches. This work also demonstrates the potential of the mosaic mode observations to effectively cover large sky areas and detect massive clusters out to redshifts ~ 1 even with shallow exposures.

The last part of the thesis provides an example of a multi-wavelength analysis of two high-

redshift ($z > 1$) systems in the framework of the XMM-*Newton* Distant Cluster Project. With the detection and studies of these high redshift systems we are for the first time able to see the assembly phase of the galaxy population of the clusters, which in nearby systems is totally passive, but at these high redshifts still show signatures of star formation.

Chapter 1

Introduction

Multi-wavelength surveys give us a comprehensive look at the population of galaxy clusters and groups in the Universe. They allow us to study cluster evolution in the full relevant redshift range, from the nearby Universe out to redshift of $z = 1$ and beyond. We can also access the full mass range spanning from 10^{13} $M_\odot$ (the group regime) to $\sim 10^{15}$ $M_\odot$ (most massive clusters). Observations in different parts of the electromagnetic spectrum offer us outlook on the individual cluster components: the galaxy population from UV through optical to infrared bands, the intracluster medium (ICM) in X-rays and via the Sunyaev-Zel'dovich effect (SZE) and also the dark matter (indirectly through gravitational lensing). The multi-wavelength approach thus brings about many synergies: e.g. X-ray and SZE studies give us a way to safely detect clusters, study their thermodynamical evolution and provide good precision estimates of the total mass, while optical observations then can establish the redshifts of the systems and investigate the processes shaping their galaxy populations.

Cluster studies are, however, not motivated only by astrophysical interests, but are also part of cosmological investigations. The mass distribution of the cluster population and its evolution with redshift are very sensitive to the cosmological parameters and allow us to constraint not only the parameters describing the matter content of the Universe (baryonic and dark matter), but ultimately shed light on its most enigmatic component - the Dark Energy.

In order to access the full potential of such studies, we need to answer several important questions. Firstly, what are the selection functions of these surveys, what kind of systems are they sensitive to and why do they miss others? Since each surveying approach probes clusters and groups in a different way it is not surprising that they will be more sensitive to different parts of the cluster population and have different systematics. Simulations can give us estimates of their selection functions, but comparing cluster samples extracted from a common test field is crucial to gain full understanding of these surveying methods. Secondly, the total cluster mass is the most important physical parameter of the cluster, but from observations it is accessible only indirectly through scaling relations from an observable parameter. Construction of good (unbiased and low scatter) mass scaling relations is crucial for future applications of cluster surveys. A multi-wavelength cross-comparison can again test the assumptions and selection effects of each approach and thus help to pave the way for future large surveys.

Most of the present work has been done in the framework of the XMM-BCS project. This

project tries to answer these questions by combining optical, mid-infrared and X-ray observations in a single test field covered also by the SZE surveys conducted by the South Pole Telescope and Atacama Cosmology Telescope. This project is introduced in detail in Chapters 4 and 5, where we describe our first results.

Before that, however, we provide three introductory chapters that give an overview of the basic concepts relevant for studies presented in this work. Chapter 2 contains a concise introduction to clusters of galaxies, their main components and relevant undergoing physical processes. We also highlight the observational signatures of clusters and discuss their detection in the main surveying approaches. The cosmological perspective of the clusters is reviewed in Chapter 3. We describe the evolution of clusters within the large-scale structure of the Universe and how this can be related to the background cosmology. We also discuss how the survey selection function enters this kind of studies.

The data analysed in the course of this work were obtained with the XMM-Newton X-ray telescope. Therefore, we describe this instrument in Chapter 4, where we also provide an introduction to the basic concepts of X-ray imaging. The chapter closes with a detailed description of the mosaic mode observations by XMM-Newton. The material covered here also comprises technical descriptions of analysis recipes for this new type of data developed during this thesis' work.

The next three chapters collect research papers from the XMM-BCS cluster survey and the XMM-*Newton* Distant Cluster Project (XDCP). In Chapters 5 we provide first results from the 6 deg^2 core region of the XMM-BCS survey. We construct here a catalog of 46 X-ray selected clusters and groups of galaxies. We provide for them photometric redshift estimates and physical parameters determined from their X-ray luminosities. The photometric redshifts are confirmed for a subsample of clusters with spectroscopic measurements and a first comparison with optical mass estimates is carried out. We provide extensive test of our X-ray analysis pipeline and give an outlook on the ongoing studies based on this cluster catalog. Chapter 6 introduces the 8 deg^2 extension of the survey and provides the analysis of two very massive X-ray selected clusters, one at low- and the second at high redshift. These systems were also independently detected through their SZE signature by the South Pole Telescope and are thus the first systems to be found by all major cluster search methods in survey conditions. We find good agreement between the X-ray and SZE estimated properties of these clusters.

In Chapter 7 we provide the analysis of two high redshift ($z > 1$) systems detected in X-rays by the XDCP survey. We confirm one of these to be a bona fide cluster at redshift $z = 1.185$. We provide its physical properties and investigate the galaxy population which shows signs of ongoing star formation in many of its members. For the second system we find the X-ray detection to be coincident with a dynamically bound galaxy system at $z = 1.358$. Optical spectroscopy, however, reveals the presence of a central active galactic nucleus, which can be a dominant source of the detected X-ray emission from this system. We discuss cluster identification challenges in the high-redshift, low-mass cluster regime and provide upper limits on X-ray parameters for this system.

We summarize the main results of the thesis in the closing Chapter 8 and provide conclusions and outlook on future work for these projects.

Chapter 2

Clusters of galaxies

One of the most astonishing features of our Universe is that the matter distribution on its largest spatial scales ($\sim 10^{24}$ m) was seeded by quantum fluctuation on the sub-atomic scales[1] (i.e. below $\sim 10^{-15}$ m). The theory that bridges this incredible dynamical range and describes the distribution and evolution of the matter in the Universe is the hot Big Bang model with an inflationary phase.

In this picture, the Universe originated $\sim$ 13.8 Gyrs ago from a phase of extremely high temperatures and densities and underwent a brief, but very efficient exponential expansion phase - the inflation. It was during this phase that the quantum world left its imprint in the distribution of matter that we now observe on cosmic scales. The inflationary expansion smoothed out the matter density field, leaving only minuscule inhomogeneities - those that can be seen as one part in 10^5 density fluctuations in the cosmic microwave background, giving us a snapshot of the matter distribution 300 000 years after the Big Bang.

It is still one of the largest mysteries, why our Universe had such a particularly low entropy in the beginning.[2] Nonetheless, the time evolution of gravitationally interacting systems looks much different from a system filled with gas (where gravitation is negligible, Fig. 2.1). Remarkably, gravity drives clumping and collapse of structures (thus exhibiting trends exactly opposite to the gas system). On cosmic scale this leads to the formation of the large scale structure (LSS) of the Universe and thus also to the assembly of the most massive, bound object - clusters of galaxies.[3]

Roughly 85% of the total gravitational mass involved in the dynamical evolution of the LSS consists of a weakly interacting, collisionless form of matter - the so-called dark matter (DM, often the term "cold dark matter" (CDM) is used to stress that the kinetic energy of the DM particles in the early development phases of the LSS is much smaller than their rest energy).

---

[1]We took here the scale of $\sim$ 100 Mpc as a typical range where the large-scale distribution of matter becomes nearly homogeneous. The lower bound characterizes the regime of atom nuclei. In principle, the link could be extended down to the *Planck scale* $l_P = \sqrt{Gh/2\pi c^3} \approx 10^{-35}$ m, where G is the gravitational constant, h the Planck constant and c the speed of light.

[2]And how is this question connected to the fundamental question of the arrow of time and the second law of thermodynamics.

[3]At the end of this chain of clumping/collapse one finds black holes, as the highest entropy regions in the Universe. Also notable is a curious fact, that the existence of gravitationally bound structures enables a negligible part of baryonic matter to get organized into self-aware structures, some of which take interest in the cosmic structure formation.
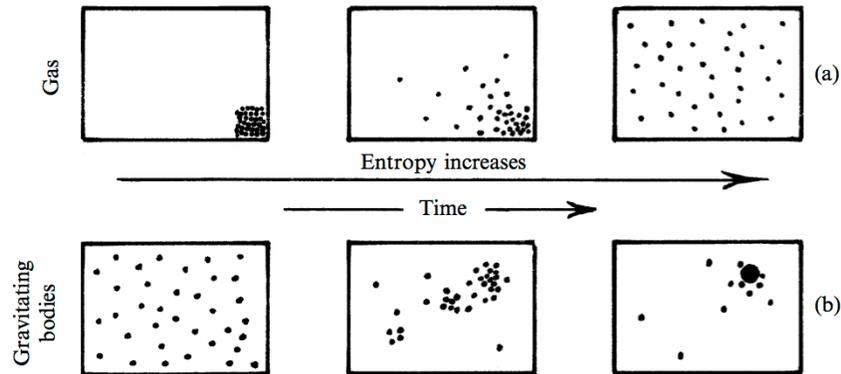
Figure 2.1: Comparison of entropy increase with time for two different systems. In both cases we start from a low entropy initial state. In the top row we have a gas in a closed box. It evolves from a low entropy state of being concentrated in one corner to reaching thermal equilibrium by spreading and filling the whole box. If gravity is introduced (bottom row), the evolution looks quite the opposite. Here a low entropy initial state consists of uniformly spread gravitating bodies. Entropy increases as clumping occurs. If the particles are only weakly interacting, collisionless a characteristic filamentary web is formed - as is the case of the large scale structure of the Universe (see also Fig. 2.2). Image credit: Penrose (2005).
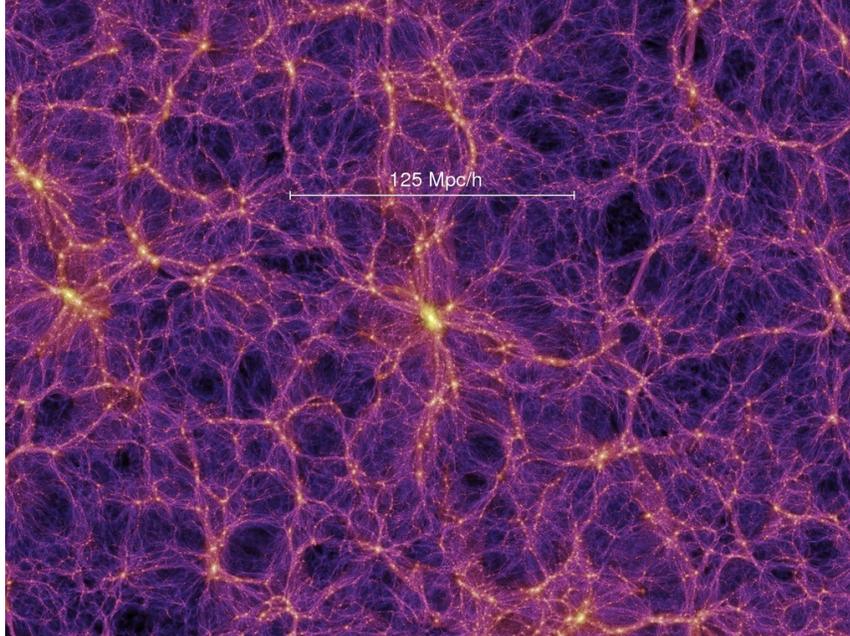
Figure 2.2: The large-scale structure of the Universe from the Millennium Run simulation. The central object at the node of several filaments is a massive cluster of galaxies. Image credit: Springel et al. (2005).

Table 2.1: Galaxy cluster fact sheet.

Parameter	Value
dark matter	$\sim 85\%$
intracluster medium	$\sim 15\%$
stars	$\sim 5\%$
virial mass	$10^{13} - 10^{15}$ M$_\odot$
temperature	$\sim 0.5 - 10$ keV ($10^7 - 10^8$ K)
virial radius	$1 - 2$ Mpc
ICM density	$10^{-5} - 10^{-1}$ cm^{-3}
X-ray luminosity	$10^{43} - 10^{45}$ erg/s
metallicity	$0.2 - 0.5$ Z$_\odot$
redshift range	$0- \sim 2$

The shape of the matter distribution is thus determined not only by the initial density field and the kinematics of the expansion of the Universe, but also by the composition of the matter field, where ordinary baryonic matter is only a subdominant component.

All these factors (and their interactions) then cause that the large-scale distribution of matter that we observe at the current epoch has a remarkable filamentary structure (Fig. 2.2). We can directly study the LSS in galaxy surveys and using weak lensing tomography. Numerical N-body simulations are nowadays able to reproduce the statistical properties of the distribution across a large range of scales.

The densest regions of the filamentary web are its nodes. These places, where several filaments intersect, are typically occupied by clusters of galaxies. Since the gravitationally driven structure formation is a bottom-up process, smaller DM (e.g. galactic) halos collapse first. The more massive the object is, the later its formation occurs. Since the Big Bang, the largest structures that could collapse and virialize up to now are clusters of galaxies (up to masses of few times 10^{15} M$_\odot$).[4] In the mass range below 10^{14} M$_\odot$ we find smaller systems - groups of galaxies - populating lower density regions along the filaments. The lowest density regions of the LSS contain almost no galaxies and are called voids.

Clusters are not only at the crossroads of the LSS, but also in a sense at a crossroad between two viewpoints. They can be approached from the global, cosmological perspective as being tracers of the evolution and growth of dark matter halos and tools to study the background cosmology. The second approach is to study the astrophysical processes that determine the thermodynamical state and evolution of their gas content - the intracluster medium (ICM) - and their galaxy population. Naturally, both these approaches are indispensable to get a complete picture of clusters.

The most stunning illustration of the three cluster constituents (the DM halo, ICM and the galaxies) is the *Bullet Cluster* 1E 0657-56 (Markevitch et al. 2002; Clowe et al. 2006). The system consists of a main component undergoing a merger with a smaller, compact component (the

---

[4]Superclusters, collections of several clusters and groups, are not yet virialized.
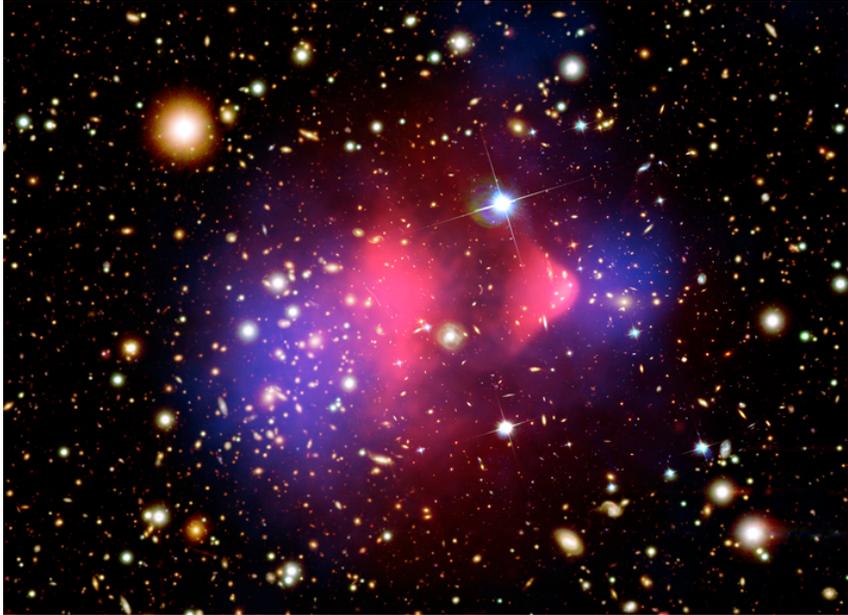
Figure 2.3: The Bullet Cluster (1E 0657-56) at $z = 0.296$. Overlayed on the optical image, we display the X-ray emission observed by the Chandra satellite in pink and the weak lensing mass reconstruction in blue. The collisionless DM and the galaxy overdensities are coincident, while the ICM was separated during the core passage. X-ray image: Markevitch et al. (2002), optical image and weak lensing map: Clowe et al. (2006).

"bullet"). The merger happens almost exactly in the plane of sky, giving us an unprecedented view into the inner workings of a cluster. Figure 2.3 shows the optical image of the cluster with the two distinct galaxy concentrations belonging to the two systems well separated after the core passage (galaxies are essentially non-collisional during a cluster merger). The observed X-ray emission is shown in pink. Unlike the galaxies and DM particles, the ICM is collisional and is thus lagging behind the galaxies. The bullet-shaped ICM emission is trailing a shock front that was driven into the plasma by the collision. Most remarkably, from the small distortions of the shapes of the background galaxies by the gravitational potential of the foreground cluster (i.e. weak gravitational lensing) we can reconstruct the distribution of the otherwise invisible DM content. The weak lensing reconstructed mass concentrations are shown in blue. Since DM is collisionless, its position coincides with the galaxy population. This system provides the best empirical evidence for the existence of dark matter and an exceptional view of three components of the cluster. The energy required to separate the components makes cluster mergers one of the most energetic events in the Universe since the Big Bang (the power (energy per unit time) of merger events is surpassed only by the most energetic gamma ray bursts, but the total energy is, in fact, unmatched).

Table 2.1 summarizes the basic properties of a galaxy cluster. In the following sections we describe the three cluster components individually and review the most important ongoing processes.

2.1 Dark matter content of galaxy clusters

The collisionless, weakly interacting dark matter constitutes roughly 85% of the cluster total mass ($10^{13} - 10^{15}$ M$_\odot$). Clusters were in fact the first objects[5] to hint at the existence of an invisible (but dominant) matter component in the Universe. Zwicky (1933) measured the radial velocities of galaxies in the Coma cluster, and found the total cluster mass to be almost a factor of ten larger than expected from the summed mass of all galaxies (i.e. the visible matter). He posited, that the cluster must contain huge amounts of some invisible matter (part of which was later detected as the X-ray emitting intracluster medium (Sect. 2.2) but the majority is indeed DM).

When a virialized object is formed, the DM settles in a quasi-equilibrium state. The density profile of the DM halos in simulations were found to be universal and essentially independent of the halo mass (we say *scale independent* or *self-similar*). The most commonly used description of the density profile was provided by Navarro, Frenk and White, 1997 (the so-called NFW profile) based on dark matter N-body simulations:

$$\rho_{\mathrm{DM}}(r) = \frac{\rho_s}{\left(\frac{r}{r_s}\right)\left(1 + \frac{r}{r_s}\right)^2} , \tag{2.1}$$

where r_s is the characteristic scale length and ρ_s is the central DM density. The NFW profile has a characteristic central cusp described by the central slope $\rho_{\mathrm{DM}}(r) \propto r^{-1}$, while at larger distances ($r \gg r_s$) the density drops as $\rho_{\mathrm{DM}}(r) \propto r^{-3}$.

Recent advances in N-body simulations have, however, shown that three-parameter models, in particular the *Einasto profile*, provide a better description of the three dimensional density profiles than the NFW profile (Merritt et al. 2005, 2006, and references therein). The Einasto profile was first introduced by Einasto (1965).[6]

For the purposes of describing the 3D density distribution of DM halos, the Einasto profile is often written in the form:

$$\rho_{\mathrm{DM}}(r) = \rho_e \exp\left\{-d_n\left[(r/r_e)^{1/n} - 1\right]\right\} , \tag{2.2}$$

where ρ_e is the density at radius r_e, which defines a sphere containing half of the total mass. The index n is the *shape parameter* and it controls the curvature of the profile. Typical values of this parameter are in the range $4 \lesssim n \lesssim 7$. The d_n term is only a function of n and can be obtained from an approximation (Merritt et al. 2006):

$$d_n \approx 3n - 1/3 + 0.0079/n, \text{ for } n \gtrsim 0.5 . \tag{2.3}$$

The Einasto profile has been verified to hold exceptionally well across 7 orders of magnitude in mass in various N-body simulations. The NFW model still remains widely used, especially for the analysis of observational data, which often does not reach the precision required to distinguish between the two models.

---

[5]Although shortly before Zwicky, Oort (1932) found indirect evidence for missing matter in the galactic plane from the observed perpendicular acceleration of stars. See also Einasto (2009).

[6]The profile is essentially an independent derivation (and re-parametrization) of the well-known Sérsic profile (Sérsic 1963) used among others to fit surface brightness profiles of elliptical galaxies.

2.2 The intracluster medium

Only roughly one third of the total baryon mass in a cluster is locked within galaxies as part of the stellar population and interstellar gas. The majority of baryons are in the form of a hot, diffuse gas in the intergalactic space within the potential well of the cluster. This plasma is the so-called *Intracluster medium* (ICM) and contributes with 15% to the total mass of the cluster.

The ICM is a vestige of the inefficiency of galaxy formation, which leaves most of the gas not bound in galaxy sized halos. During cluster formation the ICM undergoes adiabatic shock heating by the infalling cold gas. Eventually, the ICM thermalizes and a quasi-equilibrium state is established. In this state the virial theorem links the gravitational potential energy with the mean kinetic energy of the ICM particles (or galaxies) as:

$$2\langle E_{\text{kin}} \rangle + \langle E_{\text{pot}} \rangle = 0 . \tag{2.4}$$

The typical ICM densities are $10^{-5} - 10^{-1}$ particles per cm^3 (from the outskirts to the densest cool cores) and the gas is heated up to $10^7 - 10^8$ K. This implies that the ICM is an optically thin plasma in collisionally ionized equilibrium.

The composition of the ICM is largely primordial, with Hydrogen being by far the most dominant element. The metallicity of the gas (i.e. abundance of elements heavier than Helium) is roughly $0.2 - 0.5 \, Z_{\odot}$. These metals are injected into the ICM from the galaxies' stellar population, e.g. through stellar winds from the asymptotic giant branch population and most importantly supernova explosions. Type Ia supernovae contribute primarily Fe, Ni, Si, S, Ar and Ca but produce only small amounts of O, Ne and Mg. Supernovae type II create predominantly O, Ne and Mg but also other α-elements like Si, S, Ar, Ca and additionally Fe and Ni. One can use the difference in yields to determine the supernova type Ia/II fractions, constrain explosion models and learn about enrichment and transportation processes in the ICM (e.g. de Plaa et al. 2007; Werner et al. 2006; Simionescu et al. 2008, 2009b; Lovisari et al. 2011).

These processes have a determining influence on the spatial distribution of the metals. The abundance pattern of the elements exhibit radial trends (e.g. Sato et al. 2009; Tokoi et al. 2008; Matsushita et al. 2007; Sanders and Fabian 2002), specific spatial distribution in the ICM (e.g. due to the active galactic nucleus of the central galaxy, Simionescu et al. 2008, 2009b) and many other effects for which we refer the reader to the reviews of Böhringer and Werner (2010) and Werner et al. (2008).

2.2.1 X-ray properties of clusters

Plasma heated to temperatures $\gtrsim 10^7$ K (equivalent to $\gtrsim 1$ keV) radiates in the X-ray band. Since the ICM is optically thin and in a highly ionized state, essentially every emitted photon escapes the cluster volume.

The primary mechanism of the *continuum emission* is the thermal bremsstrahlung (i.e. free-free emission). This electromagnetic radiation is produced by the acceleration of a charged particles (in the case of ICM free electrons), when deflected by another charged particle (such as an atom nucleus). Since in the ICM Hydrogen is the major constituent, the deflectors are
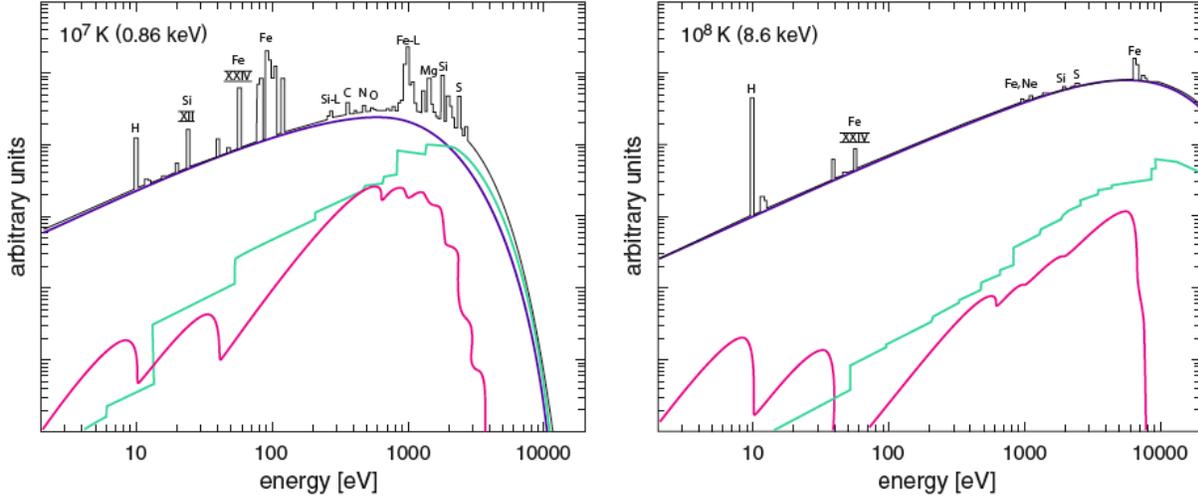
Figure 2.4: X-ray spectra of the ICM for solar abundance and at different plasma temperatures (left: 10^7 K and right: 10^8 K). Line colors mark the different contributions to the overall spectrum (black): the largest contribution comes from the continuum emission of the thermal bremsstrahlung (purple). Contribution from the recombination radiation emission is shown in green and 2-photon radiation in magenta. Line emission is more prominent the lower is the temperature of the cluster. We designate the major emission lines by the elements from which they originate. Image credit: Böhringer and Werner (2010).

typically protons (recall that Hydrogen is fully ionized). The electron velocity distribution in the ICM follows the Maxwellian distribution and a complete analysis of requires accounting not only for binary Coulomb collisions, but as well for the collective (dielectric) properties of the whole plasma. The full treatment can be found in e.g. Bekefi (1966), here we only provide the final relation for the emissivity.

The bremsstrahlung emissivity $\epsilon(\nu)$[7] at frequency ν is given by

$$\epsilon(\nu) \approx 6.8 \times 10^{-38} Z_i^2 \, n_e \, n_i \, g^{ff}(\nu, T) \, e^{-\frac{h\nu}{kT}} T^{-1/2} \text{ erg s}^{-1}\text{cm}^{-3}\,\text{Hz}^{-1} , \qquad (2.5)$$

where T is the plasma temperature, n_e and n_i are the number densities of electrons and ions, respectively. Z_i is the ion charge and the term $g^{ff}(\nu, T)$ corrects for quantum mechanical effects and distant collisions (the Gaunt factor). We denote h to be the Planck constant and k the Boltzmann constant.

The bremsstrahlung spectrum (Fig. 2.4) determines the global shape of the cluster's spectrum with line emission superimposed on it (see below). The overall normalization of the spectrum (i.e. the flux per unit emitting volume) depends primarily on the square of the electron density (the $n_i n_e \approx n_e^2$, term of Eq. 2.5). The squared density dependence is a characteristic of emission processes originating in two-body interactions. The (projected) density of the ICM is thus the most straightforward physical parameter that can be estimated from a cluster X-ray spectrum.

---

[7]Emissivity is the luminosity per unit volume and frequency interval.

Temperature, on the other hand, determines the curvature of the spectrum. The shape of the spectrum is roughly flat for low frequencies (in the X-ray band), $\nu \ll kT/h$, but around photon energies $\approx kT$ the spectrum has an exponential cut-off. The cut-off, determined by the $e^{-\frac{h\nu}{kT}}T^{-1/2}$ term, depends on the temperature - the higher the temperature of the ICM the later (i.e. at higher energies) the cut-off occurs. For limited band spectroscopy (typically $0.5 - 10$ keV), this implies that higher temperature systems will have "flatter" spectra. As an example compare the right and left panels of Fig. 2.4.

Fig. 2.4 also shows the emission line complexes observable in the ICM. The most prominent X-ray line feature in cluster spectra is the K-shell emission line complex of hydrogen-like iron Fe XXVI at ~ 6.7 keV (the K_α line). Other important features visible in Fig. 2.4 are attributed to Mg, Si, S, C, N and O. The strength of the lines determines the abundance of the given elements. From the energy of the line we can determine the redshift of the cluster (this might be useful in specific cases when optical spectroscopy is not available, but the X-ray spectrum is good enough to obtain the redshift from the K_α line).

In addition to the free-free bremsstrahlung emission and the bound-bound de-excitation line emission there are additional processes contributing to the overall emission: the free-bound recombination continuum emission (with characteristic edges notable in Fig. 2.4) and the so-called two photon emission which allows otherwise forbidden bound-bound transitions by emitting two photons (thus splitting the transition energy into two parts giving rise to continuum emission).

Contemporary ICM radiation codes, most notably the MeKaL model of Mewe et al. (1985); Kaastra (1992); Liedahl et al. (1995) and APEC of Smith et al. (2001), are able to fully account for these emission processes. These radiative codes are implemented in the widely used spectral fitting packages such as: XSPEC,[8] SPEX[9] and via XSPEC's libraries also in SHERPA[10] and ISIS[11]. The detailed physics of the emission mechanisms is covered by the review of Kaastra et al. (2008b).

2.2.2   Spatial distribution of the cluster X-ray emission

One of the most important observational markers of clusters is that they are *extended* sources of X-ray emission (this holds also for Sunyaev-Zel'dovich effect observations, Sect. 2.2.6). This fact is utilized in cluster surveys, which often necessitate a simple description of the surface brightness (SB) distribution.

The most common description of the SB profile was derived by Cavaliere and Fusco-Femiano (1976). It describes the cluster potential as that of a self-gravitating sphere (the *King model*, King 1966) and allows the gas density ρ_{gas} to be related to the total DM density ρ_{DM} through a simple power law as $\rho_{gas} \propto \rho_{DM}^\beta$. The gas temperature is assumed to be constant. For the three dimensional radial gas density profile this implies:

---

[8]http://heasarc.nasa.gov/docs/xanadu/xspec/
[9]http://www.sron.nl/index.php?option=com_content&task=view&id=125&Itemid=279
[10]http://cxc.harvard.edu/sherpa/
[11]http://space.mit.edu/cxc/isis/

$$\rho_{\mathrm{gas}}(r) = \frac{\rho_{\mathrm{gas}}^0}{\left[1 + \left(\frac{r}{r_{\mathrm{c}}}\right)^2\right]^{\frac{3\beta}{2}}} \ , \tag{2.6}$$

where ρ_{gas}^0 is the core density of the profile, r_{c} is the so-called core radius and sets the characteristic extent scale of the source. The β parameter controls the steepness of the profile and lends its name to this model - the *beta model*.

Plugging this 3D density distribution into the bremsstrahlung emissivity (Eq. 2.5) and integrating along the line-of-sight then gives the angular X-ray SB profile:

$$S(\theta) = \frac{S_0}{\left[1 + \left(\frac{\theta}{\theta_{\mathrm{c}}}\right)^2\right]^{3\beta-\frac{1}{2}}} \ , \tag{2.7}$$

with S_0 being the central SB and θ_{c} is the angular core radius.

The typical value found for the beta parameter is $\beta = 2/3$ (Jones and Forman 1984) and this fixed value is often used in surveys when the photon statistics is too small to constrain both β and θ_{c} (e.g. Sect. 5.3.1).

Naturally, this description is necessarily simplified and we often find clusters with rich morphologies and substructures (an example is the Bullet cluster in Fig. 2.3). These can be quantified in several ways, the most common being the power ratio method (Buote and Tsai 1996) and the center shift method (Mohr et al. 1993). For recent examples of their utilization see Jeltema et al. (2005); Böhringer et al. (2010) and Weißmann et al., in prep.

Another important example of clusters not conforming to the beta model are the so-called *cool core clusters* (see Sect. 2.2.3). This class of clusters has very steep SB peaks in the centers, while the simple beta model predicts a flat core. In these cases we often resort to using a *double beta model*, which has two components (each described by Eq. 2.7), one modeling the SB of the steep core and the other the outskirts.

As a final note to this section, we discuss the cosmological surface brightness dimming. In an arbitrary cosmology, we relate the observed flux f of an object to its luminosity L (i.e. the volume integral of the emissivity) in a way to reproduce the inverse square law in the flat Euclidean space: $f = L/(4\pi d_{\mathrm{lum}}^2)$. The distance defined by this relation is the so-called *luminosity distance*, d_{lum}. Analogously, the *angular distance* d_{ang} is defined so that the Euclidean relation between the physical linear scale $\mathrm{d}l$ and the apparent angular scale θ is again recovered in an arbitrary cosmology, i.e. so that $\mathrm{d}l = \theta d_{\mathrm{ang}}$. It can be shown (e.g. Hogg 1999) that the redshift dependence of the two distance measures is

$$d_{\mathrm{lum}} \quad \propto \quad (1 + z) \tag{2.8}$$
$$d_{\mathrm{ang}} \quad \propto \quad (1 + z)^{-1} \ , \tag{2.9}$$

and also $d_{\mathrm{lum}} = d_{\mathrm{ang}}(1 + z)^2$. Given that a solid angle element $\mathrm{d}\Omega$ depends on the square of d_{ang} we find that the total cosmological dimming of the bolometric surface brightness is given by:

$$I_{\mathrm{bol}}(\text{observed}) = \frac{I_{\mathrm{bol}}(\text{emitted})}{(1 + z)^4}. \tag{2.10}$$

This equation is an expression of the so-called *Tolman's law*. The $1/(1 + z)^4$ decrease makes it very challenging to detect high redshift clusters in X-ray surveys. As we will see in Sect. 2.2.6, the Sunyaev-Zel'dovich effect is not constrained by this limitation and is thus particularly suitable for detection of very massive, high redshift systems.

2.2.3   Cool cores and AGN feedback

As we already alluded to, there exists a class of clusters, the so-called cool core clusters, which exhibit very dense, cool cores, that give rise to a characteristic, highly peaked SB distribution.

Since the X-ray emissivity depends on the square of the density (Eq. 2.5), the radiative losses in these particularly dense regions are much higher than in the outer parts of the cluster. Energy loss leads to more cooling and thus to more gas condensation. This runaway process causes the cooling time of the gas to become smaller than the Hubble time[12] and thus large quantities of gas should fall out of the X-ray regime, undergo star-formation, and be observable in UV and optical light exhibiting typical tracers of cool gas like Hα, CO and H$_2$ emission. The predicted mass deposition rates of cool gas were are of the order 10^2 M$_\odot$/year. This mechanism would allow the brightest cluster galaxies (BCGs, see Sect. 2.3.1) to grow up to present time.

These clusters were termed *cooling flow* clusters and first models describing the gas cooling were developed in the 1970s (Silk 1976; Fabian and Nulsen 1977; Mathews and Bregman 1978). Several pieces of evidence were found that gas cooling indeed occurs: BCGs in the centers of presumed cooling flows often exhibit signs of star formation activity, are often more luminous than their non-cooling flow counterparts and in several cases also associated H$_\alpha$, CO and H$_2$ emission was detected (McNamara and O'Connell 1989; Egami et al. 2006a,b; Cavagnolo et al. 2008).

In most cases, however, the strength of these signatures implies mass deposition rates of cool gas one to two orders of magnitude smaller than those calculated from the simple cooling flow models. The final resolution of this issue came only with the launch of the XMM-*Newton* X-ray satellite (Sect. 4.1). With its two reflection grating spectrometers, it was able to look for unambiguous tracers of cool gas in the soft X-rays. However, Peterson et al. (2001, 2003) found no emission lines that would indicate the presence of gas cooler than a factor ~ 0.3 of the virial temperature of the clusters. To distinguish between the old cooling flow model and the more modest scenario, we use the term *cool core clusters* (Molendi and Pizzolato 2001) to indicate that in the given cluster cooling indeed occurs (and hence the peaked SB profile etc.), but at much lower rate than the "cooling flow" model would predict.

These findings implied that there is a fine-tuned energy input into the central parts of the ICM that would provide enough heat to prevent almost all of the gas from cooling out of the X-ray band. Several mechanism were proposed, but energy feedback from the central active galactic nuclei (AGN) was soon recognized as the most crucial by Böhringer and Morfill (1988) and Binney and Tabor (1995).

The connection of AGNs with cool core clusters and their direct interaction with the ICM

---

[12]The Hubble time is defined as $t_H = 1/H_0$, where H_0 is the Hubble constant (i.e. Hubble parameter at redshift $z = 0$). The Hubble time is the age of Universe at current epoch, $t_H = 13.75 \pm 0.11$ Gyr (Jarosik et al. 2011).
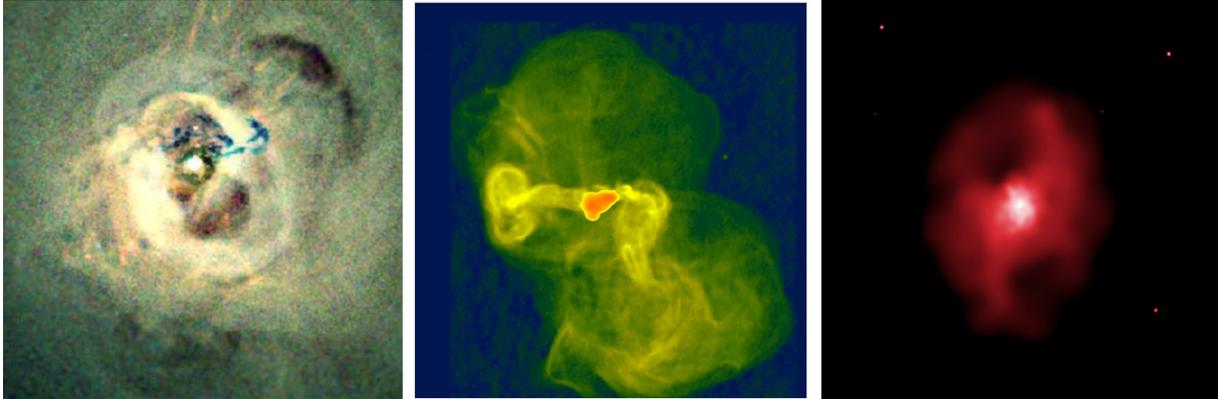
Figure 2.5: **Left:** Detailed Chandra X-ray pseudo-color image of the center of the Perseus cluster. The observation reveals bright loops, ripples, and jet-like streaks, all caused by the activity of the AGN in the core of NGC 1275 (the central galaxy of the core). The image is ~ 5 arcmin per side. Source: Fabian et al. (2006). **Middle:** Radio image of the galaxy M87 in the center of the Virgo cluster. The image reveals the detailed structure of the radio-emitting bubbles powered by the jets from the supermassive black hole at the galaxy's center. The jet on the left is roughly 20 kpc long. The image was taken by the Very Large Telescope (VLA, Owen et al. 2000). **Right:** The Chandra image of the galaxy cluster MS 0735.6+7421 shows two vast cavities - each ~ 200 kpc in diameter. The cavities are dark in the X-ray because they contain very little hot gas. They are filled with a two-sided, elongated, magnetized bubble of extremely high-energy electrons that emit radio waves. This is the most energetic known AGN outburst (McNamara et al. 2005). The image is 4.2 arcmin per side.

was confirmed by multiwavelength studies. Radio observations revealed that cool core clusters often harbor central radio sources associated with the BCGs (e.g. Burns 1990). The central AGN can undergo multiple phases of activity, where it drives jets of relativistic particles into the ICM. The jets initiate sound waves propagating outwards, can drive weak shocks and create lobes filled with relativistic particles. The lobes can detach and the bubbles buoyantly rise in the ICM. The plethora of these processes is demonstrated in the three panels of Fig. 2.5.

All these processes are able to deposit mechanical energy into the ICM and thus offset the cooling effect. The activity of the AGN is episodic such that the ICM - AGN interaction is largely self-regulating and well tuned (e.g. low AGN activity leads to more cooling of the ICM, cool gas sinks into the BCG and feeds the next activity cycle). The energy scale of these processes is remarkable - each AGN outburst is estimated to inject between 10^{58} and 10^{61} erg into the ICM. This amount of energy is sufficient to suppress cooling flows assuming a $\sim 10^8$ year long AGN duty cycles (time between two outbursts, Bîrzan et al. 2004; Rafferty et al. 2006). In addition to energy deposition, rising bubbles entrain the enriched gas around the BCG and provide a mean of metal transportation and mixing.

These fascinating processes have been studied in detail in many cool core systems, e.g.: M87, the nearest cool core, at the center of the Virgo cluster (Churazov et al. 2001; Forman et al. 2007; Simionescu et al. 2007, 2008, 2010; Werner et al. 2010), the Perseus cluster (Fabian et al.

2003a,b, 2006; Sanders and Fabian 2007), Hydra A (McNamara et al. 2000; Nulsen et al. 2002, 2005; Simionescu et al. 2009a,b), the cluster MS0735.6+7421, which has up to now the largest observed energy release ($\sim 10^{61}$ ergs), analysed by McNamara et al. (2005) and a couple of other systems. A comprehensive review of the field can be found in McNamara and Nulsen (2007).

2.2.4 X-ray scaling relations

In the previous section we have discussed some of the interesting ("micro-") physics present in clusters (and particularly in their cores). While this makes each system to some degree completely unique, there is also a lot of regularity found in the cluster population. For example the underlying DM halos are self-similar and easily scalable for different masses (Sect. 2.1). This gives hope that we can look at clusters also from a global, more reductive point-of-view. Ultimately, only a single cluster parameter - the total cluster mass - is the most fundamental link to the background cosmology.

Hydrostatic mass estimates

As the gas settles in the DM potential well during the cluster assembly phase (or after a major merger), it takes only about 1 Gyr until it reaches a quasi-hydrostatic equilibrium state. Under the assumptions of spherical symmetry the integrated total mass within a radius r can be derived from the pressure equilibrium equation:

$$\frac{dp_{\text{gas}}(r)}{dr} = -\rho_{\text{gas}}(r)\frac{G\,M_{\text{tot}}(<r)}{r^2} = \frac{k}{\mu\,m_{\text{p}}}\frac{d}{dr}\Big(\rho_{\text{gas}}(r)\,T_{\text{X}}(r)\Big)\,, \tag{2.11}$$

where μ is the mean molecular weight of the ICM ($\mu \approx 0.6$) and m_{p} is the proton mass. We can obtain the input gas density profile $\rho_{\text{gas}}(r)$ from X-ray surface brightness measurements (Sect. 2.2.2) and the temperature profile $T_{\text{X}}(r)$ from spatially resolved spectroscopy (typically fitting the spectra in circular bins). The total gravitating mass $M_{\text{tot}}(<r)$ mass within radius r is then

$$M_{\text{tot}}(<r) = -\frac{k\,T(r)\,r}{G\,\mu\,m_{\text{p}}}\left(\frac{d\ln\rho_{\text{gas}}}{d\ln r} + \frac{d\ln T}{d\ln r}\right)\,. \tag{2.12}$$

This approach of estimating the total cluster mass has however two important caveats. The first one is, that the mass estimate is only valid to the extent to which the thermal pressure equilibrium holds. If there is an additional pressure support in the ICM unaccounted by Eq. 2.12, then the hydrostatic mass estimate will be biased low. The extra support can originate from subsonic bulk motions of the gas and turbulences. Therefore the expectation is that this bias will be larger for disturbed clusters.

The extent of the systematic effect in X-ray mass measurements has been studied in many hydrodynamical N-body simulations, e.g. Lau et al. (2009); Piffaretti and Valdarnini (2008); Jeltema et al. (2008); Nagai et al. (2007); Rasia et al. (2006); Lewis et al. (2000) and Evrard (1990). All these simulations found a presence of the bias on roughly $\lesssim 10\%$ level (the range of biases is $\sim 5 - 25\%$, depending on the details of the simulations, radius of interest and several other criteria).

Beyond simulations, non-thermal pressure support can be quantified in real data by comparing gravitational lensing mass measurements (which are independent of the assumption of hydrostatic equilibrium) with X-ray estimates. This is a challenging task because lensing studies have their own systematics, e.g. projection effects, since the lensing signal is sensitive to all mass along the line of sight. A good understanding and control of these systematics is crucial for non-thermal pressure support studies. Currently, several X-ray - weak lensing samples have been constructed and the found X-ray mass bias is roughly in agreement with the predictions from simulations (e.g. Zhang et al. 2010; Richard et al. 2010; Mahdavi et al. 2008; Allen 1998, and references therein).

The second caveat of the Eq. 2.12 has an observational character. Using this equation to estimate the total mass of the system requires to have fairly deep X-ray data (e.g. in order to be able to measure the temperature one needs $\gtrsim 500$ counts per radial bin). This is not always possible, especially in survey settings, when we have typically around ~ 100 counts for the whole cluster. In these cases we can use the so-called *scaling relations* - relations between some simpler, observable parameter (e.g. the integrated luminosity within an aperture) and the total mass.

2.2.5   Self-similar scaling relations

The existence of simple scaling relations for clusters is a direct prediction of the virial theorem (Eq. 2.4), if a few assumptions hold (most of them we have already listed): A) spherical symmetry of clusters, B) ICM is in hydrostatic equilibrium, C) the gas mass fraction $f_{gas} = M_{gas}/M$ is constant, where M is the total mass, D) X-ray emission comes only from the bremsstrahlung contribution and E) the DM halos are self-similar. Kaiser (1986) derived the following relations:

M-T relation The virial Eq. 2.4 can under these assumptions be simplified to:

$$\frac{3kT}{\mu m_{\mathrm{p}}} - GM/r = 0 \,, \tag{2.13}$$

given that for a spherically symmetric cluster $M \propto r^3$ we have

$$T \propto \frac{M}{r} \propto M^{2/3} \tag{2.14}$$

L-T relation The integrated bolometric bremsstrahlung luminosity (assumption D) within the aperture r is equal to the volume integral of the emissivity given by Eq. 2.5. This gives the proportionality

$$L \propto \rho_{gas} T^{1/2} r^3 \propto T^{1/2} M \,, \tag{2.15}$$

where we utilized assumption C so that $\rho_{gas} \propto M_{gas}/r^3 \propto f_{gas} M/r^3 \propto const$. This yields simply

$$L \propto T^2 \,. \tag{2.16}$$

M-L relation Finally, plugging Eq. 2.14 into Eq. 2.16 we have the mass - luminosity relation

$$L \propto M^{4/3} \, . \tag{2.17}$$

M-Y_X and L-Y_X relations Kravtsov et al. (2006) suggested to use the Y_X parameter, an X-ray analogue to the integrated Compton parameter (see Eq. 2.34 in Sect. 2.2.6), as a low scatter mass proxy. The Y_X parameter is defined simply as the product of gas mass and temperature, $Y_X = M_{gas}T$. From the already derived relations we get:

$$Y_X \quad \propto \quad M^{5/3} \text{ and} \tag{2.18}$$
$$Y_X \quad \propto \quad L^{5/4} \, . \tag{2.19}$$

These relations, however, hold only for the virial values of the parameters at redshift zero. In practice we determine the observables in an aperture where the cluster density reaches a fixed overdensity δ with respect to the critical density of the Universe at the redshift of the cluster. Typical choices of δ are 200 (which is close to the virial overdensity in an Einstein-de Sitter Universe) and 500 (often close to the outermost radius at which we have X-ray coverage of the cluster with current instruments). This introduces an additional scaling factor[13] that can be expressed through the evolution factor of the Hubble parameter $E(z) = H(z)/H(z = 0)$, where $H(z)$ is the Hubble parameter at the cluster's redshift z. The final self-similar scaling relations for $\delta = 200$ are given by:

$$M_{200} \quad \propto \quad E(z)^{-1}T^{3/2} \tag{2.20}$$
$$L_{200} \quad \propto \quad E(z)T^2 \tag{2.21}$$
$$L_{200} \quad \propto \quad E(z)^{7/3}M_{200}^{4/3} \tag{2.22}$$
$$Y_{X,200} \quad \propto \quad E(z)^{2/5}M_{200}^{5/3} \tag{2.23}$$
$$Y_{X,200} \quad \propto \quad E(z)^{-9/5}L_{200}^{5/4}. \tag{2.24}$$

A large effort has been made to confirm the predicted dependencies and their redshift evolution. Currently, the scaling relations can be considered to be well established for nearby systems ($z \lesssim 0.3$), e.g. Markevitch (1998); Reiprich and Böhringer (2002); Pratt et al. (2009); Arnaud et al. (2007) and many others. In this range the redshift evolution seems consistent with the self-similar scenario, although the slopes can differ (e.g. the L-T relation is significantly steeper). In fact, it is the relations involving the luminosity that exhibit the largest deviations from the self-similar scaling relations. The deviations hint at non-negligible effect of non-gravitational processes, e.g. the heating and cooling mechanism described in Sect. 2.2.3. The feedback mechanisms then can lead to modifications of the gas mass fraction especially in the central regions of the clusters and thus to changes in luminosity (e.g. Böhringer et al., in prep.).

---

[13]Potentially an additional factor relating the ΛCDM cosmological model to the Einstein-de Sitter cosmology can also be introduced (for an overview see Böhringer et al., in prep.).

The evolution of the scaling relations at higher redshifts is still not well established. One of the obstacles is to obtain sizable samples of high redshift clusters ($z \gtrsim 0.8$). In addition, these samples have to be constructed from surveys with well controlled selection functions, since unaccounted selection effects can mask evolutionary effects (Stanek et al. 2006; Pacaud et al. 2006, 2007; Vikhlinin et al. 2009a; Mantz et al. 2010a). These issues are investigated in depth by Reichert et al. (submitted), who extends these studies beyond $z \gtrsim 0.8$.

2.2.6 The Sunyaev-Zel'dovich effect

In the previous chapters we focused mostly on X-ray studies of the ICM. The thermal electron population of the ICM, however, also interacts with the photons of the cosmic microwave background (CMB) leading to the so-called *thermal Sunyaev-Zel'dovich effect* (SZE), first described by Sunyaev and Zel'dovich (1970, 1972). We give here a brief overview of the physical processes behind the SZE following the approach of Birkinshaw (1999).

Elements of the SZE

Electrons in the ICM can scatter low energy CMB photons via inverse Compton scattering. Although the scatterings are usually still referred to as inverse-Compton processes, they might better be described in this limit as Thomson scattering, since the thermal electron population is almost completely non-relativistic[14] and the CMB photons have low energy. For these low-energy interactions the scattering optical depth is $\tau_e \approx n_e\,\sigma_T\,R_{\mathrm{eff}} \sim 10^{-2}$, where σ_T is the Thomson scattering cross-section, n_e the electron density and R_{eff} the effective geometrical light path length (e.g. roughly the cluster's diameter). On average a single scattering produces only a small change of the mean photon energy $(\Delta\nu/\nu) \approx (kT/m_e c^2) \sim 10^{-2}$, where m_e is the electron mass. The overall change in brightness of the CMB is on the 10^{-4} level, i.e. roughly an order of magnitude larger than the cosmological signal from the primordial anisotropies.

The change in the photon energy (frequency) is described by the Compton scattering equation:

$$\epsilon' = \frac{\epsilon}{1 + \frac{\epsilon}{m_e c^2}\,(1 - \cos\phi)}\,, \tag{2.25}$$

under the assumption that the electron is at rest before the interaction ($\epsilon \ll m_e c^2$). The photon energies before and after the interaction are ϵ and ϵ', respectively, and ϕ is the angle by which the photon is deflected in the encounter (the angle between the post-scattering paths of the electron and deflected photon).

Given that both the CMB and the Maxwellian velocity distribution of the electrons are almost isotropic, photons scattered away from our line of sight are replaced by photons from other directions scattered *into* our line of sight. This means that there is no observable change in the number of detected photons independently from whether there is an intervening cluster or not!

---

[14]ICM temperatures are $\lesssim 10$ keV, except for a few cases where shock heating occurs, but this is always only in small, confined regions.

How is then possible that we indeed see a change in the brightness of the CMB sky towards clusters?

The reason for this is, that although the number of photons is conserved in these processes their energy spectrum is modified. The CMB photons (a low temperature system) and the ICM gas (hot system) are in interaction and thus energy flows from the ICM to the CMB photons as required by the second law of thermodynamics. This flow is mediated on the particle level by the fact, that the up-scattering of photons ($\epsilon' > \epsilon$ in Eq. 2.25) is slightly more likely than the converse.[15] We will provide here a brief simplified derivation which gives insight into the basic principles of this effect.

Let us denote $\beta = v/c$, where v is the electron velocity and c the speed of light (for a 4 keV plasma $\beta \approx 0.14$) and further in the electron rest frame we denote the photon impact angle to be θ and the angle after scattering θ'. Eq. 2.25 then can be rewritten as

$$\nu' = \nu\,(1 + \beta\mu')\,(1 - \beta\mu)^{-1}\,, \tag{2.26}$$

where ν and ν' are the pre- and post-scattering photon frequencies and we denoted $\mu = \cos\theta$. It is convenient to express the resulting scattering in terms of the logarithmic frequency shift defined as

$$s = \log(\nu'/\nu)\,. \tag{2.27}$$

Finally, the probability that the photon experiences a frequency shift s after a single scattering on an electron with velocity β is:

$$P(s,\beta)\,ds = \int p(\mu)\,d\mu\,\phi(\mu',\mu)\left(\frac{d\mu'}{ds}\right)ds\,, \tag{2.28}$$

where $p(\mu)\,d\mu$ is the probability of the photon having the impact angle θ before the scattering (just from the simple Thomson scattering geometry) and $\phi(\mu',\mu)\,d\mu'$ the probability of scattering from this angle to angle θ'. The $\phi(\mu',\mu)$ distribution function was derived by Chandrasekhar (1950) and we display only the final $P(s,\beta)$ function for several values of β in Fig. 2.6 (left).

As can be seen, $P(s,\beta)$ is slightly asymmetric, with up-scatterings (positive s) being slightly more likely. The asymmetry and broadening increases with increasing mean electron velocity (i.e. increasing ICM temperature). Since the velocity distribution of the electrons is Maxwellian (we denote it $p_e(\beta)$), the probability of a frequency shift s for a single photon and single scattering is given by the convolution:

$$P_1(s) = \int_{\beta_{\min}}^{1} p_e(\beta)\,d\beta\,P(s,\beta). \tag{2.29}$$

Electrons with velocities smaller than $\beta_{\min}$ can not cause a frequency shift s. The effect of single scattering on the CMB spectrum then is

$$I(\nu') = \int_{-\infty}^{\infty} P_1(s)\,I_0(\nu)\,ds\,, \tag{2.30}$$

---

[15]Photons interact with more "head-on" electrons than those traveling in the same direction as the photon.
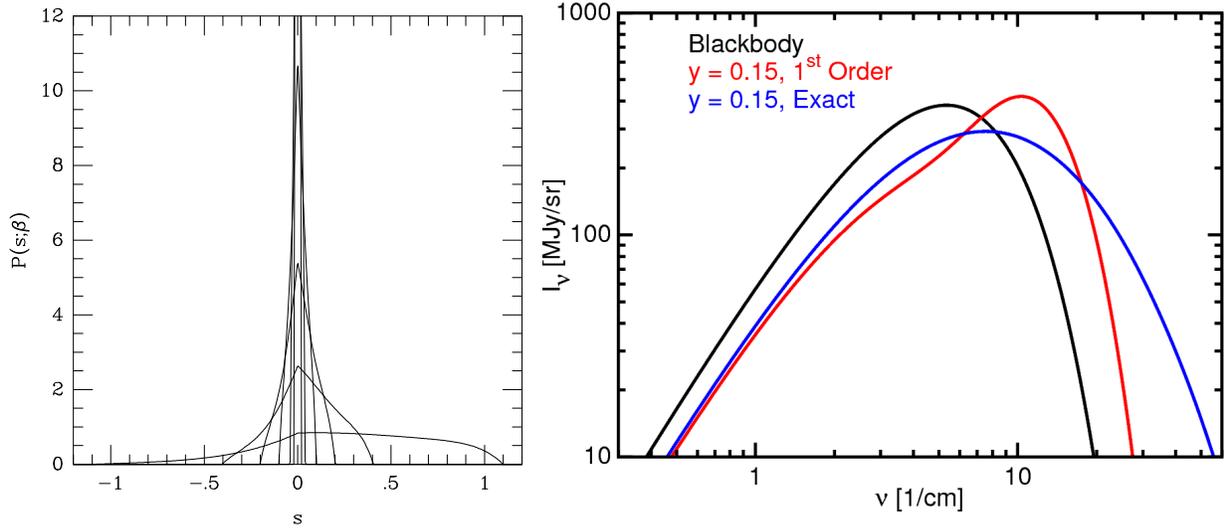
Figure 2.6: **Left:** The inverse Compton scattering probability function $P(s, \beta)$ (Eq. 2.28), for $\beta = 0.01, 0.02, 0.05, 0.10, 0.20$ and 0.50, where $\beta = v/c$. The probability distribution is increasingly asymmetric and broadened as β increases. **Right:** The spectrum of the CMB (black body, black line) and its distortion after a passage through the ICM of an unrealistically massive cluster with a Compton parameter of $y = 0.15$. The red line shows the curve often displayed in literature (e.g. Sunyaev and Zel'dovich 1980; Carlstrom et al. 2002), but which was obtained by a first order approximation not applicable to this high values of y. The blue curve shows the exact non-relativistic solution for $y = 0.15$. See text for more discussion. Image courtesy of E. L. Wright, `http://www.astro.ucla.edu/~wright/SZ-spectrum.html`.

where $I_0(\nu)$ is the incident CMB spectrum (black-body):

$$I_0(\nu) = \frac{2 \, h \, \nu^3}{c^2} \left(e^{h\nu/kT_{\mathrm{CMB}}} - 1 \right)^{-1} . \tag{2.31}$$

The purpose of this simplified treatment we provided here was to highlight the basic mechanisms at work. We made several important simplifications - we allowed only a single scattering and assumed the Thomson scattering to hold for all values of β. The proper description of the non-relativistic scattering process in this case is provided by the Kompaneets equation (Kompaneets 1956) and the full derivation of the impact of the electrons on the CMB spectrum was first given by Sunyaev and Zel'dovich (1970, 1972). In the following we will provide only the final results and their implications for cluster observations.

Observational signatures of the SZE

The SZE causes an increase in the CMB intensity in the high frequency (Wien) part of the spectrum and a decrement in the Rayleigh-Jeans tail. The transition occurs at a frequency of $\nu_0 \approx 218$ GHz, equivalent to a wavelength $\lambda \approx 0.14$ cm. Clusters thus can be seen as "shadows"

in the background (in the Rayleigh-Jeans part of the spectrum) caused by a minuscule decrease of the order of ~mK in the temperature surface brightness of the CMB.

The shape of the SZE spectrum is depicted in Fig. 2.6 (right). The original black body spectrum is shown in black. The red line shows the distorted spectrum for an unrealistically massive cluster with $y = 0.15$ (roughly 1000 times more massive than real clusters). As was pointed out by E. L. Wright[16] this curve (to be found in e.g. Sunyaev and Zel'dovich 1980; Carlstrom et al. 2002), was obtained using the first order approximation in Sunyaev and Zel'dovich (1980) (their Eq. A7) to the Sunyaev-Zel'dovich effect, and is not applicable for $y = 0.15$. The exact solution is shown in blue (computed using Eq. A8 of Sunyaev and Zel'dovich 1980) and is significantly wider than the approximation. Note that this still does not include relativistic corrections. The first order approximation is still appropriate for real clusters.

The decrement in the CMB is equal to

$$\Delta I(\nu) = -2\, y\, I(\nu) \,, \tag{2.32}$$

where y is the so-called *Compton parameter* defined as

$$y \equiv \frac{\sigma_T\, k_B}{m_e\, c^2} \int T_e\, n_e\, dl \,, \tag{2.33}$$

The integration runs along the line-of-sight. The decrement $\Delta I(\nu)$ is defined as the difference in the CMB intensity between the distorted spectrum in the direction of the cluster and the black body spectrum of the unobstructed CMB.

Eq. 2.33 shows that the SZE is completely redshift independent.[17] This is very different from the X-ray observations, where the cosmological redshift dimming causes a fast decline of the surface brightness $\propto (1 + z)^{-4}$ (Sect. 2.2.2). In the case of SZE the redshift dimming is exactly compensated by the increase of the CMB intensity $\propto (1 + z)^4$ (at higher redshift we are probing a younger Universe where the CMB temperature is higher). This is illustrated in Fig. 2.7 on the example of three clusters at redshifts between $0.2 - 0.8$. The dimming of the X-rays is evident, while the SZE decrement is comparable even for the most distant object. This gives SZE surveys the ability to have a nearly redshift-independent selection function and thus allow to detect many distant clusters.

This advantage started to be utilized by large area surveys carried out by large, single dish telescopes: the South Pole Telescope (SPT, Staniszewski et al. 2009; Vanderlinde et al. 2010; Williamson et al. 2011; Foley et al. 2011), the Atacama Cosmology Telescope (ACT, Marriage et al. 2010; Hincks et al. 2010) and by the *Planck* space mission (Planck Collaboration et al. 2011a,b). The delivered samples have significantly higher median redshifts compared to X-ray selected cluster catalogs. We provide a brief overview of the advances in the field in Sect. 5.1.

An additional feature of the SZE signal is that the Compton parameter is proportional to the integrated pressure along the line-of-sight (compare Eq. 2.33 with the ideal gas pressure

---

[16]http://www.astro.ucla.edu/~wright/SZ-spectrum.html

[17]The integrated Compton parameter within a solid angle would depend on the aperture size and thus the angular distance.
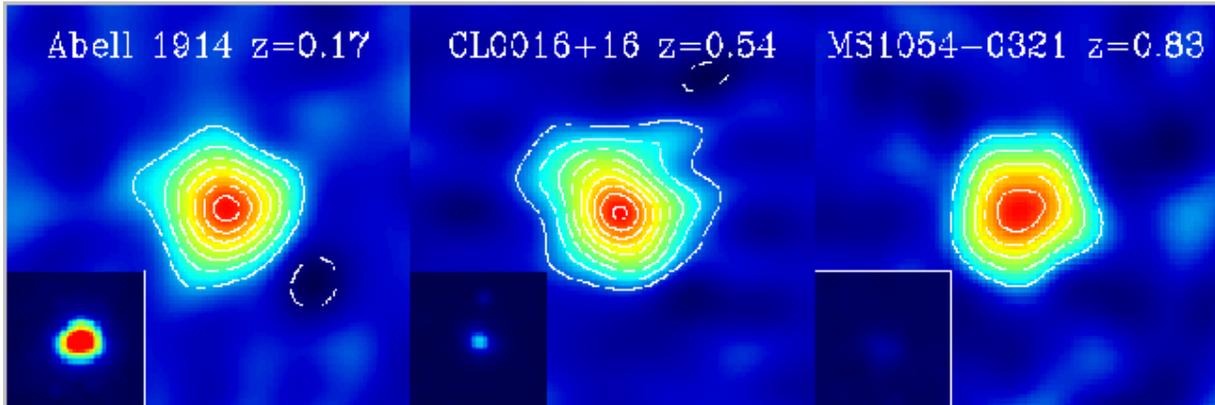
Figure 2.7: Comparison of SZE images and X-ray images (small insets, from *ROSAT*) of three clusters at redshifts $z = 0.2, 0.5$ and 0.8. While the SZE signal stays comparable across the whole distance range, the X-ray surface brightness is quickly decreasing with the redshift. This demonstrates the great strength of SZE observations to detect distant clusters. Credit: J. Carlstrom and J. Mohr, 2002.

$p = n\,k\,T$). The surface area integrated Compton parameter is therefore

$$Y = \int y\,\mathrm{d}A \approx \int n_{\mathrm{e}} T_{\mathrm{e}}\,\mathrm{d}V \approx M_{\mathrm{gas}} T_{\mathrm{e}}\,, \tag{2.34}$$

which shows that Y is proportional to the product of gas mass and temperature, and is thus expected to be a good, robust total cluster mass indicator with low scatter, relatively insensitive to the dynamical state of a cluster and a nearly self-similar evolution with redshift. This was confirmed by several cosmological simulations (da Silva et al. 2004; Motl et al. 2005; Nagai 2006) and by now also by observational data (Planck Collaboration et al. 2011b; Melin et al. 2011; Andersson et al. 2010; Afshordi et al. 2007) and see also Sect. 6.3.

More details on the SZE effect and related issues (such as the kinematic SZE, non-thermal SZE and relativistic corrections) can be found in the reviews of Birkinshaw (1999); Carlstrom et al. (2002) and Rephaeli (1995).

2.3 The galaxy population of the clusters

Although the galaxy populations of clusters contribute only $\lesssim 5\%$ to the total mass (roughly one third of the baryonic mass), they were the first markers that allowed clusters to be recognized as distinct astrophysical objects. Indeed, the first cluster catalogs were compiled by looking for galaxy overdensities by Abell (1958) and Zwicky and Kowal (1968).

Each cluster comprises hundreds to thousand galaxies bound by the gravitational potential of the DM halo (Fig. 2.8). The number of galaxies given a suitable selection criterion - the cluster richness - was one of the first cluster classification schemes (first proposed by Abell 1958).
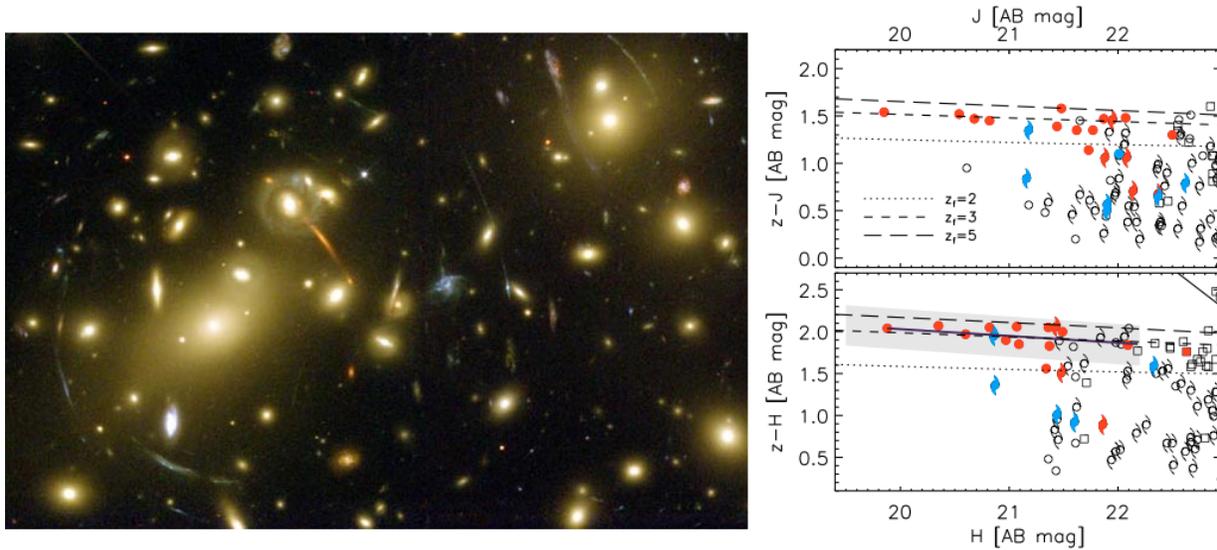
Figure 2.8: **Left:** Optical image of the cluster Abell 2218. The cluster is an exceptional example of a gravitational lens. Numerous background galaxies are multiply lensed and some even distorted into large arcs. The supergiant brightest cluster galaxy is coincident with the center of the lensing potential. Credit: Hubble Space Telescope, NASA. **Right:** Colormagnitude diagrams of the very distant cluster XMMU J2235-2557. Although the cluster is at redshift $z = 1.39$, it exhibits a well populated, very tight red sequence - a good evidence of the evolved state of the clusters galaxy population. Only spectroscopic members and galaxies with photoz values in the range $0.96 < z < 1.82$ are shown. The shape of all symbols are coded according to their morphological classification: circles for early-type galaxies (ellipticals and S0), spirals for late-type galaxies and squares for faint objects with no reliable classification. Filled symbols show spectroscopically confirmed members with (in blue) and without (in red) [O II] emission lines. The dotted, dashed and longdashed lines show the expected location of the red sequence based on the Kodama and Arimoto (1997) models for different formation redshifts. The dark purple line in the lower panel shows a fit to the red sequence galaxies within the gray shaded region. Figure is taken from Strazzullo et al. (2010).

The fact that these galaxies really belong to a distinct system, rather than being only a fluctuation in the background galaxy number counts, can be established by looking at their morphological and photometric properties.[18]

Galaxy evolution in cluster environments

It was realised early in the optical studies that the morphological census of the galaxies within clusters is different compared to the field galaxies (Oemler 1974; Dressler 1980). This so-called morphology-density relation describes the decrease of the fraction of late-type galaxies (e.g.

---

[18]Of course, the definitive test is to obtain spectroscopy for these galaxies and confirm them to be at the same redshift.

spirals) when moving from the field towards more dense regions (i.e. cluster cores). At the same time the fraction of early-type galaxies (ellipticals and S0) is increasing. This difference compared to field galaxies gives a hint that the environment has to play an important role in the evolution of the galaxies. In particular, the denser environment facilitates more frequent galaxy-galaxy interactions as well as the interaction with the ICM via mergers and colorfully named processes like gas stripping, strangulation and galaxy harassment. Boselli and Gavazzi (2006) provide a review of how these dire processes affect the evolution of unsuspecting galaxies.

Mergers and stripping of material from galaxies also leads to creation of the *intracluster light* (ICL) - the aggregate of stars dispersed in the intergalactic space inside the cluster. Observations of the ICL are very hard due to its low surface brightness and complications in separating it from extended stellar halos of the galaxies. Therefore, the total amount of ICL in clusters and galaxy groups is not very well constrained. Estimates range from 5% to 25% of the total cluster light (e.g. Da Rocha et al. 2008; Krick and Bernstein 2007; Feldmeier et al. 2004a,b), but could be up to 50% in the immediate region of the brightest cluster galaxy (BCG, Zibetti 2008). The properties of the BCGs and the ICL suggest a direct physical link between them (e.g. their colors and elongation axes are similar). With deeper observations and improvement in the methodology we will be able to get better constraints on the ICL fraction and investigate its properties also in intermediate systems.

Major morphological transformations also appear to be linked to quenching of star formation. The optical properties of early-type galaxies are determined by their old population of cool stars, while late-type galaxies are still star forming and have a large population of hot young stars dominating their optical emission. The prevalence of passively evolving (i.e. not showing signs of on-going star formation) red elliptical galaxies is observable in the color-magnitude diagram of the cluster as the so-called *red sequence* (see Sect. 2.3.2).

2.3.1 Brightest cluster galaxies

One of the most striking example of environmental effects on the evolution of galaxies is the presence of the so-called brightest cluster galaxies (BCG) in most clusters. These galaxies are extremely massive, luminous elliptical[19] galaxies with very large spatial extents. They are usually found very close to the center of the DM potential wells and thus coinciding with the peak of the X-ray emission (except for extreme cases like the Bullet cluster). BCGs often harbor an AGN, which in some cases can undergo stages of outbursts and thus interact with the ICM (this is connected to the problematics of cool cores, see Sect. 2.2.3).

The luminosity gap between the BCG and the second ranked galaxy is so large that it has to be explained by a special formation mechanism (e.g. Loh and Strauss 2006). A possible formation scenario was proposed by Ostriker and Tremaine (1975) - the so-called galactic cannibalism model. In this picture, at the cluster center where the galaxy density is the largest, the BCG grows through successive merging and coalescence with its neighbour galaxies. The process is

---

[19]In fact, more than 50% of the BCGs belong to a special sub-type of ellipticals designated as the cD galaxies (from "central dominant"). Galaxies of this type are found in cluster cores exclusively (and typically in the more massive, mature clusters). Only supergiant ellipticals with very extended stellar halos are included in this sub-type.

driven by dynamical friction and the often very extended halo of the BCG is created from the tidally stripped material from the merging galaxies.

Dubinski (1998) has however shown that cannibalism is not sufficient for the full build up of BCGs. Currently the most favoured scenario is known as the *dry merger* model and is supported by both simulations (Puchwein et al. 2010; Murante et al. 2004; De Lucia and Blaizot 2007) and observations (e.g. Whiley et al. 2008; Bell et al. 2006). A dry merger occurs between two bright, passive galaxies and does not trigger star formation. Therefore the color of the coalesced galaxy does not change significantly, which explains the apparent flattening of the RS at the bright end observed in some clusters (e.g. Skelton et al. 2009). This model can also give account for the flat surface brightness and color profiles (compered to standard ellipticals, see e.g. Tonry 1987; von der Linden et al. 2007; Mackie 1992; Andreon et al. 1995; Roche et al. 2010) and relatively uniform stellar population of the BCGs across all radii (Brough et al. 2007).

2.3.2   The cluster red sequence

The color-magnitude[20] diagram (CMD) is a powerful diagnostic tool for optical cluster studies. It allows to roughly estimate the cluster redshift in cases when its not available. In cases where we have spectroscopic redshifts it serves as a great tool to study the galaxy population and its star-formation history.

Baum (1959) noticed that the red cluster galaxies occupy a special locus in a color-magnitude plane clustering in a tight sequence populated by red galaxies - the so-called *red sequence* (RS). This sequence is quite universal, with the color difference in first approximation stemming from the cosmological redshift. If we assume a simple stellar population model for the galaxies, we can use the position of the RS to get an estimate of the cluster redshift (this is one of the possible approaches to obtain photometric redshifts, see also Sect. 5.4).

If the redshift of a cluster is known, one can estimate the age of the stellar population from the normalization of the RS and from the scatter around the relation we can get information on the star formation history. If the star formation occurred in a single, short time period, the stellar populations of the RS galaxies will be similar and the scatter will be small. The slope of the RS (more luminous RS galaxies are redder) is attributed to a so-called *metallicity sequence* (Kodama and Arimoto 1997). Supernova explosions enrich the intrastellar gas in the galaxy with metals. The retention of this gas is more effective for the more massive galaxies. Metal rich gas however produces stellar populations that are cooler (thus redder) than stars in metal poor environment.

As we approach higher redshifts ($z \approx 1$ and beyond), we are on average observing the clusters and their galactic population in earlier evolutionary stages. The expectation is that the red sequences will be less tight and not as well populated as in the case of low redshift clusters. However many high redshift clusters (especially the more massive ones) do exhibit well developed RS even at these high redshift. On the other hand, lower mass systems might not yet have well

---

[20]The "color" is defined as the difference of observed magnitudes through two filters: color = $m(\lambda_1) - m(\lambda_2)$, where $m(\lambda)$ is the magnitude measured in a band centered on the wavelength λ. The standard use is to require $\lambda_1 < \lambda_2$, so that higher value of the color means a "redder" appearance relative to the base magnitude.

populated RS (as an example see Sect. 7.3.3).

Another redshift dependent effect is the so-called *Butcher-Oemler effect* (Butcher and Oemler 1978), manifesting itself as an increase of the blue galaxy fraction with increasing redshift. The effect is quite sensitive to background galaxy contamination and potential selection effects originating from the definition of the blue galaxies, but in many cases it has been confirmed also by spectroscopic studies. In fact, there is also a *spectroscopic* Butcher-Oemler effect - the increase of the fraction of cluster galaxies exhibiting spectroscopic features typical for young stellar populations (e.g. Dressler et al. 1999; Poggianti et al. 1999, 2006).

2.3.3 The galaxy luminosity function

Another important global characteristic of the cluster galaxy population is the *luminosity function* defined as the number density ϕ of galaxies with a given luminosity L. The most widely used parametrization of the luminosity function was given by Schechter (1976):

$$\phi(L)\,dL = \phi_0 \left(\frac{L}{L^*}\right)^\alpha \exp\left(\frac{L}{L^*}\right) \frac{dL}{L^*}\,, \tag{2.35}$$

where ϕ_0 is the normalization of the number density, L^* the characteristic luminosity and α the faint end slope ($\alpha = 1 - 1.5$). The distribution predicts an exponential decrease of the number density of galaxies with luminosities $> L^*$, while the behavior (steepness) of the faint end is determined by the slope parameter. An example is displayed in Fig. 2.9. The luminosity function normalization is typically parametrized by the m^* magnitude, defined as the observed magnitude in the given band corresponding to a galaxy with a luminosity L^*. The parameters of the Schechter function depend on the galaxy selection criteria and it holds only if galaxies of a single type (e.g. ellipticals) are included.

The observed universality of the Schechter function is quite remarkable and hints at a deeper underlying physical cause, i.e. the galaxy luminosity depends on its stellar content and star formation activity, which can be linked to the total mass of the galaxy and its merger and star formation history. The *mass* distribution of the galaxies is connected to the mass distribution of DM halos for which the Press-Schechter (Press and Schechter 1974) distribution is still a good approximation (and has the same functional form as Eq. 2.35). The total integrated luminosity of the cluster galaxies is thus a relatively good cluster mass proxy (albeit inferior to X-ray and SZ mass proxies, see Sect. 2.2.4). The Schechter function is then often used to extrapolate the total luminosity in order to include the contributions of the faint (but numerous) galaxies not observed directly.

2.3.4 Optical cluster detection

As we mentioned, clusters were first identified in optical data. Since the pioneering work of Abell (1958) and Zwicky and Kowal (1968) much progress has been made in the field of optical cluster searches. However, the basic principle - searching for overdensities in the number density of galaxies - stayed the same.[21]

---

[21]Although, fortunately, the work has been automatized, saving us from Abell's toils.
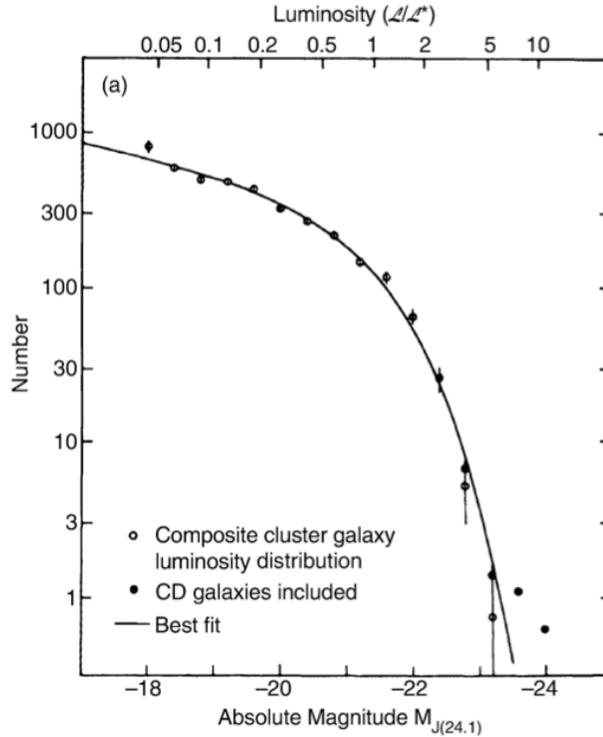
Figure 2.9: The Schechter galaxy luminosity function for 13 clusters of galaxies. The top x-axis shows the L^* normalised luminosities, while the bottom axis the absolute J band magnitudes. Credit: Schneider (2006).

The most common detection algorithms are based on the *friends-of-friends* (FoF) algorithm (and its variations) first proposed by Huchra and Geller (1982); Geller and Huchra (1983). The algorithm aims at linking neighbouring galaxies within a chosen linking distance. If the density of linked galaxies in an area exceeds the density in a field region at the required minimal significance level, the galaxies are flagged as a cluster candidate.

An alternative approach is to use a *Voronoi tesselation algorithm* to partition the sky area around each galaxy. By construction[22] the area of the cells in dense regions (like clusters) is smaller than in field regions. An example of this algorithm is the Voronoi Galaxy Cluster Finder of Ramella et al. (2001).

While both algorithms can in principle be run only using the information on the two dimensional distribution of galaxies in the plane of sky, much improvement can be made if we are able to incorporate additional information into the search method and/or use some of the special features of the cluster galaxy population. These markers, such as those we described in previous sections, can help us design suitable selection criteria which increase the signal-to-noise contrast of the cluster searches.

Since clusters are peaks in the three dimensional galaxy distributions, the simplest extension

---

[22]A Voronoi cell contains all the points of the plane (or volume in > 2 dimensional space) closer to the center of the given cell than to any other central point.

of the FoF detection algorithms is to use the redshift information (if available) in the form of spectroscopic or photometric redshifts. This approach was implemented in many spectroscopic surveys, e.g. the Center for Astrophysics Redshift Survey (CfA survey, Geller and Huchra 1983), the Las Campanas Redshift Survey (Tucker et al. 2000), the Sloan Digital Sky Survey (SDSS, Berlind et al. 2006), the Two Degree Field Galaxy Redshift Survey (2dFGRS, Eke et al. 2004), the 2-Micron All Sky Redshift Survey (2MRS, Crook et al. 2007) and many more (see also references in the listed works).

Another information that can be used is that the cluster galaxies conform to the Schechter luminosity function (Eq. 2.35). In this approach the spatial and luminosity distribution at the given sky position are jointly modeled and assumed to be a superposition of a background component and contribution from the cluster population. This approach is the so-called *matched filter approach* introduced by the Palomar Distant Clusters Survey Postman et al. (1996).

As we have seen in Sect. 2.3.2, the cluster red sequence is a very universal characteristic of clusters. The Cluster Red Sequence (CRS) detection method of Gladders and Yee (2000) utilizes this fact by looking for cluster overdensities in galaxy catalogs which are successively sliced in color allowing to find red sequences at different redshift. Conveniently, one obtains this way also an estimate of the cluster's redshift. While this detection algorithm is insensitive to clusters without well developed RS (e.g. very young systems and particularly high redshift, low mass systems), mature, massive clusters have been found to have a RS at place already at high redshifts, $z > 1$ (e.g. at $z \approx 1.4$ in Fig. 2.8).

The maxBCG cluster detection method (Bahcall et al. 2003) is another method that relies on the presence of a RS in the cluster, but also complements it with information on galaxy morphology particularly looking for a population of ellipticals led by a BCG.

A host of other methods exists and can be utilized in different conditions (e.g. weak lensing shear cluster detection, surface brightness fluctuation method for drift-scan surveys etc.). Combining any (or several) described methods with other available multi-wavelength data (e.g. Schuecker et al. 2004) is also very promising.

2.4   Overview of cluster review papers

The aim of this chapter was to give only a brief overview of the main topics concerning cluster physics and cosmology. Fortunately, there are several good reviews covering all these aspects (and several additional) in much more detail. We provide here an annotated (but certainly non-exhaustive) list of valuable papers that provide good introductions to many of the topics and that might be particularly of interest for people who are new to the field.

Historically, the first major cluster review is by Sarazin (1988). It focuses is on the ICM and X-ray observations, but the cluster galaxy population is also covered. The review is somewhat outdated but quite comprehensive. A newer review by Voit (2005) has a comparatively broad scope with a lot of space devoted to the process of linking the theoretical cosmological predictions to the actual cluster observables. The second focus of the review is the thermodynamics of the ICM.

To the same topic (and particularly the non-thermal processes) is dedicated the series of

reviews led by Kaastra et al. (2008a).[23] From this collection we name only the general overviews by Diaferio et al. (2008) and Kaastra et al. (2008b) and overview of non-thermal processes by Rephaeli et al. (2008). The rest of the reviews explore these and several other topics on a deeper level and are also very worthwhile.

The processes of metal enrichment of the ICM and their X-ray diagnostics are covered by Schindler and Diaferio (2008); Werner et al. (2008). These topics as well as a state-of-the-art review of topics of X-ray spectroscopy are to be found in Böhringer and Werner (2010). Physics of cluster mergers is explored in Sarazin (2002) and the connected topics of shocks and cold fronts are discussed (and richly illustrated) by Markevitch and Vikhlinin (2007). The current status of the cool core problem is summarized in Peterson and Fabian (2006) and the associated question of heating and the ICM - AGN interaction is reviewed by McNamara and Nulsen (2007).

A comprehensive derivation of the Sunyaev-Zel'dovich effect, its observations and cosmological studies are covered in the review papers by Birkinshaw (1999), Rephaeli (1995) and Carlstrom et al. (2002). While we did not devote much space to the optical (and infrared) properties of the clusters a thorough review with many further references can be found in Biviano (2008). Cluster environment has a very large impact on the evolution of its galaxies. These processes are reviewed by Boselli and Gavazzi (2006).

Our current understanding of clusters does not rely only on observations, but also on the knowledge gained by simulations. In the recent years there was a plethora of review papers covering many aspects of this extensive field. We will name only few: Borgani et al. (2008a,b); Dolag et al. (2008a,b); Borgani and Kravtsov (2009); Norman (2010).

Besides these review papers, a general, entry level introduction to clusters can be also found in the textbook of Schneider (2006) and in the review collection of Plionis et al. (2008). The structure formation processes and the growth of clusters in their cosmological environment are described in several text books and review articles, e.g. Peebles (1993), Dodelson (2003) and Padmanabhan (1999). We provide a brief overview of these topics in the next chapter.

---

[23]The ADS code of the review collection is "2008SSRv..134".

Chapter 3

Tracing cosmic evolution with clusters of galaxies

Clusters are the nodal points of the cosmic web and the most massive virialized objects in the present Universe. The most fundamental link between the cluster population and the background cosmology arises through the dependence of the cluster abundance and its time-evolution on the cosmological parameters. This connection is described by the theory of structure formation.

3.1 Structure formation in the Universe

The model that best describes the structure formation, as seen in observational data and simulations, is the so-called *bottom-up hierarchical model*. In this picture, the quantum fluctuations in the post-inflationary Universe seed the initial density perturbations in the matter field. As we learn from the CMB temperature fluctuations, the matter density field at redshift $z \approx 1100$ contained inhomogeneities at the level of one part in 10^5. The density field can be described at location $\mathbf{x}$ by the relative density contrast

$$\delta(\mathbf{x}, t) = \frac{\rho(\mathbf{x}, t) - \overline{\rho}(t)}{\overline{\rho}(t)} \, , \tag{3.1}$$

taken with respect to the spatially averaged matter density $\overline{\rho}(t)$ at time t. Overdense regions ($\delta > 0$) grow by gravitationally attracting matter from their neighbourhood. While an overdense region continues to accrete more matter, its expansion is gradually slowing down with respect to its environment. The evolution of the density field is linear as long as the density contrast is small ($|\delta| \ll 1$). Eventually, the density of a region can reach the critical density and then it starts to recollapse in a time-symmetric fashion (i.e. the recollapse time would be equal to the time taken to reach critical density - assuming that the overdensity collapses to a point mass).

The above described scenario is the so-called *spherical top hat collapse model*. The underlying idea of this approach is based on the Birkhoff theorem within the framework of the theory general of relativity, which states that a spherically symmetric subregion can evolve independently from its background (analogously to the evolution of a closed Universe). This simplified

approach neglects possible deviations from spherical symmetry, external tidal forces, etc., but is a good description for the initial (linear) phases of the overdensity growth. Once however δ approaches unity the evolution of the collapsing region becomes non-linear. While some insight even into this regime can be obtained analytically with the Press-Schechter formalism (see next section), ultimately the most realistic description of structure formation can be obtained only from large cosmological simulations such as the *Millenium Run* (see Fig. 2.2, Springel et al. 2005).

For real systems, rather than collapsing to a point mass, the recollapse gives rise to a fully formed, virialized dark matter halo with some gas content. In the bottom-up hierarchical structure formation model the first halos to collapse are the galactic ones and with passing time larger and larger halos are formed, eventually up to cluster scales in the present Universe. The virialization itself is mainly driven by the *violent relaxation* processes (Lynden-Bell 1967) and to a minor extent by two body interactions and dynamical friction. Note that these processes are of course not part of the spherical collapse model but rather its extension to the final phases of cluster formation.

3.1.1 Cluster mass function

Now that we have an insight into the evolution of a single dark matter halo in the expanding Universe, we can look at the ensemble properties of the whole population. A simple analytical description is provided by the Press-Schechter formalism (Press and Schechter 1974), which in its original form is based on the spherical top hat model of halo collapse. The formalism is based on the observations that even though virialized objects are non-linear structures, the non-linear evolutionary processes should not significantly modify the *mass* contained in collapsed objects. In addition, the initial density field $\rho(\mathbf{x}, t_0)$ is approximately Gaussian and thus a simplified linear model is expected to provide a good description of the *mass function $n(M, z)$* - the spatial density of halos with virial mass M at redshift z.

In order to describe the growth of overdensities, let us denote δ_c to be the density contrast in the units of *critical* density of the Universe $\rho_c = 3H_0^2/8\pi G$ (as opposed to the mean matter density used in Eq. 3.1). In order to obtain a reference value, in the idealized spherical collapse model the point of virialization is taken to be the moment when the homogeneous sphere would recollapse to a point mass. The virial density contrast can be obtained by linear extrapolation of the time-symmetric recollapse and its value is $\delta_{sc}^v \approx 1.69$ in an Einstein-de Sitter cosmology[1] ($\Omega_M = 1$, $\Omega_{DE} = 0$, which also implies $\rho_c = \overline{\rho}_M$).

In the linear model, the growth of the density perturbations is described by the growth factor $D(z)$. The linearized overdensity of an object that virialized at redshift z has grown by

$$\delta_c(z) = \delta_{sc}^v D(z = 0)D(z)^{-1}, \tag{3.2}$$

---

[1]Although at present epoch the energy density of the Universe is dominated by the dark energy contribution, at earlier epochs, when the initial phases of cluster formation occurred, the matter density Ω_M is close to unity. Kitayama and Suto (1996) provide a formula to calculate δ_{sc} for arbitrary Ω_M.

where the linear growth factor (e.g. Carroll et al. 1992) is defined as

$$D(z) = 2.5 \, \Omega_m H_0^2 H(z) \int_z^\infty \frac{(1 + z')}{H(z')^3} \mathrm{d}z' \,, \tag{3.3}$$

and $H(z)$ is the Hubble parameter at redshift z,

$$H(z) = H_0 \sqrt{\Omega_m (1 + z)^3 + \Omega_\Lambda} \,. \tag{3.4}$$

Given the assumed Gaussian distribution of overdensities, the probability of a given object with mass M having an overdensity larger than δ_c is

$$p(\delta_c(z), M) = \frac{1}{\sqrt{2\pi}\sigma} \int_{\delta_c(z)}^\infty \exp(-\delta^2/2\sigma^2) \mathrm{d}\delta = \frac{1}{2}\mathrm{erfc}\left(\frac{\delta}{\sqrt{2}\sigma}\right) \,, \tag{3.5}$$

where erfc(x) is the so-called error function. The number of virialized halos of a given mass depends on the mean matter density (the closer is the density to the critical value the more regions can cross-over and start to recollaps). The second moment of the matter density distribution - the variance - is, however, also important. Large variance implies broader wings of the distribution and thus also more regions with density above the critical threshold. The variance of the density distribution $\sigma(M, z)^2$ has to be specified at a certain mass scale M, which is practically done by smoothing the matter density field at this scale by an appropriate filtering function W (window function). The variance thus can be written as

$$\sigma(M, z)^2 = \frac{1}{2\pi^2} \int_0^\infty k^2 P(k, z) |W(k)|^2 \mathrm{d}k \,. \tag{3.6}$$

The integration is for simplicity performed in the Fourier space, where the convolution of the matter power spectrum $P(k, z)$ (see Sect. 3.3) with the window function $W(k)$ is a simple multiplication. The wavenumber k is given by the inverse length scale. In the Press-Schechter formalism, the window function is a top-hat filter and the mass and linear scales are related simply through $R(M) = \sqrt[3]{3M/(4\pi\bar{\rho})}$. The variance is usually normalised by the σ_8 parameter, the variance of the density field smoothed with a top-hat filter at $8h^{-1}$ Mpc radius (roughly the transition scale to the non-linear regime).

The power spectrum at redshift z can be obtained by evolving the primordial spectrum, which is usually assumed to be the scale free Harrison-Zel'dovich spectrum $P(k) \propto k^n$, with $n = 1$.[2] The evolution of the power spectrum is handled by the means of the so-called *transfer function*, which for the case of pure cold dark matter was calculated by Bardeen et al. (1986) (the so-called BBKS formalism) with additional modifications imprinted by the baryons that can be accounted for by an approach developed by Sugiyama (1995). The full treatment of the power spectrum evolution can be obtained with numerical codes such as `camb`.[3] A simplified approximation valid in the vicinity of σ_8 (i.e. applicable to the cluster scales), that allows to bypass the exact BBKS treatment, if approximate results are sufficient, is provided by Viana and Liddle (1996).

---

[2]An exponent close to 1 is a generic prediction of the inflationary models.
[3]`http://camb.info/`

The number density of objects with mass between M and $M + \mathrm{d}M$ can be obtained by differentiating $p(\delta_c(z), M)$ from Eq. 3.5 and dividing by the volume (i.e. $M/\overline{\rho}_\mathrm{M}$). In a general fashion this can be written as:

$$n(M, z)\mathrm{d}M = -f(\sigma)\frac{\overline{\rho}_\mathrm{M}(z)}{M\sigma(M, z)}\frac{\mathrm{d}\sigma}{\mathrm{d}M}\mathrm{d}M , \qquad (3.7)$$

where $f(\sigma)$ is the so-called *multiplicity function*.[4] From Eq. 3.5 we obtain specifically for the Press-Schechter mass function

$$f(\sigma) = \sqrt{\frac{2}{\pi}}\delta_\mathrm{c}\sigma(M, z)^{-1}\exp\left(\frac{-\delta_\mathrm{c}^2}{2\sigma(M, z)^2}\right) . \qquad (3.8)$$

The general form of Eq. 3.7 provides a unified framework for expressing not only analytic or semi-analytic approximations of the mass function e.g. the described Press-Schechter function or the ellipsoidal collapse model of Sheth et al. (2001) but can also accommodate mass functions obtained from cosmological N-body simulations (e.g. Jenkins et al. 2001; Reed et al. 2003; Warren et al. 2006; Reed et al. 2007; Tinker et al. 2008).

In Fig. 3.1, we compare the Press-Schechter, Jenkins et al. (2001) and Tinker et al. (2008) mass functions. The Press-Schechter mass function systematically overestimates the number of low mass objects while underestimating the abundance of high-mass halos. Tinker et al. (2008) for the first time introduces the redshift dependence of the multiplicity function (i.e. $f = f(\sigma, z)$ rather than just $f(\sigma)$) required to reach mass function calibration precisions at the level of $\lesssim 5\%$. The Jenkins and Press-Schechter functions are compared also in Fig.3.2 where they are displayed next to the measured number density of halos from the Millenium simulation for several redshifts in the range $z \approx 0-10$. As can be seen the Jenkins mass function is a good description of the halo density mass-redshift distribution. The figure is also a great demonstration of the hierarchical structure formation paradigm, showing the increase of number densities of ever more massive halos as we approach the current epoch at $z = 0$.

3.2   Survey number counts

The direct application of the number density function from Eq. 3.7 is the cosmological modelling of cluster surveys and deriving constraints on the cosmological parameters. The number density function can also be used to obtain forecasts for future surveys. The cosmological constraints originate from the structure growth dependence on cosmological parameters (particularly Ω_M and σ_8) as described in the previous section with an additional dependence on the survey's volume. The total number of clusters in the redshift interval $(z, z + \mathrm{d}z)$ detectable by a survey with a solid

---

[4]Bond et al. (1991) provide a derivation of the Press-Schechter formalism based on the so-called excursion-set theory. In this picture the evolution of the matter field is modelled as a Brownian random walk with a presence of an absorbing barrier. The height of the barrier is set by the critical overdensity $\delta_\mathrm{c} = 1.69$ required for the collapse of the overdensity (the value is independent of the mass of the collapsed object). This approach provides us with the physical interpretation of the multiplicity function as the distribution function of the first up-crossings of this barrier during the random walk.
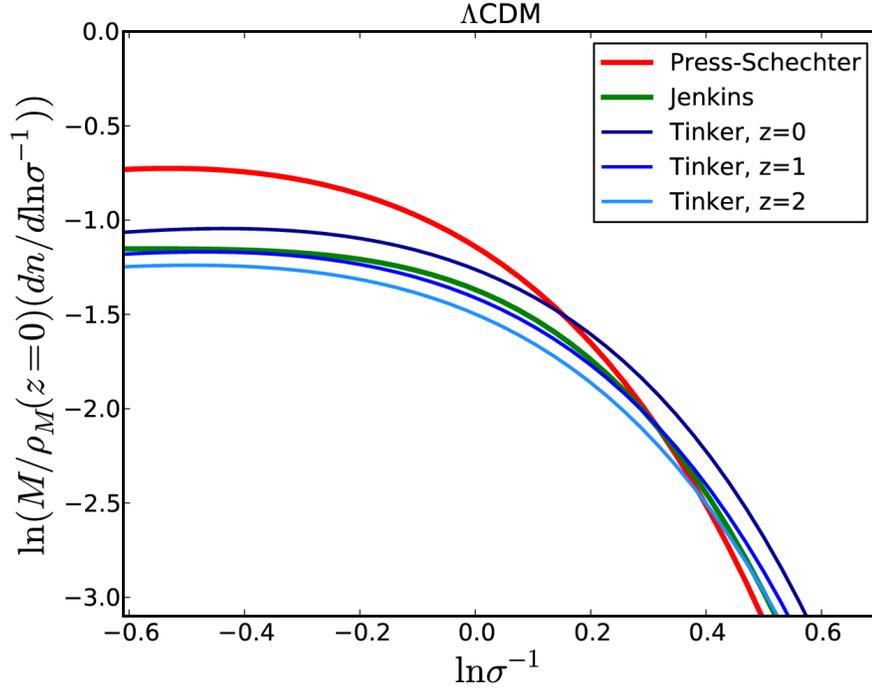
Figure 3.1: Comparison of halo mass functions. The red line shows the analytic prediction of the Press and Schechter (1974) formalism, while the green and blue lines are obtained from simulations. The green line displays the mass function of Jenkins et al. (2001) while the blue lines show the relation of Tinker et al. (2008) for three redshifts. All the curves are calculated for a flat ΛCDM cosmology with $\Omega_M = 0.3$ and $\Omega_\Lambda = 0.7$.

angle $\Delta\Omega$ is

$$\frac{dN}{dz}(z) = \Delta\Omega \frac{d^2V}{dzd\Omega}(z) \int_0^\infty \frac{dn(M,z)}{dM}(z)P_{sel}(M,z)\,dz \,, \qquad (3.9)$$

where $dV^2/dzd\Omega$ is the comoving volume element. The selection function $P_{sel}(M,z)$ gives the probability of detecting a cluster with mass M at redshift z. The function is normalised to unity and has a range of $(0,1)$. In the simplest case, the selection function is close to a fixed mass limit at all redshifts, i.e. $P_{sel}(M) = \Theta(M - M_{min})$, where Θ is the Heaviside step function, $\Theta = 1$ if $M \geq M_{min}$ and 0 otherwise. This particularly favourable case is indeed a good first approximation to the selection function of SZE surveys (see Sect. 2.2.6). The differential number counts then simplify to

$$\frac{dN}{dz}(z) = \Delta\Omega \frac{d^2V}{dzd\Omega}(z) \int_0^\infty \frac{dn(M,z)}{dM}(z)\Theta(M_{min})\,dz = \Delta\Omega \frac{d^2V}{dzd\Omega}(z) \int_{M_{min}}^\infty \frac{dn(M,z)}{dM}(z)\,dz \,. \quad (3.10)$$

Fig. 3.3 (left) displays the predicted cluster counts for the SPT survey. The curves are obtained by integrating Eq. 3.10 in thin redshift shells with width $\delta z = 0.05$ for three different cosmologies. The only parameter varying between the curves is the dark energy equation of state parameter w.
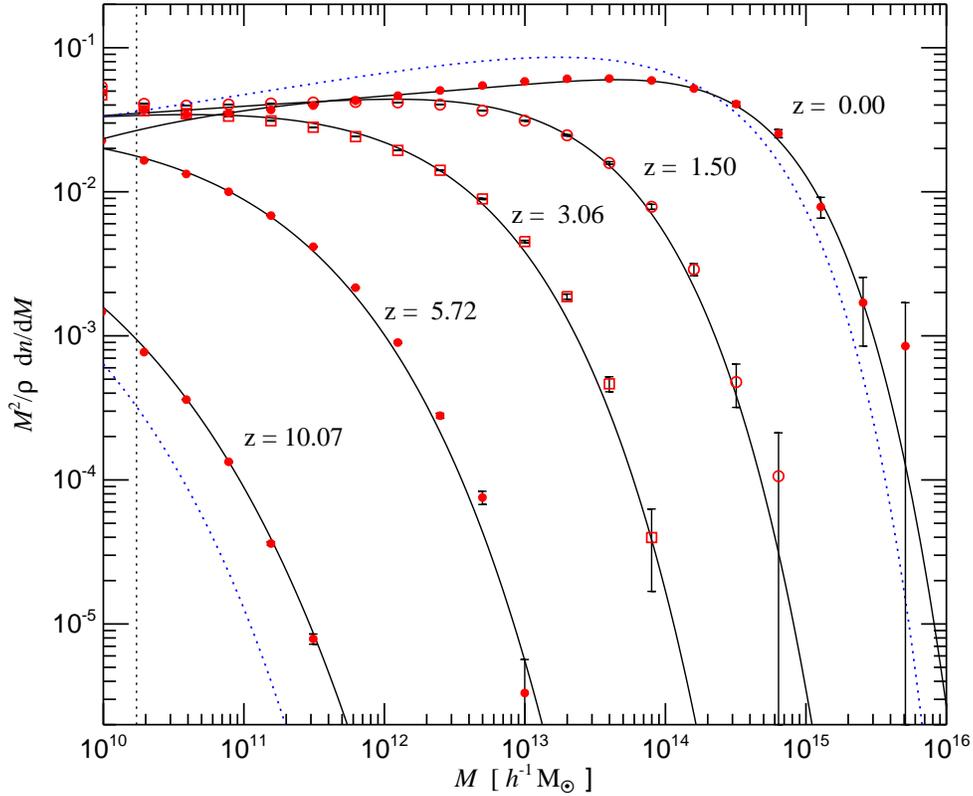
Figure 3.2: Multiplicity function (differential number counts) of the dark matter halos measured in the Millenium Run simulation (red points, Springel et al. 2005). Solid black lines show the predictions from the mass function of Jenkins et al. (2001), the dotted lines are the predictions from the Press-Schechter formalism for the two redshifts $z = 0$ and $z = 10.07$.

The difference between the curves is largest for higher redshifts ($z > 1$), i.e. in this range it is the easiest to distinguish between the different cosmologies and the constraints on the cosmological parameters are the tightest.

In the case of X-ray surveys, we often encounter flux limited samples, where the selection function is in the first approximation dependent only on the source flux and a flux threshold f_{min}. Here the connection between observations and theory becomes more complex. From the theoretical point of view we have a prediction of the distribution as a function of halo mass. However, mass itself is not a direct observable. In this case we have to resort to the use of a directly observable mass proxy (such as luminosity) and use the appropriate scaling relations (see Sect. 2.2.4) to bridge this gap. Uncertainties in the scaling relation parameters and their evolution, however, propagate through the calculation and impede the constraining power. There are several additional concerns that have to be taken into account (e.g. the size of the aperture, the parameters of the halo dark matter density profile etc.). Also the selection function is usually a complicated function of several other parameters beyond the source flux (e.g. source extent, off-axis angle)
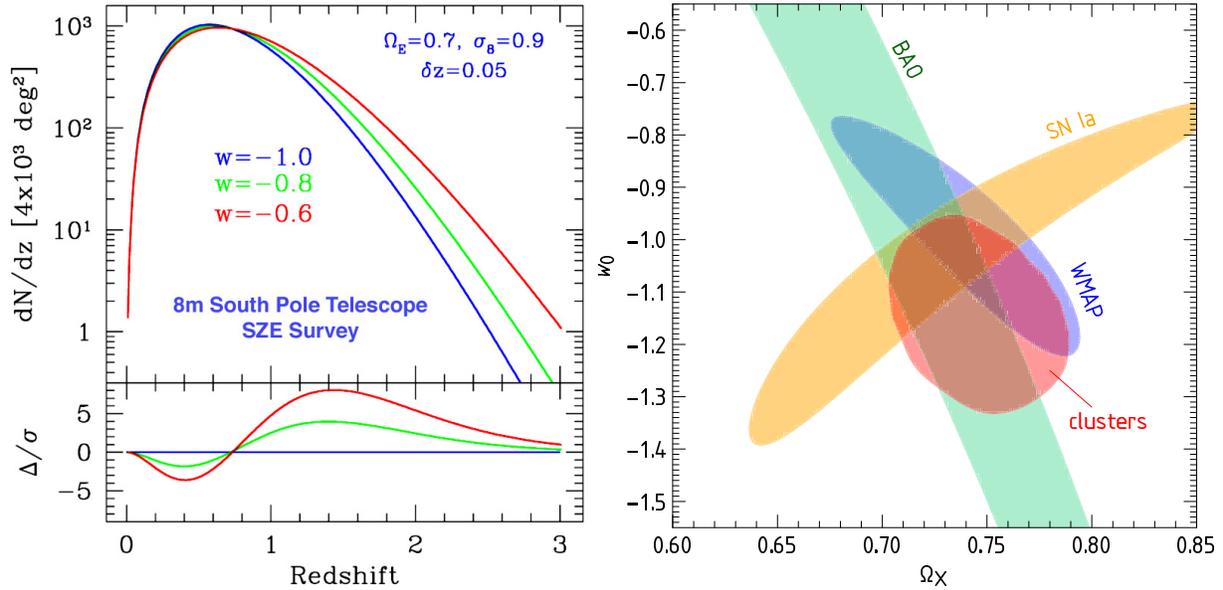
Figure 3.3: **Left:** Cluster number function (Eq. 3.10) for a mass limit integrated in narrow redshift bands $\delta z = 0.05$. The different curves show the sensitivity of the cluster abundance on the equation of state of the dark energy w_0 (the remaining cosmological parameters are kept fixed to $\Omega_M = 0.7$ and $\sigma_8 = 0.9$). The bottom panel demonstrates the prevailing contributing factor to this sensitivity from the relative difference of the curves with respect to the $w_0 = -1$ case. For redshifts $z \lesssim 0.7$ the determining factor is the volume term (the geometrical part), while for higher redshifts the major contribution comes from the structure growth factor. The curves differ the most at redshift $z > 1$ (i.e. here the information gain is the largest). Image credit: J. Mohr. **Right:** Cosmological constraints on the dark energy density (here designated as Ω_X) and its equation of state parameter w_0. Constraints from cluster abundance are shown in red along results from CMB studies (blue), supernovae (yellow) and baryonic oscillations in green. As can be seen from the area of the confidence regions, cluster have comparable constraining power as the other cosmological probes, while exhibiting different dependencies (and thus also degeneracies) on the cosmological parameters. This makes the combination of all these approaches particularly strong. Image taken from Vikhlinin et al. (2009a).

which can be taken into account only by extensive Monte Carlo simulations (Pacaud et al. 2006, 2007; Vikhlinin et al. 2009a; Sahlén et al. 2009; Mühlegger 2010).

Despite these complications cluster number counts (and the evolution of the cluster mass function) remain a powerful test of cosmology (Schuecker et al. 2003; Vikhlinin et al. 2009b; Mantz et al. 2010b). This cosmological test is most sensitive to the Ω_M and σ_8 parameters. The constraining power of the cluster abundances based on measurements of the redshift evolution of the mass function $\mathrm{d}^2 n(M, z)/\mathrm{d}M\mathrm{d}z$, is demonstrated in Fig. 3.3 (right) where clusters are used along with supernovae, CMB and baryonic oscillation studies to constrain the dark energy density and its equation of state parameter w_0. The information contributed by the clusters (in red) is comparable to the other tests and their combination gives the most stringent constraints.
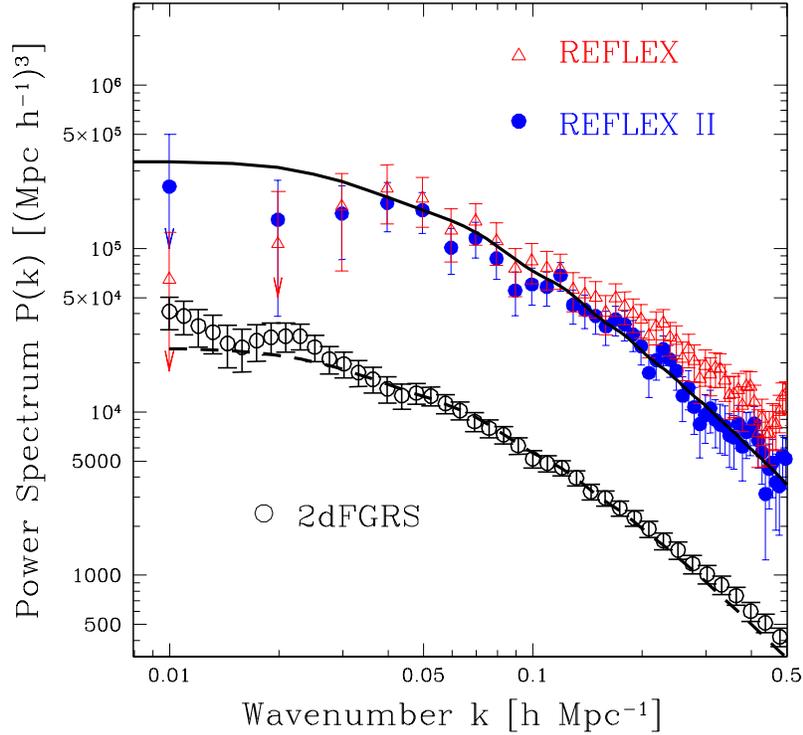
Figure 3.4: The REFLEX and REFLEX II power spectra from Schuecker et al. (2001) (red triangles) and Balaguera-Antolínez et al. (2011) (blue circles), respectively. For comparison, the measured galaxy power spectrum from the 2dFGRS survey Cole et al. (2005) is also plotted (open circles). The dashed lines represent the ΛCDM galaxy power spectrum convolved with 2dFGRS window function. The solid line shows the cluster power spectrum in ΛCDM cosmology convolved with both the REFLEX II window function and the biasing function (for details see Balaguera-Antolínez et al. 2011).

3.3   Cluster power spectrum

The background cosmology does not only leave its imprints in the redshift evolution of the cluster number counts (dn/dz) and the evolution of the cluster mass function ($d^2n/dMdz$), but also in the *spatial* distribution of the clusters. This can be characterised by the two-point correlation function[5] $\xi(R, z)$ or alternatively by the cluster power spectrum (Fig. 3.4). The cluster power spectrum $P(k, z)$ is the Fourier transform of the *linear* two-point correlation function $\xi_{\text{lin}}(R, z)$

$$P(k, z) \equiv \langle |\delta(\mathbf{k}, z)|^2 \rangle = \frac{1}{2\pi^2} \int dr \, r^2 \, \xi_{\text{lin}}(r, z) \, \frac{\sin(kr)}{kr} \ . \tag{3.11}$$

The cluster population is however a biased tracer of the matter power spectrum, since clusters are more likely to be found in regions that were slightly overdense on the largest scales (and

---

[5]The probability of finding two objects at separation R in excess to a random distribution:
$\xi = < \rho(x)\rho(x + R) > /\overline{\rho}^2 - 1$.

thus it was easier for the cluster-scale overdensities to exceed the critical density limit). The observed two-point correlation function $\xi(R, z)$ can be related to the correlation function of the underlying matter distribution through the effective bias factor b_{eff} averaged over all halos, so that $\xi(r, z) = b_{\text{eff}}(z)^2 \xi_{\text{lin}}(r, z)$. The effective bias can be expressed as (Matarrese et al. 1997)

$$b_{\text{eff}}(z) = \frac{1}{n(z)} \int_0^\infty f(M, z) b(M, z) \frac{dn(M, z)}{\text{d} \log M} \text{d} \log M \, , \tag{3.12}$$

where $f(M, z)$ is the multiplicity function introduced in Sect. 3.2 and $b(M, z)$ is the linear bias relating dark matter halos of mass M to the mass density fluctuation. This factor can be calibrated by numerical calibrations, e.g. Tinker et al. (2010) and references therein.

In the cluster regime, the most interesting results from this type of analysis were derived from the REFLEX survey (ROSAT-ESO Flux-Limited X-ray cluster survey, Böhringer et al. 2000, 2001; Guzzo et al. 2009) which comprises 447 X-ray selected clusters. This statistically complete sample is utilised with its large area to get a precise measurement of the two-point correlation function (Collins et al. 2000) and the cluster power spectrum (Schuecker et al. 2001). Their cosmological modelling then yielded constrains the cosmological parameters (Schuecker et al. 2003), especially the matter density Ω_M and the σ_8 parameter. The first study of the power spectrum in the extension of this survey (the REFLEX II survey with 911 clusters, Böhringer et al., in prep.) is also already available (Fig. 3.4, Balaguera-Antolínez et al. 2011).

It is noteworthy that the power spectrum/two-point correlation function cosmological modelling comes at no extra cost for an X-ray survey (provided a large enough area has been covered) and can be combined with cluster count measurements to gain even more leverage for the determination of cosmological parameters (Schuecker et al. 2003; Pierre et al. 2010). These constraints can be further improved by future X-ray surveys such as eROSITA, which will be able to measure the power spectrum as a function of redshift and thus directly probe the evolution of the growth function.

3.4 Other cosmological tests with clusters

Beyond the cluster mass function and power spectrum (and their redshift evolutions), the cluster population can be used in several additional ways to constrain cosmological parameters. Here we briefly overview the cosmological tests based on the angular distance Hubble diagram and the so-called gas mass fraction test.

3.4.1 Angular distance Hubble diagram

Combining X-ray observations with SZE measurements can be used as a purely geometrical cosmological test (i.e. dependent only on the kinematics of the expansion of the Universe, not on the growth of structure). This test utilises the different electron density dependencies of the X-ray surface brightness ($\propto n_e^2$, Eq. 2.5) and the SZE ($\propto n_e$, Eq. 2.33) in order to obtain the angular distance d_A (defined in Sect. 2.2.2). It can be shown (Cavaliere et al. 1977;
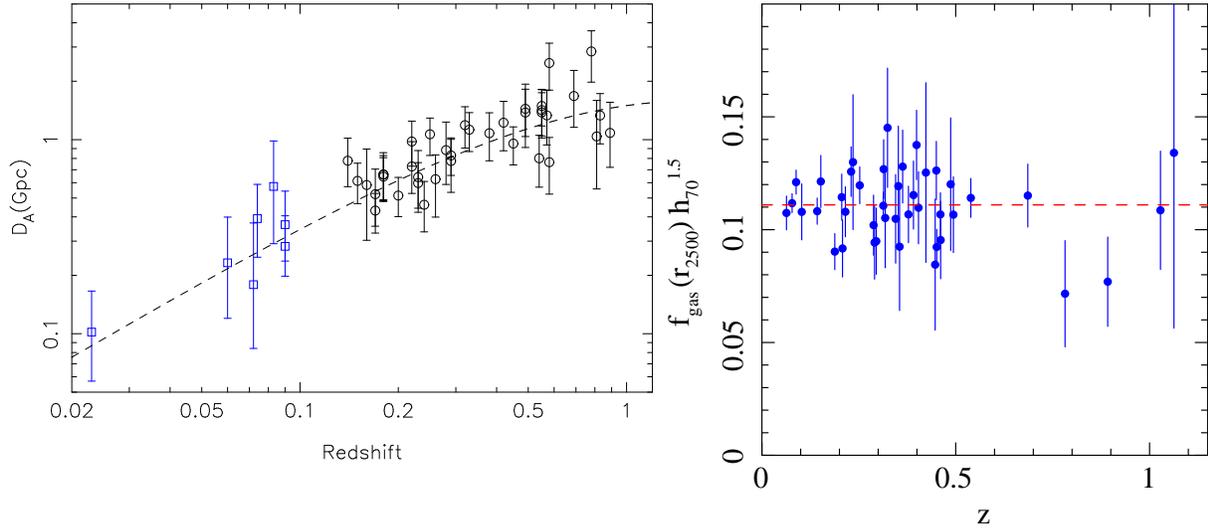
Figure 3.5: **Left:** Angular distance Hubble diagram from Bonamente et al. (2006), based on 38 clusters in the redshift range $0.1 < z < 0.9$ (black points). The dashed line show the angular diameter curve using the best-fit Hubble constant $H_0 = 76.9$ km s^{-1} Mpc^{-1}. Blue squares are from the low-redshift sample of Mason et al. (2001); they are not included in the fit. **Right:** Cluster gas mass fraction (f_{gas}) measurements for 42 clusters from Allen et al. (2008). For the correct cosmological model the $f_{gas}(z)$ is expected to be constant with redshift for massive, relaxed clusters.

Cavaliere and Fusco-Femiano 1978; Silk and White 1978) that d_A is related to the central values of the electron temperature $T_e(0)$, X-ray surface brightness $S_X(0)$ and the CMB temperature decrement $\Delta T(0)$ in the following way:

$$d_A \propto \frac{\Delta T(0)}{S_X(0) T_e^3(0) \theta_c} \, , \tag{3.13}$$

where θ_c is the characteristic scale of the cluster along the line of sight[6] (usually the angular core radius of the density profile). Since the line of sight scales are not observable directly, we must rely on the assumption of spherical symmetry and use the measurements in the plane of sky. Although individual clusters might exhibit various elongations along the line of sight, in a statistical sample of clusters the effect of elongations is vanishing due to the random orientations of the cluster main axes.

We can then utilise the angular distance redshift dependence (i.e. the angular distance Hubble diagram) to constrain the cosmological parameters, particularly the Hubble parameter (Fig. 3.5, Bonamente et al. 2006). In addition, this test can be combined with the dN/dz test to increase the constraining power (e.g. Khedekar and Majumdar 2010; Molnar et al. 2004), which is an important prospect particularly given the already ongoing large area SZE surveys with SPT, ACT and *Planck* (see Sect. 2.2.6).

---

[6]The angular distance itself enters the relation through the line of sight element $dl = d_A d\zeta$, where $d\zeta$ is the dimensionless length element.

3.4.2 The gas mass fraction cosmological test

The potential wells of the most massive clusters are so deep that they are able to retain essentially all their gas content. The ratio of the baryonic mass to the total cluster mass, $f_{gas} = M_B/M_{tot}$ is therefore expected to be close to its cosmological value Ω_B/Ω_M. Measurements of the apparent evolution of the cluster gas mass fraction can thus be used to probe the acceleration of the Universe (Allen et al. 2008, 2004, and references therein). The constraining power of this cosmological test originates from the apparent dependence of the determination of f_{gas} on the angular distance $f_{gas} \propto d_A^{1.5}$, or alternatively expressed from its independence on the redshift if the correct cosmological model is assumed (see Fig. 3.5, right). The advantage of this approach is that it requires only X-ray data (the gas mass is determined from the X-ray density and temperature measurements, Sect. 2.2.5) and the cluster sample does not necessitate knowledge of the selection function. The sample, however, has to be restricted to very massive, relaxed clusters where the assumption of $f_{gas}(z) \approx const.$ holds the best according to numerical simulations (Eke et al. 1998; Crain et al. 2007). In the low-mass systems/group regime non-gravitational processes play a much important role and modify the gas mass fraction (see e.g. Giodini et al. 2009).

Allen et al. (2008) derived constraints from Chandra observations of 42 hot, dynamically relaxed galaxy clusters obtaining $\Omega_M = 0.28\pm0.06$ and dark energy density $\Omega_{DE} = 0.86\pm0.21$ (for a non-flat ΛCDM model). The significance level of the detection of dark energy is comparable to that of type Ia supernovae studies. These two tests and also cosmic microwave background measurements can all be combined to help break the degeneracies between the cosmological parameter determinations. The gas mass test also bears a large potential to provide stringent constraint also on the equation of state parameter (and its redshift evolution) in the future with planned X-ray missions such as the International X-ray Observatory (IXO).

Chapter 4

Analysis of the XMM-*Newton* survey data

The backbone of this thesis is surveying for clusters of galaxies and their characterization in X-ray observations. All the X-ray data analysed here, whether connected to the XMM-BCS survey (obtained by dedicated observations) or to the XDCP project (archival data), was obtained with the XMM-*Newton* X-ray telescope.

In this chapter, we therefore provide a brief overview of XMM-*Newton* with a focus on its characteristics relevant in a survey context (as opposed to e.g. observations aiming to collect deep spectroscopic data). We will also discuss the new mosaic mode observations, which were implemented only recently to increase the observational efficiency of shallow surveys and whose first scientific utilization is part of this thesis. In the final section of this chapter, we delineate more technical details concerning the analysis, source detection and spectroscopy of mosaic data.

4.1 Overview of the XMM-*Newton* mission

XMM-*Newton*[1] was launched on 10th December 1999 from Kourou in French Guiana with an Ariane-5 carrier. After an initial orbit correction it settled on its final, highly elliptical geocentric orbit with an apogee of $114\,000$ km (roughly one third of the distance to the Moon) and a perigee of $7\,000$ km. The orbital time is 48 hours, but only part of the orbit outside Earth's radiation belts can be used for observations (elevations $\gtrsim 50\,000$ km). This constraint leaves about 130 ks of observation time per orbit, usually distributed between a few independent observations (observations can last between $2 - 130$ ks).

The satellite itself is one of the largest instruments built in Europe with 10 m length, a span of 16 m and launch a weight of 3.8 tons. The size and weight of the instrument were determined by its performance requirements (e.g. effective area, resolution etc. and naturally technological limitations) which were in turn driven by the science questions to be addressed.[2] An illustration of the telescope with its main parts is shown in Fig. 4.1.

---

[1]The "XMM" abbreviation stands for X-ray Multi-Mirror Mission, derived from its nested mirror design.

[2]More technical data can be found on the official XMM-*Newton* ESA web page: http://sci.esa.int/science-e/www/area/index.cfm?fareaid=23

The payload consists of three identical co-aligned X-ray telescopes. The mirrors have a Wolter type 1 design (Wolter 1952, see also Fig. 4.2), each with 58 nested parabolic and hyperbolic mirror shells. The total geometric effective area at 1.5 keV energy is $\sim 1\,550$ cm^2 for each telescope, i.e., $\sim 4\,650$ cm^2 in total. This is the largest effective area on a focusing X-ray telescope ever and will be surpassed only by *eRosita* (to be launched in 2012). The focal length of the telescopes is 7 493 mm.

There are five instruments in the focus of these mirrors - three CCD cameras (the European Photon Imaging Cameras - EPIC) and two Reflection Grating Spectrometers (RGS).

The most sensitive CCD of the three is the EPIC PN[3] detector (Strüder et al. 2001). It consists of twelve backside-illuminated CCDs on a single wafer segmented into four individual quadrants, each having three CCD subunits with a format 200×64 pixels (4.1″ per pixel). The quantum efficiency of the PN detector is very high $QE(PN) > 90\%$ over a broad energy range. In order to fully harvest this great sensitivity, the PN detector is the only detector in the focus of its X-ray telescope.

X-ray radiation collected by the two remaining mirror modules is shared by one of the MOS CCD cameras (receiving $\sim 44\%$ of emission) and one of the RGS spectrometers. The two identical MOS (Metal Oxide Semiconductors, Turner et al. 2001) cameras have seven 600×600 pixel CCDs (1.1″ per pixel, front-illuminated). MOS detectors have a slightly lower quantum efficiency than PN, $QE(MOS) > 40 - 85\%$.

An additional technical difference between PN and MOS is that the PN chips lack frame store buffers. Without a buffer, the PN pixels register incoming X-ray events also during the column readout phase (systematic shifting of charges along a column toward the readout node), which lasts a fraction[4] of the integration phase. Since these events are registered during the gradual charge shift, it gets assigned a wrong coordinate along the read-out axis (RAWY coordinate). Especially for bright sources this leaves an imprint as a smeared event streak along the pixel column. These events are called out-of-time events (OoT) and are corrected for during the data analysis process in a statistical way.

For details on the Reflection Grating Spectrometers we refer the reader to den Herder et al. (2001) who provide a detailed description of the instrument. The XMM-*Newton*'s payload also includes the Optical Monitor (OM) - an optical/ultraviolet telescope with a 30 cm diameter aperture, which allows for simultaneous observations with the X-ray instruments.

4.2 Elements of X-ray analysis

The basis of this thesis is the detection of clusters and groups of galaxies in X-ray images. Accordingly, before we go on with a more technical description of analysing mosaic mode data, we will explain the basic terms of X-ray imaging but focus mostly on topics relevant to source detection.

There are several differences between optical (also infrared and UV) telescopes and X-ray imaging instruments. The basic principle is the same - in both cases we have a system of mirrors

---

[3]We capitalize "PN" for better legibility.

[4]For full frame mode the out-of-time fraction is 6.3% and 2.3% for the extended full frame mode.
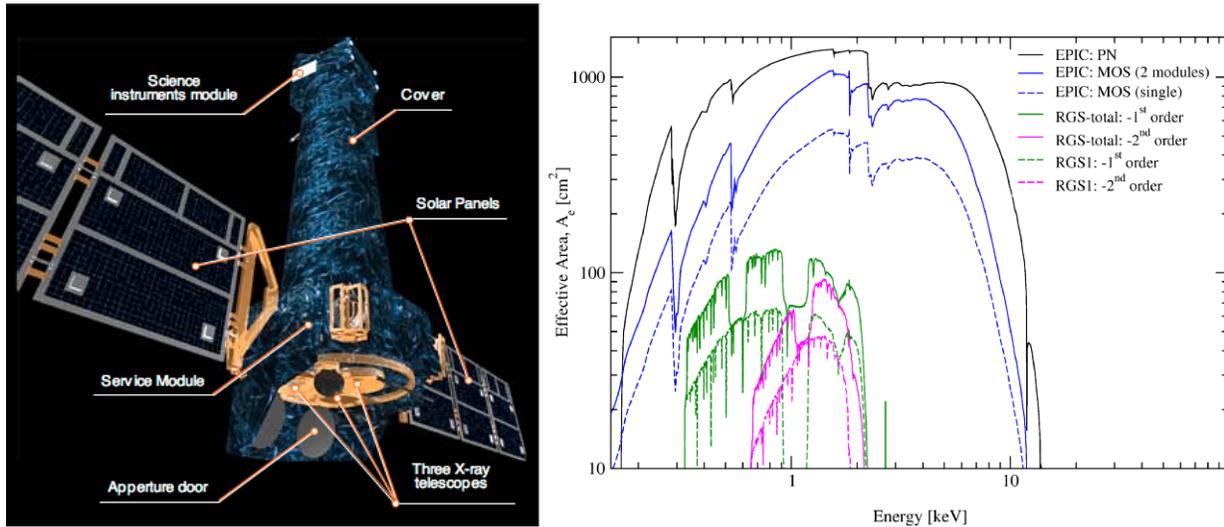
Figure 4.1: **Left:** The XMM-*Newton* X-ray observatory (artists impression, courtesy of ESA). **Right:** On-axis effective area of the individual instruments of XMM-*Newton*. The plot is taken from the XMM user handbook, Ness et al. (2010).

focusing radiation onto the detectors (nowadays CCD arrays).

However, due to high energies and comparatively low number of X-ray photons the CCDs in X-ray regime can be operated in a *single photon counting mode* - i.e. for each detected X-ray photon, its position, detection time but also energy is recorded, e.g. allowing to obtain direct low resolution non-dispersive spectroscopy. Higher energy resolution can be achieved by introducing grating spectrometers into the light path - as is the case of RGS gratings on board of XMM-*Newton*.

The need to focus high energy photons leads to another large difference compared to optical telescopes - the X-ray mirror system.

4.2.1 X-ray mirrors

Focusing X-ray photons is a much more complicated task than in the optical regime. Given the photons' high energies, they are highly penetrating and thus reflection can occur only at very high incidence angles.[5] X-ray telescopes thus typically utilize *grazing incidence* (i.e. incidence at very high angles), to direct the optical path of the X-ray photons toward the focal point. The value of the smallest possible incident angle depends on several factors - but most importantly on the energy of the photons and the density of the mirror material. The higher the density, the smaller is the possible incidence angle (i.e. higher possible angle between the beam and the mirror plane). Therefore, X-ray mirrors are typically made of heavy elements, e.g. in case of XMM-*Newton* the mirror coating is made of gold.

The focusing of X-rays within the telescope is usually achieved by a special mirror design.

---

[5]The angle between the beam and the normal to the reflecting plane.
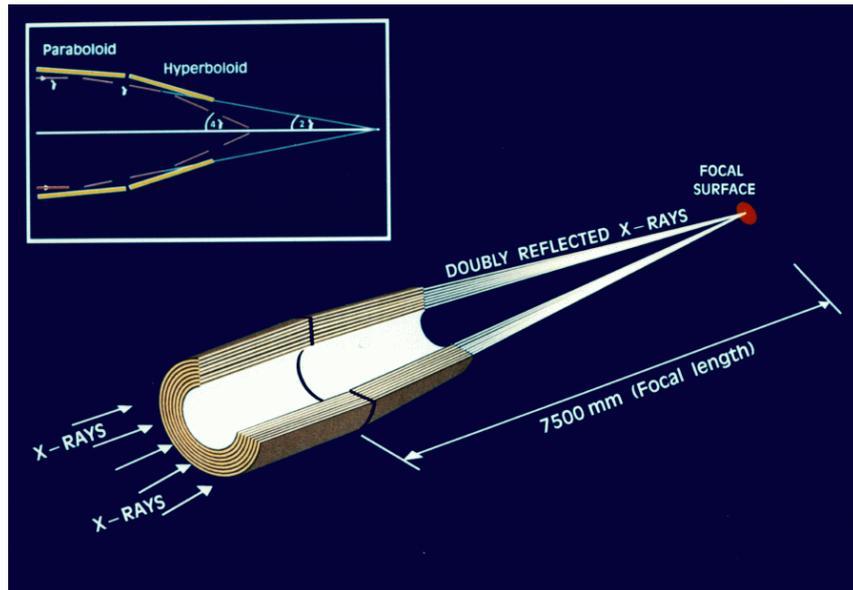
Figure 4.2: The Wolter type 1 mirror design of the XMM-*Newton* satellite. The light path of a doubly reflected photon is displayed in the inset. XMM-*Newton* has 58 nested parabolic and hyperbolic mirror shells. Credit: ESA/ESTEC, Ness et al. (2010).

Several solutions were developed by Wolter (1952), including the so-called Wolter type I design. This system consists of two mirror surfaces, the first one parabolic and the second one hyperbolic (Fig. 4.2). Only doubly reflected photons are properly focused (first reflection from the parabolic and the second from the hyperbolic mirror). While also other possible designs exist, this solution is the most common in X-ray telescopes. It was used in the first X-ray imaging instrument on board of a satellite[6] - the Einstein Observatory and is also on board of the missions currently in orbit - XMM-*Newton* and *Chandra*.

However, the requirement of high incidence angles implies only small geometric area facing the source and collecting incident photons. This constraint is alleviated by nesting several layers of mirrors within each other (see again Fig. 4.2).[7] Each mirror is manufactured by a mirror replication technology using an aluminium mandrel and has to be carefully polished to a precision of only a few atoms. The mirrors are finally mounted into a supporting structure called the spider wheel, which holds them in place. A more detailed discussion on X-ray mirror theory can be found in Friedrich et al. (2008) and Aschenbach (1985).

The particular mirror system of the given X-ray telescope determines its imaging properties and influences several parameters important for the purposes of source detection - the point spread function and the effective area and its vignetting.

---

[6]X-ray telescopes were used also before that on rocket experiments.
[7]Mirror nesting has also the advantage that it blocks out photons that would reach the detector accidentally after only a single reflection (i.e. unfocused photons).

4.2.2 Point spread function

The radiation field of a source interacts on its way to the detector with the components of the telescope. These interactions affect the intensity distribution of the source and therefore the observed distribution is the convolution of the source's intrinsic intensity distribution on the sky and the point spread function (PSF):

$$I_{\mathrm{D}}(x, y) = \int_{-\infty}^{\infty} \int_{-\infty}^{\infty} \mathrm{d}\zeta \, \mathrm{d}\xi \, PSF(x - \zeta, y - \xi) I(\zeta, \xi), \qquad (4.1)$$

where $I_{\mathrm{D}}(x, y)$ is the intensity on the detector at position (x, y). The shape of the PSF function is measured on ground in a testing facility.[8] The shape of the PSF is typically non-trivial, differs for each module and is a function of the off-axis angle. A gallery of PSF shapes for all three cameras is displayed in Fig. 4.3 (top). As can be seen, the three different telescopes have different PSF shapes, with MOS1 and MOS2 having a slightly superior resolution to PN. The width of the PSF is usually characterized by either its full width at half maximum (FWHM) or half energy width (HEW).[9] We summarize their on-axis values (from both in-orbit and ground measurements) in Table 4.1.

Importantly, there is also a strong dependence of size and shape of the PSF on the off-axis angle. As an example, we display the PN PSF in $3'$ steps in Fig. 4.3. The increasing elongation is due to off-axis aberration (astigmatism), but the PSF also exhibits increasing complexities in its core, especially for off-axis angles $\gtrsim 12'$.

Good knowledge of the PSF is a necessity for reliable source detection. Groups and clusters of galaxies are in theory easily selected in X-rays, since they make up the majority extended extragalactic sources.[10] Indeed, in both XMM-BCS and XDCP surveys, we take the detection of an extent as one of the main cluster selection criteria (see e.g. Sect. 5.3.1). However, a source can be spatially resolved only if its extent is larger than the PSF. The PSF is also needed to obtain reliable X-ray photometry of the given source.[11] For these purposes Equation 4.1 is simplified to be one dimensional by taking only an azimuthally averaged PSF model.[12] As can be seen in Fig. 4.4 (left), the azimuthally averaged PSF profile is well described by a King profile of the form:

$$PSF(r) = \frac{A_0}{\left[1 + \left(\frac{r}{r_{\mathrm{c}}} \right)^2 \right]^{\alpha}}, \qquad (4.2)$$

---

[8]In-orbit calibration using observations of point sources has also been performed (see below).

[9]FWHM is the diameter of the distribution where it falls to half of its peak probability. HEW is the diameter of a circle containing half of the total energy under the distribution.

[10]Barring for the moment large, usually nearby, elliptical galaxies with extended X-ray halos. Also those often exhibit several smaller satellites and seem to form a smooth transition to so-called fossil groups, eventually up to groups and clusters of galaxies. Diffuse emission (albeit much fainter) is observed also in nearby spiral and irregular galaxies from the intrastellar matter.

[11]This is done during the maximum-likelihood source fitting by the `emldetect` task of SAS. We provide more details in Sect. 5.3.1.

[12]For the one dimensional intensity distribution of a point source one usually takes a Dirac δ-function, for an extended source a beta model (special case of a King profile, see Sect. 2.2.2).
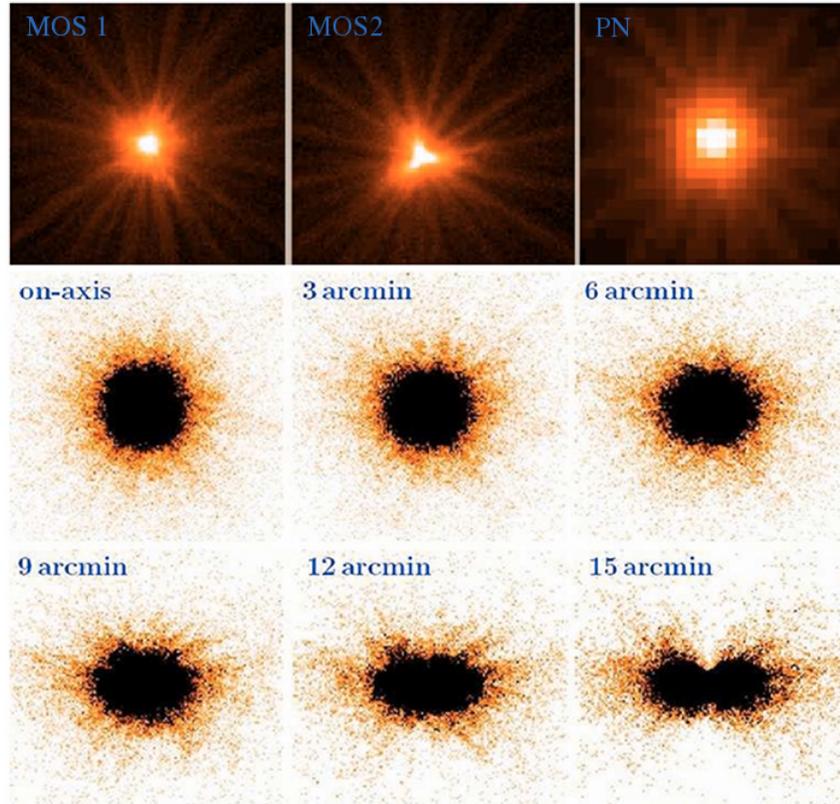
Figure 4.3: **Top:** The on-axis point spread function (PSF) of MOS1, MOS2 and PN. The shape of the PSF is different for each camera, with MOS2 having a slightly triangular shape. The pixel size is 1.1″ for the MOS cameras and 4.1″ for PN. The color scale is square root to visualise the wings of the point spread function. The star-like pattern is created by the spider wheel which supports the telescope mirrors. Credit: ESA/ESTEC, Ness et al. (2010). **Bottom:** Example of the variation of the size and shape of the PN camera's PSF. The images are shown in off-axis angle steps of 3 arcmin as provided by the XMM-*Newton* calibration database. We inverted the color scheme (i.e. black areas are the brightest) for better visualization of the PSF's core. The gradual broadening and asymetrization of the PSF poses a problem for source detection at higher off-axis angles, especially for low surface brightness objects like clusters of galaxies. Image taken from Fassbender (2008).

with the normalization A_0, core radius r_c and index α. In general however, even for this simplified description, we have to take into account the dependence of these parameters on the off-axis angle and energy. This can be done by empirical best-fit relations available from the XMM-*Newton* Calibration Documentation archive[13] which were obtained from in-orbit observations of point sources by S. Ghizzardi (for PN in document XMM-SOC-CAL-TN-0029, 2002 and for the MOS cameras in XMM-SOC-CAL-TN-0022, 2001).

---

[13]`http://xmm.vilspa.esa.es/external/xmm_sw_cal/calib/documentation.shtml`

	PN	MOS1	MOS2
FWHM ['']	$< 12.5^{\dagger}/6.6$	4.3/6.0	4.4/4.5
HEW ['']	15.2/15.1	13.8/13.6	13.0/12.8

Table 4.1: Full width at half maximum (FWHM) and half energy width (HEW) of the PN, MOS1 and MOS2 cameras as measured in orbit (first number) and at the calibration facility on the ground (second number). † Value is an upper limit.
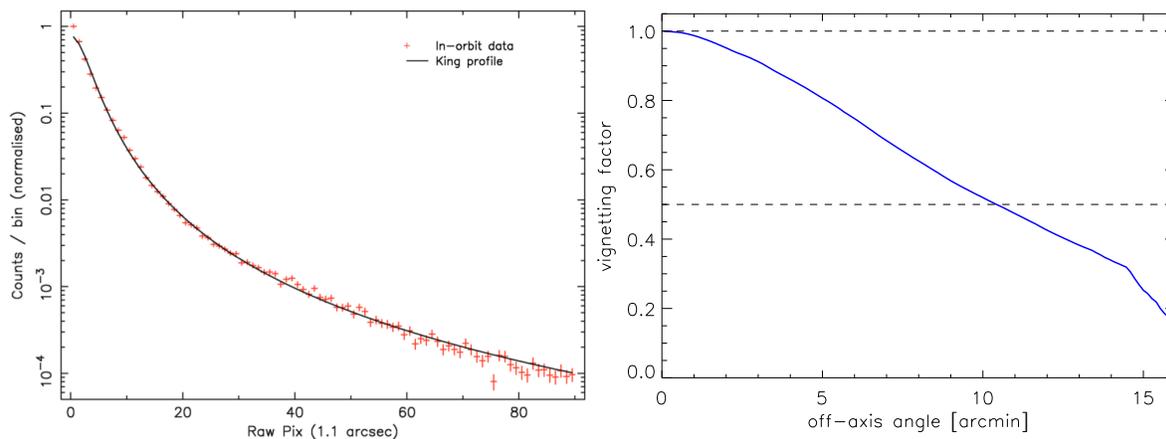
Figure 4.4: **Left:** Radial surface brightness distribution for an on-axis PSF (red crosses) for MOS1 in the $0.75 - 2.25$ keV energy range, obtained from an in-orbit observation of a point source. The best-fit King profile is overlayed in a solid black line. Image from Ness et al. (2010). **Right:** The XMM-*Newton* vignetting function averaged over all three X-ray telescopes with the PN aim point used as the reference point. The dashed lines indicate the 100% and 50% effective area levels (vignetting factor $V(\theta) = 1$ and $V(\theta) = 0.5$, respectively). The image is taken from Fassbender (2008).

4.2.3 Effective area

The efficiency of an X-ray instrument can be characterized by its *effective area*, which is related to its limiting sensitivity per unit time. The effective area depends on the geometric area exposed to the source (i.e. for Wolter type 1 mirrors, the more nested mirrors, the larger the effective area), but also on their reflectivity (function of energy and depends on the coating material of the mirror), filter transmission and the quantum efficiency of the detector. We have listed these parameters for XMM-*Newton* in Sect. 4.1 and the energy dependency of the effective area is displayed in Fig. 4.1. The effective area (and thus in turn the sensitivity of the instrument) is the highest in the $\sim 0.5 - 2$ keV band. The X-ray spectrum of clusters peaks also roughly in this range and therefore this band is typically taken as the standard reference band for the flux and luminosity determination.[14] XMM-*Newton* is the highest sensitivity instrument in this

---

[14]Scharf (2002) provides the optimal XMM detection bands for yielding the highest signal-to-noise for detecting galaxy clusters and groups, by taking into account the exact spectral distribution for different temperatures and

range - improving on ROSAT's sensitivity by roughly ten fold and ∼ 4 times more sensitive than Chandra.

The effective exposure time (i.e. the total on-source time folded with the effective area) is for practical purposes mapped for each image pixel creating thus an *exposure map*. An example of an exposure map for a standard observation is shown in Fig. 5.2 and for mosaic observations in Fig. 4.6. As can be seen, the exposure (and thus the local effective area) is not uniform across the whole detector, but is highest around the aim point of the observations and decreases with off-axis angle. Photons arriving at higher off-axis angles have less mirrors for double-reflection and at the same time there is more mutual obstruction due to the dense nesting of mirror shells.

The azimuthally averaged vignetting function is shown in Fig. 4.4 (averaged over all three detectors, PN aim point taken as the center). The vignetting reaches 0.5 (i.e. 50% of the on-axis exposure) by ∼ 10.5′ off-axis angle. Beyond ∼ 14.5′ the vignetting starts a steep decline due to reaching the field of view edge of some of the detectors.

We conclude by referring to the review of Davis (2001), who provide first principle derivation of equations defining the exposure maps and ancillary region files. Recently, Spiga (2011) also provides an analytical formula for the treatment of off-axis exposure area calculation, providing thus a faster alternative to standardly used ray tracing simulations.

4.2.4 CCD detectors

At the focus of the mirror system of an imaging X-ray telescope like XMM-*Newton*, one finds a CCD[15] chip array. An incident X-ray photon induces through the internal photoelectric effect the production of an electron cloud at the detector cell (called detector pixel[16]). The electric charge is gathered in the cell's potential well and eventually shifted to and read out by the read out electronics. The quantity measured by the detector electronics is the total charge of each pixel - the so-called pulse height amplitude (PHA). The charge depends on the photon energy, but the conversion (i.e. the response function) is a complicated function of both energy and pixel position. The full conversion from PHA to energy requires both the *redistribution matrix* (contained in the RMF file) and the *ancillary region file* (ARF). We will not provide more details here, but refer the reader to the XMM-*Newton* Handbook (Ness et al. 2010) and Davis (2001).

4.2.5 X-ray imaging

Now that we have all the basic elements required, we can write down the basic equation of X-ray imaging, which relates the observed X-ray counts to the surface brightness distribution of the source on the sky:

$$C(h, \mathbf{p}) = \tau_{\text{eff}} \int d\lambda \, A(h, \lambda, \mathbf{p}) S(\lambda, \mathbf{p}), \tag{4.3}$$

redshifts. Following Fassbender (2008) we utilize the $0.35 - 2.4$ keV band as an ancillary single detection setup optimized for $z > 1$ clusters detection (see Sect. 5.3.1).

[15]*Charge Coupled Device*.

[16]Detector pixels are usually binned into larger units when creating an image - the so-called image pixel.

where $C(h, \mathbf{p})$ is the number of detected counts at position $\mathbf{p} = (x, y)$, with the pulse height amplitude h. A is the local effective area (normalized to the on-axis exposure, we absorbed the redistribution matrix into this factor for simplicity) and $S(\lambda, \mathbf{p})$ is the surface brightness distribution of the source convolved with the PSF function $PSF(\lambda, \mathbf{p})$ according to Eq. 4.1. We have denoted the on-axis exposure time in seconds as τ_{eff}. The integral extends over all wavelengths[17] λ contributing to a PHA value equal to h.

In practice, we extract images in a finite band (e.g. $0.5 - 2$ keV) corresponding to some Δh PHA interval. In relatively narrow bands we can neglect the energy dependence of the effective area and remove it from the integrand of Eq. 4.3 by assuming a constant value at a reference wavelength λ_0 from the $\Delta\lambda$ interval:

$$C(\Delta h, \mathbf{p}) \approx \tau_{\text{eff}} A(h, \lambda_0, \mathbf{p}) \int_{\Delta\lambda} d\lambda \, S(\lambda, \mathbf{p}) . \tag{4.4}$$

This approximation holds the best, if the chosen band is as narrow as possible. The whole energy range, however, should not include an edge (see Fig. 4.1, e.g. note the relatively flat effective area in the $0.5 - 2$ keV band and the sudden drop just beyond 2 keV - this is the Au M edge). For broader bands one can combine several piece-wise constant maps, potentially also weighted by taking into account the source spectral distribution for better precision (again see Ness et al. 2010; Davis 2001).

The total effective area can be broken down into several independent factors:

$$A(E, \theta) = A_{\text{G}} \cos(\theta) \cdot \mathcal{R}(E) \cdot V(\theta) \cdot T(E) \cdot QE(E) , \tag{4.5}$$

where we dropped from the notation any dependence on the spatial location beyond the off-axis angle. The A_{G} term is the full actual geometric area of the individual mirror shells where on-axis photons could stream in. For a photon at an off-axis angle θ this area is diminished by the $\cos\theta$ factor. $\mathcal{R}(E)$ is the reflectivity of the mirror's coating, $V(\theta)$ the vignetting function (Fig. 4.4, left). We have denoted the transmission function of the filter as $T(E)$ (see Sect. 4.3.1 for a brief discussion on filters). Finally, $QE(E)$ is the energy dependent quantum efficiency of the detector.

With exposure maps defined in this way, we can convert detected counts into count rates and adding the information from the RMF and ARF matrices eventually to fluxes in a given band. For clusters of galaxies detected by the XMM-BCS survey we implement this procedure in an iterative way in the framework of the *growth curve analysis* (Böhringer et al. 2000). The details of the iterative procedure are provided in the Sect. 5.3.3.

Naturally, the picture that we built up in the previous sections is rather simplified. We have neglected several additional effects that have to be taken into account, when analysing a real observation, e.g.: the presence of X-ray and instrumental backgrounds, soft-proton flaring, quiescent soft proton contamination, presence of chips in anomalous (hot) states, pile-up effects etc. Handling of several of these effects is however described in sections 5.2.
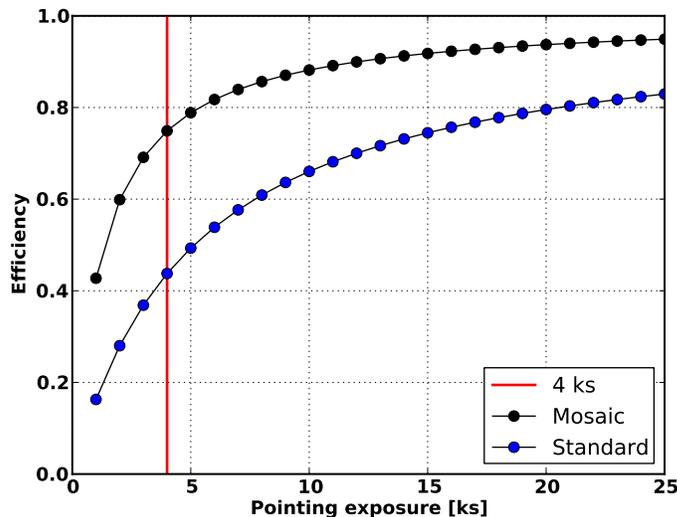
Figure 4.5: Comparison of mosaic mode observation efficiency (black) with standard pointing mode as a function of pointing exposure time. The mosaic mode is much more efficient, especially for shallow ($\lesssim$ 15 ks) observations. The red line marks the 4 ks per pointing limit policy imposed starting from AO-10 (in year 2010).

4.3   Mosaic mode observations

The original design of XMM-*Newton* did not include an operation mode intended for large area observations (e.g. raster, dithering or tracking mode). Until AO-8[18] (in year 2008) such observations would require several independent pointings. However, covering large sky-areas with low exposure pointings lead to very low observing efficiency (see Fig. 4.5), mainly due to the long setup times.

In order to improve the efficiency of large area (i.e. larger than field of view), shallow observations (i.e. exposure times comparable to instrumental setup times), the XMM-*Newton* science operation team implemented a completely new observational mode - the *mosaic mode*. It is very rare that a new feature like this one is added for a mission in orbit. In the following, we explain the main differences of the mosaic mode with respect to the standard observations.

4.3.1   Overheads in standard observations

Before collecting science data, a *standard* observation starts by operational and instrumental setups. The operational overhead consists of pointing the telescope to the target coordinates (standardly, the term *slew* is used) and the acquisition of a reference star needed to establish

---

[17]Wavelength relates to the energy of the photon E as $\lambda = hc/E$, here h is the Planck constant not the PHA value.

[18]AO - Announcement of Opportunity, XMM-*Newton*'s annual call for observation proposals.

the attitude[19] of the telescope for the required nominal astrometrical precision. The duration of the slew and its path depend on the relative positions and attitudes of the current and previous pointings. The telescope collects X-ray photons during the slew, but these are usually not useful for the observer and are not included in the observation's science data. The data from slews are collected in the Slew Data Files and are accessible from the XMM-*Newton* slew web portal.[20]

Once the pointing towards the desired coordinates is secured, the instrumental setups are carried out. These setups include the overheads for the EPIC, RGS and OM instruments, but only the EPIC times are significant. The EPIC setup is mainly due to measurement (respectively upload for MOS) of the camera's zero charge levels - the so-called *offset tables*.

The EPIC cameras are sensitive not only to X-ray photons, but also to infrared, optical and ultraviolet photons. This effect is called optical loading. To reduce this effect, each of the three X-ray telescopes is equipped with a filter wheel which has three aluminised blocking filters: the "thin", "medium" and "thick" filters. The thicker the filter, the smaller is the optical loading, but also the larger is the loss of sensitivity, especially in the soft X-ray band. However, residual contamination by visible light affects the definition of the proper energy scale, e.g. an optically generated photo-electron would boost the energy scale zero level by ~ 3.6 eV.

The offset table is thus an instrument map that contains the amount by which the measured zero levels are shifted with respect the true level (this includes the optical loading and several other instrumental sources) for each pixel. During the observation, the energy of each event is reduced by the value of the corresponding pixel in the offset map, before it is transmitted to the ground.

For the MOS this effect can be suppressed by taking into account the information on the zero level *around* given event. This information is also transmitted to the ground and can thus be subtracted in the ground processing steps. The MOS cameras thus operate with pre-calculated offset tables which are uploaded during the instrumental overhead phase (this takes typically $\lesssim 1$ ks). For the PN, the offset map is computed specifically (with the filter wheel in closed position) for each observation before its beginning. The procedure takes ~ 4 ks (there is a slight frame mode dependence).

After the offset tables are established, the filter wheels are set to the desired filters for the given observation and the observation itself begins. For each standard observation the whole process repeats which clearly impedes the operational efficiency if the exposure times are close to ~ 4 ks.

We note that there are additional setup procedures and more subtle issues during the offset table calculations (e.g. X-ray loading etc.), that we omitted here for simplicity, but can be found in the XMM-*Newton* User Handbook and calibration documents referenced therein.

---

[19]Under attitude we understand the full information on the orientation of the telescope - it includes the coordinates of the aim point of the observation and the azimuthal (so-called roll) angle of the satellite.

[20]http://xmm.esac.esa.int/external/xmm_products/slew_results/web_slew.shtml

4.3.2   The structure of a mosaic mode observation

The efficiency gain for shallow, large area observations carried out in the mosaic mode is achieved by significantly reducing the instrumental overheads by suppressing the upload (for MOS) and calculation (for PN) of the EPIC offset tables for every pointing beyond the first observation in a mosaic.

A mosaic mode observation thus starts as a standard pointing with the operational setup and establishment of the offset tables. Then the first observation is taken in a standard fashion. After this is done, the telescope slews to the next pointing in the mosaic. Data is collected also during the slew and injected into the observation's eventlist - since typically a mosaic is used to cover a contiguous area these photons can be relevant for the observer. The attitude reconstitution during a slew is slightly degraded compared to a stable pointing but the astrometrical precision is still on a $\sim 1''$ scale (i.e. still sufficient given the $4''$ binning of standard science images). Then the second stable pointing of the mosaic commences. The offset tables calculated before the first observation are used in the whole sequence. The whole process is repeated for each pointing in the given mosaic.

The total duration of a mosaic mode observation t_{obs}^{M} is thus:

$$t_{obs}^{M} = t_{setup} + n \times t_{exp} + (n-1) \times t_{slew}\,, \tag{4.6}$$

where t_{setup} is the instrumental overhead, n is the number of pointings, t_{exp} the exposure time of a single pointing and t_{slew} the slew time between two consecutive pointings. Observing the same sequence in a standard way (i.e. by individual pointings) would yield a total time t_{obs}^{S}:

$$t_{obs}^{S} = n \times t_{setup} + n \times t_{exp} + (n-1) \times t_{slew}\,. \tag{4.7}$$

If we define the observational efficiency as the ratio of the actual total exposure time spent in the stable pointings[21] to the total time, i.e. $\eta = n \times t_{exp}/t_{obs}$, we can see how standard pointings (blue line in Fig. 4.5) compare to a mosaic mode (black line) for different exposure times. For the plot we used the official values of $t_{setup} = 4$ ks and $t_{slew} = 1.2$ ks and $n = 20$ for illustration. The efficiency gain is larger for shorter observations (i.e. when t_{exp} is close to t_{setup}), e.g. for $t_{exp} = 3.5$ ks (as is the case of the mosaic extension of our XMM-BCS survey), the efficiency of the mosaic is $\eta^{M} \approx 0.72$ compared to $\eta^{S} \approx 0.41$, if we would have used standard pointings.

The mosaic mode thus unlocked completely new areas in the exposure time - sky area phase space and makes observations possible, that in the past had prohibitively low operational efficiencies. Large area surveys such as the XMM-BCS can immediately benefit from this new opportunity. Other uses of the mode can include observations of large extended sources (e.g. supernova remnants etc.) where planning pointings with smaller offsets can result in a highly uniform coverage (in terms of exposure), e.g. if the offsets between two neighbouring pointings is comparable to the off-axis angle where the vignetting factor reaches 0.5 ($\sim 10.5'$, see Fig. 4.4).

We close this section by listing several practical constraints and caveats for designing and planning mosaic mode observations:

---

[21]Technically, in a mosaic the slews can also constitute science time and would thus increase our figure of merit even further.

- The first field of the mosaic must not have bright optical (UV) sources, in order to be able to calculate reliable offset tables.

- Since one offset table is used for all observations, the pointings beyond the first one have the PN zero charge level established with lower precision than they would have in an individual pointing. The difference is, however, for all practical purposes negligible.

- If a pointing within mosaic has a bright optical source the offset table from the first observation might be an underestimate of the true zero-charge level. Avoiding bright sources is thus slightly more important when planning a mosaics.

- The offset table computed for PN through the closed filter may result in a slightly degraded spectral resolution for sources producing a significant optical loading. For sources without optical loading (and for MOS data in general) the spectral resolution is unaffected.

- As already mentioned, the attitude reconstruction during a slew is slightly worse than for a stable pointing. This again makes practically no impact for contiguous areas. If the mosaic covers a non-contiguous area, photons collected during the slew have to be discarded anyway.

- The distance between two consecutive pointings can not be larger than $1°$. The minimal distance is set mainly by the PSF of the telescope and is equal to $12''$.

- The lowest allowed exposure time is 2 ks, in order to set a threshold for minimal observing efficiency. For exposure times $t_{exp} \gtrsim 15$ ks the efficiency gain compared to a standard mode is not very significant. As of AO-10 (2010), a policy setting a maximum of 4 ks exposure per pointing was established.

- Maximal exposure time is set by the visibility of the target field within the given orbit - i.e. if the field is visible during the whole orbit it can be observed for maximum ~ 130 ks. If larger depth is required one has to stack two or more mosaics.

- The observations have to be carried out in Full Frame mode and the filters can not be changed during the mosaic.

- The RGS instruments can work in a continuous mode similarly to the EPIC cameras, but OM exposures can be taken (if desired) only during stable pointings.

- There are several differences in the reduction and analysis of mosaic mode data compared to standard observations, which we will discuss in the next sections.

4.4   Analysing mosaic mode observations

In this section we describe the analysis of mosaic mode observations. The mosaic extension of the XMM-BCS survey (Sect. 6.2.1) was the first scientific utilization of this mode and development of an analysis pipeline was part of this thesis work.

We describe the analysis of the data in greater detail than there was space for in Šuhada et al. (2010), especially given the fact that the details of the analysis are not available in manuals. We will specifically highlight the differences compared to standard observations. This section is fairly technical and assumes a good knowledge of the XMM-*Newton* Science Analysis Software (SAS) and standard X-ray data reduction and analysis. We refer the reader to the SAS User Handbook for description of the individual tasks mentioned further in the text. The description of the data analysis pipeline for standard data is provided in Sect. 5.2 and Fassbender (2008).

For the analysis in this work we used SAS version 10.0.0. Since a mosaic observation comprises several individual pointings its analysis has higher memory demands and therefore it is advisable to set the SAS parameter `SAS_MEMORY_MODEL` to "high".

Mosaic mode data are provided in a standard Orbit Data Files (ODF) - with one ODF set for the whole mosaic and not for each pointing. The ODF files are compatible with standard tools and can be calibrated and filtered in a standard way with the `epchain` (for PN) and `emchain` (for MOS) tasks in order to create eventlists.

Depending on the mosaic design and scientific objectives there are two possibilities: a) one can either split the mosaic into individual pointings or b) continue to treat the mosaic in one piece. Approach a) is desirable if the mosaic pointings are non-overlapping and has the advantage that after the split we have one standard eventlist for each stable pointing (and per camera) which can be processed with upstream pipeline tasks in a completely standard way. To treat the mosaic as a whole makes sense only for contiguous mosaics. It has the advantage for source detection, because this way we can take advantage of the higher total exposure in the overlap areas of two adjacent pointings and also utilize the counts detected during the slews. This procedure however brings a few complications in the data processing. We will start by discussing this approach and then we will return to the question of splitting the mosaic into individual parts.

4.4.1   Single piece mosaic handling

Since the mosaic ODF is SAS compliant we can use the standard SAS tasks to extract higher data products from the eventlists e.g. extracting light curves, images and spectra using `evselect` and exposure maps with `eexpmap`. We will go through all the main steps of a typical observation analysis, focusing on the differences compared to a standard analysis and provide work-around recipes.

After creation of the eventlists from the mosaics ODF, we filter out periods contaminated by soft-proton flaring - for example by a (multi-step) sigma clipping method (see Sect. 5.2). Extraction of light curves from eventlists and subsequent good-time-interval filtering are exactly the same as for standard observations.

Images, spectra and exposure maps can also be created in a standard way for the whole mosaic (naturally, everything is more time costly than for a standard single field). The main challenges are encountered during the source detection step with the SAS tasks `eboxdetect` and `emldetect`. The calculations done by these tasks are very memory intensive. The amount of memory required depends on the size[22] of the mosaic (more importantly than on the total

---

[22]We mean here the area of the mosaic on the sky and more specifically the size of its minimal bounding box,

exposure time) and on the exact setup of the source detection tasks - e.g. local detection requires less memory than map mode, single band detection less than multiple bands etc. (for explanation of the different setups see Sect. 5.3.1). Source detection in mosaic data will therefore often lead to a memory overflow and a crash. Depending on the specific architecture of the machine on which we run these tasks, setting the `imagebuffersize` parameter[23] of both `eboxdetect` and `emldetect` improves the performance, but still might not be sufficient for most applications. As an example, we have found that `imagebuffersize=2000` works best on the machine used for the XMM-BCS analysis[24] and allowed to run all the standard detection setups (i.e. including the 5 bands times 3 detector setups requiring a simultaneous analysis of 15 images, exposure and background maps) on ~ 1 deg^2 sky segments. Larger areas with larger buffer size allowances always caused a crash. Machines with more available RAM can process larger chunks, but the maximal segment size can be established only by trial and error.

If a mosaic does not fit inside a ~ 1 deg^2 bounding box (see footnote 22) we can split it to several smaller segments and carry out the source detection on them. This approach was also taken when analysing the XMM-BCS mosaics.

First we use an image or exposure map of the whole mosaic to design a segmentation pattern covering the whole mosaic and consisting of boxes with sides maximally 1° long. Especially when interested in extended sources like clusters of galaxies, it is conservative to allow for $\gtrsim 1.5$ arcmin overlaps between segments. This assures that each extended source (with extent typically around $1 - 2$ arcmin) will be fully covered at least on one of the segments. The segmentation patterns for the three mosaics of the extension of the XMM-BCS survey are shown in Fig. 4.6.

For each segment, we have to extract PN, MOS1 and MOS2 eventlist and create all the input files (images and exposure maps) required by the source detection tasks. Eventlist for a given segment can be obtained by recalculating the attitude of the mosaic eventlist using the position and size of the box segment. We therefore copy the original mosaic eventlist into a separate directory for each segment to be extracted and process each of the eventlists with the `attcalc` task with its keywords set to:

`eventset =` path to the given mosaic eventlist copied to the segment's directory

`withatthkset =` yes

`atthkset =` path to the original attitude history time series (this file is part of the ODF set, named with the pattern: *ATTTSR*.FIT).

`refpointlabel =` user

`nominalra =` right ascension of the center of the box segment

`nominaldec =` declination of the center of the box segment

---

i.e. there is a dependence on the layout of the pointings, too - more compact mosaic designs have smaller memory requirements. As an example see Fig. 4.6, where extension C is much more memory intensive than A and B, although it has the same number of pointings and roughly the same total exposure time.

[23]This parameter is not listed in the SAS manual but is accepted by both `eboxdetect` and `emldetect`.

[24]A 32 bit architecture with 3.7 GB RAM memory.
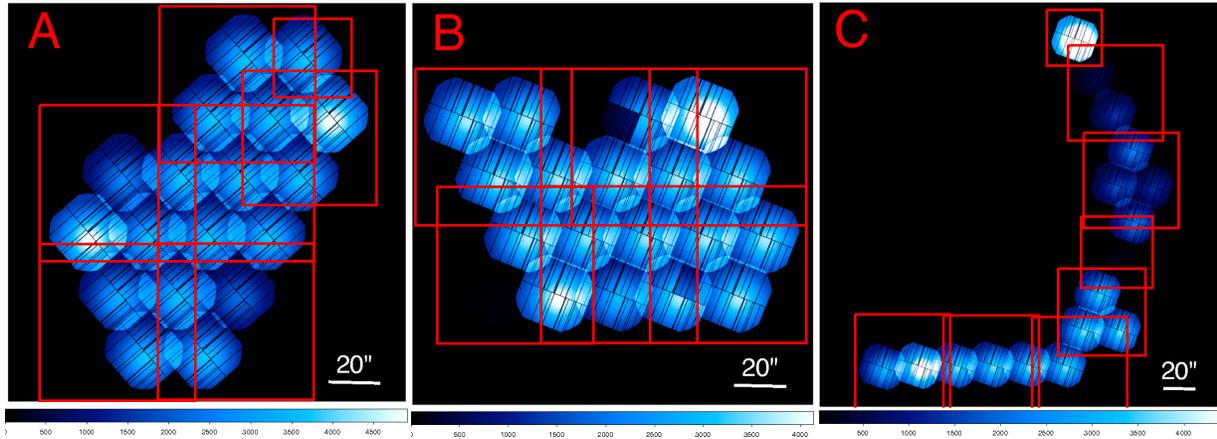
Figure 4.6: PN exposure maps in the $0.5 - 2$ keV band for the three mosaic observations of the XMM-BCS field (OBSID: A - 0604870301, B - 0604873401 and C - 0604873901). The color bar scales are linear, exposures are in seconds. The red boxes show the segmentation patterns (see Sect. 4.4.1). The full XMM-BCS field is displayed in Fig. 5.1.

imagesize = size of the box segment in degrees.

This way we produce eventlists, which can be further processed to obtain images, exposure and background maps as well as local- and map-mode source list in the source detection steps in a standard way. After obtaining the final `emldetect` source lists for each mosaic in the segment, we can merge them into a single list for the whole mosaic area. Some sources lying in the overlap areas of two mosaics will have duplicate entries in the merged source list (or three or more entries in the overlaps of three or more segments). These duplicates can be removed (or more conservatively flagged) using a 5″ matching radius. This radius was found to perform very well, keeping two distinct but nearby sources while removing the duplicate entries.

There are two caveats to the described procedure:

1) Since the mosaic segments (and whole mosaics in general) consist of several pointings, for any given point in the mosaic the information on the actual aim point of the telescope and its position angle can not be kept in the eventlist header. This information is however needed to properly calculate the off-axis angle and pointing orientation at any given point, which in turn are required to evaluate the shape and size of the PSF local to this point. The PSF would then be used in the maximum likelihood source fitting step by `emldetect`. Instead, a warning message is raised and an on-axis PSF model is used instead of the proper one. On the other hand, using a mosaic we are able to utilize the larger exposure time (and thus higher sensitivity) where the pointings overlap. We can note however, that it is in principle possible to reconstruct the proper PSF for each point (see next section) and the current limitation is given only because `emldetect` takes the pointing information from the image header (which has only a single keyword for the whole mosaic and not for each individual pointing). A fully self-consistent PSF treatment for mosaic data would thus require a redesign of the `emldetect` task.

2) The second caveat considers spectroscopy from mosaiced eventlists. Currently (i.e. up to SAS 10.0.0), the `backscale` task, used to calculate the area scaling factors of the spectra, is not

compatible with mosaic eventlists. There are two work-arounds to this problem. One can either extract the stable pointing in which the spectroscopy target lies as described in the next section. `Backscale` can then be used safely with the stable pointing eventlists. If the spectroscopy target falls into two or more pointing within the mosaic we can extract spectra from each split pointing and fit them simultaneously. This approach should be generally preferred to merging spectra. The second possibility is to use a detection mask to calculate the area scaling coefficients directly from the mosaic, bypassing `backscale` completely.

4.4.2 Splitting mosaic into individual pointings

Splitting the mosaic into individual pointings can be advantageous, particularly if it consists of disjunct pointings. This can be achieved by good-time-interval filtering of low-level eventlists (i.e. immediately after obtaining the mosaic eventlist form the ODF files).

In the first step, we have to obtain a list of start and stop times of the stable pointings within the mosaic sequence. This information is kept in the spacecraft attitude history file distributed with the observation data files (named *ATS.FITS, we will say ATS file hereafter). There is only a single ATS file for the whole orbit - i.e. if there were other observations scheduled in the same orbit they are also logged in this file (also the slews and position settling phases). There are four possible *types* of operational phases from the attitude point-of-view. They are identifiable by the `TYPEID` columns of the ATS file with these four possible values: **C** - closed-loop slew, **O** - open-loop slew, **S** - settling phase, and finally **P** - stable pointing.

Both P and S type of phases are usable and thus the individual pointings of interest can be identified as having `TYPEID==S` or `TYPEID==P` and the `VALTIME` parameter (signifying the start time of the given phase) between the start and end time of the mosaic itself (listed as the `OBSSTART` and `OBSSTOP` keywords in the header of the first extension of the mosaic eventlists[25]).

The number of entries (rows) filtered out this way will be equal to the number of individual pointings in our mosaic. From the filtered ATS file we will keep for each pointing the following entries:

VALTIME - the beginning time of the given pointing.

VALDUR - duration of the pointing in seconds.

VIEWRA - right ascension of the pointing. The parameter corresponds to the RA_PNT keyword in a standard observation eventlist header.

VIEWDECL - declination of the pointing. The parameter corresponds to the DEC_PNT keyword in a standard observation eventlist header.

ASTPOS - the astrometrical positional angle in degrees. The parameter might be required during the attitude recalculation phase, depending on the required output (see below).

ROLLANG - the roll-angle of the pointing in degrees.

---

[25]Note that these are not the same as the `DATE-OBS` and `DATE-END` keywords of the ATS file, which refer to the start and end of the whole *orbit*.

In order to extract a single pointing eventlist from the original mosaic pointing we have to calculate its good-time-interval. This is done in the following way: 1) GTI_START = VALTIME - T_0, converted to seconds, where T_0 is the canonical XMM-*Newton* time zero point[26] and 2) GTI_STOP = GTI_START + VALDUR. The good time filtering can be done as usual, e.g. by creating a text file with the GTI_START and GTI_END parameters (single line, space delimited), converting it to a GTI compliant fits file with the gtibuild task and using evselect to extract the eventlist from the input mosaic eventlist.

The resultant eventlist then contains only the counts gathered during the given pointing. We can update its header information with the corresponding entries from the ATS table (e.g. DEC_PNT, RA_PNT etc.). We can also update the keyword OBJECT to a value that uniquely identifies the pointing within the mosaic sequence (optional, but useful).

In the final step we have to recalculate the attitude of the extracted eventlist (since at this stage the attitude still refers to the center of the mosaic rather than the pointing itself). This is done with the attcalc task with its keywords[27] set to:

eventset = path to the just extracted single *pointing* eventlist

withatthkset = no

refpointlabel = user

nominalra = the value of the pointing's RA_PNT keyword

nominaldec = the value of the pointing's DEC_PNT keyword

This procedure has to be repeated for each pointing (each filtered ATS entry) and yields standard, fully compatible, single pointing eventlist. Those can be further processed to obtain images, exposure and background maps as well as local- and map-mode source lists in the source detection steps. All the data products required for spectroscopy (spectra, redistribution matrices and ancillary region files) can be extracted without problems as well. Currently, the SAS task emosaicproc is also available for splitting mosaics into individual pointings. The task is in development stage and does not allow the users to directly carry out extended source detection, change the parameters of the detection algorithm (e.g. detection and extent likelihood thresholds, custom input file names, etc.) or handle PN OoT events. These features, however, can in principle be added by modifying the source code of emosaicproc or by customizing the relevant upstream detection pipeline modules.

---

[26]1997-12-31T23:58:56.0

[27]Similarly as we seen in the previous Sect. 4.4.1. Keywords not listed here should be left unset.

Chapter 5

The XMM-BCS galaxy cluster survey

I. X-ray selected cluster catalog from the initial 6 deg^2

*R. Šuhada, J. Song, H. Böhringer, J. Mohr, A. Finoguenov, R. Fassbender, G. Chon,
M. Mühlegger, D. Pierini, G. W. Pratt, M. Verdugo, A. Zenteno, S. Desai, C. C. Ngeow,
W. A. Barkhouse, S. M. K. Alam, R. Armstrong, M. Brodwin, S. M. Hansen, F. W. High, H. Lin,
A. Rest, R. C. Smith and D. L. Tucker*

Abstract
The XMM-BCS project is a coordinated X-ray, optical and mid-infrared cluster survey in a field
also covered by Sunyaev-Zel'dovich effect surveys. The aim of the project is to study the cluster
population in a 14 deg^2 field. The uniform multi-wavelength coverage will also allow us for the
first time to comprehensively compare the selection function of the different cluster detection
approaches in a single test field and perform a cross-calibration of mass scaling relations.

In this work, we present a catalog of 46 X-ray selected clusters from the initial 6 deg^2 survey
core. We describe the XMM-BCS source detection pipeline and derive physical properties of the
clusters. We provide photometric redshift estimates derived from the Blanco Cosmology Survey
imaging data and spectroscopic redshift measurements for a low redshift subset of clusters from a
NTT observing campaign. The photometric redshift estimates are found to be in good agreement
with the spectroscopic values.

Our multi-wavelength approach gives us a comprehensive look at the cluster and group pop-
ulation up to redshifts $z \approx 1$. From the present sample, we derive the cluster $\log N - \log S$ using
an approximation to the survey selection function and find it in good agreement with previous
studies.

We compare optical mass estimates from the Southern Cosmology Survey available for part
of our cluster sample with our X-ray mass estimates derived from the X-ray luminosity. Weak
lensing masses available for a subset of the cluster sample are in agreement with our estimates.
Optical masses based on cluster richness and total optical luminosity are, however, found to be
significantly higher than the X-ray values.

5.1 Introduction

The formation of the cold dark matter (CDM) dominated large-scale structure of the Universe is hierarchical with smallest objects collapsing first. With passing time more and more massive structures are able to decouple from the Hubble flow and enter the non-linear regime, collapse and eventually virialize. The statistical properties of the matter density field (e.g. its power spectrum) as well as the growth of the structures are strongly dependent on the background cosmology and can be thus used to put constraints on cosmological models.

From this point of view, clusters occupy a very important place in the structure formation scenario, by being the most recent (i.e. redshifts $z \lesssim 2$ - coincident with the onset of the dark energy dominance) and thus also the most massive structures ($10^{13} - 10^{15}$ M$_\odot$) to virialize. The cluster abundance is therefore exponentially sensitive to the growth of the large scale-structure and to the underlying cosmological parameters (Haiman et al. 2001; Majumdar and Mohr 2003; Haiman et al. 2005).

The key parameter in cosmological tests of this type - the total mass of clusters (identified with dark matter halos) - is itself not a direct observable. Fortunately, in first approximation, clusters are virialized and their growth is gravitationally driven and therefore self-similar. This allows us to link their mass to some suitable observable quantity originating from baryonic components of the cluster - its galaxy population and the intra-cluster medium (ICM). The ICM is directly observable in X-rays or through the distortion of the Cosmic Microwave Background (CMB) imprinted by the ICM thermal electron population via inverse Compton scattering (the so-called Sunyaev-Zel'dovich effect (SZE), Sunyaev and Zel'dovich 1972).

Since the ICM closely traces the DM potential, it offers better (i.e. lower scatter) mass-proxies than those available from optical observations of the cluster's galaxy population (e.g. Reyes et al. 2008). In X-rays, the simplest and observationally least expensive mass-proxy is the X-ray luminosity L_X (Reiprich and Böhringer 2002; Pratt et al. 2009; Mantz et al. 2010a).

For the SZE experiments the most direct way to estimate the cluster mass is from the source signal-to-noise ratio (e.g. Williamson et al. 2011; Vanderlinde et al. 2010), but more importantly, through the integrated Compton parameter Y_{SZ}. Numerical simulations suggest that Y_{SZ} should be an excellent proxy of cluster mass (da Silva et al. 2004; Motl et al. 2005; Nagai 2006). First cross-comparisons of X-ray and weak lensing studies are generally finding good agreement between the mass estimates and no significant deviation from the self-similar predictions (Planck Collaboration et al. 2011a,b; Melin et al. 2011; Andersson et al. 2010; Marrone et al. 2009; Bonamente et al. 2008).

If deeper X-ray observations are available, we can use the spectroscopic temperature T_X, gas mass M_g and their combination $Y_X = T_X M_g$ (the X-ray analogue to the Y_{SZ} parameter, Kravtsov et al. 2006; Vikhlinin et al. 2009a; Arnaud et al. 2010) as good mass proxies. Using the Y_X parameter Vikhlinin et al. (2009a) put a strong constraint on the cosmological parameters including the dark energy equation of state. From a methodological point of view, this is interesting for two reasons: **1)** it shows that useful cosmological constrains can be obtained already from relatively small samples of clusters of galaxies, demonstrating the exceptional potential of this type of cosmological tests; and **2)** already this modest sample is practically systematic-limited, especially due to uncertainties in the mass estimation.

There are many factors that affect the scaling relations and the intrinsic scatter of the cluster populations around these relations: presence of cool cores (Markevitch 1998; O'Hara et al. 2006; Motl et al. 2005; Pratt et al. 2009), substructures and the cluster's dynamical state (Böhringer et al. 2010; Jeltema et al. 2008), non-gravitational physics (Nagai 2006), etc. In addition, one has to account for the Malmquist and Eddington bias when determining the scaling relations from a sample of clusters by proper treatment of the selection and mass functions (especially for L_X, Pacaud et al. 2007; Vikhlinin et al. 2009a; Mantz et al. 2010a,b). As our cluster samples cover broader redshift ranges potential deviations from self-similar evolution of the scaling relations also become an important question.

In summary, in order to be able to well constrain cosmological models with cluster samples we need: **1)** large cluster samples covering redshifts beyond unity; **2)** good knowledge of the cluster selection function's dependence on relevant observables and the distributions of these observables in the cluster population; **3)** a reliable, low scatter mass-proxy with a known evolution in the redshift range of interest.

Surveying for clusters in SZE has a large potential with regards to all three requirements, having an almost redshift independent selection very close to a selection function with a fixed mass limit at all redshifts and a robust mass-proxy in the Y_{SZ} parameter. Two ground-based large-area cluster surveys are currently underway: one by the South Pole Telescope (SPT) and one by the Atacama Cosmology Telescope (ACT). Both have already delivered their first SZE-selected cluster samples (Williamson et al. 2011; Vanderlinde et al. 2010; Marriage et al. 2010; Staniszewski et al. 2009) as well as observations of already known clusters (Plagge et al. 2010; Hincks et al. 2010). Also the *Planck* space mission has delivered its first cluster catalog (Planck Collaboration et al. 2011a).

While, the SZE surveying approach is a very interesting new channel to do cluster cosmology, in these early stages there is still a lot of work to be done to understand the systematics like e.g. the influence of radio/sub-mm sources and primary CMB fluctuations on the selection, the mass calibration and sensitivity to cluster outskirts.

Multi-wavelength follow-up of SZE selected clusters is essential, but selection function studies require also comparison of blind surveys. To this end we are conducting the XMM-BCS cluster survey. The survey field covers a 14 deg^2 area in the overlap region of the SPT and ACT surveys. The field has full coverage with the 4m CTIO telescope at Cerro Tololo, Chile, in the framework of the Blanco Cosmology Survey (BCS) in *griz* bands and *Spitzer* observations in the mid-infrared. With this optical to mid-IR coverage we are able to provide robust photometric redshift estimates out to redshifts ≈ 0.8 (≈ 1 including *Spitzer* data). The X-ray coverage consists of XMM-*Newton* observations split into two distinct parts. The 6 deg^2 core of the X-ray survey field was observed with 42 standard, individual pointings (with ~ 10 ks effective exposure time). In this work, we present an initial cluster catalog based on these observations.

After SPT commenced its operations, it was soon found that the mass threshold of contemporary SZE surveys is higher than expected. In order to offer a larger overlap between the SZE and X-ray selected cluster samples, we carried out an extension of the X-ray survey by covering an additional 8 deg^2 in three large-area fields utilizing the new mosaic mode type of observations. These observations allowed us to cover a significantly larger area in a very time-efficient way. First results as well as details on the analysis of this type of XMM-*Newton* observations are de-

scribed in Šuhada et al. (2010). We demonstrate there the feasibility of blindly detecting clusters found with current generation SZE experiments in only ~ 3 ks long XMM-*Newton* observations (including tentative spectroscopic temperature measurements) in the case of two SPT detected clusters (Vanderlinde et al. 2010). The final 14 deg^2 X-ray cluster catalog is expected to roughly double the number of clusters in the present sample and this sample will then be interesting also for its cosmology-constraining power.

The X-ray cluster catalog is also going to be used for selection function comparison with optical and mid-infrared cluster searches. A direct comparison with lower significance SPT detections is underway (note that the cluster catalog in Vanderlinde et al. (2010) and Williamson et al. (2011) include only $> 4.5\sigma$ detections). Stacking analysis of SZE detections without X-ray counterparts and vice versa will also be explored in upcoming work.

In addition, radio observations with ATCA (The Australia Telescope Compact Array) are planned and we have already initiated an optical follow-up of several clusters from the present sample with the GROND instrument on the 2.2 meter telescope in La Silla, Chile, with the aim to study the galaxy population of the clusters.

The paper is organized as follows: in Sect. 5.2 and 5.3 we describe the analysis of the X-ray observations and cluster detection pipeline. The optical data, photometric redshift estimation and spectroscopic campaign are detailed in Sect. 5.4. In Sect. 5.5 we provide our cluster sample, the physical parameters of the detected clusters and determine the survey's preliminary statistical properties. We also cross-correlate our cluster catalog with known sources and carry out a detailed comparison with the optically selected sample of Menanteau et al. (2009) and Menanteau et al. (2010) (M09 and M10 hereafter). Sect. 5.6 discusses the X-ray error budget and gives an outlook on the upcoming work in the context of the XMM-BCS survey. We give our conclusions in Sect. 5.5. In the appendices we provide ancillary information for the individual clusters, a preliminary comparison of our simplified sensitivity function calculations with realistic simulations and a cross-comparison with the XMM-LSS cluster survey.

Throughout the article we generally refer to objects in our sample as "clusters" regardless of their mass. The term "group" will be used to refer to systems with masses $\lesssim 10^{14}$ M$_\odot$. We will refer to individual objects by their identification number (ID). Proper object names are listed in Table 5.7. We adopt a ΛCDM cosmology with $(\Omega_\Lambda, \Omega_M, w, H_0) = (0.7, 0.3, -1, 70$ km s^{-1} Mpc^{-1}). Estimated physical parameters are given in apertures corresponding to factor 200 and 500 overdensities with respect to the *critical* density of the Universe at cluster redshift.

5.2 XMM-*Newton* data reduction

The XMM-*Newton* coverage of the XMM-BCS survey core consists of 42 partially overlapping pointings with offsets of 22.8 arcmin covering a total area of about 6 deg^2 (see Fig. 5.1). The observing time was allocated in the frame of an *XMM*-Newton *Large Program* during AO6. Four additional observations were carried out in AO7 to replace fields with large losses due to soft-proton flaring. The observation of field F09 (Table 5.1) was carried out in two parts. The total observing time amounts to ~ 580 ks, with an average total nominal time per pointing of ~ 15 ks (including instrument setup time and high background periods). Table 5.1 displays the basic
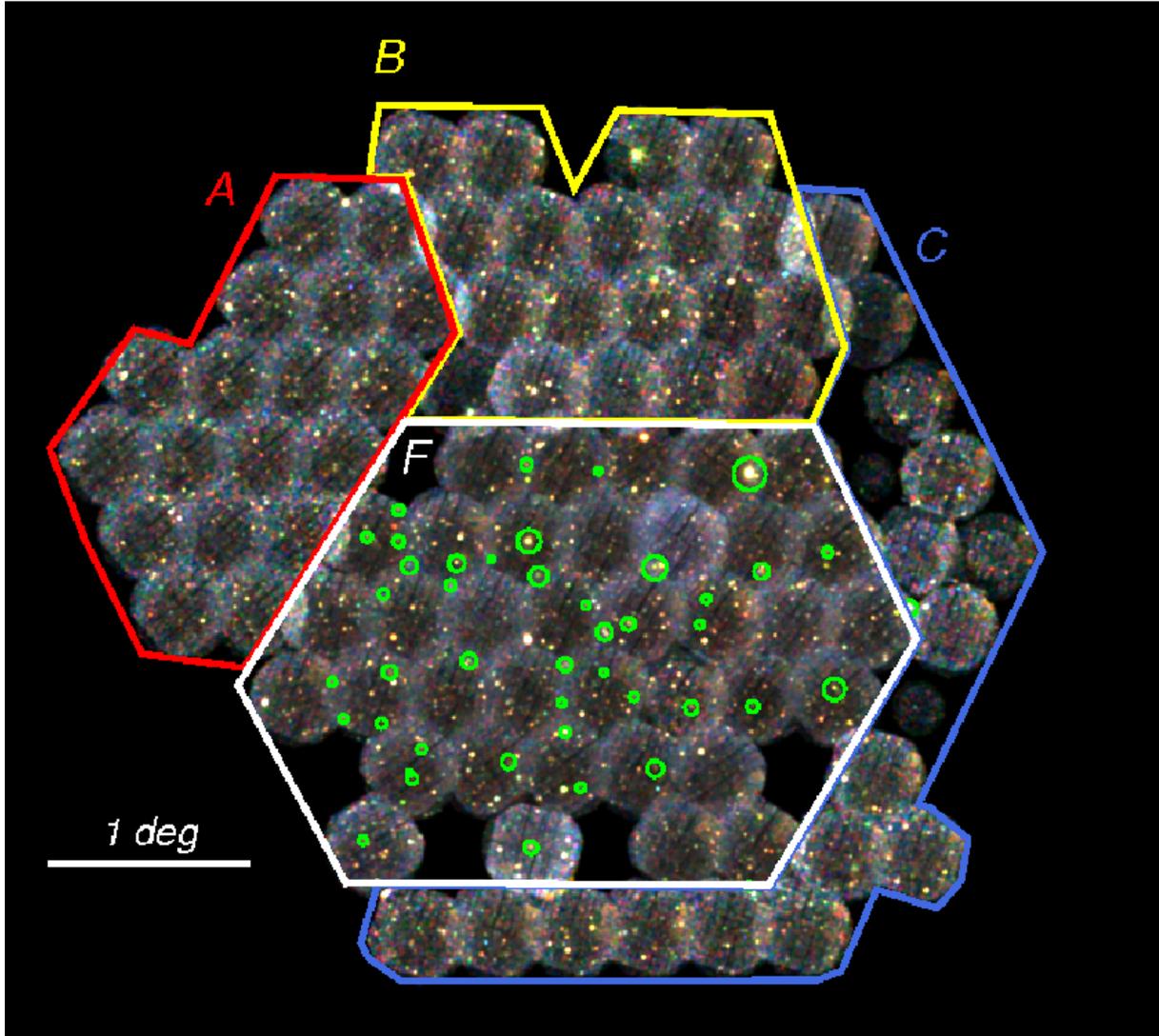
Figure 5.1: Mosaic X-ray image of the 14 deg^2 XMM-*Newton* sky survey. The false color image was constructed from the surface brightness in the $0.3 - 0.5$, $0.5 - 2.0$ and $2.0 - 4.5$ keV bands. White region (F) marks the 6 deg^2 core of the survey presented in this work. Regions A, B and C constitute the extension of the survey by mosaic mode observations. The missing fields have significant losses due to soft proton flares. Green circles mark the positions of the present cluster sample and have a radius equal to r_{500}.

information about the individual pointings. The THIN filter was used in all observations. The EPIC PN camera was operated in full frame mode.

The full XMM-BCS X-ray field is displayed in Fig. 5.1. The core region presented in this work is inside the white boundaries (region F). Regions A, B and C mark the three mosaic extensions of the survey. The five missing fields in region F have been completely lost due

to flaring (F03, F05, F42) or had large time losses due to flaring and have very high residual quiescent soft proton contamination (F07 and F13).

The EPIC data was processed with the XMM-*Newton* Standard Analysis System (SAS) version 7.1.0. We reduced and calibrated the raw observational data files with the SAS tasks `epchain` for the EPIC PN detector and `emchain` for both MOS detectors. Events in bad pixels, bad columns and close to the chip gaps are excluded from further analysis.

The eventlists were screened for high background periods caused by soft proton flares. We reject time intervals with background count rate above the 3σ limit from the mean level in the $12 - 14$ keV band for PN and $10 - 12$ keV band for MOS1 and MOS2. The mean background count rate is determined by fitting a Gaussian model to the distribution of counts in the light curve binned in 100 second intervals. After this first cleaning step, we apply the same 3σ clipping procedure in the $0.3 - 10$ keV band on 10 second binned light curves to conservatively remove time intervals affected by low energy flares. An example of a two-step cleaned light curve is displayed in Fig. 5.2.

Time lost due to flaring in our observations amounts typically to $\sim 20\%$ of the full effective observing time. Six observations of the initial fields from AO6 were too heavily affected by the flaring even after the two step cleaning. Three of these fields have been replaced by observations in AO7 (F01b, F02b, F35b) and the partially lost field F04 was also reobserved.

Detection and analysis of faint diffuse sources like clusters of galaxies in shallow surveys can be additionally affected by low energy soft protons with a roughly constant flux. This so-called quiescent soft proton background can not be detected based on light curve screening due to its small temporal variations, especially not in observations with short duration. In order to characterize possible contamination from this part of the non-X-ray background, we applied the diagnostics developed by De Luca and Molendi (2004), based on the ratio of X-ray flux in the $8 - 10$ keV inside and outside the field of view of each detector. The diagnostic reveals that the our data has the overall high quality required for our purposes. The vast majority of fields is not contaminated by quiescent soft proton background at all in any of the detectors. Five fields (F04, F06, F16, F25, F32) have a slight contamination with negligible effect on data analysis and derived results. Fields F07, F13 have significant time loses due to flaring periods (particularly in PN) and in addition are now found to have strong residual quiescent contamination. There is no cluster found in these fields in the present sample. Field F32 is affected in a similar way as well Here, however, the exposure time after flare removal is larger and we were able to identify two clusters (ID 476 and 139) in this observation.

The double component background model (see Sect. 5.3.1) used for source detection and characterization can in principle account to first order for such an enhanced background by increasing the unvignetted part of the background model. The vignetting function of such particle background has a different shape than the vignetting of the X-ray photons, but it is known only tentatively. We expect the errors from such first order approximation to be small compared to other sources of uncertainty (including the shot noise itself). We thus decide to include into our analysis also fields with strong residual quiescent contamination, but parameters derived for sources in these fields should be handled with caution.

We treat out-of-time-events (OOTE) for the PN detector in a standard way. For each observation, we generate an OOTE eventlist with the `epchain` and remove time periods identified in

Table 5.1: The individual XMM-*Newton* pointings. Quoted exposures are effective exposures with high background periods filtered out.

Field ID		RA (J2000)	Dec (J2000)	Exposure times (ks)		
OBSID	Internal			PN	MOS1	MOS2
0505380101	F01	23:21:38.4	-56:07:34.4	observation lost due to flaring		
0554561001	F01b	23:22:00.1	-56:09:03.3	7.8	10.4	10.4
0505380201	F02	23:24:23.5	-56:07:13.2	observation lost due to flaring		
0554560201	F02b	23:24:43.8	-56:09:03.0	10.2	13.2	13.2
0505380301	F03	23:27:07.0	-56:07:16.3	observation lost due to flaring		
0505380401	F04	23:29:50.6	-56:07:16.0	5.2	6.9	6.9
0554560901	F04b	23:30:11.7	-56:09:01.2	3.1	12.7	12.7
0505380501	F05	23:32:34.6	-56:07:12.8	observation lost due to flaring		
0505380601	F06	23:35:39.3	-56:08:18.7	5.6	10.6	10.6
0505380701	F07	23:20:49.3	-55:45:35.1	4.4	9.6	9.6
0505380801	F08	23:23:31.4	-55:45:39.2	9.3	9.1	0.0
0505380901	F09	23:26:12.7	-55:46:10.2	2.3	6.0	6.0
0505384801	F09b	23:26:11.6	-55:46:30.2	7.3	9.8	9.8
0505381001	F10	23:28:55.3	-55:45:39.2	9.7	12.6	12.6
0505381101	F11	23:31:37.8	-55:45:39.7	7.2	9.7	9.7
0505381201	F12	23:34:19.5	-55:45:42.6	10.8	13.5	13.5
0505381301	F13	23:37:01.4	-55:45:39.2	2.3	10.6	10.6
0505381401	F14	23:19:29.9	-55:23:01.1	10.8	13.9	13.9
0505381501	F15	23:22:09.7	-55:23:23.1	7.4	9.9	9.9
0505381601	F16	23:24:50.3	-55:23:26.3	3.2	11.7	11.7
0505381701	F17	23:27:29.7	-55:23:45.9	7.3	10.0	10.0
0505381801	F18	23:30:10.5	-55:23:41.1	11.3	15.2	15.2
0505381901	F19	23:32:51.0	-55:23:38.5	7.4	8.9	8.9
0505382001	F20	23:35:31.3	-55:23:44.6	10.5	13.9	13.9
0505382101	F21	23:38:12.0	-55:23:43.7	4.8	8.2	8.2
0505382201	F22	23:18:20.7	-55:00:13.1	11.8	14.3	14.3
0505382301	F23	23:20:58.9	-55:00:36.3	7.3	10.0	10.0
0505382401	F24	23:23:37.8	-55:00:35.5	7.5	10.0	10.0
0505382501	F25	23:26:16.6	-55:00:42.1	15.2	20.6	20.6
0505382601	F26	23:28:55.2	-55:00:49.1	9.4	12.1	12.1
0505382701	F27	23:31:34.3	-55:00:51.0	6.1	11.9	11.9
0505382801	F28	23:34:12.9	-55:00:55.7	7.1	9.8	9.8
0505382901	F29	23:36:51.9	-55:00:54.2	7.3	9.9	9.9
0505383001	F30	23:19:41.6	-54:37:27.7	12.7	16.4	16.4
0505383101	F31	23:22:18.6	-54:37:53.3	7.4	10.0	10.0
0505383201	F32	23:24:56.1	-54:37:52.3	11.6	13.6	13.6
0505383301	F33	23:27:32.7	-54:38:04.7	13.0	15.9	15.9
0505383401	F34	23:30:10.6	-54:38:00.9	9.1	11.9	11.9
0505383501	F35	23:32:29.0	-54:36:00.3	observation lost due to flaring		
0554560601	F35b	23:32:47.7	-54:38:05.8	7.7	11.4	11.1
0505383601	F36	23:35:25.6	-54:37:57.3	8.6	11.8	11.8
0505383701	F37	23:21:08.8	-54:15:02.4	7.5	9.9	9.9
0505383801	F38	23:23:44.6	-54:15:01.5	8.7	11.5	11.5
0505384901	F39	23:25:58.1	-54:14:20.2	5.5	6.8	6.8
0505384001	F40	23:28:56.6	-54:15:15.2	9.4	12.2	12.2
0505384101	F41	23:31:32.4	-54:15:13.7	9.9	12.5	12.5
0505384201	F42	23:33:49.9	-54:13:13.3	observation lost due to flaring		
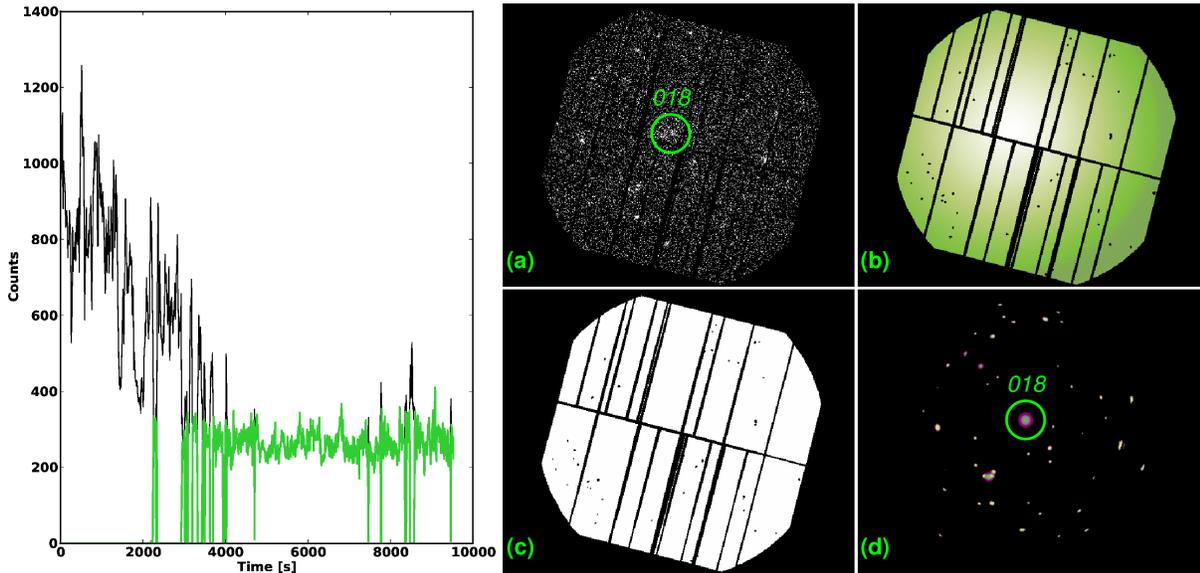
Figure 5.2: **Left:** The black line shows the 10 second-binned PN light curve in the $0.3 - 10$ keV band for the field F04. The beginning of the observation was affected by flaring. The green curve shows the light curve after the two-step cleaning (see Sect. 5.2), which safely removed all contaminated time intervals. **Right:** Examples of the detection pipe products for field F04 in the $0.5 - 2$ keV band of the PN detector: **a)** counts image, **b)** double-component background model, **c)** binary detection mask, **d)** reconstruction of all the detected sources. The green circle (2 arcmin. radius) marks the cluster ID 018.

the two step cleaning process of the main PN eventlist. Whenever an image is extracted from the PN eventlist, we extract also an image with the same selection criteria from the OOTE eventlist, scale this image with a factor of 0.063 (full frame readout mode) and subtract it from the main PN image.

5.3   Source detection

As the main source detection algorithm we utilize the sliding box technique and a maximum likelihood source fitting in their improved implementation in the SAS tasks `eboxdetect` and `emldetect`. A detailed description of the work flow and configuration of our detection pipeline developed for the XMM-*Newton* Distant Cluster Project (XDCP) can be found in Fassbender (2008), here we only summarize the main steps.

Source detection is carried out in three different schemes:
(i) the standard three band scheme: provides continuous, non-overlapping coverage in three energy bands: $0.3 - 0.5$ keV, $0.5 - 2.0$ keV and $2.0 - 4.5$ keV.
(ii) the optimized single band scheme: covers the $0.35 - 2.4$ keV band and was chosen to maximize the signal-to-noise-ratio for clusters of galaxies with a large range of redshifts and temperatures (see also Scharf 2002). This bandpass is expected to maximize the number of detected

photons especially for high redshift systems ($z \gtrsim 1$)

(iii) the five band spectral matched scheme: uses five partially overlapping bands ($0.3 - 0.5$, $0.35 - 2.4$, $0.5 - 2.0$, $2.0 - 4.5$ and $0.5 - 7.5$ keV). This scheme is equivalent to a single band detection in the full $0.3 - 7.5$ keV range, where the energy intervals in the overlaps have higher weighting. The shape of the weighting function roughly mimics the expected continuum spectrum shape of a hot cluster (Fassbender 2008). This setup was used only to confirm detections from the first two schemes and we do not use any results derived from it in the current work.

We have also carried out a detection using a wavelet detection algorithm developed for the COSMOS project by Finoguenov et al. (2007). Every cluster presented in our current sample has also been confirmed by this approach. In addition, we have identified four systems (Table 5.9) with a wavelet detection but no SAS-based detection in any setup. All four systems are coincident with significant galaxy overdensities. We find many interloping X-ray point-sources in these systems (a potential source of misclassification in the SAS detections). Even after conservative point source removal, residual contamination makes all the estimated X-ray parameters highly uncertain. These detections are not included in the statistical description of the sample (e.g. the $\log N - \log S$ relation) and are listed here only for completeness.

5.3.1 Source list generation

In order to obtain the raw source lists, we extract images from the cleaned eventlist for each detector and each band required in the given detection scheme (e.g. in the three band scheme three images for each detector, in total nine images per field). We run the sliding box detection algorithm (`eboxdetect` in the so-called *local* mode) on these images. The background for each potential source is estimated only locally in a detection cell of 5×5 pixels in 4 successive runs with the number of pixels per cell doubled in each iteration. Sources detected by this procedure are then excised from the images, creating an image usable for proper background estimation.

We model the background of each detector and band individually with a *double component background model*. This background model is a linear combination of two templates based on vignetted and unvignetted exposure maps, taking into account the sky X-ray background (vignetted component) and the particle and instrumental background (unvignetted in the first approximation).

The final sliding box detection is then run utilizing the fitted background model instead of a locally estimated background. For all sources above the detection threshold we carry out a maximum likelihood fitting (with the `emldetect` task). A beta profile with a fixed beta value of $\beta = 2/3$ convolved with the two dimensional point-spread function (PSF) is fitted to each source. The fit is carried out for all three detectors and all the bands in the given detection scheme *simultaneously*. The free parameters of the fit are the source position, normalization of the model (for each detector and band) and the core radius, θ_c, characterizing the source extent. If the extent of the source is not statistically significant, the source is refitted as a point source with extent fixed to zero.

The *detection* likelihood of a source is given by the `det_ml` parameter in the `eboxdetect` and `emldetect` tasks, defined as $det\_ml = -\ln P_{rand}$, where P_{rand} is the probability of observed counts arising from pure random Poissonian fluctuations. In each step of the detection process,

the minimum detection likelihood is set to 6, roughly equivalent to a $\gtrsim 3\sigma$ detection in terms of signal-to-noise ratio.

The *extent* likelihood `ext_ml`, defined analogously to characterize the probability of the source being extended, is required to be ≥ 3 in the three-band scheme and ≥ 5 in the single band scheme (corresponding approximately to minimum extent significances of $\sim 2\sigma$ and $\sim 3\sigma$ respectively).

For a more detailed discussion and justification of the chosen detection schemes and thresholds we refer to Fassbender (2008), who also demonstrates the performance of the described source detection methods on over 450 archival XMM-*Newton* observations in the framework of the XDCP project. A description of the used SAS tasks can be found in the SAS 7.1.0 reference manual.[1]

In the current work, we aim for the best possible survey completeness including the high redshift end of the cluster distribution and reliable source classification especially close to the detection thresholds. This is also helped by combining different detection schemes and setting relatively low extent thresholds. The increasing source contamination close to the detection threshold is treated with careful screening using the optical data and ancillary X-ray information (e.g. quality flags described in Appendix 5.8.1).

The detected sources create a raw master list of extended source *candidates*. Each of these candidates is then screened visually with optical imaging data (4 band BCS imaging) and accepted to the presented cluster catalog only if a significant overdensity of galaxies in the photometric redshift space is found (Sect. 5.4). The available *Spitzer* imaging for the whole field will be used in the future to confirm $z > 1$ systems, where the depth of the BCS imaging is not sufficient anymore.

The purely X-ray based selection function will be developed in subsequent work based on simulations, where completeness and contamination of different detection schemes will be studied. Guided by extensive simulations of X-ray observations (Mühlegger 2010), we are going to be able to get a high precision description of the survey selection function. This evaluation is still in progress. A statistically well defined cluster sample will be drawn from the current catalog (plus its 8 deg^2 extension) and used to study the evolution of the cluster X-ray luminosity function and perform cosmological tests.

Treatment of MOS CCDs in anomalous state

A special note is required concerning the anomalous states of CCD#4 of the MOS1 and CCD#5 of the MOS2 detectors and their effect on extended source detections. The occurrence of these anomalous states is becoming more frequent. Half of our fields have the MOS2 CCD#5 in the anomalous state and $\sim 20\%$ have an anomalous MOS1 CCD#4 (some observations are affected by both). These anomalous ("hot") states are characterized by high overall background count rates with atypical hardness ratios. The most affected are the soft bands (see Kuntz and Snowden 2008a).

We check for the presence of a hot chip in an observation by comparing count rates extracted

---

[1] `xmm.esac.esa.int/sas/7.1.0/`
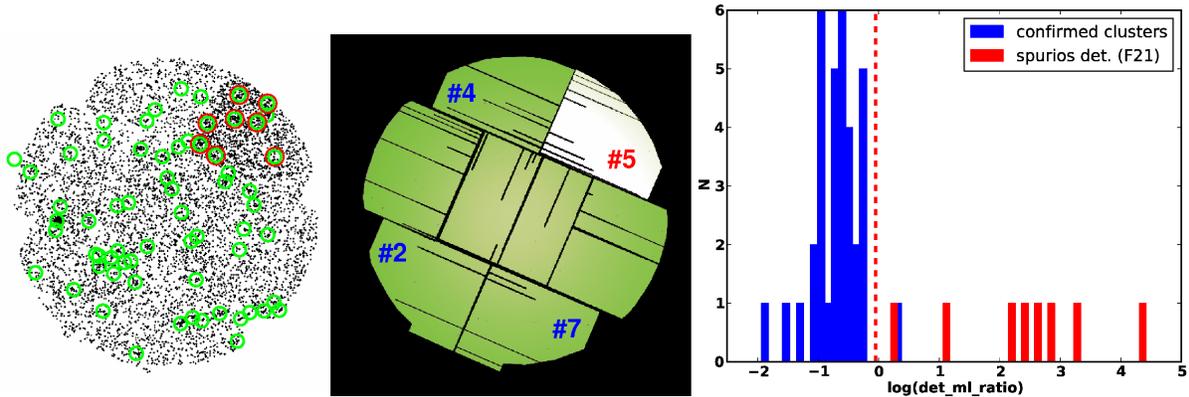
Figure 5.3: **Left:** Image of field F21 taken by the MOS2 camera in the $0.5 - 2.0$ keV band. The MOS2 CCD#5 is visibly in an anomalously high ("hot") with an enhanced background. Sources detected in this field are marked by green circles. Sources with red circles were automatically flagged as possibly spurious detections caused by the presence of the hot chip. **Middle:** A composite background model for the same detector and band created by fitting the double component model independently to the CCD#5 and the rest of the chips. The three blue-marked chips are the reference chips used to identify hot chips in the observations. **Right:** The ratio of the total detection likelihood(log scale) from the MOS2 chip in the $0.3 - 0.5$ and $0.5 - 2.0$ keV bands to the total detection likelihoods from all other detectors and bands (log scale). Blue bars show the confirmed clusters from our sample, the red bars the 8 flagged sources from field F21 (from the left panel). The vertical line marks where the soft band MOS2 detection constitutes 90% of the total detection likelihoods in all detectors. The flagged sources were confirmed as spurious by the optical data. A single confirmed cluster (ID 275) appears above the threshold, but is *not* flagged as spurious since it would have been above the detection likelihood even without the MOS2 detection (i.e. not meeting all the required criteria described in Sect. 5.3.1).

from the suspected chip and the mean count rate of three other chips in symmetrical positions around the central chip (i.e. the mean count rate of CCD#2, CCD#4, CCD#7 of MOS2 and CCD#3, CCD#5, CCD#7 of MOS1 detector). These reference chips were selected, because they best match the area, shape and position of the affected chips (see middle panel of Fig. 5.3). The count rates calculated in the $0.3 - 2.0$ keV band from the three reference chips are then averaged to reduce shot noise and a chip is flagged hot, if its count rate is more than 10% higher than the mean count rate from the reference chips. This threshold is chosen to be very conservative and was found to perform excellently, since chips in anomalous states have typically count rates $50 - 100\%$ higher than the reference rate.

The exceptionally high background of the hot chips leads to many spurious extended source detections, when left untreated (see Fig. 5.3). We flag sources as possibly spurious detections caused by the presence of a hot chip if at the same time: 1) they lie on a chip that was flagged hot, 2) are extended, 3) the detection likelihood from the given hot MOS detector in the soft bands (sum of the $0.3 - 0.5$ and $0.5 - 2.0$ keV bands) accounts for more than 90% of the total detection likelihood and 4) the source would be under our detection threshold without the detection on

the affected chip. We still visually checked every flagged source also in the optical images and confirmed the classification of these sources as spurious.

An example of this procedure can be seen in Fig. 5.3. The observation of field F21 has a hot MOS2 CCD#5, clearly visible as an enhanced background (in the raw image in the left panel and in the model background in the middle). The 8 extended sources detected on this chip were flagged as a possibly spurious based on the described criteria. The detection likelihood ratio (the MOS 2 detection likelihood in the soft bands over the total detection likelihood) of these 8 sources are displayed on the left panel of Fig. 5.3 (red) as compared to the sample of confirmed clusters in our sample (blue).

A similar criterion can be applied in principle also to spurious point source detections. An additional improvement can be achieved by weighting the input detection likelihoods by the number of pixels in the detection aperture in order to avoid a possible bias, if a source has a low detection likelihood in one of the reference detectors only because it falls on a chip gap or is (partially) out of field-of-view.

In addition, we make an attempt to model the high background of the hot chips by fitting in first approximation the double component model to a hot chip only and another double component model to the remaining chips. The two parts of the background model are then combined to create a composite background map for the full detector area (middle panel of Fig. 5.3). All the extended sources on hot chips flagged as spurious with the described detection likelihood test, are not detected when the composite background maps are utilized, confirming the reliability of our classification. The effect of using a composite background instead of a standard background on detections coming from the remaining, non-anomalous chips is minor, since the two background models in these areas differ typically by less than 5%, and only the softest bands of each detection scheme are affected. For the source characterization in observations affected by hot chips we use exclusively composite background maps.

5.3.2   Growth curve analysis

The X-ray flux of the clusters is the most direct physical parameter obtained from observations and allows us to determine the X-ray luminosity L_X and estimate other key parameters as the temperature and mass of the cluster from scaling relations.

A typical cluster of galaxies in relatively shallow observations like ours appears as a faint diffuse source with typically of the order of $\gtrsim$ 100 source photons registered (total from all three standard bands and detectors). Thus in order to get a reliable measurement of the flux and trace the emission of the cluster as far out possible, we have to employ a robust method. In this work we utilize the *growth curve method* developed for the REFLEX and NORAS cluster samples derived from the *ROSAT* all sky survey by Böhringer et al. (2000). Here we summarize the procedure.

For each source, we extract images, exposure maps and background maps in the $0.5-2.0\,\mathrm{keV}$ band, excluding all point sources detected by the pipeline. MOS1 and MOS2 products are then directly co-added, since the difference in their response matrices is small. We run the growth curve program on the PN and co-added MOS images independently.
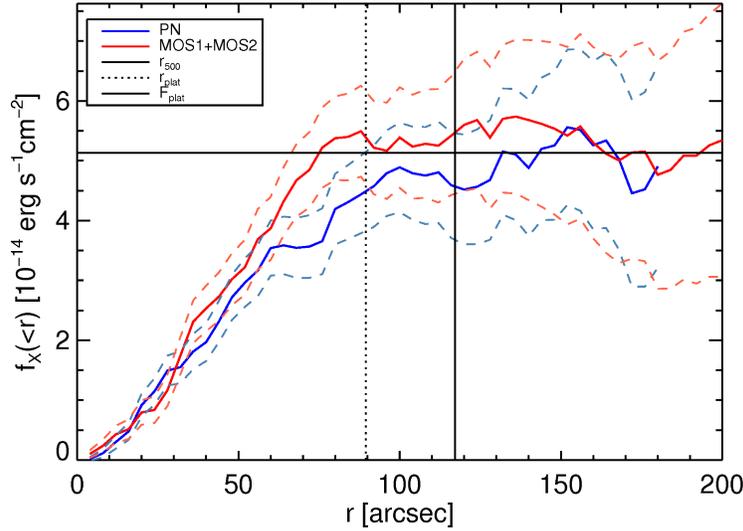
Figure 5.4: Example of the growth curve analysis of source ID 018 (photo-z=0.39). The cluster's redshift and luminosity are close to the median values of the entire sample. The curves show the encircled cumulative flux as a function of radius (PN: blue curve, combined MOS: red). The PN and MOS curves are in good agreement. Dashed lines mark the flux measurement error bars which include the Poisson noise and an additional 5% systematic error from the background estimation. The estimated plateau flux is $F_{plat} = 5.24 \times 10^{-14}$ erg s^{-1} cm^{-2} (horizontal line), reached at $r_{\mathrm{plat}} \sim 90$ arcsec. The vertical line signifies the estimated r_{500} radius of the source, $r_{500} = 0.6$ Mpc (~ 117 arcsec). In this case, the plateau radius is slightly smaller than r_{500} and the flux and luminosity for r_{500} had to be extrapolated from their plateau values. The required extrapolation is only $\sim 2\%$ in this case. See Sect. 5.3.3 for details.

In this analysis we use the X-ray center coordinates obtained from the beta model fitting procedure in the source detection step. We also explored the possibility of recentering by minimizing the dipole moment of the count distribution (see e.g. Böhringer et al. 2010). This procedure usually yielded centers very close to the best-fit coordinates, but for faint sources often completely diverged. The best-fit coordinates were always found to be a good description of the detected X-ray emission centroid.

Counts are extracted from the image in concentric rings starting from the center and scaled by the exposure time. In this way we obtain the total (source + background) count rate profile. The expected background count rate is estimated from the background map and subtracted for each ring from the total count rate, obtaining the source count rate profile. The *growth curve* is the cumulative background subtracted source count rate profile (see Fig. 5.4).

We term the full aperture inside which a stable growth curve can be obtained, the *extraction radius* r_{ext} (typically a $150 - 200$ arcsec aperture). It is adjusted for each source individually (increased for brightest, most extended sources or trimmed for sources close to the edge of FOV or to a partially blended systems) and includes the source itself as well as enough sky region to check the reliability of the double component background subtraction.

If the background model describes the local background accurately, the growth curve levels off to a flat plateau at the outer edge of the source. To estimate the total detected cluster emission, we first calculate the *significance radius* r_{sig}, defined as the radius outside which the source signal increases less than the 1σ uncertainty in the count rate. The significance radius thus gives the outermost radius where the potential increase of the growth curve becomes less than 1σ significant. This radius is found to be typically slightly smaller than the radius where the source signal-to-noise ratio decreases below unity.

To alleviate the effect of shot noise, r_{sig} is determined by smoothing the growth curve in 20 and 48 arcsec windows (5 and 12 pixels respectively). For most clusters the two estimates are in agreement. In the remaining cases, the local background usually exhibits irregular features not captured by the double component model and we select the more appropriate r_{sig} and plateau after visual inspection.

In addition, a single multiplicative correction factor to the background model can be set, if the plateau exhibits a significant residual slope. This additional factor corrects the overall normalization of the double component model locally inside r_{ext}. The average background correction factors are -2% (i.e. a 2% decrease compared to the default double component background) for PN and 0% for MOS (with standard deviations 7% and 8%, respectively). More than 3/4 of the present sample have correction factors smaller than 10%. Reiprich (2001) and Reiprich and Böhringer (2002) used a similar correction procedure utilizing a second order polynomial to obtain stable plateaus. In our case, a simple correction factor turned out to be sufficient and not leading to background over-fitting.

After setting the background correction, the total source count rate is estimated as the count rate of the plateau. The flat plateau of the growth curve outside r_{sig} is then fitted with a line. If the slope of the line is less than 0.8% per radial bin, the plateau fit is accepted and the plateau count rate CTR_{plat} is estimated as the mean of the fitted line. If the slope is still not negligible, an additional attempt is made to find a stable plateau by iteratively removing the outermost and innermost (still outside r_{sig}) bins. We note that in $\sim 80\%$ cases the first simple fit is fully acceptable and no further iterations are necessary. For more detailed description of the iterative process and quality flags of the plateau fit see Sect. 5.8.1 in the appendix. The aperture corresponding to the plateau count rate CTR_{plat}, the *plateau radius* r_{plat}, is defined simply as the radial distance where the growth curve first reaches CTR_{plat}.

We provide a performance test of our X-ray photometry method on the example of the XMM-LSS cluster catalog (Pacaud et al. 2007) in Appendix 5.8.4. The main advantages of the growth curve method thus are: **(i)** Excellent sensitivity allowing us to trace cluster emission to the outermost faint outskirts. **(ii)** It makes no assumptions about the source profile unlike methods based on beta model fitting, which is fully degenerate in the regime with $< 400 - 500$ counts and is known to not be an appropriate description of cluster emission for irregular and cool core clusters. **(iii)** The method allows to check and correct the background modelling which is done for the whole field of view, by adjusting several parameters to the conditions local to each analyzed source. **(iv)** The PN and combined MOS growth curves are treated completely independently. Their comparison provides us with an important consistency check and allows us to treat instrument specific features in the background separately.

5.3.3 Physical parameter estimation

With a stable PN and MOS growth curve at hand we determine all the relevant physical parameters of the clusters in an iterative way.

In a given iteration, we measure the count rate inside the actual r_{500} aperture. From the estimate of the temperature T_{500} (from the previous iteration), we calculate the energy conversion factor (ECF) for PN and MOS, assuming a MeKaL spectral model (Mewe et al. 1985; Kaastra 1992; Liedahl et al. 1995) with T_{500}, abundance of 0.3 times solar abundance and the hydrogen column density set to the Galactic value derived from the HI observations of Kalberla et al. (2005).

To account for the spatial variation of the spectral response of the detectors we calculate a response matrix for each source individually in a 150 arcsec aperture centered on the source for the THIN filter. The MOS2 response matrix is used to calculate the ECF of the co-added MOS count rates.

With the obtained ECFs the PN and MOS count rates are converted to flux. From the flux and known redshift of the source the k-corrected X-ray luminosity $L_X(< r_{500})$ is calculated.

The flux and luminosity estimates inside the plateau radius r_{plat} from the growth curve method do not require any assumption about the spatial distribution of the source emission. However, in some cases the actual value of r_{500} is greater than r_{plat} (i.e. outside the region with directly measurable emission), and therefore an extrapolation correction is applied to the flux and luminosity. We correct for the missing flux by extrapolating the source emission with a beta model between the plateau radius and current estimate of r_{500}. The β and r_{core} of the beta model are estimated from the actual estimate of T_{500} using the scaling relations of Reiprich and Böhringer (2002). Owing to the good sensitivity of the growth curve method allowing us to trace cluster emission out to large radii, the required extrapolation is minor. The mean correction is $\sim 2\%/\sim 3\%$ for PN/MOS ($\sim 27\%$ at maximum).

The final source flux and luminosity in the $0.5 - 2.0$ keV band are then obtained by averaging of the PN and MOS fluxes weighted with their inverse squared errors. Sources for which the PN and MOS estimates do not agree or one of the estimates is missing (e.g. source outside of the FOV of a given detector) are flagged (Table 5.7 in the appendix). An X-ray photometric quality flag is also assigned to each source based on the quality of the plateau fit, portion of pixels outside the detection mask, presence of anomalous features in the X-ray background and visual screening.

The $L_X(< r_{500})$ is then used to update the values of T_{500}, M_{500}, r_{500}, and $Y_X(< r_{500})$ in the current iteration. We utilize the $L - T$, $L - M$ and $L - Y_X$ scaling relations from Pratt et al. (2009). These scaling relations are best suited for our purposes for several reasons. They were derived from XMM-*Newton* observations (removing possible calibration issues between relations derived from different instruments) of a representative cluster sample (REXCESS, Böhringer et al. 2007). The sample covers a great range of the cluster luminosity function without a bias towards a morphological structure type (like e.g. presence of a cooling core or merging activity). The distribution of REXCESS clusters according to their morphology is therefore closer to the distribution of clusters expected to be detected in surveys conditions. Additionally, the $L - M$ relation is based on the $L - Y_X$ and $Y_X - M$ scaling relation, which is found to be more robust than previ-

ous direct $L - M$ calibrations (Arnaud et al. 2007). We use the relation coefficients from BCES orthogonal fits (Akritas and Bershady 1996), which do not treat T_{500} as the independent variable, since our only measured independent variable is in fact $L_X(< r_{500})$. At this stage it is impossible to safely detect and remove emission from possible cooling cores because of the limited resolution of XMM-*Newton*. Therefore we opt not to do so and use the relations that include the core regions.

The redshift range covered by the REXCESS sample is relatively small ($z < 0.2$). In this range no significant deviations from the self-similar evolution were found. Since our sample extends out to $z \approx 1$, where deviations are expected, we test how large is the influence of a slower than self-similar evolution on the estimated physical parameters in Sect. 5.6.1. The exact form of the evolution is still an open question (Arnaud 2005; Pacaud et al. 2007) with the first solid detection made only recently by the Chandra cosmology project (see Vikhlinin et al. 2009a). The exact shape of the evolution law is still not well constrained and thus can not be reliably incorporated into the parameter determination. The REXCESS sample also does not sample the temperature distribution below ~ 2 keV, where a substantial part of our sample is lying.

We then use the M_{500} estimate to obtain a new r_{500} radius from $r_{500} = \sqrt[3]{3M_{500}/4\pi 500\rho_C(z)}$, where $\rho_C(z)$ is the critical density of the Universe at redshift z. In the next iteration this new r_{500} aperture is used to recalculate the luminosity and the whole process is repeated until converging to a final solution.

The described algorithm was also applied to the clusters SPT-CL J2332-5358 and SPT-CL J2342-5411 in Šuhada et al. (2010) detected in the extension of the XMM-BCS survey. These sources have been independently analysed by Andersson et al. (2010) using deeper data (from XMM-*Newton* for the first cluster and from *Chandra* for the second). Their results are in good agreement[2] with our values, demonstrating that our method yields robust results. We discuss several possible sources of systematic errors of this procedure in Sect. 5.6.1. Physical parameters determined for the present cluster sample are displayed in Table 5.6.

As a summary we provide here a compilation of scaling relations used to estimate the parameters in Table 5.6. The bolometric luminosity based scaling relations for r_{500} as described above are taken from Pratt et al. (2009):

$$M = 2 \times 10^{14} \, \mathrm{M_\odot} \left(\frac{h(z)^{-7/3}L}{1.38 \times 10^{44} \, \mathrm{erg \, s^{-1}}} \right)^{1/2.08} \tag{5.1}$$

$$T = 5 \, \mathrm{keV} \left(\frac{h(z)^{-1}L}{7.13 \times 10^{44} \, \mathrm{erg \, s^{-1}}} \right)^{1/3.35} \tag{5.2}$$

$$Y_X = 2 \times 10^{14} \, \mathrm{M_\odot} \, \mathrm{keV} \left(\frac{h(z)^{-9/5}L}{5.35 \times 10^{44} \, \mathrm{erg \, s^{-1}}} \right)^{1/1.04} . \tag{5.3}$$

---

[2]For SPT-CL J2342-5411 ($z_{\mathrm{photo}} = 1.08$) the agreement is very good overall, for SPT-CL J2332-5358 ($z_{\mathrm{photo}} = 0.32$) our spectroscopic temperature estimate is higher than the Andersson et al. (2010) value (but consistent within the error bars). Mass and the Y_X parameter in this particular case were calculated from the temperature scaling relations and are therefore overestimated. In the present work, the X-ray luminosity is the only direct cluster observable.

In order to estimate the mass in the r_{200} aperture, we use the approximation provided by Hu and Kravtsov (2003) to iteratively calculate the parameters of a NFW profile (Navarro et al. 1997) from the M_{500} mass and assuming the Bullock et al. (2001) relation for the concentration parameter calculation. The NFW profile was then used to extrapolate the mass from the r_{500} to r_{200}. The beta model extrapolation correction is calculated with the beta model parameters obtained from scaling relations of Reiprich (2001), see also Finoguenov et al. (2007):

$$r_{core} = 0.07 \times r_{500} \left(\frac{T}{1\,\mathrm{keV}} \right)^{0.63} \quad \text{and} \quad \beta = 0.4 \left(\frac{T}{1\,\mathrm{keV}} \right)^{1/3}. \tag{5.4}$$

5.4 Photometric redshift estimation

In order to measure the photometric redshifts (photo-zs) of the X-ray selected systems in our sample, we applied the red-sequence redshift estimator to the Blanco Cosmology Survey imaging data which covers two 50 deg^2 patches of the southern sky and includes the full area of the present XMM-*Newton* survey. The details of the method will be provided in Song et al. (submitted), here we give its brief summary.

The raw data has been reduced and processed using the data management system developed for the upcoming Dark Energy Survey (Ngeow et al. 2006). At the time of preparation of this paper, the status of the processing pipeline is not fully complete. This affects the accuracy of photometric redshift presented here within $5 - 7\%$. The overall uncertainty of the photo-zs is on the $\sim 10\%$ level.

The red-sequence redshift estimator utilizes all available filters, (g-, r-, i-, and z) to search for redshift peaks in the density distribution of galaxies within a radius of 0.8 Mpc centered on the X-ray detection. The contribution of background galaxies is estimated from a surrounding $36' \times 36'$ sky patch and statistically subtracted. For each X-ray cluster candidate the whole redshift range from $z = 0$ to $z = 1.05$ is scanned through using simultaneously two colors that bracket the 4000 Å break at the given redshift. This suppresses false overdensity peaks at transitional redshifts where the 4000 Å break moves between two adjacent bands (e.g. the transition between the g and r band around $z \approx 0.35$). Once a peak in redshift space is identified, we refine the redshift estimate by fitting a Gaussian function to the redshift density distribution. We then select cluster members in a stripe (0.05 width in color) around the estimated red-sequence. The final cluster redshift value is calculated as the inverse color error weighted mean redshift of the selected member galaxies. This assures that the reliability of the photo-z values for the whole system is always better than for any individual galaxy. An example of the galaxy density distribution in the redshift space for cluster ID 018 is shown in Fig. 5.5 (its redshift is close to the median redshift of the cluster sample). In a few cases two or more solutions were found by our algorithm. For these systems we visually check the obtained redshift distributions and select the more likely solution given the positions of galaxies with respect to the X-ray emission.

The described photo-z estimation method allows us to measure the cluster redshift with good precision up to $z \approx 0.8$ even for X-ray selected groups. While care was taken to obtain reliable results also for $z \gtrsim 0.8$ systems (see Fig. 5.6 for two examples), here the already obtained *Spitzer* mid-infrared observations will provide an important improvement in subsequent work.
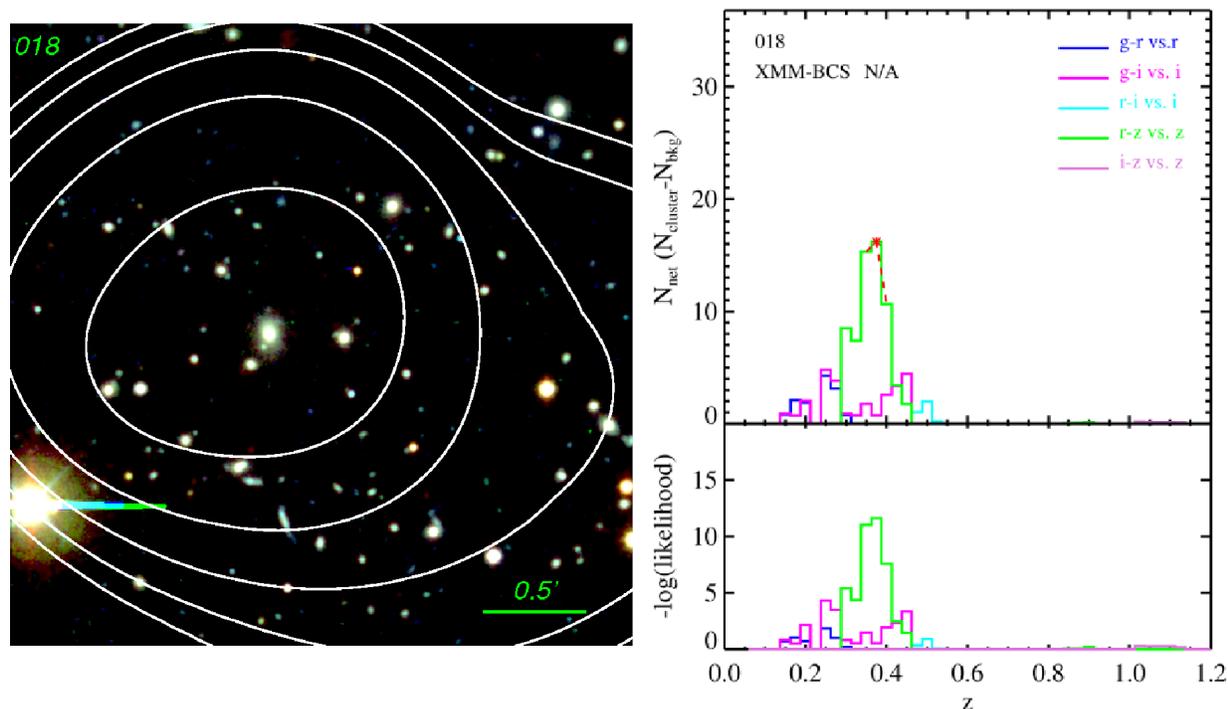
Figure 5.5: **Left:** Pseudo-color image of source ID 018 from the Blanco Cosmology Survey in *riz* bands. X-ray contours are overlaid in white. Right: Galaxy photometric redshift histogram for the same source. The bottom panel shows the S/N distribution for this source. The estimated redshift is $z = 0.39$.

The final photometric redshifts are presented in Table 5.6. A more detailed analysis of optical counterparts for our systems including luminosity and richness estimates will be presented in a companion paper (Song et al., in prep.).

5.4.1 Spectroscopic redshifts

Spectroscopic redshifts are required to identify the clusters as compact objects, to derive precise physical parameters and later for cosmological modeling. In order to make a first step towards these goals we have carried out spectroscopic observations of a subsample of our clusters in the redshift range $z = 0 - 0.4$.

The observations made use of the EFOSC2 instrument at the 3.6 m New Technology Telescope (NTT) in La Silla, Chile. The observations were carried out in September 2010, with typical exposure times of 840 seconds (two spectra per cluster, 420 seconds each). Our long slit observations have been obtained using Grism #4. The slits (1.5″ width) were placed on the BCG and an additional cluster member candidate.

A standard reduction process was applied to the data using IRAF tasks.[3] The observations

---

[3]`iraf.noao.edu`
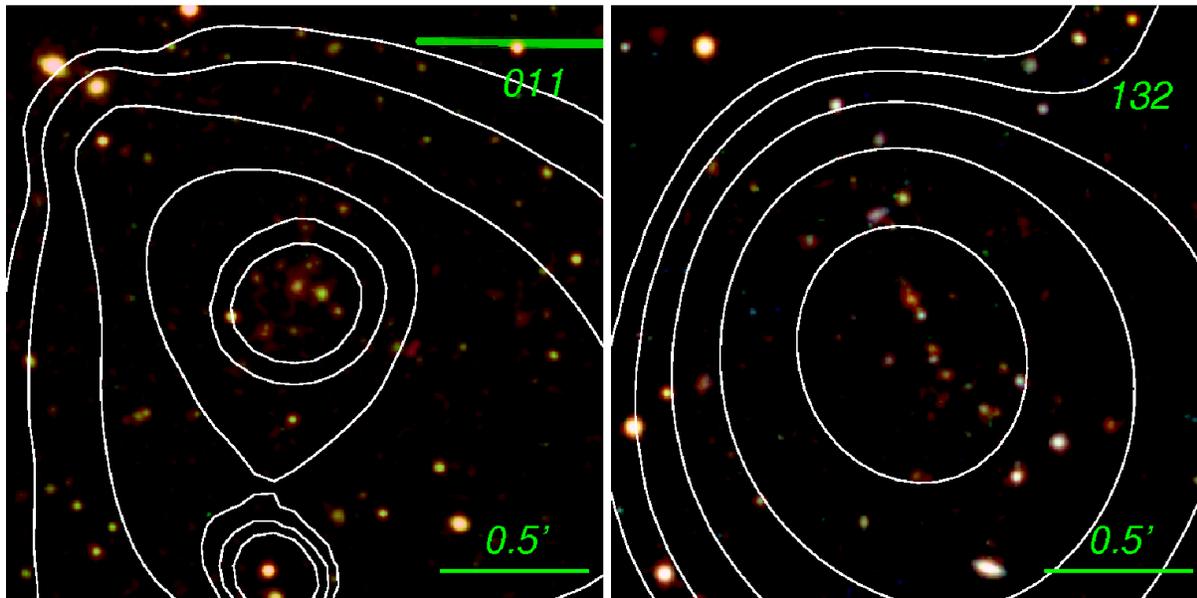
Figure 5.6: Pseudo-color images in the *riz* bands of the two X-ray detected (white contours) systems with secure photo-z values above $z > 0.9$. Both clusters have a BCG coincident with the center of the X-ray detection.

were bias subtracted, cleaned from cosmic rays, and flat fielded. For each galaxy we have obtained two spectra which were sky subtracted and combined to increase the signal-to-noise ratio. The wavelength calibration was carried out by comparison with exposures of He and Ar lamps.

The final spectra were then correlated with a database of galaxy templates. The galaxy redshifts have been primarily anchored by the H and K lines and the 4000Å break. Spectroscopic redshifts have been secured in total for 12 BCG galaxies. In four systems a second member galaxy in the slit had good signal-to-noise ratio in order to safely estimate its redshift as well. In all four cases the galaxies were found to have concordant redshifts with the BCG value. The spectroscopic redshifts of the galaxies are summarized in Table 5.2 along with our photo-z estimates. We compare the two redshift sets in Sect. 5.5.4.

5.5   Results

5.5.1   Galaxy cluster sample

Table 5.6 provides the physical properties determined for the 46 clusters in the present sample. The measured X-ray luminosity of the systems (Sect. 5.3.3) and the photometric and spectroscopic redshifts (Sect. 5.4 and 5.4.1) are used as inputs for the cluster scaling relations to estimate further physical parameters. Ancillary X-ray information on the individual clusters can be found in Table 5.7.

Table 5.2: Spectroscopic redshift for 12 clusters in the redshift range $z = 0 - 0.4$. The redshifts were obtained from long-slit spectroscopic observations at the NTT telescope. The redshifts of the BCG galaxies are in the z_{spec}^{A} column. Four clusters have a redshift for one additional member galaxy (z_{spec}^{B}). Photometric redshifts z_{photo} are taken from Table 5.6. For five systems we also provide the photometric redshifts from the SCS survey (M09, M10).

ID	z_{spec}^{A}	z_{spec}^{B}	z_{photo}	$z_{\text{photo}}^{\text{SCS}}$
70	0.152	0.152	0.17 ± 0.03	0.12
94	0.269		0.29 ± 0.04	
127	0.207	0.209	0.22 ± 0.02	
139	0.169		0.18 ± 0.01	
150	0.176	0.173	0.20 ± 0.02	0.14
152	0.139		0.17 ± 0.02	
227	0.346		0.35 ± 0.04	
430	0.206	0.205	0.18 ± 0.01	
457	0.1		0.10 ± 0.01	
476	0.102		0.10 ± 0.01	0.1
511	0.269		0.26 ± 0.02	0.2
547	0.241		0.22 ± 0.02	0.18

We display the X-ray luminosity of our systems as a function of redshift in Fig. 5.8. The redshift, temperature and mass distributions are shown in Fig. 5.7. The median redshift of the cluster sample is $z = 0.47$. Six of the systems have photometric redshifts $z > 0.8$. Three of these have redshifts consistent with unity, although the photo-z uncertainty in this regime is large. The median temperature of the clusters is ~ 2 keV and the median M_{500} mass 9×10^{13} $M_{\odot}$ (based on luminosity scaling relations). We are thus able to probe the cluster/group transition regime practically at all redshifts out to $z \approx 1$.

5.5.2 Survey sky-coverage

The simplest statistical characteristics of a cluster survey are its area coverage as a function of limiting flux (*sky-coverage function*) and the cumulative surface density of the detected objects above the given flux limit as a function of flux - the so-called $\log N - \log S$ relation.[4]

In order to properly determine the survey's sky coverage, good knowledge of the survey's selection function is necessary. For the simple case when the selection function is the function of only flux, the sky coverage is then the selection function of the survey scaled by its geometric area. Especially for the case of extended sources the situation is more complex, since the selection function depends also on other parameters (e.g the source extent and off-axis angle). These effects can only be accounted for by Monte Carlo simulations. At this moment, without the simulations at hand, we can still provide a preliminary, empirically calibrated sky coverage calculation and cluster $\log N - \log S$ relation. We will demonstrate, that these simple approaches

---

[4]We use the standard notation of this relation, but keep writing f_X as the source flux rather than S.
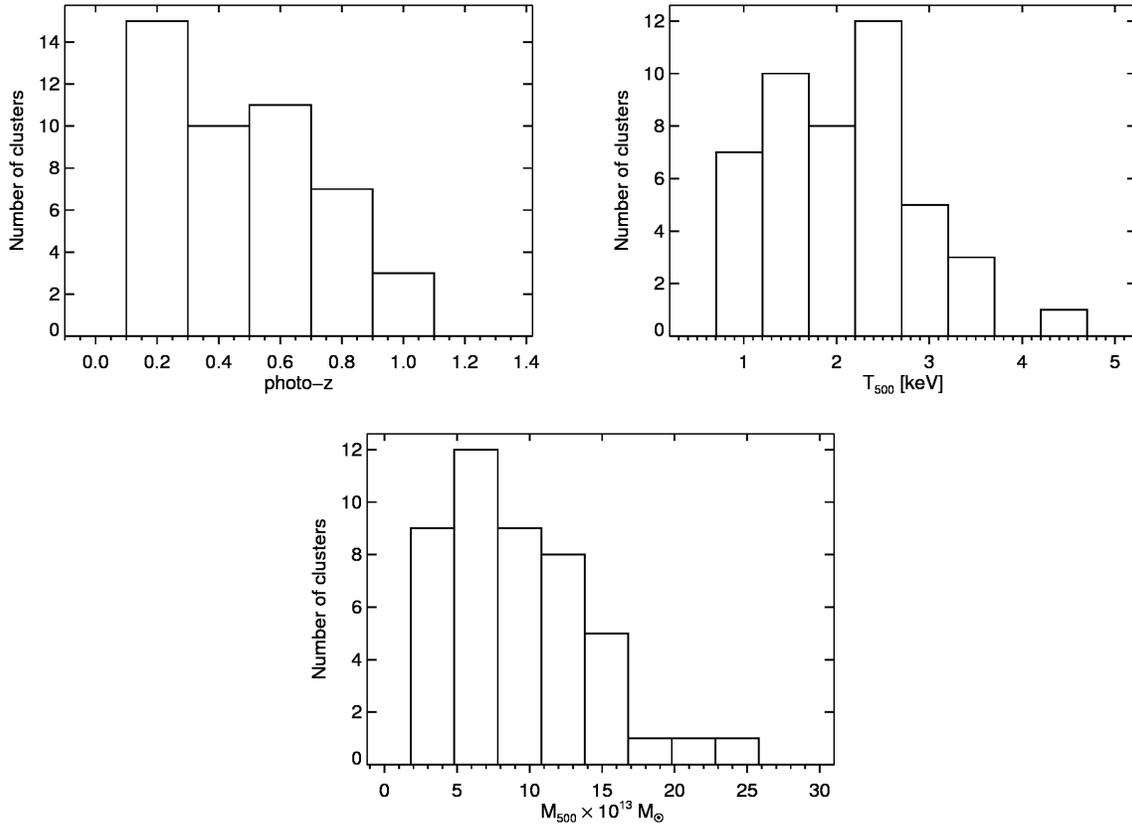
Figure 5.7: **Top left:** Redshift distribution of the presented cluster sample based on the photometric redshifts obtained with the red sequence fitting method. **Top right:** X-ray temperature distribution estimated from the L-T scaling relation of Pratt et al. (2009). **Bottom:** Distribution of the cluster masses in the r_{500} aperture calculated from the luminosities using the L−M scaling relation from Pratt et al. (2009) (see Sect. 5.3.3).

show good agreement with the design aims for the survey depth and previous measurements of the cluster $\log N - \log S$ function.

While our source detection pipeline utilizes multiple detection bands and likelihood thresholds (Sect. 5.3) we will for simplicity (and ability to compare our results with published work) characterize detections made in the standard $0.5 - 2$ keV band with a 3σ detection threshold and a 5σ extent significance.

In order to obtain the survey sensitivity function for extended sources, we first calculate the point source sensitivity for each field. This is a simpler task since it does not require treatment of the source extent. We calculate the point source sensitivity function by analytically inverting the detection likelihood calculation (described in Sect. 5.3.1) and obtaining the minimal count-rate necessary for a point source to be detected at the required detection threshold given the local background and exposure in the detection cell.
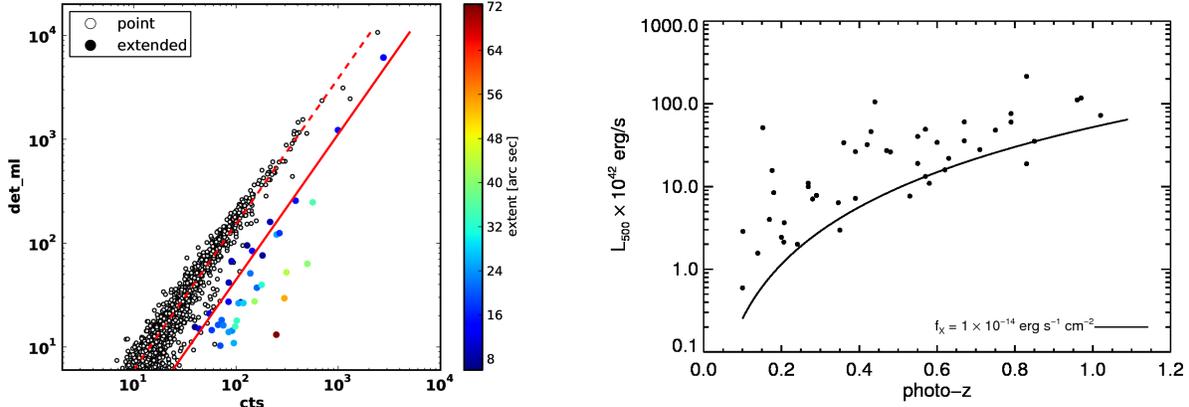
Figure 5.8: **Left:** Detection likelihood (det_ml) as a function of total detected source counts (PN detector only) for point sources (open circles) and the detected clusters (full circles). Clusters are color coded by their extent (beta model core radius). Dashed red line shows the best fit linear relation in the det_ml - counts plane for point sources. The solid line shows the same relation for extended sources (with slope fixed to the point-source fit). Typically, an extended source has to have 2.4 times more counts than a point source to be detected at the same det_ml value. See Sect. 5.5.2 for details. **Right:** Luminosity in the $0.5 - 2$ keV band (object rest-frame) for the presented cluster sample as a function of redshift. The line shows the luminosity of a cluster with a measured flux 1×10^{14} erg s^{-1} cm^{-2} (unabsorbed, observer rest-frame).

The procedure is repeated for each survey field and the results are combined for the whole survey area. In the areas where two or more fields overlap, we compare the sensitivity maps pixel-by-pixel taking the highest reached sensitivity (i.e. lowest local count-rate limit) at the given position. This procedure is chosen because the present catalog was derived from the detection pipeline that ran on each field individually. An alternative approach is to combine the fields before detection - reaching slightly deeper flux-limits in the overlapping areas.[5] This comes at the cost of losing the information on the local PSF shape used by the maximum-likelihood fitting algorithm, since the same sky location in two different observations is imaged at different off-axis and position angles and thus with different PSF. Both approaches give comparable results and we opt here to characterize the main scheme (i.e. detection on individual fields).

The median *point* source sensitivity calculated in this way for the whole survey area is 3.7×10^{-15} erg s^{-1} cm^{-2} for a energy-conversion factor[6] of 1.5×10^{-12} erg s^{-1} cm^{-2}. The corresponding sky coverage as a function of flux is displayed in Fig. 5.9.

In the next step, we attempt to obtain a first order approximation to the sky coverage function for the *extended* sources by a simple scaling to the point source function. In Fig. 5.8 (left) we

---

[5]This was done for the ancillary catalog using the wavelet detection algorithm.

[6]Assuming a power law spectrum with $\Gamma = 1.7$ and $n_H = 1.25 \times 10^{20}$ cm^{-2} (median value of the galactic column density in the survey field) and using an on-axis PN response file.
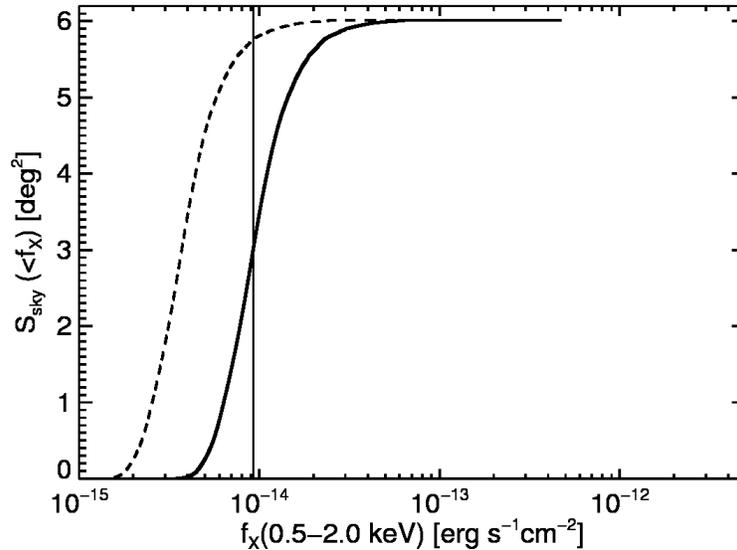
Figure 5.9: The survey sky coverage. Dashed line shows the sky coverage as a function of limiting point source sensitivity in the $0.5 - 2.0$ keV band. The empirically estimated extended source sensitivity is shown with a solid line. The median point source sensitivity of the survey is 3.7×10^{-15} erg s^{-1} cm^{-2}, median sensitivity for the extended sources 9.3×10^{-15} erg s^{-1} cm^{-2} (vertical line).

show the dependence of the detection likelihood (i.e. the `det_ml` parameter) on the total detected source counts for point sources and the confirmed clusters from our sample (full circles).

Photons from extended sources are distributed over a larger area and thus require more counts to reach a given detection likelihood compared to point sources. For those, a simple linear relation in the log-log plane is a good description of the counts-`det_ml` relation (dashed red line in Fig. 5.8). Since the number of our clusters is small a similar linear relation for them is only very weakly constrained. We therefore fix the slope to the value from the point source fit leaving only the intercept as a free parameter (solid red line). The offset of the extended-source best-fit line translates to a factor of 2.4 between the total required counts of point and extended sources at any given `det_ml`. Fixing the slope has also the advantage that the offset is independent of the selected detection threshold. The best fit line roughly follows the locus of clusters with extent (beta model core radius) close to the median value of $\sim 20''$. The solid red line in Fig. 5.8 (left) thus roughly gives the detected counts for a cluster with a *typical* extent detected with a given likelihood. We then use this offset factor to scale up the point source sky coverage function (see Fig. 5.9). The median flux limit for such sky-coverage is 9.3×10^{-15} erg s^{-1} cm^{-2} (using the median ECF of our sample). In Fig. 5.8 we display the luminosity-redshift plane for our survey. The luminosity threshold for a flux limited sample ($f_{\min} = 1 \times 10^{-14}$ erg s^{-1} cm^{-2}) is also shown, demonstrating a rough agreement with our calculation. Note that in the present sample we also include fainter sources than this threshold (the lowest cluster flux is $\sim 6 \times 10^{-15}$ erg s^{-1} cm^{-2}).

This approach underestimates the effect of clusters with larger extent - and thus overestimates the sky coverage at given flux.[7] However, since the detection probability itself is a strong function of source extent, the only way to properly account for its effect is through realistic simulations.

We present examples of preliminary sky coverage functions for extended source detection on several (non-XMM-BCS) fields based on such Monte Carlo simulations (Mühlegger 2010) in Fig. 5.15, discussed in Sect. 5.8.3. These first results validate our attempt to model to first approximation the extended source sky-coverage by scaling the point source curve and also confirm that the scaling factor between them is roughly ~ 2.4 (this scaling factor is expected to hold only for simulations with roughly same depth as ours, ~ 10 ks).

5.5.3   Cluster $\log N - \log S$

We now use this empirical sky-coverage in order to calculate the survey's $\log N - \log S$, defined in standard way as:

$$N(> f_X) = \sum_{i=1}^{N_C} \frac{1}{\Omega(f_X^i)} \mathrm{deg}^{-2}, \tag{5.5}$$

where N_C is the total number of clusters and $\Omega(f_X^i)$ is the extended source sky-coverage corresponding to the flux of the i-th cluster. We characterized the survey sky coverage only for a hypothetical single band ($0.5 - 2$ keV) detection scheme. Since such a detection scheme is not part of our pipeline, we opt to draw a subsample from our cluster catalog derived from the three band scheme (which includes the $0.5 - 2$ keV). We consider for this calculation only clusters that would have also been detected in this hypothetical single band run by setting the same detection- and extent likelihood thresholds used for the sky-coverage calculation in the previous section.

This requires us to recover the actual $0.5 - 2$ keV band detection likelihoods from the total `det_ml` parameter, which includes contributions from all three detection bands. As we described in Sect. 5.3, `det_ml` can be interpreted as `det_ml` $= -\ln P_{\mathrm{rand}}$, with P_{rand} being the probability of a false detection arising from pure Poissonian fluctuations. The actual definition of this parameter is slightly more complex:

$$\mathtt{det\_ml} = -\ln(1 - \Gamma(0.5\nu, L)), \tag{5.6}$$

where Γ is the incomplete gamma function and its arguments are the number of degrees of freedom of the `emldetect` fit (for extended sources $\nu = 3+$ the number of detection bands times number of instruments) and L is the sum of all the individual likelihoods (using the C statistics of Cash 1979). This definition effectively converts the joint likelihoods to two degrees of freedom allowing to compare detections from different combination of bands and instruments. However, for the conversion to a single band detection likelihood, we need the original individual likelihoods which we obtain by numerically inverting Eq. 5.6 for each source.

We then calculate the joint detection likelihood from all three instruments in the single, $0.5 - 2$ keV, band (all three detection probabilities being independent) and subsequently calculate the new `det_ml` parameter normalized back to 2 degrees of freedom using Eq. 5.6. The number

---

[7]The fit with a free slope gives an offset factor of ~ 4, the fit being skewed towards the locus of very extended clusters.
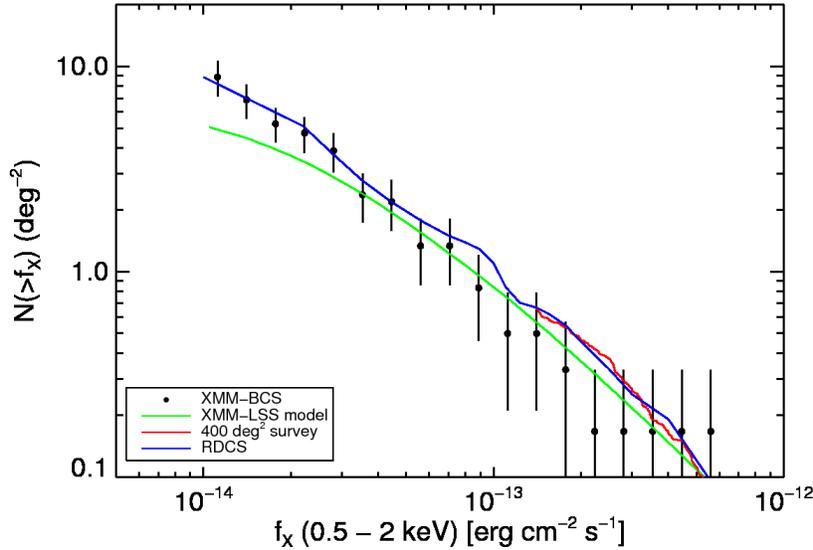
Figure 5.10: The $\log N - \log S$ of the present sample in the $0.5 - 2.0$ keV band. Fluxes are calculated in the r_{500} aperture. Results from several surveys are also shown: RDCS (the ROSAT Deep Cluster Survey, Rosati et al. 1998), 400 deg^2 survey (Burenin et al. 2007; Vikhlinin et al. 2009a) and the XMM-LSS (Pacaud et al. 2007). See Sect. 5.5.3 for details.

of clusters that have this new single band `det_ml` parameter above the required threshold (i.e. equivalent to $\sim 3\sigma$) is 40.

Finally, we calculate the $\log N - \log S$ according to Eq. 5.5 and the variance of the number counts as $\sigma^2 = \sum_{i=1}^{N_C} 1/\Omega(f_X^i)^2$. The recovered curve (see Fig. 5.10) is in good agreement with the $\log N - \log S$ of other surveys: e.g. the RDCS survey (the ROSAT Deep Cluster Survey, Rosati et al. 1998), 400 deg^2 survey (Burenin et al. 2007; Vikhlinin et al. 2009a) and the XMM-LSS survey[8] (Pacaud et al. 2007). Since the area and depth of the XMM-LSS survey are a good match to our survey we discuss their comparison in more detail in Sec. 5.8.4.

We note, that we used the fluxes in the r_{500} aperture for our calculation whereas the XMM-LSS uses a fixed physical aperture of 0.5 Mpc (typically very close to r_{500}), RDCS $\sim 80-90\%$ of the total flux (i.e. integrated out to infinity) and the 400 deg^2 survey the full total flux. We have chosen r_{500} because: **a)** it requires less extrapolation based on a beta model whose parameters are typically highly uncertain and is itself not necessarily a good description of the surface brightness profiles and **b)** it is the most natural choice when comparing to theoretical predictions. However, assuming a typical cluster with $r_{500} = 0.5$ Mpc well described by a beta model with $(\beta, r_{core}) = (2/3, 180 \, \text{kpc})$ the flux extrapolated to infinity would be higher by $\sim 1/3$ moving our curve along the x-axis to higher fluxes only very slightly - even closer to the RDCS and 400 deg^2 survey's

---

[8] Note that the XMM-LSS curve is only digitized from the figure in Pacaud et al. (2007) since the original curve is no longer available (Pacaud, private com.).
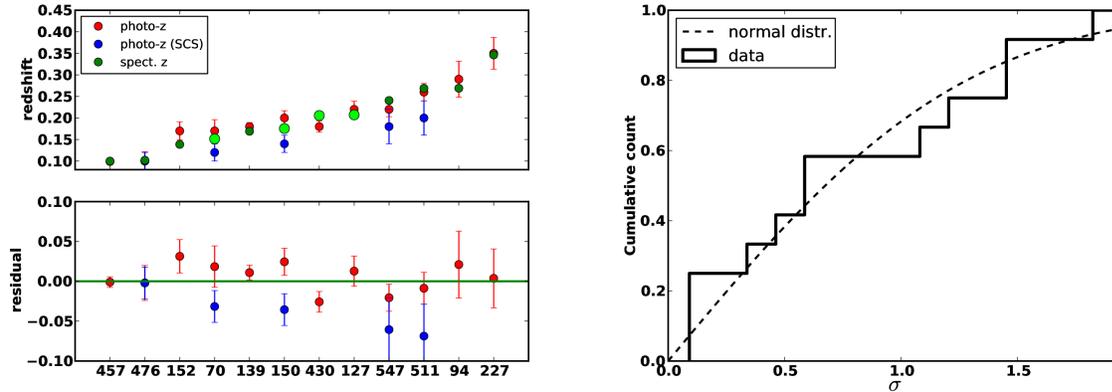
Figure 5.11: Consistency test of our photometric redshift estimates with spectroscopic measurements in the redshift range $z = 0 - 0.4$. **Left:** Comparison of our photometric redshift estimates (red, 1σ error bars), with spectroscopic values (green). Brighter green points mark clusters, where we have two concordant galaxy redshifts, while darker green color indicates clusters for which only the BCG has a spectroscopic redshift. The photometric redshifts obtained by the SCS survey (M09, M10) are shown in blue. The x-axis displays the cluster ID number. The objects are sorted in increasing redshift order. The bottom panel shows the residuals of the photo-z values with respect to the spectroscopic measurement. **Right:** Cumulative histogram of the difference between the photometric and spectroscopic redshift normalized by the 1σ uncertainty of the photo-z values, i.e. $D = |z_{\mathrm{photo}} - z_{\mathrm{spec}}|/\sigma_{\mathrm{photo}}$. The dashed line shows the expectation for the Gaussian distribution. Both curve are in good agreement, with a Kolmogorov-Smirnov test confirming that the distribution of the D values is Gaussian at the 96% confidence level.

relations.

Uncertainties of the flux estimation (including the uncertainty of the photo-zs) affect the $\log N - \log S$ only in a minor way. The main source of uncertainty (not included in the error bars) is our current lack of knowledge of the survey selection function (and thus only tentative description of the sky-coverage). The good agreement with previous work gives, however, support to the present preliminary approach.

5.5.4   Comparison of spectroscopic and photometric redshifts

For a subsample of 12 clusters ($z < 0.4$) we have obtained spectroscopic redshifts of their BCG and in four cases also for an additional member galaxy (Sect. 5.4.1). We compare the spectroscopic redshifts with our photo-z values in Fig. 5.11 (left). Our photometric values (red points) agree well within the error bars with the spectroscopic redshifts of the BCG (green points, brighter green points mark the clusters with two concordant redshifts). Blue points mark the photo-zs for five of the systems obtained by the SCS survey (M09, M10). These values exhibit a systematic bias toward lower redshifts, with a mean relative difference of 19%. A similar

trend is also visible in Fig. 5.12 (top left) where we compare our photo-z values with the SCS measurements for all clusters common to both samples.

The right panel of Fig. 5.11, displays the comparison of the absolute difference of our photometric and spectroscopic estimates in units of photo-z error, $D = |z_{photo} - z_{spec}|/\sigma_{photo}$. A comparison with a Gaussian expectation shows an agreement at the 96% confidence level, confirming both the good precision of our photo-z estimates and realistic description of their errors.

The present spectroscopic sample covers only part of the redshift range and does not allow us to check the photometric redshift calibration at higher redshift. However, the good agreement at low z supports the photo-z method used.

5.5.5 Cross-correlation with known sources

The XMM-BCS field has an excellent multi-wavelength coverage and has been already studied by the Southern Cosmology Survey (M09, M10, McInnes et al. 2009) who identified in optical data a number of clusters in this area. Due to a significant overlap with our cluster catalog we will address a more detailed comparison in Sect. 5.5.6.

In search of other known sources coincident with our clusters, we make use of both the NASA/IPAC Extragalactic Database[9] and the SIMBAD Astronomical Database.[10]

First we looked for associated known clusters. For this query a search radius of 60″ was selected, finding a single match - the cluster 400d J2325-5443 (alternative name: [BVH2007] 240) identified in the 160 Square Degree ROSAT Survey (Vikhlinin et al. 1998a; Mullis et al. 2003) at spectroscopic redshift $z = 0.102$. This cluster is coincident with our cluster ID 476 with photometric redshift of 0.1 being in full agreement with the spectroscopic value. The source is also part of the 400 Square Degree ROSAT Survey. See Appendix 5.8.2 for more details on this source.

We also list galaxy matches, if they are within a 16 arcsecond search radius from the X-ray center in Table 5.8 (in the appendix) with matches coming from the 2 Micron All Sky Survey Extended objects catalog and the APM galaxy survey (Skrutskie et al. 2006; Maddox et al. 1990, respectively). Out of 13 matches, only two galaxies have known spectroscopic redshifts, both obtained in the frame of the 6dF Galaxy Survey (Jones et al. 2004). The first is 2MASX J23254015-5444308 at $z = 0.101$ coincident with the brightest galaxy in cluster ID 476. The redshift value is concordant with the redshift from the 160/400 Square Degree ROSAT surveys. The second match is the brightest cluster galaxy of the system ID 150 at redshift $z = 0.176$, again in good agreement with our estimated photo-z of 0.2.

As can be seen, the survey field has a wealth of multi-wavelength data, but very little spectroscopic measurements. This makes the ongoing spectroscopic follow-up program very important, as redshifts are essential for full utilization of the available data sets.

Radio sources coincident with the X-ray detected clusters can bias the SZE signal (filling the decrement). We checked for intervening radio sources by cross-correlating our cluster catalog with the NED database with a 1 arcmin search radius. We find 11 radio sources detected at 843

---

[9]nedwww.ipac.caltech.edu
[10]simbad.u-strasbg.fr/simbad/

Table 5.3: Radio sources within 60″ from the X-ray centers of the detected clusters. The quoted flux density S is at 843 Mhz (36 cm) for the SUMSS sources and at 4.85 GHz (6.2 cm) for the PMN detected object. The radio counterparts were obtained from the NASA/IPAC Extragalactic Database.

ID	Object Name	R.A. (deg)	Dec (deg)	S (mJy)	separation (″)
018	SUMSS J232952-560723	352.4677	-56.1231	14.9 ± 0.8	56
035	SUMSS J233345-553817	353.4416	-55.6382	16.7 ± 0.8	6
044	SUMSS J231654-545406	349.2274	-54.9019	8.0 ± 1.0	14
109	SUMSS J232737-541622	351.9047	-54.2730	26.1 ± 1.2	9
110	SUMSS J233003-541424	352.5146	-54.2402	13.3 ± 1.1	6
189	SUMSS J233044-560123	352.6860	-56.0233	15.1 ± 0.8	36
210	SUMSS J233406-554708	353.5253	-55.7857	7.9 ± 0.7	3
288	SUMSS J233459-545535	353.7495	-54.9265	41.5 ± 1.6	37
426	SUMSS J232138-541849	350.4092	-54.3137	12.7 ± 1.9	14
534	SUMSS J232446-552432	351.1951	-55.4089	41.1 ± 1.5	17
546	SUMSS J233113-543025	352.8076	-54.5071	25.6 ± 1.3	26
150	PMN J2330-5436	352.5075	-54.6097	52.0 ± 8.0	34

MHz by the Sydney University Molonglo Sky Survey (SUMS, Mauch et al. 2003). The source PMN J2330-5436, $\sim$ 30 arcsec from cluster ID 150, was detected by the Parkes-MIT-NRAO (PMN) southern survey at 4.85 GHz (Gregory et al. 1994). The list of all identified radio sources is given in Table 5.3.

5.5.6 Cross-correlation with the Southern Cosmology Survey clusters

The Southern Cosmology Survey (SCS) carried out an optical clusters search using the Blanco Cosmology Survey imaging data. Menanteau et al. (2009, hereafter M09) provided a catalog of optically selected clusters with photo-z < 0.8 in a 8 deg^2 field partially overlapping with the 6 deg^2 region presented in this work. Menanteau et al. (2010, M10) then followed up this work by creating a cluster catalog using the full $2005 - 2007$ BCS survey data (i.e. $\sim$ 70 deg^2, thus fully covering also the whole XMM-BCS field), detecting 105 clusters with $M > 3 \times 10^{14}$ M$_\odot$ and photo-z< 0.8.

Combining both these catalogs, we find in total 30 SCS clusters whose optical coordinates lie inside our 6 deg^2 region.[11] Out of these 30 systems, 26 come from the M09 catalog (which contains clusters also below the mass limit applied in M10), two are included in both M09 and M10 and an additional two clusters are from M10. For the two clusters in both M09 and M10 we will use the updated parameters from M10.

The SCS catalog provides the BCG coordinates for each system while our catalog lists the X-ray centroids. For cross-correlation of the two catalogs we take a conservative 60″ matching

---

[11] In present work we thus do not consider SCS clusters that lie only partially in the 6 deg^2 or in the 8 deg^2 extension.

radius, which yields 19 clusters. We summarize the properties of matched clusters in Table 5.4 and provide a more detailed comparison of their parameters in the next two sections.

Comparison of photometric redshifts

First, we turn to the comparison of the photometric redshifts for the 19 matches. M09 and M10 utilize the BPZ code (Benítez 2000) to estimate photo-zs while our method is based on the red-sequence method as described in Sect. 5.4. For the SCS clusters we use the photo-z errors published in McInnes et al. (2009) where possible (the M09 and M10 catalogs do not provide error bars). For the remaining cases we assume a 15% error, which is the mean precision of the photo-zs where errors are available.

As can be seen in Fig. 5.12 (top left) there is no case of catastrophic disagreement. We find a gap in the SCS photo-z distribution in the $0.35 - 0.5$ photo-z range that is not present in our redshift distribution. The most important feature is, however, the systematic offset between the photo-z estimates. The SCS photo-zs are on average $\sim 20\%$ lower than our values. This trend roughly holds in the whole redshift range, as can be seen from the photo-z residuals plotted against redshift in Fig. 5.12, bottom left). We found a similar bias when comparing the SCS photo-zs to the spectroscopic subsample in Sect. 5.5.4. For the five systems with spectroscopic redshifts the photo-zs were on average underestimated by $\sim 19\%$.

In order to investigate potential sources of the discrepancy we check whether the photo-z residuals depend on any of the available parameters, most importantly the richness parameter N_{200}, integrated optical luminosity L_{200}^{opt} and the BCG-X-ray centroid offset. However, we do not find any statistically significant dependence.

X-ray - optical mass comparison

M09 and M10 provide rough mass estimates for their clusters based on the optical proxies N_{200} and L_{200}^{opt} using the scaling relations from Reyes et al. (2008). The richness estimator N_{200} is defined as the number of E/S0 ridgeline cluster members brighter than $0.4L^*$. The integrated cluster luminosity L_{200}^{opt} is the summed r band luminosity of the member galaxies included in the N_{200} calculation. Both parameters are calculated within an aperture where the *galaxy* density equals $200/\Omega_{\mathrm{M}}$ times the *mean* density of galaxies in the Universe. Fortunately, Johnston et al. (2007) found that this aperture is an unbiased estimate of the radius where the *matter* density is 200 times the *critical* density of the Universe, i.e. the optical masses and our X-ray estimates come from roughly the same apertures and can thus be directly compared.

Table 5.4: The 19 SCS clusters recovered in the XMM-BCS survey. SCS References: M09 - Menanteau et al. (2009), M10 - Menanteau et al. (2010). The optical masses $M(L_{200}^{\mathrm{opt}})$ and $M(N_{200})$ are taken from M09 and M10, the weak lensing mass measurements are provided by McInnes et al. (2009). The X-ray mass estimates obtained in the present work are taken from Table 5.6. The ID of the X-ray counterpart and its distance from the BCG are listed in the last two columns. The masses are in units of $10^{13}\,M_\odot$.

SCS ID	Ref.	photo-z	$M(L_{200}^{\mathrm{opt}})$	$M(N_{200})$	M_{200}^{wl}	M_{200}^{X}	XMM-BCS ID	separation
SCSO J233430.2-543647.5	M09	0.35	36	61	−	14.2 ± 3.0	357	26.6″
SCSO J232211.0-561847.4	M09	0.61	56	46	$4.7^{+26.1}_{-4.7}$	18.3 ± 4.0	527	1.6″
SCSO J232540.2-544430.9	M09	0.10	21	86	$2.3^{+8.9}_{-2.3}$	10.7 ± 2.3	476	3.2″
SCSO J232230.9-541608.3	M09	0.12	16	100	$8.5^{+9.2}_{-5.9}$	25.0 ± 5.1	70	0.6″
SCSO J233000.4-543707.7	M09	0.14	12	43	−	12.9 ± 2.6	150	1.7″
SCSO J232419.6-552548.9	M09	0.18	12	25	< 2.6	4.2 ± 1.1	547	1.0″
SCSO J233215.5-544211.6	M09	0.20	17	33	$10.2^{+8.4}_{-6.1}$	9.7 ± 2.1	511	10.0″
SCSO J233037.1-554338.8	M09	0.20	10	27	$16.2^{+10.7}_{-7.7}$	7.9 ± 1.7	34	2.3″
SCSO J232200.4-544459.7	M09	0.27	17	39	$2.6^{+8.6}_{-2.6}$	17.6 ± 3.6	136	3.9″
SCSO J233522.6-553237.0	M09	0.29	22	32	$8.5^{+16.0}_{-8.5}$	4.8 ± 1.2	528	17.4″
SCSO J232956.0-560808.3	M09	0.32	20	39	$21.3^{+27.5}_{-17.3}$	15.2 ± 3.2	18	1.7″
SCSO J232839.5-551353.8	M09	0.32	10	17	$16.9^{+20.1}_{-13.2}$	19.8 ± 4.2	88	36.2″
SCSO J232633.6-550111.5	M09	0.32	28	32	< 4.8	16.5 ± 3.4	126	3.1″
SCSO J233003.6-541426.7	M09	0.33	9	29	$28.1^{+20.7}_{-14.7}$	14.6 ± 3.1	110	7.4″
SCSO J232619.8-552308.8	M09	0.52	12	21	$28.1^{+33.4}_{-22.2}$	11.8 ± 2.6	82	9.5″
SCSO J231651.0-545356.0	M10	0.36	27	39	−	31.6 ± 6.5	44	24.7″
SCSO J232856.0-552428.0	M10	0.57	35	20	−	8.3 ± 1.9	90	6.7″
SCSO J233420.0-542732.0	M10	0.56	36	27	−	17.2 ± 3.7	158	41.6″
SCSO J233556.0-560602.0	M10	0.64	47	25	−	7.2 ± 1.7	386	31.3″
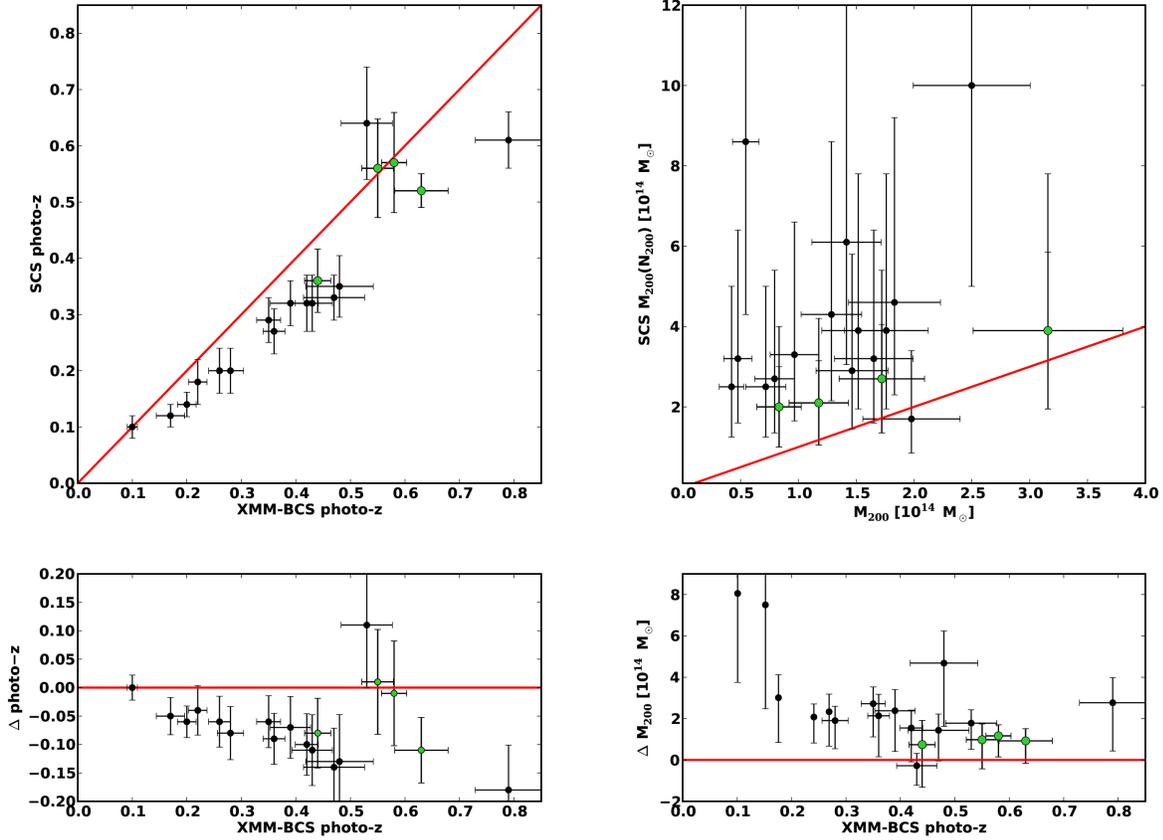
Figure 5.12: **Top left:** Comparison of photometric redshifts for the 19 common cluster from our sample and the SCS cluster survey from Menanteau et al. (2009) and Menanteau et al. (2010). **Top right:** Comparison of masses for the same cluster sample in the r_{200} aperture determined from the measured X-ray luminosity through scaling relations (x-axis) and the mean of the optically determined masses $M(L_{200}^{opt})$ and $M(N_{200})$ (Table 5.4). The red line marks equality in both top panels. **Bottom left:** Photo-z difference $\Delta = $ photo-z(SCS) $-$ photo-z(XMM-BCS) as a function of our estimates of redshifts. **Bottom right:** M_{200} difference $\Delta = M_{200}$(SCS) $- M_{200}$(XMM-BCS) as a function of our estimates of redshifts. The optical masses are significantly higher than the X-ray estimates especially at the low and high redshift ends. See text for discussion. Green points in all plots mark clusters from M10, black points those from M09.

In Fig. 5.12 (top right) we compare our X-ray masses with the optical masses $M(N_{200})$ calculated from the N_{200} parameter. The optical masses are estimated to be accurate within a factor of two (M09), where this factor should include also the uncertainty in extrapolating the Reyes et al. (2008) scaling relations to higher redshifts (the scaling relations were calibrated for redshifts $z < 0.3$). We used the factor two uncertainty to calculate the $M(N_{200})$ error bars in Fig. 5.12. We find that the optical masses are significantly higher than the X-ray mass estimates M_{200} by a

factor of ∼ 2.6 (median value).

Reichert et al. (submitted) investigates X-ray luminosity based scaling relations on a large compilation of cluster samples from the literature. They find only very few systems deviating from the mean $L - M$ relation by more than a factor two (i.e. with actual mass two or more times higher than the luminosity prediction). We thus do not expect our masses to be underestimated by similar factors even in individual cases. The observed bias in mass goes in the opposite direction as that found in the photo-zs (i.e. photo-zs were underestimated while masses overestimated). The photo-zs, however influence the mass estimates and therefore it is not straightforward to disentangle all the factors contributing to this discrepancy. The influence of the redshift uncertainty is likely more important for nearby systems, where it translates to larger differences in the angular size of the aperture. The discrepancy of the $M(L_{200}^{\mathrm{opt}})$ masses is similar. We note here, however that the $M(L_{200}^{\mathrm{opt}})$ masses in M09 were obtained from the scaling relations of Reyes et al. (2008) prior to their erratum-correction.[12]

Bottom right panel of Fig. 5.12 displays the mass residuals versus our photometric redshifts, but no clear trend is found. We check for dependence on additional factors (similarly to the photo-z analysis in previous section), but again find no statistically significant relations. We note, that the four clusters from M10 agree with our measurements better than all but one cluster from M09.

McInnes et al. (2009) provides weak lensing mass measurement for the clusters found in M09. This includes 13 clusters found in our sample (for two of these systems only upper limits could be set). We compare the weak lensing masses with our X-ray estimates in Fig. 5.13. The agreement is significantly better than for $M(N_{200})$ masses, although the scatter and uncertainty in the weak lensing mass estimates is large. From their full sample, McInnes et al. (2009) also noted that the $M(L_{200}^{\mathrm{opt}})$ seem to overestimate the total mass compared to their weak lensing estimates.

An in-depth comparison of optical and X-ray masses will be addressed in an upcoming work, where we will provide also our own measurements of N_{200} and L_{200}^{opt} (Song et al., in prep.). This will allows us to properly investigate the presence of potential biases in the different mass estimators methods and calibrate our own relations.

Parameter upper limits for X-ray non-detections

For the 11 SCS clusters that lie in the core area of our survey but have no X-ray counterparts we provide X-ray flux upper limits in Table 5.5 and a mass limit using the SCS photo-z value.

The flux limits were calculated using the same procedure as we used for the survey sky coverage calculation (Sect. 5.5.2, i.e. calculating the minimal flux needed for the source to be detected at the given position and our detection threshold).

The flux was then converted to luminosity using the photometric redshift from either M09 or M10. We calculated the mass upper limits from the $L - M$ scaling relation as detailed in Sect. 5.3.3. The obtained upper limits on the mass are considerably lower than the M09/M10 estimates.

We also check for possible miss-classification (or confusion in presence of a central AGN)

---

[12]Scaling relations with the updated coefficients are available at: `arxiv.org/abs/0802.2365`.
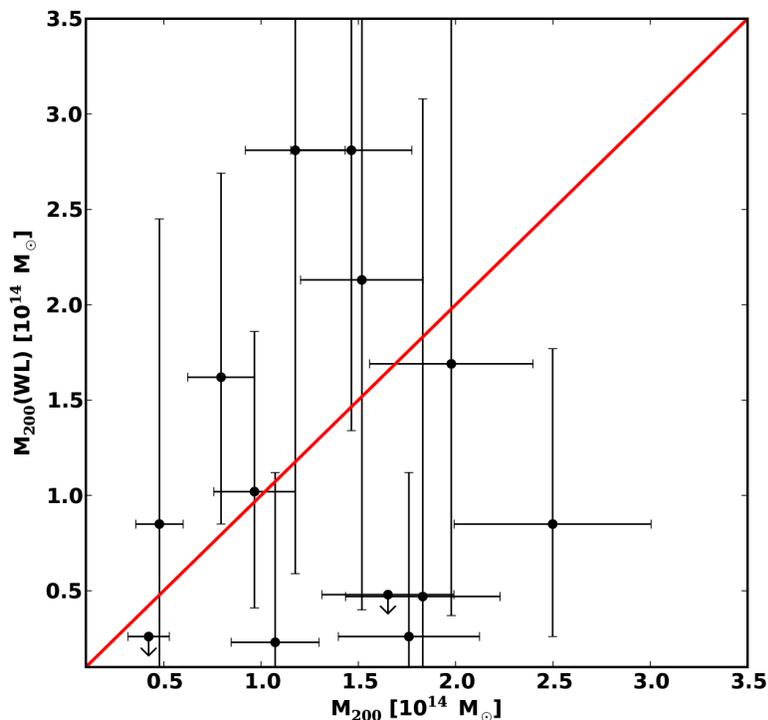
Figure 5.13: Comparison of X-ray masses (M_{200}, x-axis) with the weak lensing measurements (M(WL), y-axis) from McInnes et al. (2009) for 13 clusters in our sample. Although the scatter and uncertainties are large, the agreement is considerably better than with the optical masses $M(N_{200})$ displayed in Fig. 5.12.

by cross-correlating the positions of these 11 clusters with our X-ray *point* source catalog with a threshold of 16″. In this aperture we find no matches (except clusters ID 528 and ID 547 which have also valid X-ray cluster detections, see Table 5.4). Thus the non-detection of these clusters are very likely caused by their low flux rather than incorrect classification.

5.6   Discussion

In this section we discuss the additional effects that influence the precision of the physical parameters provided in our catalog. We also give an outlook on the upcoming work in the context of the XMM-BCS survey.

Table 5.5: The 11 SCS clusters from Menanteau et al. (2009) that lie in the XMM-BCS core survey are but have no X-ray cluster detection we provided flux and mass upper limits.

SCS ID	photo-z (SCS)	f_X^{lim} (10^{-14} erg s^{-1} cm^{-2})	L_{500}^{lim} (10^{43} erg s^{-1})	M_{500}^{lim} (10^{13} M$_\odot$)
SCSO J232829.7-544255.4	0.68	0.79	1.6	5.5
SCSO J233106.9-555119.5	0.19	0.69	0.1	1.3
SCSO J233550.6-552820.4	0.22	0.68	0.1	1.6
SCSO J232156.4-541428.8	0.33	0.88	0.3	2.8
SCSO J233231.4-540135.8	0.33	1.59	0.6	4.0
SCSO J233110.6-555213.5	0.39	0.73	0.4	3.1
SCSO J233618.3-555440.3	0.49	1.51	1.4	5.9
SCSO J232215.9-555045.6	0.56	0.84	1.1	4.8
SCSO J232247.6-541110.1	0.57	0.72	0.9	4.4
SCSO J232342.3-551915.1	0.67	1.22	2.4	7.0
SCSO J233403.7-555250.7	0.71	0.56	1.3	4.7

5.6.1 Error budget of the X-ray analysis

For the present catalog, we restricted ourselves to provide only formal statistical errors for the estimated parameters (Table 5.6) that include the Poisson errors of the flux measurement, a 5% systematic error from the background modeling and the intrinsic scatter of the scaling relations. Although we used the bolometric luminosity to calculate further physical parameters, here we assumed the intrinsic scatter found in the $0.5-2$ keV luminosity relations. This scatter is slightly larger than the bolometric one and it gives a more realistic error estimates since the band luminosity is, in fact, our only direct observable, while the temperature required for the bolometric correction is not. We determine physical parameters with following precision (mean across the whole redshift and flux range): flux and luminosity to $\sim 16\%$, T_{500} and M_{500} to $\sim 30\%$, and Y_{500} to $\sim 60\%$.

In this section we discuss several additional sources of systematic errors and their impact on the estimated fluxes and other parameters. All below reported relative errors are obtained by averaging over the whole cluster sample. Several of the considered effects are redshift dependent, but we typically allow broad parameter ranges and thus our uncertainty estimates are rather conservative.

1) Good precision photometric redshifts are crucial for the determination of each physical parameter. Photo-z estimates in the present work have a mean error of $\sim 10\%$ and show good agreement with the available spectroscopic measurements (Sect. 5.5.4). In order to estimate the impact of the photo-z uncertainty on the measured physical parameters we offset the redshifts (Table 5.6) by their 1σ errors to both sides and rerun the iterative physical parameter estimation procedures (see Sect. 5.3.3).

We find that, for the flux $f_X(< r_{500})$, all values are consistent within their 1σ uncertainty and for most clusters the relative difference is below the $\sim 2\%$ level (Fig. 5.14, left). Change in the photo-z affects the flux in a complex way - it is entering directly the energy-conversion factor
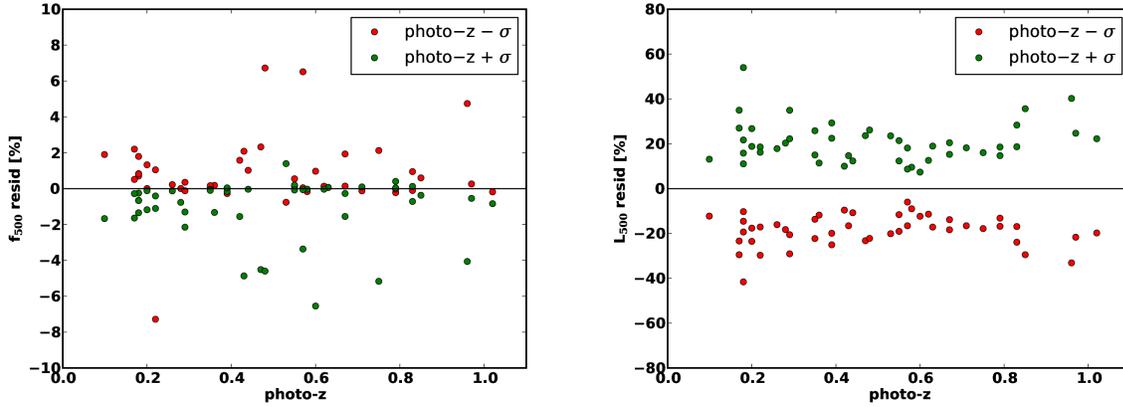
Figure 5.14: **Left:** The effect of the photometric redshift uncertainty on the determined flux in the r_{500} aperture. **Right:** The effect of the photometric redshift uncertainty on the determined luminosity in the r_{500} aperture. Green points mark the relative difference of flux (luminosity) for photo-z increased by $1\,\sigma$ compared to the mean value. Red points are for the case when we decrease the photo-zs by the same amount.

(ECF) calculation (lower redshift leads to a lower ECF), and also during the iterative process through the scaling relations, which then feed back into the aperture size itself as well as the temperature which again affects the ECF value. This complex dependence explains the scatter of the flux residuals in Fig. 5.14, leading to different convergence points for different input photo-zs. Interestingly, a lower photo-z value leads to a *higher* flux in the r_{500} aperture. The reason is that the direct effect of decreasing the photo-z would be to a lower temperature and mass and thus also reduce the r_{500} value. However, the redshift dependence of the angular distance is stronger and thus the *angular* size of the r_{500} aperture is actually larger for lower redshifts, which leads to the increase in the $f_X(< r_{500})$ values (we confirm this explanation by checking the flux in fixed sky apertures).

For luminosities the photo-z errors translate into a $\sim 20\%$ uncertainty (Fig. 5.14, right). Here the dependence is dominated by the cosmological redshift dimming and thus higher redshifts yield also higher luminosities. If we now use the perturbed redshift and luminosity values to recalculate temperatures and masses, we find that the T_{500} values vary on the $\sim 7\%$ level, while for M_{500} the uncertainty is on the $\sim 5\%$ level.

2) In the present work, we have utilized the bolometric luminosity scaling relations of Pratt et al. (2009) based on the REXCESS cluster sample (Böhringer et al. 2007). The direct application of these scaling relations, however, requires extrapolations both to higher redshifts (the REXCESS cluster sample includes only local clusters with $z \lesssim 2$) and to the low-mass regime of groups of galaxies.

The physical parameters provided in Table 5.6 were obtained by assuming the redshift evolution of the cluster scaling relations to be self-similar. This is a standard assumption supported by predictions of a purely gravitationally driven cluster growth (e.g. Kaiser 1986). However, there

is increasing evidence, that the evolution of the luminosity scaling relations is slower than the self-similar expectation (see Reichert et al. (submitted) and references therein). We test the influence of this assumption by using the simplified approach proposed by Fassbender et al. (2011a) by removing the self-similar evolution factor from the relations (the "no evolution" scenario). This approach is consistent with the more detailed analysis of Reichert et al. In this picture, the predicted temperatures are on average higher by 10% and masses by 18% compared to the self-similar scaling relations. At the high redshift end ($z > 0.8$) this effect is even more important ($\sim$ 20% and 30% increase, respectively), while for $z < 0.2$ the effect is less than 5%.

3) The Galactic hydrogen column densities reported by the LAB HI survey (Kalberla et al. 2005) are systematically lower by $\sim$ 27% than the Dickey and Lockman (1990) values in the whole survey area. The effect on the derived luminosities is, however, only marginal ($\sim$ 1.5%).

4) In order to quantify the effect of possible deviations of the cluster metallicity from the mean value of 0.3 solar, we bracket the possible metallicities in the very conservative range of (0.1, 0.6) solar. The corresponding range of $L_X(< r_{500})$ deviations from the fiducial value (for 0.3 solar metallicity) is (-1.2%, 1.5%), i.e. lower metallicities lead to higher luminosities and vice versa.

5) We also test the quality of the flux extrapolation correction described in Sect. 5.3.3. The correction coefficients are calculated by integrating a beta model between (r_{plat}, r_{500}), if $r_{plat} < r_{500}$. We use Eq. 5.4 to estimate the β and r_C parameters. Alternatively, we can use the canonical value $\beta = 2/3$ and r_C obtained from the maximum likelihood fit in the source detection step. The two extrapolation method give fluxes (and luminosities) differing on average for the whole sample by 2%. For individual objects the relative difference of fluxes is clearly correlated with the amount of extrapolation needed and is roughly of the size of the correction itself. This means that the extrapolation is currently very weakly constrained. Fortunately, for the vast majority of clusters it plays only a minor role.

6) The combined MOS1 and MOS2 counts are converted to flux and luminosities using the MOS2 response matrix (see Sect. 5.3.3). We have chosen the MOS2 response matrix over the MOS1, because some sources lie on the missing MOS1 CCD#6, where no meaningful response matrix can be calculated. If the MOS1 response is used instead, the luminosities obtained purely from the combined MOS detectors are on average lower by 2% (excluding clusters detected on the position of the missing MOS1 chip). The final $L_X(< r_{500})$ calculated as the weighted average of the individual PN and MOS luminosities is affected by less than 1.3%.

7) The response matrices used in our analysis are calculated for a fixed radius of 150 arcsec. This range is roughly the average extraction radius of our clusters (i.e. from which growth curves are extracted and local background estimated). We calculate response matrices for two additional radii - 60 arcsec and 240 arcsec, to check how the spatial averaging of the spectral response impacts the derived ECFs and thus flux and luminosity. In this very conservative range of extraction radii we found the average effect to be of the order of 2.5%.

8) The uncertainties in the absolute normalization of the effective area of the detectors decrease the flux measurement precision. Nevalainen et al. (2010) found an agreement between $0.5 - 2$ keV fluxes measured by PN and both MOS cameras to be better than $\sim 5 - 7\%$ and for ACIS on *Chandra* and the PN found the fluxes to differ only by 2%.

9) We also tried to run the physical parameter estimation procedure (Sect. 5.3.3) from sev-

eral initial values of T_{500}/r_{500}. The iteration procedure always converged to the same solution, confirming its independence from the starting values.

We will provide tests of photometric accuracy of the growth curve method in a subsequent publication based on simulations using realistic backgrounds (i.e. using our survey fields as background for the simulated clusters).

A proper understanding of a realistic error budget of a cluster sample is crucial for its modelling in the cosmological context. From our analysis we find that most effects are typically on the $\sim 2\%$ level (under conservative assumptions) and the major contributing factors are the uncertainty of the photo-z measurements and the required extrapolations of the scaling relations (both in the range of $5 - 30\%$ depending on the parameter and the redshift of the system). For a few clusters an additional significant source of uncertainty is connected with the flux extrapolation. A full self-consistent treatment of the error propagation (including their full covariance matrices) and its impact on the cosmological modeling of the sample will be addressed in subsequent work.

5.6.2 Project outlook

The present sample establishes the observational base of the X-ray part of the XMM-BCS survey. In upcoming work we will use the available multi-wavelength data to follow several lines of investigations, some of which have already been initiated:

- The X-ray cluster catalog will be extended to cover the whole 14 deg^2 area. The preliminary source catalog is already available and we will follow up this work by estimating the photometric redshifts and physical parameters for the clusters in the same way as presented in this work. The full cluster catalog is expected to comprise ~ 100 clusters and groups of galaxies.

- We will calculate the selection function based on Monte Carlo simulations developed by Mühlegger (2010). This analysis will allow us to construct a well controlled subsample from the full cluster catalog that will be suitable for cosmological modelling.

- A more detailed analysis of optical properties of the clusters presented in this sample will be provided in Song et al., in prep. We will provide here measurements of the N_{200} and L_{200}^{opt} parameters and investigate their mass scaling relations.

- A detailed comparison of the X-ray, optical and mid-infrared cluster samples will allow us to gain good understanding of the selection function of each method. We will study the cluster/group population in this field and establish its multi-wavelength properties. The *Spitzer* imaging data will also be used to improve the photometric redshift estimates, especially for distant systems with redshift $z \gtrsim 0.8$.

- We have initiated further X-ray-SZE studies based on a cooperation with the SPT collaboration. The current SPT cluster samples of Williamson et al. (2011) and Vanderlinde et al. (2010) include only sources with minimal detection significance of 5σ. There are only two clusters in the 14 deg^2 above this threshold, SPT-CL J2332-5358 and SPT-CL J2342-5411,

independently detected also in our survey (Šuhada et al. 2010). Using our X-ray selected cluster catalog we can also safely investigate lower significance SPT detections. As a first example, cluster ID 044, (XBCS 231653.1-545413) was found to have a direct SPT detection at the 4.2σ level (B. Benson, private communication). Another approach is a stacking analysis of the SZE data for the X-ray selected clusters. Here, a preliminary analysis of the top eleven clusters ranked by their X-ray predicted SPT detection significance yields a $\gtrsim 6\sigma$ detection. We will explore both approaches in more depth in upcoming work, but already now it is clear, that with a joint SZE and X-ray analysis we are able to explore a completely new mass regime for the SZE surveys.

- The multi-wavelength coverage of the field provides opportunities also for non-cluster science. As an example, we have detected a total of 3065 X-ray point sources in the survey (1639 in the core region and 1426 in the extension). Most of these point sources are AGN and using the available multi-wavelength data we will be able to carry out a study with a focus on the obscured AGN population.

5.7   Conclusions

- We have provided the analysis of the 6 deg^2 XMM-*Newton* field in the framework of the XMM-BCS survey. We have carried out X-ray source detection and constructed a catalog of 46 clusters and groups of galaxies.

- Based on four band optical imaging provided by the Blanco Cosmology Survey we have confirmed that these X-ray detections are coincident with overdensities of red galaxies. Using the red sequence method we have measured the photometric redshifts of these systems.

- We have initiated a spectroscopic follow-up program by carrying out long slit spectroscopy observations using the EFOSC2 instrument at the 3.6 m NTT telescope at La Silla, Chile. We have obtained spectroscopic redshifts for BCG galaxies in 12 clusters and in four cases also for one additional member galaxy. This sample covers the redshift range $0 < z < 0.4$ (i.e. roughly up to the median redshift of the sample) and constitutes the first spectroscopic information for the field. We find good agreement between our photometric estimates and the spectroscopic values, but the spectroscopic sample has to be extended in redshift, in order to be able to provide a rigorous calibration of the photo-zs.

- Using the redshift information we measured the X-ray luminosities for our cluster sample. From luminosity scaling relations we estimate their most important physical parameters, e.g. mass, temperature and the Y_X parameter. We discuss the influence of several factors on the precision of the provided estimates. The uncertainty of the photometric redshift estimates and the extrapolation of the scaling relations to high redshift systems and into the group regime are identified as the most important factors that determine the overall errors in the physical parameters. We verify our X-ray parameter estimation method by

analysing the C1 sample of the XMM-LSS survey (Pacaud et al. 2007). We find good agreement between the parameters provided by both pipelines.

- The present sample of clusters and groups of galaxies covers the redshift range from $z = 0.1$ to redshift of $z \approx 1$ with a median of $z = 0.47$. The median temperature of the clusters is ~ 2 keV, and the median M_{500} mass 9×10^{13} M$_\odot$ (based on luminosity scaling relations). With our XMM-*Newton* observations we are thus able to effectively probe the cluster/group transition regime practically at all redshifts up to $z \approx 1$.

- We provide a preliminary, simplified calculation of the survey sky coverage which does not require extensive Monte Carlo simulations. Using this calculation we characterize our cluster sample by its $\log N - \log S$ relation. We find good agreement with the relations established by the RDCS survey (Rosati et al. 1998), 400deg^2 survey (Burenin et al. 2007; Vikhlinin et al. 2009a) and the XMM-LSS project (Pacaud et al. 2007).

- We carried out first comparisons with optical studies available from the Southern Cosmology Survey (SCS, Menanteau et al. 2009, 2010). In this preliminary investigation we find the SCS photometric redshifts biased low by $\sim 20\%$ with respect to our estimates (both photometric and spectroscopic, where available). We find a discrepancy between the X-ray and optical mass estimates, with optical masses being significantly higher. We compare our masses to weak lensing mass measurements available for 13 clusters in our sample from McInnes et al. (2009). The weak lensing masses are found to be in a much better agreement with our X-ray estimates.

Table 5.6: Physical parameters of the clusters sample. Notes: [†] cluster was detected in observations strongly affected by flaring; [◦] cluster is heavily affected by blending with a nearby source (see Sect. 5.8.1). Notes for redshifts: [a] spectroscopic redshift; [b] a high redshift system for which secure photometric redshift estimate is not possible from the current photometric catalog (the provided parameters are tentative).

ID	R.A. (J2000) (deg)	Dec (J2000) (deg)	z (photo.)	r_{plat} (arcmin/r_{500}^{-1})	F_{plat} (10^{-14} erg s^{-1} cm^{-2})	r_{500} (kpc)	F_{500} (10^{-14} erg s^{-1}cm^{-2})	L_{500} (10^{43} erg s^{-1})	T_{500} (keV)	M_{500} (10^{13} M$_\odot$)	Y_{500} (10^{13} M$_\odot$ keV)	M_{200} (10^{13} M$_\odot$)
011[†]	351.8070	−56.0615	0.97 ± 0.10	0.7/0.6	2.80 ± 0.42	577 ± 54	2.85 ± 0.43	11.8 ± 1.8	3.4 ± 1.0	16.4 ± 4.6	4.8 ± 2.9	24.3 ± 6.8
018	352.4828	−56.1360	0.39 ± 0.04	1.5/0.7	5.14 ± 0.50	633 ± 58	5.21 ± 0.51	2.6 ± 0.3	2.3 ± 0.7	10.9 ± 3.0	1.8 ± 1.1	15.2 ± 4.2
032	352.1778	−55.5662	0.83 ± 0.07	1.6/1.0	8.06 ± 0.68	702 ± 64	8.00 ± 0.66	21.5 ± 1.8	4.2 ± 1.2	25.0 ± 6.9	10.8 ± 6.4	37.0 ± 10.2
033	352.0448	−55.8400	0.79 ± 0.05	1.1/0.9	2.94 ± 0.25	593 ± 54	2.94 ± 0.25	7.6 ± 0.6	3.0 ± 0.9	14.4 ± 4.0	3.5 ± 2.1	21.0 ± 5.8
034	352.6538	−55.7270	0.28 ± 0.02	1.7/0.8	2.84 ± 0.45	536 ± 50	2.89 ± 0.46	0.7 ± 0.1	1.5 ± 0.4	5.8 ± 1.6	0.5 ± 0.3	7.9 ± 2.2
035	353.4388	−55.6387	0.67 ± 0.05	1.2/0.9	2.02 ± 0.32	560 ± 53	1.95 ± 0.31	3.6 ± 0.6	2.4 ± 0.7	10.5 ± 3.0	1.8 ± 1.1	15.0 ± 4.2
038[◦]	353.5130	−55.8156	0.39 ± 0.05	1.1/0.7	1.30 ± 0.20	503 ± 47	1.33 ± 0.20	0.7 ± 0.1	1.5 ± 0.4	5.4 ± 1.5	0.4 ± 0.3	7.5 ± 2.1
039	349.8214	−55.3244	0.18 ± 0.04	2.3/0.7	9.12 ± 0.56	586 ± 53	9.33 ± 0.57	0.8 ± 0.1	1.6 ± 0.5	6.8 ± 1.9	0.7 ± 0.4	9.2 ± 2.5
044	349.2212	−54.9036	0.44 ± 0.02	2.4/1.1	17.14 ± 1.15	787 ± 72	16.75 ± 1.10	10.5 ± 0.7	3.6 ± 1.0	22.2 ± 6.1	7.5 ± 4.4	31.6 ± 8.6
069	350.9631	−54.8923	0.75 ± 0.07	1.7/1.3	2.22 ± 0.43	560 ± 53	2.03 ± 0.35	4.8 ± 0.8	2.6 ± 0.7	11.6 ± 3.3	2.2 ± 1.4	16.7 ± 4.7
070	350.6286	−54.2691	0.152[a]	3.2/0.6	83.67 ± 1.70	819 ± 74	85.85 ± 1.75	5.1 ± 0.1	3.0 ± 0.8	18.1 ± 4.9	4.6 ± 2.7	25.0 ± 6.8
081	351.8470	−55.2624	0.85 ± 0.12	0.4/0.4	1.01 ± 0.17	497 ± 47	1.05 ± 0.18	3.5 ± 0.6	2.3 ± 0.7	9.1 ± 2.6	1.4 ± 0.9	13.2 ± 3.7
082	351.5779	−55.3859	0.63 ± 0.05	0.9/0.7	1.32 ± 0.23	526 ± 50	1.34 ± 0.23	2.2 ± 0.4	2.0 ± 0.6	8.3 ± 2.4	1.1 ± 0.7	11.8 ± 3.3
088	352.1748	−55.2234	0.43 ± 0.04	2.5/1.3	8.50 ± 1.27	679 ± 63	7.43 ± 1.01	4.6 ± 0.6	2.7 ± 0.8	14.1 ± 3.9	3.0 ± 1.8	19.8 ± 5.5
090	352.2366	−55.4081	0.58 ± 0.02	0.8/0.7	0.76 ± 0.18	481 ± 47	0.78 ± 0.18	1.1 ± 0.2	1.6 ± 0.5	6.0 ± 1.8	0.6 ± 0.4	8.3 ± 2.4
094	353.0185	−55.2120	0.269[a]	1.3/0.6	4.83 ± 0.53	583 ± 54	5.02 ± 0.55	1.1 ± 0.1	1.7 ± 0.5	7.4 ± 2.1	0.8 ± 0.5	10.1 ± 2.8
109	351.9058	−54.2705	1.02[b]	0.7/0.7	1.45 ± 0.21	510 ± 48	1.47 ± 0.21	7.3 ± 1.1	2.8 ± 0.8	12.0 ± 3.4	2.6 ± 1.6	17.7 ± 5.0
110	352.5161	−54.2388	0.47 ± 0.06	1.4/0.8	3.77 ± 0.49	605 ± 56	3.47 ± 0.47	2.7 ± 0.4	2.3 ± 0.7	10.4 ± 2.9	1.7 ± 1.0	14.6 ± 4.1
126	351.6393	−55.0206	0.42 ± 0.02	1.9/1.0	5.48 ± 0.41	643 ± 59	5.38 ± 0.40	3.2 ± 0.2	2.4 ± 0.7	11.8 ± 3.2	2.1 ± 1.3	16.5 ± 4.5
127	351.8492	−55.0648	0.207[a]	0.8/0.3	2.58 ± 0.29	499 ± 46	2.91 ± 0.33	0.4 ± 0.1	1.2 ± 0.4	4.4 ± 1.2	0.3 ± 0.2	5.9 ± 1.6
132	352.0084	−54.9292	0.96 ± 0.17	1.3/1.1	2.91 ± 0.34	571 ± 53	2.74 ± 0.31	11.1 ± 1.2	3.3 ± 0.9	15.7 ± 4.4	4.4 ± 2.7	23.3 ± 6.5
136	350.5036	−54.7500	0.36 ± 0.02	2.4/1.1	8.29 ± 0.76	673 ± 62	8.15 ± 0.68	3.4 ± 0.3	2.5 ± 0.7	12.6 ± 3.5	2.4 ± 1.4	17.6 ± 4.8
139[†◦]	351.3953	−54.7212	0.169[a]	1.9/0.6	4.83 ± 0.65	517 ± 48	5.01 ± 0.67	0.4 ± 0.1	1.3 ± 0.4	4.6 ± 1.3	0.3 ± 0.2	6.2 ± 1.7
150	352.5015	−54.6184	0.176[a]	2.9/0.8	18.25 ± 0.89	654 ± 59	18.48 ± 0.91	1.6 ± 0.1	2.0 ± 0.6	9.4 ± 2.6	1.3 ± 0.7	12.9 ± 3.5
152	352.4168	−54.7886	0.139[a]	0.9/0.3	2.50 ± 0.41	448 ± 42	2.97 ± 0.49	0.2 ± 0.1	1.0 ± 0.3	2.9 ± 0.8	0.1 ± 0.1	3.9 ± 1.1
156	353.8815	−54.5865	0.67 ± 0.06	0.8/0.6	3.35 ± 0.24	614 ± 56	3.43 ± 0.24	6.0 ± 0.4	2.8 ± 0.8	13.9 ± 3.8	3.2 ± 1.9	19.9 ± 5.5
158	353.6032	−54.4586	0.55 ± 0.03	1.4/0.9	3.57 ± 0.54	617 ± 58	3.58 ± 0.54	4.0 ± 0.6	2.5 ± 0.7	12.1 ± 3.4	2.3 ± 1.4	17.2 ± 4.8
210	353.5240	−55.7859	0.83 ± 0.09	0.7/0.7	0.55 ± 0.11	451 ± 43	0.56 ± 0.11	1.9 ± 0.4	1.9 ± 0.5	6.6 ± 1.9	0.8 ± 0.5	9.5 ± 2.7
227	350.5425	−55.4199	0.346[a]	1.1/0.6	1.51 ± 0.19	506 ± 47	1.56 ± 0.20	0.6 ± 0.1	1.4 ± 0.4	5.3 ± 1.5	0.4 ± 0.3	7.2 ± 2.0
245	351.0160	−55.0225	0.62 ± 0.03	0.8/0.7	0.97 ± 0.18	500 ± 48	0.99 ± 0.18	1.6 ± 0.3	1.8 ± 0.5	7.0 ± 2.0	0.8 ± 0.5	9.9 ± 2.8
275	353.6991	−55.2736	0.29 ± 0.03	1.7/0.8	2.93 ± 0.45	541 ± 51	2.95 ± 0.45	0.8 ± 0.1	1.5 ± 0.4	6.0 ± 1.7	0.5 ± 0.3	8.2 ± 2.3
287	354.2119	−55.2988	0.57 ± 0.04	0.9/0.7	0.98 ± 0.35	501 ± 54	1.00 ± 0.36	1.3 ± 0.5	1.7 ± 0.5	6.7 ± 2.1	0.7 ± 0.5	9.3 ± 3.0
288	353.7523	−54.9164	0.60 ± 0.04	1.8/1.2	2.75 ± 0.63	580 ± 56	2.44 ± 0.48	3.4 ± 0.7	2.4 ± 0.7	10.7 ± 3.1	1.9 ± 1.2	15.3 ± 4.4
357	353.6200	−54.6066	0.48 ± 0.06	2.0/1.2	3.56 ± 0.47	596 ± 55	3.16 ± 0.40	2.6 ± 0.3	2.2 ± 0.6	10.1 ± 2.8	1.6 ± 0.9	14.2 ± 3.9
386	353.9763	−56.0928	0.53 ± 0.05	0.7/0.6	0.66 ± 0.17	468 ± 47	0.67 ± 0.18	0.8 ± 0.2	1.5 ± 0.4	5.2 ± 1.6	0.4 ± 0.3	7.2 ± 2.2
430	351.3891	−55.7327	0.206[a]	1.3/0.6	1.59 ± 0.33	455 ± 44	1.69 ± 0.36	0.2 ± 0.1	1.0 ± 0.3	3.3 ± 1.0	0.2 ± 0.1	4.4 ± 1.3
444	354.0839	−55.5189	0.71 ± 0.05	0.9/0.7	1.27 ± 0.25	521 ± 50	1.29 ± 0.26	2.8 ± 0.6	2.2 ± 0.6	8.8 ± 2.5	1.3 ± 0.8	12.6 ± 3.6
457	352.1177	−54.2472	0.1[a]	1.6/0.5	1.98 ± 0.52	387 ± 39	2.29 ± 0.60	0.1 ± 0.1	0.7 ± 0.2	1.8 ± 0.5	< 0.1	2.4 ± 0.7
476[†◦]	351.4166	−54.7412	0.102[a]	2.3/0.5	10.27 ± 1.18	508 ± 47	11.04 ± 1.27	0.3 ± 0.1	1.2 ± 0.3	4.1 ± 1.1	0.2 ± 0.1	5.5 ± 1.5
502	349.9334	−54.6400	0.55 ± 0.05	0.7/0.5	1.55 ± 0.14	540 ± 50	1.61 ± 0.14	1.9 ± 0.2	2.0 ± 0.6	8.1 ± 2.2	1.1 ± 0.6	11.4 ± 3.2
511	353.0628	−54.7006	0.269[a]	1.5/0.6	4.41 ± 0.71	574 ± 54	4.53 ± 0.73	1.0 ± 0.2	1.7 ± 0.5	7.1 ± 2.0	0.7 ± 0.4	9.7 ± 2.7
527	350.5456	−56.3127	0.79 ± 0.06	1.0/0.8	2.26 ± 0.37	568 ± 54	2.27 ± 0.37	6.0 ± 1.0	2.7 ± 0.8	12.6 ± 3.6	2.7 ± 1.7	18.3 ± 5.2
528	353.8357	−55.5442	0.35 ± 0.02	0.8/0.5	0.63 ± 0.21	441 ± 46	0.68 ± 0.22	0.3 ± 0.1	1.1 ± 0.3	3.5 ± 1.1	0.2 ± 0.1	4.8 ± 1.5
538	353.5258	−54.7310	0.20 ± 0.02	1.6/0.7	1.99 ± 0.81	469 ± 52	2.07 ± 0.85	0.2 ± 0.1	1.1 ± 0.3	3.6 ± 1.2	0.2 ± 0.1	4.8 ± 1.6
543	353.1806	−54.8297	0.57 ± 0.03	1.7/1.0	4.15 ± 1.13	629 ± 61	4.07 ± 0.90	4.9 ± 1.1	2.7 ± 0.8	13.2 ± 3.8	2.8 ± 1.7	18.7 ± 5.5
547	351.0815	−55.4305	0.241[a]	1.1/0.5	1.05 ± 0.33	443 ± 46	1.12 ± 0.35	0.2 ± 0.1	1.0 ± 0.3	3.1 ± 1.0	0.1 ± 0.1	4.2 ± 1.3

5.8   Appendix

5.8.1   Quality flags and ancillary information

In this section we provide additional useful ancillary data for our clusters in the form several X-ray quality flags and diagnostic parameters compiled in Table 5.7. Here is the description of the table's columns:

- **ID:** the cluster identification number.

- **BCS field:** the identification number of the BCS field, on which the cluster is lying. Some clusters lie on two or more tiles, in those cases we provide the name of the tile with the largest overlap region.

- **XMM OBSID:** The official identification number of the XMM-*Newton* pointing containing the cluster. If the cluster lies in two (or three) adjacent observations we provide the OBSID of the pointing which provides the best constraint on the cluster flux (typically the one where the cluster is at the smallest off-axis angle).

- **flag$_{HC}$:** The hot chip flag is a four character string, with the characters being either T for "true" or F for "false". The significance of the characters:
  1. character: Does the observation have a hot MOS2 CCD#5?
  2. character: Does the cluster lie on the MOS2 CCD#5?
  3. character: Does the observation have a hot MOS1 CCD#4?
  4. character: Does the cluster lie on the MOS1 CCD#4?
  For the problematics of the hot chips see Sect. 5.3.1.

- **SNR$_{Xflux}$:** The flux estimation significance determined as $F_{500}/\sigma_{F_{500}}$, where F_{500} is the source flux in the r_{500} aperture, and $\sigma_{F_{500}}$ is its error (including shot noise and 5% background modelling uncertainty, Sect. 5.3.2).

- **flag$_{inst}$:** The instrument flag equals 0 if the physical parameters of the source were obtained using the PN and both MOS cameras. If flag$_{inst}$ = 1 only PN could be used and if flag$_{inst}$ = 2 only the combination of the two MOS cameras was utilized.

- **Q_{plat}^{PN}:** The automatic plateau fit quality flag for the PN growth curves. These flags have the same meaning as in Böhringer et al. (2000). In summary, as described in Sect. 5.3.2 we fit a line to the growth curve between r_{plat} and the outer extraction radius. The flag describes the quality of this fit by calculating the ratio of the predicted count rate from the linear fit to the expectation, if the plateau was constant and equal to the estimated plateau flux. $Q_{plat}^{PN} = 1$: the growth curve shows neither significant increase nor decrease outside r_{plat}. This value is assigned if the linear extrapolation does not differ by more than 0.8% per bin from the constant value. $Q_{plat}^{PN} = 2$: marks a declining curve (decline > 0.8%/bin). A decline can occur if the background model (determined from a fit to the whole field) slightly overestimates the local background. In this case we attempt to estimate the plateau level from the 3 bins closest to r_{plat}. If the final fit is acceptable (no significant residual decline), the plateau is accepted and assigned this quality flag. $Q_{plat}^{PN} = 3$ and $Q_{plat}^{PN} = 4$: in case that the plateau is rising an attempt is made to iteratively exclude the outermost bins and in a second step also the innermost bins. This procedure helps in correcting an outer rise of the growth curve due to a neighboring source and if necessary by skipping over a few bins if the curve fluctuates in the radial range close to r_{plat}. If this procedure converges, after the exclusion of the outermost bins the plateau is accepted and flagged with $Q_{plat}^{PN} = 3$. If the procedure converges, but it required also the second step of excluding the innermost bins we assign $Q_{plat}^{PN} = 4$. If $Q_{plat}^{PN} = 5$, the plateau is rising and the increase could not be corrected for by the above described procedure. If there are only two or less radial bins outside the plateau radius can not be established and we assign $Q_{plat}^{PN} = 9$.

  $Q_{plat}^{PN} \leq 4$ mark generally good quality plateaus (naturally, the lower the flag the better). $Q_{plat}^{PN} = 5$ is a serious warning and $Q_{plat}^{PN} = 9$ is not recommended to be used at all. In fact, for the parameters in Table 5.6 we do not use plateaus with this flag with the exception for the systems ID 476 and 139 where an alternative solution is not available due to their significant blending (Appendix 5.8.2).

- **Q_{plat}^{MOS}:** The same as Q_{plat}^{PN} but applied to the MOS1+MOS2 growth curve.

- **Q_{gca}^{PN}:** Visual flag set considering the overall quality of the PN growth curve solution (taking into account the presence of chip gaps, anomalous background, potential contamination etc.). Value equal to 1 is the best (no problems), 3 the worse (to be considered as a warning).

- **Q_{gca}^{MOS}:** The same as Q_{gca}^{PN} but applied to the MOS1+MOS2 growth curve.

- **Q_{TOT}:** Overall global X-ray flag, assigned visually taking into consideration all the above flags. Sources with this flag equal to 1 (best) and 2 (only mild warnings) have high quality X-ray photometry measurements. Flag equal to 3 should be handled with care but we included them in all analyses presented in this paper.

We have identified 4 additional sources, which have confirmed optical counterparts, but the available data allows us to derive only very rough X-ray parameters. These can be considered to

have Q_{TOT} = 4 and have *not* been included in our analyses. We provide their tentative parameters in the Table 5.9.

Table 5.7: Cluster ID and proper name cross-reference table. We also list the BCS field name for each cluster and additional ancillary X-ray quality flags (see text for details).

ID	Name	BCS field	XMM OBSID	flag$_{HC}$	SNR$_{Xflux}$	flag$_{inst}$	Q_{plat}^{PN}	Q_{plat}^{MOS}	Q_{gca}^{PN}	Q_{gca}^{MOS}	Q_{TOT}
011	XBCS 232713.7-560341	BCS2327-5602	0505380301	TFFF	6.7	0	1	1	2	2	1
018	XBCS 232955.9-560810	BCS2327-5602	0505380401	TFFF	10.2	0	3	1	1	1	1
032	XBCS 232842.7-553358	BCS2327-5529	0505381001	FFFF	11.9	0	1	1	1	1	1
033	XBCS 232810.7-555024	BCS2327-5602	0505381001	FFFF	11.9	0	1	1	2	2	1
034	XBCS 233036.9-554337	BCS2332-5529	0505381101	TTFF	6.3	0	1	1	1	2	1
035	XBCS 233345.3-553819	BCS2332-5529	0505381201	FFFF	6.3	0	1	1	3	3	1
038	XBCS 233403.1-554856	BCS2332-5602	0505381201	FFFF	6.6	0	1	1	2	1	2
039	XBCS 231917.1-551928	BCS2319-5529	0505381401	FFFF	16.2	0	1	1	1	1	2
044	XBCS 231653.1-545413	BCS2316-5455	0505382201	TTFF	14.9	0	1	1	1	1	1
069	XBCS 232351.1-545332	BCS2324-5455	0505382401	TFTF	5.2	0	1	1	2	2	1
070	XBCS 232230.9-541609	BCS2324-5421	0505383801	TFTT	49.1	0	1	1	1	1	1
081	XBCS 232723.3-551545	BCS2327-5529	0505381701	TFFF	6.0	0	3	1	2	3	2
082	XBCS 232618.7-552309	BCS2327-5529	0505381701	TFFF	5.9	0	1	1	1	2	1
088	XBCS 232842.0-551324	BCS2327-5529	0505381801	FFFF	6.7	1	1	1	2	3	1
090	XBCS 232856.8-552429	BCS2327-5529	0505381801	FFFF	4.3	0	1	1	1	3	1
094	XBCS 233204.4-551243	BCS2332-5529	0505381901	TTFF	9.2	0	5	1	2	2	1
109	XBCS 232737.4-541614	BCS2328-5421	0505384001	FFFF	6.8	0	1	1	2	2	1
110	XBCS 233003.9-541420	BCS2331-5421	0505384001	FFFF	7.6	0	1	1	1	2	1
126	XBCS 232633.4-550114	BCS2328-5455	0505382501	TFTF	13.3	0	1	1	1	1	1
127	XBCS 232723.8-550353	BCS2328-5455	0505382501	TFTF	8.8	0	1	1	1	1	1
132	XBCS 232802.0-545545	BCS2328-5455	0505382601	FFFF	8.6	0	1	1	1	2	2
136	XBCS 232200.9-544500	BCS2320-5455	0505383101	FFTF	10.9	0	1	1	1	1	1
139	XBCS 232534.9-544316	BCS2324-5455	0505383201	TFTF	7.5	0	9	9	3	3	3
150	XBCS 233000.4-543706	BCS2331-5421	0505383401	FFFF	20.4	0	1	1	1	1	1
152	XBCS 232940.0-544719	BCS2328-5455	0505383401	FFFF	6.1	0	4	1	3	2	2
156	XBCS 233531.6-543511	BCS2335-5421	0505383601	FFFF	14.2	0	1	1	2	2	1
158	XBCS 233424.8-542731	BCS2335-5421	0505383601	FFFF	6.7	0	1	1	2	2	1
210	XBCS 233405.8-554709	BCS2336-5602	0505381201	FFFF	5.0	0	1	1	2	2	1
227	XBCS 232210.2-552512	BCS2323-5529	0505381501	FFFF	7.9	0	1	1	2	2	1
245	XBCS 232403.8-550121	BCS2324-5455	0505382401	TFTF	5.4	0	1	1	1	2	1
275	XBCS 233447.8-551625	BCS2336-5529	0505382001	TTFF	6.6	0	1	1	2	2	1
287	XBCS 233650.9-551756	BCS2336-5529	0505382101	TTFF	2.8	0	4	4	3	3	3
288	XBCS 233500.5-545459	BCS2335-5455	0505382801	TFFF	4.4	0	5	1	1	2	1
357	XBCS 233428.8-543624	BCS2335-5421	0505383601	FFFF	7.5	0	1	1	1	2	1
386	XBCS 233554.3-560534	BCS2336-5602	0505380601	TFFF	3.8	0	1	3	1	3	1
430	XBCS 232533.4-554358	BCS2323-5529	0505384801	FFFF	4.8	0	1	1	1	2	1
444	XBCS 233620.1-553108	BCS2336-5529	0505382001	TFFF	5.0	0	1	1	1	3	1
457	XBCS 232828.2-541450	BCS2328-5421	0505384001	FFFF	3.8	2	1	1	2	2	2
476	XBCS 232540.0-544428	BCS2324-5455	0505383201	TFTF	8.7	0	9	5	3	3	3
502	XBCS 231944.0-543824	BCS2320-5455	0505383001	TFFF	11.1	0	1	1	2	3	1
511	XBCS 233215.1-544202	BCS2331-5455	0505383501	TFFF	6.3	0	3	1	2	2	1
527	XBCS 232210.9-561846	BCS2323-5602	0554561001	TFFF	6.1	0	1	3	1	3	1
528	XBCS 233520.6-553239	BCS2336-5529	0505382001	TFFF	3.1	0	1	1	3	3	1
538	XBCS 233406.2-544352	BCS2335-5455	0505383601	FFFF	2.4	2	1	3	1	2	3
543	XBCS 233243.3-544947	BCS2331-5455	0554560601	TFTF	3.7	1	1	1	3	3	1
547	XBCS 232419.6-552550	BCS2323-5529	0505381601	TFTF	3.2	2	1	1	3	1	1

5.8.2 Notes on individual sources

Some of the identified clusters required individual treatment and in this section we provide notes for these cases:

- **ID 011**: this high redshift cluster lies on a heavily flared field F03 with no quiescent period. Therefore, the field was not used for the sensitivity function calculation and the $\log N - \log S$. The double component background model accounts in principle in the first approximation for the enhanced background and therefore we provide the basic X-ray parameters for this cluster. The diagnostic flags (Table 5.7) indicate that the growth curve solution is quite reliable, but due to the flaring all physical parameters should be treated with caution.

- **ID 038**: This source consists of two completely overlapping systems, one with photometric redshift $z = 0.39 \pm 0.05$ and the second with $z = 0.74 \pm 0.07$. Since there is no direct way to disentangle the contribution of the two sources, we will assume that all the flux comes from the more nearby system. In this case, the estimated physical parameters are upper limits.

- **ID 070**: is a nearby cluster with large extent and measured flux. It lies on a hot MOS1 CCD#4 and due to its extent it is impossible to obtain a background area on this chip uncontaminated by the source emission. Therefore we can not use the procedure described in Sect. 5.3.1, where we fit a double component model to the hot chip independently from the rest of the field. Instead we discard the data from this chip completely.

- **ID 109**: due to the limited depth of the available optical data we can provide only very tentative redshift estimate for this system.

- **ID 139 and 476**: We detect two nearby, high significance extended sources in this region (~ 1.3 arcmin apart). The systems are confirmed as independent also in redshift space by our spectroscopic measurements (ID 476 at $z = 0.102$ and ID 139 at $z = 0.169$). In order to measure the flux of each cluster we excise the other source. Due to their proximity, however, full deblending is not possible and therefore both fluxes are likely overestimated. The analysis of the sources is further complicated by the presence of a very bright X-ray point source at ~ 2 arcmin distance from the clusters and very high quiescent soft proton contamination.

  The cluster catalog of Burenin et al. (2007) based on ROSAT data includes a source with a center roughly between the two systems (i.e. very likely misclassified as a single cluster due to the limited resolution of ROSAT).

- **ID 275**: also lies on a hot MOS2 CCD#5. Its detection likelihood is completely dominated by the MOS2 detection, however the source is not flagged as spurious based on the criteria described in Sect. 5.3.1, because it would be above the detection threshold even without the MOS2 data. In this case, the background modeling of the hot chip was possible and this background was used in the subsequent growth curve analysis.

Table 5.8: Galaxies identified in the NED database to be within 16″ from the X-ray center. We list spectroscopic redshifts where available - in both cases the identified galaxies are the BCG galaxies of their cluster counterparts. Redshift reference: [a] Jones et al. (2004).

ID	Object Name	R.A. (deg)	DEC (deg)	redshift	separation
034	APMUKS(BJ) B232750.10-560012.1	352.6544	-55.7274		1.9″
039	2MASX J23191712-5519284	349.8214	-55.3245		0.5″
041	2MASX J23190212-5523195	349.7588	-55.3888		1.3″
070	2MASX J23223092-5416086	350.6289	-54.2691		0.8″
094	APMUKS(BJ) B232918.62-552918.2	353.0196	-55.2122		2.5″
127	2MASX J23272468-5503589	351.8528	-55.0664		9.6″
150	2MASX J23300047-5437069	352.5019	-54.6187	0.177^a	1.5″
152	2MASX J23294006-5447220	352.4168	-54.7895		3.1″
227	APMUKS(BJ) B231920.30-554137.6	350.5444	-55.4194		4.4″
268	APMUKS(BJ) B232326.14-554657.3	351.5618	-55.5074		14.0″
476	2MASX J23254015-5444308	351.4173	-54.7419	0.101^a	3.1″
511	APMUKS(BJ) B232929.68-545847.0	353.0645	-54.7035		10.8″
547	2MASX J23241957-5525494	351.0816	-55.4303		0.6″

Table 5.9: Physical parameters for the low quality detections.

ID	R.A. (J2000) (deg)	Dec (J2000) (deg)	z (photo.)	r_{plat} (arcmin/r_{500}^{-1})	F_{plat} (10^{-14} erg s^{-1} cm^{-2})	r_{500} (kpc)	F_{500} (10^{-14} erg s^{-1}cm^{-2})	L_{500} (10^{43} erg s^{-1})	T_{500} (keV)	M_{500} (10^{13} M$_\odot$)	Y_{500} (10^{13} M$_\odot$ keV)	M$_{200}$ (10^{13} M$_\odot$)
534	351.1993	−55.4128	0.31 ± 0.02	1.4/0.7	2.18 ± 1.11	523 ± 64	2.22 ± 1.13	0.7 ± 0.4	1.5 ± 0.5	5.6 ± 2.0	0.5 ± 0.4	7.6 ± 2.8
536	354.2994	−55.3514	0.69 ± 0.07	0.8/0.7	0.83 ± 0.23	487 ± 49	0.85 ± 0.24	1.8 ± 0.5	1.9 ± 0.6	7.1 ± 2.1	0.8 ± 0.5	10.0 ± 3.0
540	350.1461	−54.4628	0.24 ± 0.02	1.3/0.6	1.66 ± 0.46	474 ± 48	1.75 ± 0.48	0.3 ± 0.1	1.2 ± 0.3	3.8 ± 1.2	0.2 ± 0.1	5.2 ± 1.6
541	350.5048	−54.3296	0.59 ± 0.06	0.9/0.7	1.06 ± 0.30	506 ± 51	1.08 ± 0.30	1.5 ± 0.4	1.8 ± 0.5	7.0 ± 2.1	0.8 ± 0.5	9.9 ± 3.0

5.8.3 Test of sensitivity function from preliminary Monte Carlo simulations

The determination of the survey selection function is a crucial requirement for the cosmological modeling of the cluster sample, scaling relation studies etc. Due to the complex nature of extended source detection, this question can be properly addressed only by detailed Monte Carlo simulations. In the present work we utilized a simplifying approach that allowed us to get a first estimate of the sensitivity functions and the recovered $\log N - \log S$ relation (Sect. 5.5.2 and 5.5.3).

The software for the Monte Carlo simulations (Mühlegger 2010) is in an advanced development stage which allows us to carry out a preliminary test of our simplified approach.

The simulation pipeline uses the survey fields themselves and injects mock beta model clusters into the observations at random positions across the field-of-view. The field is then processed with the detection pipeline. The process is repeated on a grid of cluster fluxes and core radii and the cluster detection probability is derived as a function of these parameters. The use of real observations instead of model backgrounds allows us to derive a realistic selection function. The simulation software is described in detail in Mühlegger (2010).

Simulations are currently available for a subset of the XMM-*Newton* Distant Cluster Project (XDCP, Böhringer et al. 2005; Fassbender 2008) fields. From these fields we selected 3 observations (XMM OBSIDs 0104860201, 0111970101, 0112551101) which have similar depth to our survey fields (e.g. cleaned exposure times ~ 10 ks and enough area unaffected by the central source to safely assess the background). We processed these fields with our detection pipeline and calculated the point source sensitivity function and the scaled extended sensitivity function as described in Sect. 5.5.2. The comparison with the sensitivity function derived from the simulations are displayed in Fig. 5.15. The simple calculation (black curves) already matches the realistic calculation (red curves) very well, capturing also the transition parts of the curve. The curves from simulations include the effect of incompleteness of the output catalogs. The red curves in Fig. 5.15 are calculated for a 50% completeness level (c=0.5). The completeness of our cluster catalog can be assessed only by simulations, but is certainly higher than 50%. This means that the preliminary analytic sky coverage function overestimates the sky coverage. The use of the true sky-coverage function would lead to an increase of the weighting factor in Eq. 5.5 and would move the points in Fig. 5.10 in the relevant flux range slightly higher. The sensitivity function for a 90% completeness scenario is plotted in green and as expected yield a much smaller area for the given flux.

Additional subtle effects slightly influence this comparison, e.g. leading to different normalizations of the two curves in the saturated high-end part: **1)** All the fields have a bright source in the center of the field-of-view, which has to be excised. The excision is treated slightly differently in the simulations and in the simple calculations leading to slightly different total *geometric* area. **2)** The simulated curves were calculated for the single band detection scheme in the $0.35 - 2.4$ keV while our analytic solution for a $0.5 - 2$ keV band. The fluxes were converted to the $0.5 - 2$ keV band, but detection in these different energy ranges could cause slightly different completeness and contamination fractions.

We conclude, that our first-order approach yields a good description of the sensitivity function
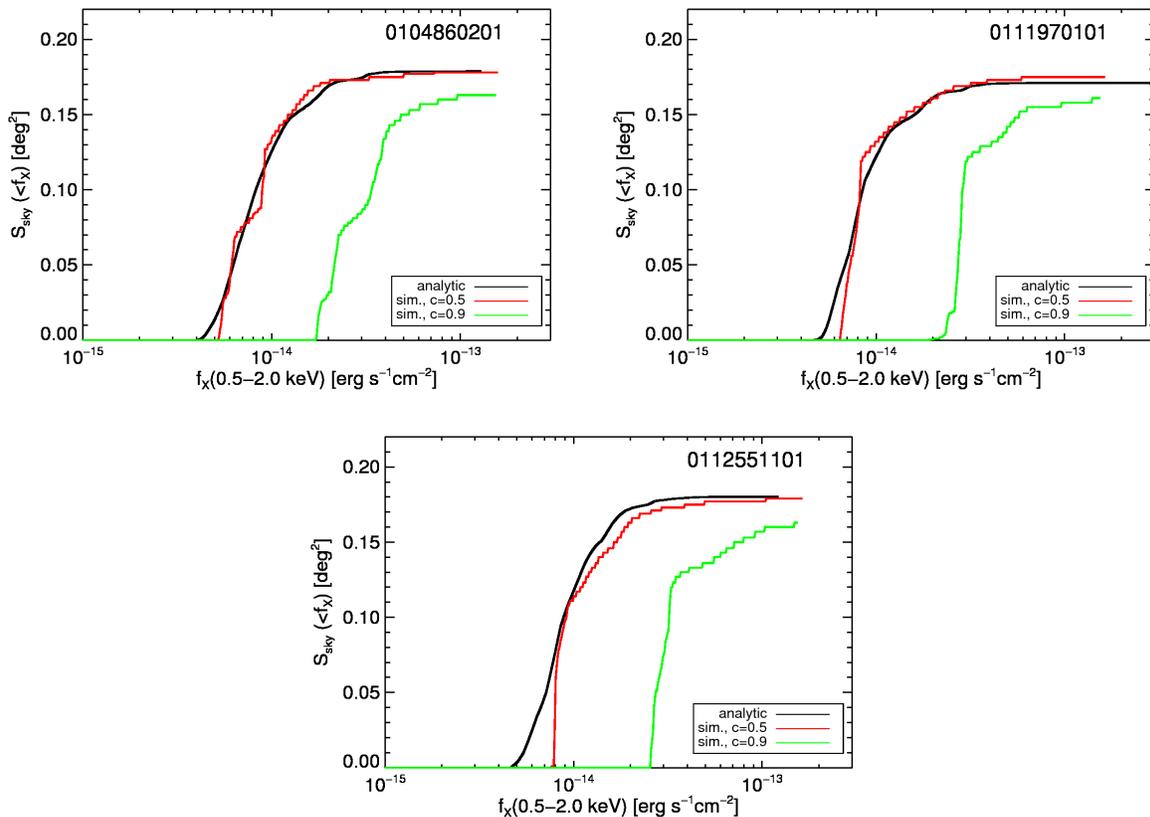
Figure 5.15: Sky-coverage for extended sources in the three CHECCS fields from Monte Carlo simulations at the 50% (red curve) and 90% (red curve) completeness level. Black solid curve shows the sky-coverage calculated by scaling the point source curve (dashed) with an offset factor of 2.4 (see Sect. 5.5.2). The simple scaling is shown to be a good first order description of the extended source sensitivity function. See Appendix 5.8.3 and Sect. 5.5.2 for details.

for a 50% completeness level. To estimate the completeness of our sample will be possible only from Monte Carlo simulations. The sensitivity functions from Sec. 5.5.2 provides sufficient precision for present applications and the preliminary $\log N - \log S$ is already in good agreement with previous findings. The described simulation pipeline will be applied to the whole XMM-BCS survey in subsequent work and the realistic selection function will be utilized for further analysis and modelling of the final cluster sample.

5.8.4 Comparison with the XMM-LSS survey

The first part of the XMM-LSS survey (the initial 5 deg^2, Pierre et al. 2007; Pacaud et al. 2006, 2007) offers an excellent match to our survey not only with respect to the area, but also to the typical depth (having only slightly higher average exposure times). Since the XMM-LSS

project has already carried out Monte Carlo simulations to calibrate their detection and source-characterization pipeline, we make here an effort to compare results derived from our XMM-BCS pipeline with their published results.

Cluster detection comparison

A full comparison of the source detection pipelines would be only of limited use and is currently impossible since only a small part of the XMM-LSS extended sources have also been spectro-scopically confirmed up to now (the so-called C1 sample of Pacaud et al. (2007)[13]). Therefore, we restrict ourselves to the reanalysis of the C1 sample.

We downloaded all the XMM-LSS fields with C1 detections[14] and fully reanalyzed them with the XMM-BCS pipeline. We confidently detected all the C1 clusters and they are among our highest ranked extended source detections.

In Fig. 5.16 we compare their detection and extent likelihoods with their respective XMM-LSS variants (SB_Detect_Likelihood and SB_Extent_Likelihood). Both sets of parameters exhibit a strong correlation, showing good consistency between both detection approaches (XMM-LSS uses a single band wavelet detection scheme). The scatter between the parameters is caused by small differences in the data reduction process, background estimation and source detection algorithms.

The C1 sample is defined by SB_Detect_Likelihood> 32, SB_Extent_Likelihood> 33. We fit a linear relation in the two log-log planes and use these cuts to convert the XMM-LSS thresholds to our parameters obtaining: det_ml> 16.4 (equivalent to $\sim 5.4\sigma$ detection in our scheme) and ext_ml> 8.3 (i.e. $\sim 3.7\sigma$ extent significance).

X-ray photometry comparison

In Fig. 5.17 we compare the fluxes in the $0.5 - 2$ keV band and 0.5 Mpc aperture measured by the XMM-LSS and by us using the growth curve method (Sect. 5.3.2). Being interested only in the flux estimation we have fixed the redshift and temperature to their spectroscopic values provided by XMM-LSS. Both methods give fluxes that are in good agreement and no significant bias is found.

We have checked the dependence of flux residuals defined here as $(f_X^{XMM-LSS} - f_X^{XMM-BCS})$ / $f_X^{XMM-BCS}$ on several parameters: the flux itself, cluster redshift, off-axis angle, fraction of missing pixels (due to chip gaps etc.), background correction factors and amount of extrapolation. We did not find any systematic effects in either PN or MOS fluxes.

This agreement is encouraging, if we take into account that the two pipelines utilize principally different approaches to the flux measurement. XMM-LSS utilizes a beta model fit to the cluster's surface brightness integrated out to a fiducial radius, while our method is completely non-parametric (except for a typically small extrapolation factor if the required aperture is larger

---

[13]Catalog available at : heasarc.gsfc.nasa.gov/W3Browse/all/xmmlssoid.html

[14]XMM OBSIDs: 0037980301, 0037980701, 0037981001, 0037981101, 0037981201, 0037981501, 0037981601, 0037981801, 0037982501, 0037982601, 0109520201, 0109520301, 0109520601, 0111110301, 0111110401, 0112680101, 0112680201, 0112680301, 0112680401, 0112680501, 0147110101, 0147110201.

than the range where the cluster emission is detected directly). Background estimation in both approaches is also markedly different.

The fluxes do not agree within the error bars for the brightest cluster in this sample (XLSS-J022145.2-034617), with our flux being by $\sim$ 15% higher. The brightest outlier in the other direction (i.e. our flux lower than the one from XMM-LSS) is XLSS-J022609.9-045805. In this case we found excessive contamination from point sources in the X-ray photometry aperture. We carefully checked and manually adjusted the automatic point source removal, which led to a net decrease of measured flux.

Interestingly, if we decide to rely only on a temperature derived from the $L-T$ the flux estimation precision is practically unchanged (the average difference is only 3%). The temperatures are also in good agreement, although the error bars are large. The mean temperature residuals are $< 1\%$ with a standard deviation of $\sim$ 23%, comparable to measurement errors. This shows that the $L-T$ scaling relation and its evolution adopted in this work from Pratt et al. (2009) is suitable for cluster samples drawn from surveys of this type. We do not find any systematic dependence of the temperature residuals on redshift, flux or flux residuals.

The cluster mass is not a direct observable in either of the two surveys. XMM-LSS gives rough estimates based on their spectroscopic measurement and beta model fit using the relation from Ettori (2000). Our estimates, using the $L-M$ relation of Pratt et al. (2009), give on average almost 40% higher masses. The mass residuals strongly amplify the temperature residuals where a unit increment of temperature residual increases the temperature more than a unit decrement of temperature residual would decrease it. This leads to a net increase of mass with respect to the XMM-LSS value.

Finally, we also check the consistency of the beta model fits between the two pipelines. Since the core radius r_{core} and the β exponent of the beta model are strongly degenerate, especially for the case of low counts profiles, our fitting procedure keeps β fixed to the canonical value of 2/3. The XMM-LSS pipeline carries out fits with both the r_{core} and β as free parameters. Despite this difference, we find good agreement between the estimated core radii (Fig. 5.18).
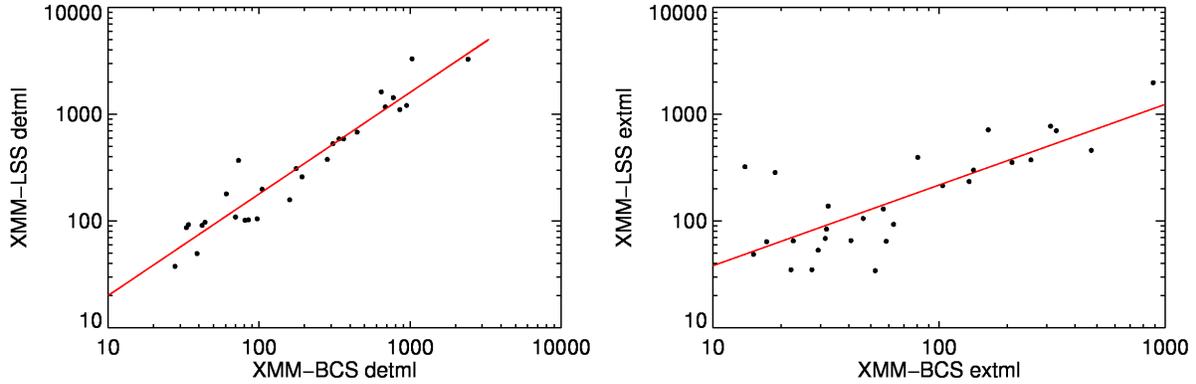
Figure 5.16: Comparison of detection (left panel) and extent likelihoods (right panel) between our pipeline (x-axis) and the XMM-LSS pipeline Pacaud et al. (y-axis 2007). The derived likelihoods are well correlated and the red line shows the best fit relations.
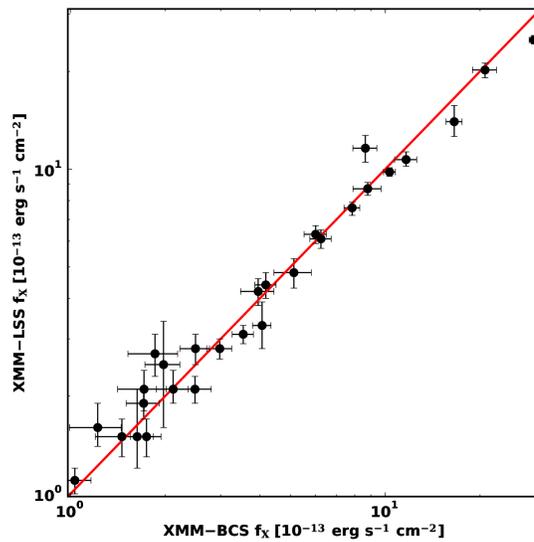
Figure 5.17: Comparison of measured X-ray fluxes of the C1 subsample of the XMM-LSS survey in the $0.5 - 2$ keV band and a 0.5 Mpc aperture (Pacaud et al. 2007, y-axis) and the fluxes measured by our pipeline (x-axis). The red line marks equality. See Sect. 5.8.4 for details of this comparison.
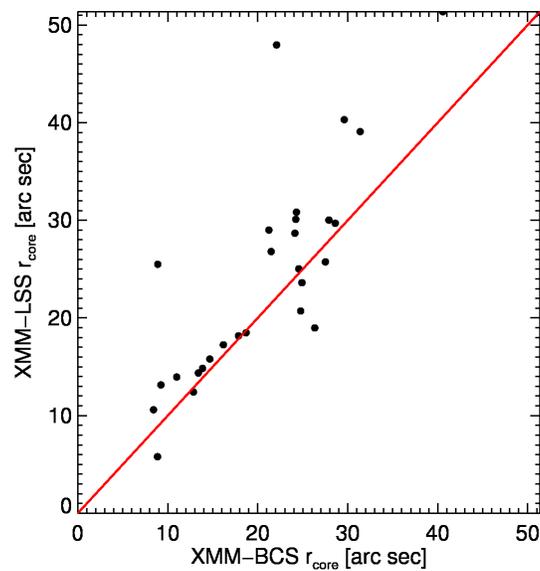
Figure 5.18: Beta model core radii for the XMM-LSS C1 sample as estimated by our pipeline (x-axis) and by the XMM-LSS estimates. Red line marks equality. The core radii are typically highly uncertain given the relatively low photon statistics. Despite this the agreement between the two estimates is good. Note that the XMM-LSS values are fitted with the beta value as a free parameter, while we fix its value to 2/3.

Chapter 6

XMM-Newton detection of two clusters of galaxies with strong SPT Sunyaev-Zel'dovich effect signatures

R. Šuhada, J. Song, H. Böhringer, B. A. Benson, J. Mohr, R. Fassbender, A. Finoguenov, D. Pierini, G. W. Pratt, K. Andersson, R. Armstrong and S. Desai

Abstract

We report on the discovery of two galaxy clusters, SPT-CL J2332-5358 and SPT-CL J2342-5411, in X-rays. These clusters were also independently detected through their Sunyaev-Zel'dovich effect by the South Pole Telescope, and in the optical band by the Southern Cosmology Survey. They are thus the first clusters detected under survey conditions by all major cluster search approaches. The X-ray detection is made within the frame of the XMM-BCS cluster survey utilizing a novel *XMM-Newton* mosaic mode of observations. The present study makes the first scientific use of this operation mode. We estimate the X-ray spectroscopic temperature of SPT-CL J2332-5358 (at redshift $z = 0.32$) to be T = $9.3^{+3.3}_{-1.9}$ keV, implying a high mass, $M_{500} = 8.8 \pm 3.8 \times 10^{14}$ M$_\odot$. For SPT-CL J2342-5411, at $z = 1.08$, the available X-ray data do not allow us to directly estimate the temperature with good confidence. However, using our measured luminosity and scaling relations we estimate that T= 4.5 ± 1.3 keV and $M_{500} = 1.9 \pm 0.8 \times 10^{14}$ M$_\odot$. We find a good agreement between the X-ray masses and those estimated from the Sunyaev-Zel'dovich effect.

6.1   Introduction

Almost 40 years after the theoretical prediction of the Sunyaev-Zel'dovich effect (hereafter SZE, Sunyaev and Zel'dovich 1972), i.e. the distortion of the cosmic microwave background spectrum by the hot gas in clusters of galaxies, we have entered a new era where the first clusters

have been discovered by large-area SZE surveys (Staniszewski et al. 2009). Two ambitious SZE cluster surveys are currently underway: by the South Pole Telescope (SPT) and by the Atacama Cosmology Telescope (ACT). Recently, the SPT released a catalog of 21 SZE-selected galaxy clusters identified in the first ~ 200 deg^2 of sky surveyed by the SPT (Vanderlinde et al. 2010, hereafter V10). Both SPT and ACT have additionally carried out observations of known clusters (Plagge et al. 2010; Hincks et al. 2010).

The SZE provides new prospects for precision cluster cosmology for two main reasons: **(1)** the SZE decrement characterized by the Comptonization parameter Y is currently considered as a robust, low-scatter proxy for cluster mass (e.g. da Silva et al. 2004; Motl et al. 2005) and **(2)** the SZE is not subject to the cosmological surface brightness dimming effect, resulting in a selection function closely corresponding to a selection with a fixed mass limit at all redshifts.

However, to be able to fully harvest the potential of the upcoming comprehensive multi-wavelength surveys, we need to have **(1)** a good understanding of the cluster selection function, **(2)** cluster redshift measurements and **(3)** a well-calibrated link between cluster observables and total cluster masses.

In order to address these issues and to best understand the results of the different survey techniques, we are conducting a coordinated multi-wavelength survey in a test region (which will be covered by both SZE surveys) in the optical by the Blanco Cosmology Survey (BCS, 100 deg^2), in the mid-infrared with *Spitzer* (14 deg^2) and in X-rays with *XMM-Newton*.

Here we present the X-ray detections of two clusters, SPT-CL J2332-5358 and SPT-CL J2342-5411. These clusters were independently detected by SPT (V10) and confirmed to be coincident with overdensities of red galaxies (High et al. 2010). In addition, SPT-CL J2332-5358 has been recently detected in the optical (SCSO J233227-535827, Menanteau et al. 2010). This source is also coincident with the X-ray source 1RXS J233224.3-535840 in the ROSAT Bright Source Catalog (Voges et al. 1999). The present *XMM-Newton* observations enable us to confirm both objects as X-ray luminous clusters of galaxies.

Throughout the article we adopt a ΛCDM cosmology with $(\Omega_\Lambda, \Omega_M, H_0) = (0.7, 0.3, 70$ km s^{-1} Mpc^{-1}).

6.2 XMM-Newton data reduction

The sources SPT-CL J2332-5358 and SPT-CL J2342-5411 were discovered as high-significance extended sources in *XMM-Newton* observations carried out in the framework of the XMM-BCS cluster survey (Šuhada et al., in prep.).

The X-ray survey currently extends over 14 deg^2 (Fig. 6.1). The core of the *XMM-Newton* field consists of a deeper region covering 6 deg^2 with 42 partially overlapping ~ 12 ks long individual pointings and three large scale (~ 2.7 deg^2 each) *mosaic mode observations*. Each of the three mosaics consists of 19 stable pointings (3.5 ks exposures) and the slews between them, with a total time ~ 90 ks per mosaic.
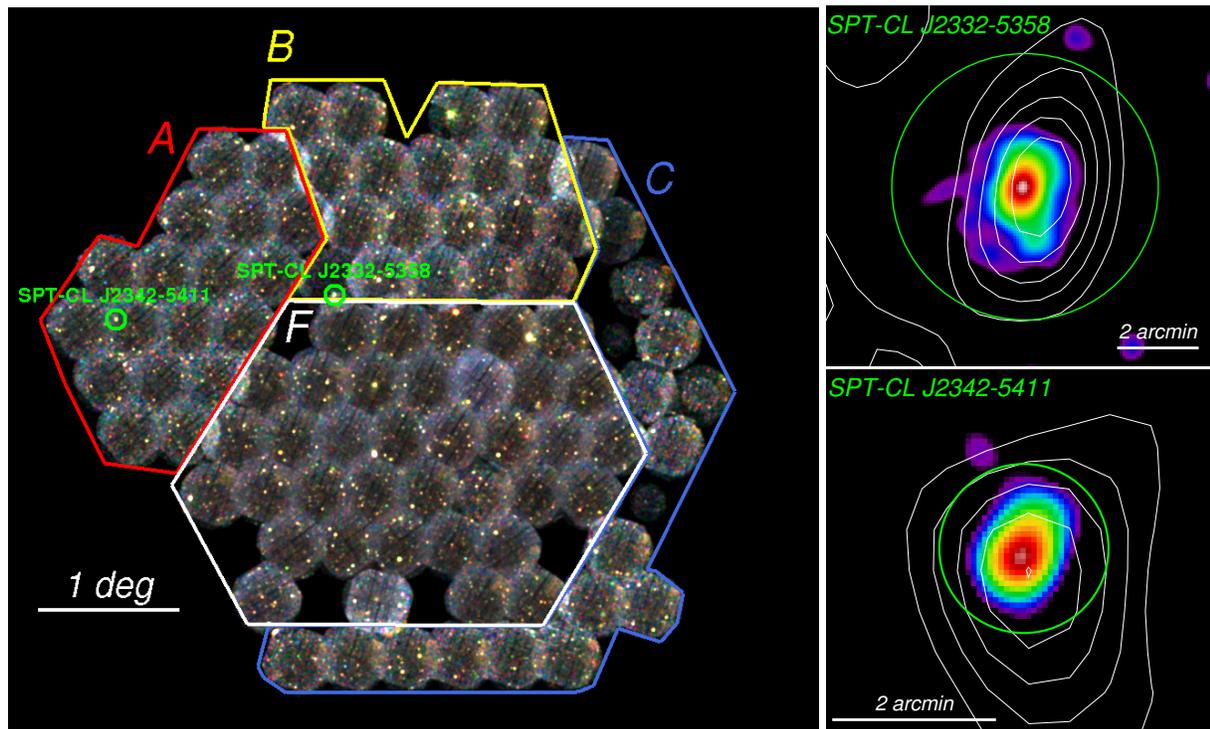
Figure 6.1: **Left:** mosaic mode *XMM-Newton* image of the whole 14 deg^2 survey field. The false color image was constructed from surface brightness images in the $0.3 - 0.5$, $0.5 - 2.0$ and $2.0 - 4.5$ keV bands. Regions A, B, and C mark the three mosaic mode observations, region F the deeper core of the survey consisting of 42 individual pointings. The green circles mark the positions of SPT-CL J2332-5358 and SPT-CL J2342-5411 with a radius equal to r_{plat} (Sect. 6.2.2) in both images. **Right:** $0.5 - 2.0$ keV images of SPT-CL J2332-5358 (top) and SPT-CL J2342-5411 (bottom) with overlaid SZE signal-to-noise contours from the SPT survey (V10).

6.2.1 XMM-Newton mosaic mode observations

The *mosaic mode observation* is a new observation mode of *XMM-Newton* and this is the first instance of its scientific use. Mosaic mode observations were designed to significantly increase the efficiency of observations covering areas larger than the field of view of the telescope. Before the implementation of this mode such observations could only be achieved by consecutive independent single pointings. Each of these individual pointings then required its own instrumental overhead, which particularly for the EPIC PN camera can be a significant part of the total observing time, especially if the required exposure times for the pointings themselves are short.

The mosaic mode observation starts as a standard observation with operational overhead (telescope pointing and guide star acquisition) followed by instrumental overhead, when a charge zero level (i.e. *offset table*) is calculated for the PN camera, which typically amounts to $3 - 4$ ks (MOS cameras are operated with fixed offset tables and their setup is negligible). After the setups are finished, the observation itself starts. In our mosaics, each stable pointing has an exposure of 3.5 ks, followed by a slew to the next field offset by $\sim 23'$. Science data are also collected during

the slew and different from the standard operating mode the observation is not interrupted by a new instrumental setup sequence, but the same offset table is used during the whole mosaic.

Without the mosaic mode, surveys of this kind would practically be unfeasible, with observing efficiency (i.e. the ratio of integration time to total time) around only 50%, compared to $\gtrsim$ 80% efficiency achieved with the present setup. More information on the mosaic mode observations can be found in the *XMM-Newton* User Handbook.[1]

6.2.2 X-ray data analysis

Both SPT-CL J2342-5411 and SPT-CL J2332-5358 were detected in the mosaic observations carried out in December 2009 (mosaic A, OBSID: 0604870301 and mosaic B, OBSID: 0604873401 respectively). We defer a more detailed description of the survey data reduction to a forthcoming publication of the X-ray cluster catalog. Here we summarize the main steps and highlight the differences of treating mosaic eventlists with respect to standard observations.

The EPIC data were processed with the current *XMM-Newton* Standard Analysis System (SAS) version 9.0.0. We calibrated the raw observational data files in a standard way. Events in bad pixels, bad columns and close to the chip gaps were excluded from further analysis. The eventlists were screened for high-background periods caused by soft proton flares following the two-step cleaning method of Pratt and Arnaud (2003), but setting a 3σ limit in both energy bands.

The clean exposure times are 71.9/72.6 ks for PN, and 85.0/88.7 ks for the MOS cameras for the entire mosaic A/B respectively. The beginning of the mosaic sequence B in the PN camera was strongly affected by soft proton flaring, therefore the effective exposure at the SPT-CL J2332-5358 location is only 0.1 ks in PN, while it is 3.1 ks in each MOS camera. The source in addition lies partially on the missing MOS1 CCD#6, yielding a total combined MOS effective exposure of only ∼ 4 ks. Local exposure times for SPT-CL J2342-5411 were ∼ 2.8 ks in PN, ∼ 2.1 ks in MOS1 and ∼ 2.3 ks in MOS2.

As the main source-detection algorithm we utilized the sliding box technique and a maximum likelihood source fitting in their current, improved implementation in the SAS tasks `eboxdetect` and `emldetect`.

Mosaic data of this extent is too extensive to fit into the memory storage during the detection process. Therefore we segmented the mosaic into several overlapping parts, which could be handled by the SAS tasks. Segmenting the mosaic into sky-chunks for source detection is preferable to splitting it into individual stable pointings, because we also wished to include counts gathered during the slews between the pointings and utilize the greater depth in the regions where two neighboring pointings overlap.

The mosaic segments have a typical size of ∼ 1 deg^2 and overlap by $\gtrsim$ 2′ along all borders. This way the input images, exposure, and background maps could be accommodated by the `ebox-` and `emldetect` tasks ran with increased memory buffer (imagebuffersize=2000 flag).

In order to get a reliable measurement of the flux and trace the emission of the clusters as far out as possible, we implemented a refined version of the *growth curve method* (Böhringer et al. 2000). The cumulative source flux as a function of radius (i.e. the growth curves) for the two

---

[1] `xmm.esac.esa.int/external/xmm_user_support/documentation/uhb/XMM_UHB.pdf`

systems are displayed in Fig. 6.2. The total source flux was determined iteratively by fitting a line to the flat part of the background-subtracted growth curve. We define the *plateau radius* (r_{plat}) as the aperture where the growth curve reaches the total flux.

For SPT-CL J2332-5358 we detected source emission out to $r_{plat} = 196''$, with total source flux of $F_{plat}(0.5 - 2.0 \, keV) = 9.38 \pm 0.50 \times 10^{-13} \, erg \, s^{-1} \, cm^{-2}$, corresponding to a total luminosity $L_{plat}(0.5 - 2.0 \, keV) = 2.67 \pm 0.14 \times 10^{44} \, erg \, s^{-1}$. Errors of the flux and luminosity include the Poisson errors and a 5% systematic error in the background estimation.

The X-ray morphology of this cluster agrees well with the SZE signal on the largest scales (Fig. 6.1) and its peak is close to the position of the brightest cluster galaxy (BCG, Fig. 6.4). We detect a significant X-ray extension up to $\sim 1.5'$ SE from the BCG. A detailed characterization of the galaxy distribution and the correlation between X-ray and optical morphology will be given in a forthcoming paper.

For SPT-CL J2342-5411 we found $r_{plat} = 62''$, $F_{plat}(0.5 - 2.0 \, keV) = 5.74 \pm 0.58 \times 10^{-14} \, erg \, s^{-1} \, cm^{-2}$ and a total luminosity $L_{plat}(0.5 - 2.0 \, keV) = 2.84 \pm 0.3 \times 10^{44} \, erg \, s^{-1}$ (Fig. 6.2, right).

X-ray spectroscopy

The available survey data,[2] although modest in exposure, allow us to get a first temperature estimate for SPT-CL J2332-5358.

In order to determine a suitable aperture for spectroscopic measurements, we created a wavelet reconstruction (Vikhlinin et al. 1998b) of the combined 0.5-2.0 keV band image. We found that a circular aperture with 70" radius well encloses the region where the cluster emission is registered at $\geq 5\sigma$ significance.

A background spectrum was extracted from an annulus concentric with the source and spanning the radial distance from $200''$ to $400''$. The inner radius was selected based on the growth-curve analysis as the radius where cluster emission is no longer observable (Fig. 6.2, left). The outer radius is constrained by the field of view. We excised all detected point sources from each extracted spectrum after a visual check.

We fitted the spectrum with a single temperature MeKaL model, fixing the column density to the galactic value $n_H = 1.62 \times 10^{20} \, cm^{-2}$ (Dickey and Lockman 1990), metal abundance to $Z = 0.3 \, Z_\odot$ and redshift to $z = 0.32$ (photometric, High et al. (2010), consistent with Menanteau et al. (2010)). To avoid biases stemming from analyzing low-count spectra, we used a minimally binned spectrum (≥ 1 cts/bin) and C-statistics.

The fitted temperature is $T = 9.3^{+3.3}_{-1.9} \, keV$ (1σ errors) for the joint fit from all three cameras (Fig. 6.3, left). In order to check for possible systematics in the background subtraction, we also fitted the spectrum using background spectra extracted from a completely independent circular region (on different chips than the source but roughly at the same off-axis angle). The test background gives a consistent result, $T = 9.4^{+3.5}_{-1.9} \, keV$.

---

[2]Due to current limitations of the `backscale` task, used to calculate the area scaling factors of the spectra, we omitted the slew part of the survey for spectroscopical purposes and filtered from the mosaic eventlist only events detected during the relevant *stable pointing* period (the slew part would contribute only a few tens of counts in this case).

Table 6.1: Basic X-ray parameters of SPT-CL J2332-5358 and SPT-CL J2342-5411. Flux and luminosity errors include the Poisson errors and a 5% systematic error in the background estimation. Errors of parameters obtained from scaling relations include the measurement errors of the luminosity and temperature, respectively, and the intrinsic scatter of the scaling relations. We assume self-similar evolution for all the scaling relations and no evolution of their intrinsic scatters (see Sect. 6.2.2).

parameter	SPT-CL J2332-5358	SPT-CL J2342-5411	units
α (J2000)[a]	$23^h\,32^m\,26.7^s$	$23^h\,42^m\,45.8^s$	
δ (J2000)[a]	$-53°\,58'\;20.4''$	$-54°\,10'\;59.2''$	
photometric redshift	0.32^b	1.08^b	
F_{500} [$0.5-2.0$ keV]	9.52 ± 0.51	0.58 ± 0.06	10^{-13} erg cm^{-2} s^{-1}
L_{500} [$0.5-2.0$ keV]	2.71 ± 0.15	2.86 ± 0.29	10^{44} erg s^{-1}
T_{500}	9.3 ± 2.6^c	4.5 ± 1.3^f	keV
r_{500}	1.3 ± 0.2^d	0.6 ± 0.1^d	Mpc
M_{500}	8.8 ± 3.8^d	1.9 ± 0.8^d	10^{14} M$_\odot$
$Y_{X,500}$	11.6 ± 9.7^e	1.1 ± 0.7^g	10^{14} M$_\odot$ keV
r_{200}	2.0 ± 0.3^d	0.9 ± 0.1^d	Mpc
M_{200}	12.4 ± 5.4^d	2.7 ± 1.2^d	10^{14} M$_\odot$

[a] X-ray coordinates based on a maximum-likelihood fit of a PSF-folded beta model to the surface brightness distribution; [b] High et al. (2010); [c] Spectroscopic temperature (Sect. 6.2.2), error bars averaged, assuming isothermality; [d] M−T relation from Arnaud et al. (2005), using relations for $T > 3.5$ keV, self-similar evolution, radii calculated analytically from the mass estimates; [e] $M_{500}-Y_X$ relation (Arnaud et al. 2007). [f] L−T relation from Pratt et al. (2009), self-similar evolution, relation for the $0.5-2$ keV luminosity, BCES orthogonal fit. [g] L−Y_X relation from Pratt et al. (2009), self-similar evolution, relation for the $0.5-2$ keV luminosity, BCES orthogonal fit. Y_X, the X-ray analogue to the Comptonization parameter Y, is the product of the gas mass and temperature (e.g. Kravtsov et al. 2006).

Based on our temperature measurement we estimated several important physical parameters (Table 6.1), including mass in r_{500} and r_{200} apertures from the M−T scaling relation, assuming self-similar evolution. For parameters obtained from scaling relations we included the measurement errors of the luminosity and temperature and the intrinsic scatter of the scaling relations. We used a beta model to extrapolate the observed flux and luminosity out to r_{500} (because the estimated r_{500} value is higher than the measured r_{plat}). This extrapolation is negligible ($\sim 1.5\%$).

The available photon statistics for SPT-CL J2342-5411 is much lower and allows us to carry out a tentative analysis only. Following the previously described procedure, we extracted the source spectrum from a $45''$ region and the background spectrum from a concentric annulus with $100''$ inner and $200''$ outer radius. Fixing the column density to the galactic value $n_H = 1.86 \times 10^{20}$ cm^{-2}, metal abundance to $Z = 0.3$ Z$_\odot$ and redshift to $z = 1.08$ (photometric, High et al. 2010), we found that the spectrum is consistent with a single temperature MeKaL model (Fig. 6.3, right). The temperature is only weakly constrained, $T = 6.7^{+5.2}_{-2.4}$ keV, and therefore we opted for the use of luminosity-based scaling relations (L−T and L−Y_X) to estimate the physical parameters of the system (Table 6.1). The evolution of the scaling relations and their

intrinsic scatter is currently not firmly established out to z ∼ 1. We assumed self-similar evolution of the scaling relations and no evolution of their intrinsic scatters. The error from these assumptions for SPT-CL J2342-5411 is expected to be smaller than the quoted measurement errors.

6.3 Discussion and conclusions

We have presented first results from the XMM-BCS cluster survey, providing X-ray detections of two SZE-selected systems, SPT-CL J2332-5358 and SPT-CL J2342-5411. The X-ray analysis is based on mosaic mode *XMM-Newton* observations - the first time observations of this kind have been carried out.

The system SPT-CL J2332-5358 ranks among the hottest known clusters (T = 9.3 keV) and is exceptionally massive ($M_{200} \gtrsim 1 \times 10^{15}$ $M_\odot$). Our mass estimate is in excellent agreement with the *ROSAT*-based result of Menanteau et al. (2010). The SZE-inferred mass reported by V10 is $M_{500} = 5.20 \pm 0.86 \pm 0.83 \times 10^{14}$ $M_\odot$, where the error bars represent the statistical and systematic uncertainties, both at 68% confidence. They note that this mass is biased low by a bright dusty point source identified in the 220 GHz SPT data. A preliminary analysis indicates that this point source decreases the SZE mass estimate by a factor of ∼1.5. This would imply a corrected SZE mass estimate of $M_{500} = 7.8 \pm 1.3 \pm 1.3 \times 10^{14}$ $M_\odot$, which agrees well with our X-ray estimate.

This is an initial study of the system SPT-CL J2332-5358. Other aspects of the system are investigated in forthcoming papers: **1)** using a deeper XMM observation Andersson et al. (in prep.) perform a detailed comparison of the X-ray and SZE properties of this cluster, **2)** a characterization of the galaxy population and morphology will be addressed in Song et al. (in prep.).

The source SPT-CL J2342-5411 belongs to the one of the most distant known clusters ($z = 1.08$) with X-ray and SZE detections. The discovery of such a distant system in both SZE and X-ray surveys demonstrates the great potential of the two observational approaches for cosmological and cluster evolution studies. The estimated mass for this system, $M_{500} = 1.9 \pm 0.8 \times 10^{14}$ $M_\odot$, is consistent with the SZE mass $M_{500} = 2.66 \pm 0.50 \pm 0.37 \times 10^{14}$ $M_\odot$ (V10).

SPT-CL J2332-5358 and SPT-CL J2342-5411 are the first galaxy clusters discovered independently in X-ray, SZE and optical surveys. These clusters exemplify the promise of multi-wavelength cluster surveys and give a glimpse of the possible synergies of current and future large-scale survey experiments, including SPT, *Planck*, *eRosita*, and the Dark Energy Survey.

6.4   Appendix

The appendix provides additional information concerning the X-ray analysis of SPT-CL J2332-5358 and SPT-CL J2342-5411.
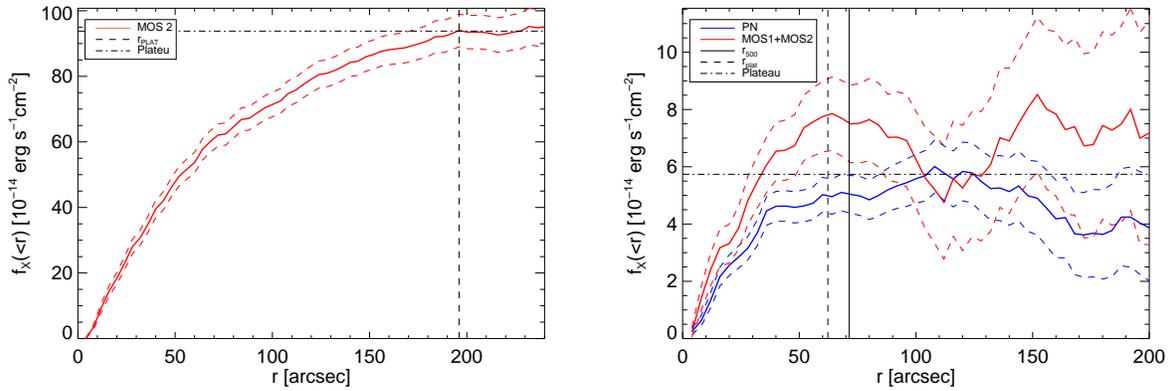
Figure 6.2: **Left:** The growth curve of SPT-CL J2332-5358: red curve shows the integrated flux as a function of outer integration radius for the MOS2 camera in the $0.5 - 2.0$ keV band. Source flux is detected out to $196''$ (r_{plat}, dashed line). The total measured flux in this aperture and band is $F_{plat} = 9.4 \pm 0.5 \times 10^{-13}$ erg s^{-1} cm^{-2} (horizontal dot-dashed level). We omitted the use of the PN and MOS1 camera for the growth curve analysis (see Sect. 6.2.2). **Right:** The growth curve of SPT-CL J2342-5411: red curve shows the integrated flux as a function of outer integration radius for the joint MOS1 and MOS2 cameras ($0.5 - 2.0$ keV band), blue curve for the PN camera. Source flux is detected out to $r_{plat} = 62''$ (dashed line). The total measured flux, estimated as the weighted average of the MOS and PN plateau fluxes, is $F_{plat} = 5.7 \pm 0.6 \times 10^{-14}$ erg s^{-1} cm^{-2} (dot-dashed level). In both panels, error bars on the growth curve indicate the Poisson error of the flux measurement including a 5% systematic error in the background estimation.
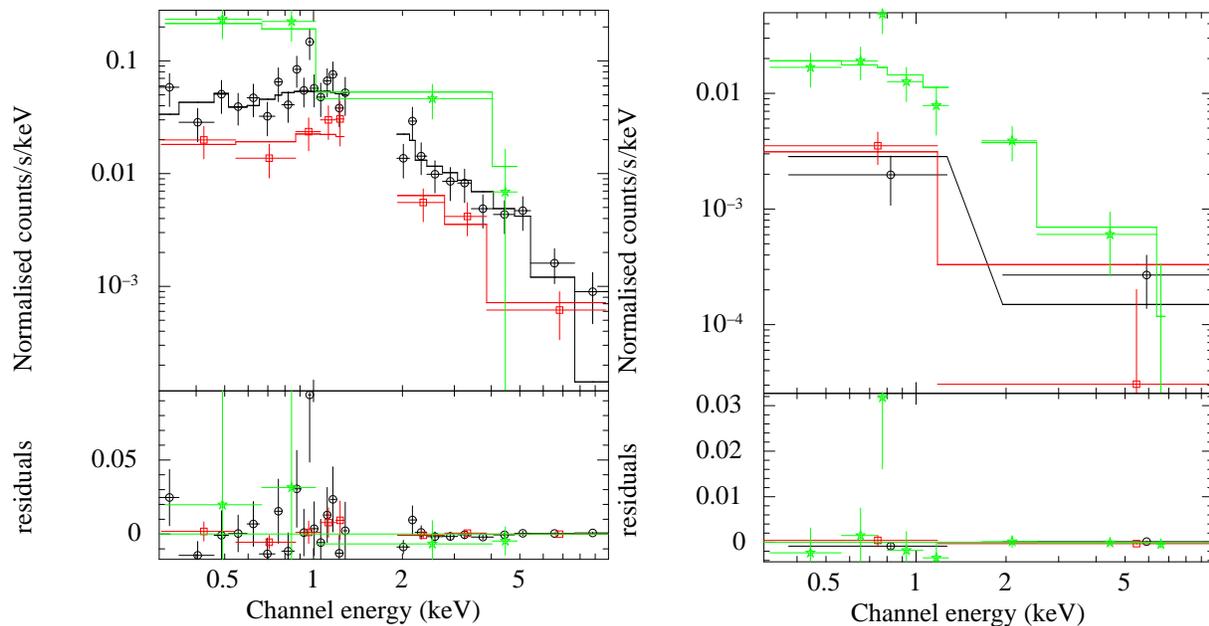
Figure 6.3: **Left:** *XMM-Newton* X-ray spectrum of SPT-CL J2332-5358 fitted with a single temperature MeKaL model which gives T = $9.3^{+3.3}_{-1.9}$ keV. The column density is fixed to the galactic value $n_{\mathrm{H}} = 1.62 \times 10^{20}$ cm^{-2} (Dickey and Lockman 1990), the metal abundance to Z = 0.3 $Z_{\odot}$ and the redshift to $z = 0.32$ (photometric). **Right:** *XMM-Newton* X-ray spectrum of SPT-CL J2342-5411. The available low-count spectrum (displayed for completeness) allows us to draw only tentative conclusions. The spectrum is consistent with a single temperature MeKaL model, with the temperature only weakly constrained to T = $6.7^{+5.2}_{-2.4}$ keV. The column density is fixed to the galactic value $n_{\mathrm{H}} = 1.86 \times 10^{20}$ cm^{-2} (Dickey and Lockman 1990), the metal abundance to Z = 0.3 $Z_{\odot}$ and the redshift to $z = 1.08$ (photometric). The spectra were binned only for display purposes, the fit was carried out with $\geq$ 1 cts/bin binning and C-statistic. Red: MOS1, black: MOS2, green: PN. See Sect. 6.2.2 for details.
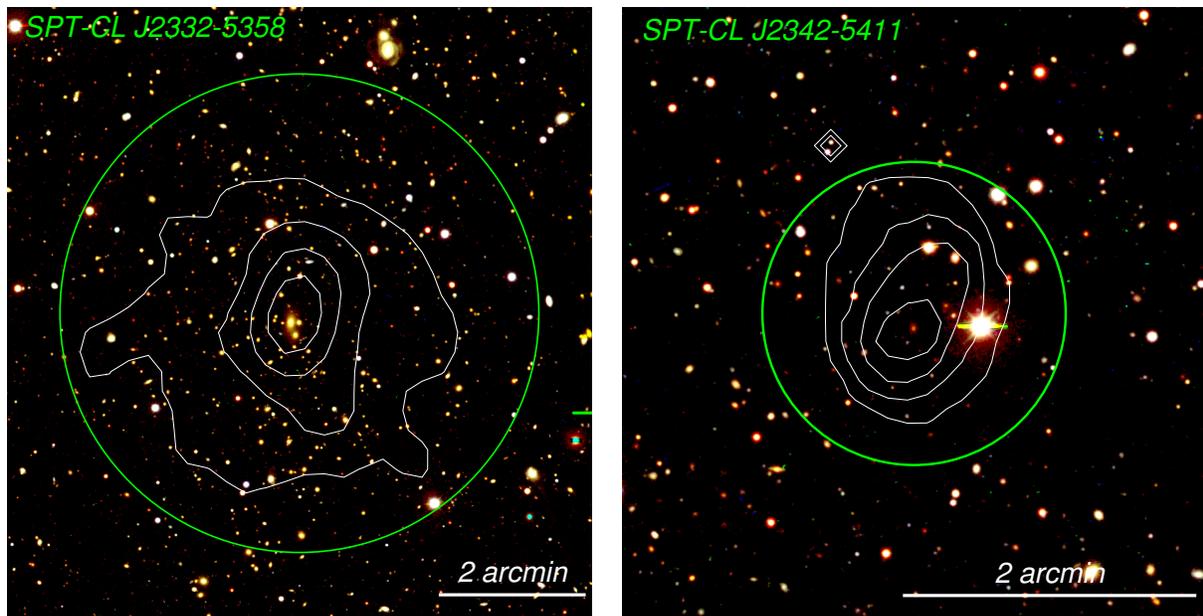
Figure 6.4: **Left:** Color image of SPT-CL J2332-5358 (photo $-$ z $= 0.32$). **Right:** Color image of SPT-CL J2342-5411 (photo $-$ z $= 1.08$). Both images were obtained from the Blanco Cosmology Survey imaging in the *gri* bands. X-ray contours are overlaid in white. Green circles show the estimated r_{plat} (see Sect. 6.2.2). Both clusters have a large BCG (brightest cluster galaxy) within few arcseconds ($\lesssim 10''$) from the X-ray emission peak.

Chapter 7

Exploring the galaxy cluster-group transition regime at high redshifts

Physical properties of two newly detected $z > 1$ systems[1]

R. Šuhada, R. Fassbender, A. Nastasi, H. Böhringer, A. de Hoon, D. Pierini, J. S. Santos, P. Rosati, M. Mühlegger, H. Quintana, A. D. Schwope, G. Lamer, J. Kohnert and G. W. Pratt

Abstract

Context: Multi-wavelength surveys for clusters of galaxies are opening a window on the elusive high-redshift ($z > 1$) cluster population. Well controlled statistical samples of distant clusters will enable us to answer questions about their cosmological context, early assembly phases and the thermodynamical evolution of the intracluster medium.

Aims: We report on the detection of two $z > 1$ systems, XMMU J0302.2-0001 and XMMU J1532.2-0836, as part of the XMM-*Newton* Distant Cluster Project (XDCP) sample. We investigate the nature of the sources, measure their spectroscopic redshift and determine their basic physical parameters.

Methods: The results of the present paper are based on the analysis of XMM-*Newton* archival data, optical/near-infrared imaging and deep optical follow-up spectroscopy of the clusters.

Results: We confirm the X-ray source XMMU J0302.2-0001 as a gravitationally bound, bona fide cluster of galaxies at spectroscopic redshift $z = 1.185$. We estimate its M_{500} mass to $(1.6 \pm 0.3) \times 10^{14}$ $M_\odot$ from its measured X-ray luminosity. This ranks the cluster among intermediate mass system. In the case of XMMU J1532.2-0836 we find the X-ray detection to be coincident with a dynamically bound system of galaxies at $z = 1.358$. Optical spectroscopy reveals the presence of a central active galactic nucleus, which can be a dominant source of the

---

[1]Based on observations obtained with ESO Telescopes at the Paranal Observatory under program ID 080.A-0659 and 081.A-0312, observations collected at the Centro Astrnómico Hispano Alemán (CAHA) at Calar Alto, Spain operated jointly by the Max-Planck Institut für Astronomie and the Instituto de Astrofísica de Andalucía (CSIC). X-ray observations were obtained by XMM-*Newton*.

detected X-ray emission from this system. We provide upper limits of X-ray parameters for the system and discuss cluster identification challenges in the high-redshift low-mass cluster regime. A third, intermediate redshift ($z = 0.647$) cluster, XMMU J0302.1-0000, is serendipitously detected in the same field as XMMU J0302.2-0001. We provide its analysis as well.

7.1   Introduction

The number of known galaxy cluster detections at high redshift ($z \gtrsim 1$) is constantly growing (see Appendix 7.5.2). Recently we have witnessed the detection of the first spectroscopically confirmed clusters at redshift > 1.6 by Papovich et al. (2010) and Tanaka et al. (2010). This distance record has been however soon overtaken by the cluster XMMU J105324.7+572348 with $z = 1.753$ (Henry et al. 2010). Finally, Gobat et al. (2011) reported on the detection of a remarkable structure which is consistent with a low mass cluster at redshift 2.07. The nature of another potentially very distant system, JKCS041 detected by Andreon et al. (2009) at a photometric redshift of 1.9, was contested by Bielby et al. (2010). Recently obtained deep z' and J imaging, however seems to confirm the presence of a cluster at $z = 2.2$ (based on a red sequence redshift estimation).

For the first time we can start constructing sizable cluster samples at $z > 1$ as a consequence of several important factors. First, there is progress in cluster search methods, both classical such as X-ray (Mullis et al. 2005; Stanford et al. 2006; Henry et al. 2010; Fassbender et al. 2011a, Nastasi et al., in prep.) and optical/mid-infrared surveys (Gladders and Yee 2005; Stanford et al. 2005; Gobat et al. 2011; Papovich et al. 2010) as well as new selection methods like surveys utilising the Sunyaev-Zel'dovich effect (SZE, Planck Collaboration et al. 2011a; Williamson et al. 2011; Vanderlinde et al. 2010; Marriage et al. 2010).

The second essential prerequisite is the availability of deep spectroscopic data, required to the confirm the cluster candidates as genuine gravitationally bound systems and to estimate their redshifts. This typically requires considerable effort and exposure times, and therefore many of the current crop of distant clusters are the results of observational campaigns spanning several years.

In addition, at $z > 1.5$ we are also nearing to the edge of capabilities of even the largest optical spectroscopic instruments, since at these redshifts the 4 000 Å-break (an important feature to anchor the redshift of passive galaxies) is redshifted beyond 10 000 Å, towards the tails of the sensitivity curves of current spectrographs, where the fringing contamination is dominant and significantly decreases the signal-to-noise ratio achievable in a given observation. Fortunately, near-infrared spectroscopy is able to overcome this problem (e.g. Tanaka et al. 2010). Existing (e.g. MOIRCS on the Subaru telescope and LUCIFER at the Large Binocular Telescope) and upcoming (KMOS at the VLT) instruments will soon be able to provide confirmation for new high redshift clusters with a much higher efficiency than the optical spectrographs.

Even though studying high redshift systems is a truly daunting task, the effort is rewarded by gaining a direct view of the earliest assembly epochs of the most massive Dark Matter (DM) halos today, their gas content - the intracluster medium (ICM) - and their galaxy populations. Since the properties of the cluster population are intrinsically connected to the underlying cosmology,

they provide a sensitive test of the cosmological parameters.

The high-mass end of the cluster mass function at high-redshift provides the best leverage when constraining cosmological parameters through their effect on the distribution and growth of the large scale structure. Since massive distant clusters are rare, this regime can be effectively probed only by surveys which are able to cover large sky areas (and hence large survey volumes) such as the SZE surveys. The selection function of these surveys is (almost) independent of redshifts and their sensitivity is limited to very massive clusters with minimal mass $3-5 \times 10^{14} \, M_\odot$ (Vanderlinde et al. 2010; Williamson et al. 2011; Marriage et al. 2010).

However, the majority of the cluster population lies below this mass threshold. Therefore, if we want to understand the thermodynamical evolution of the ICM and the evolution of the galaxy population, we have to look at lower mass systems down to the group regime. For the purpose of this paper we will consider the cluster-group transition regime to be around $\sim 1 \times 10^{14} \, M_\odot$. This threshold region can be probed by X-ray surveys, but it is at the very limit of feasibility of contemporary X-ray surveys (joint X-ray and near-infrared detections can reach slightly lower limiting masses, e.g. Finoguenov et al. 2010). Accessing this threshold population will, however, allow us to directly calibrate the mass scaling relations for less massive systems and study potential mass-dependent effects on the evolution of the galaxy population of the clusters.

Already a simple consideration from the virial theorem (Kaiser 1986) predicts a tight link between the ICM's properties (luminosity, temperature, gas mass) and the total mass (i.e. including DM). These quantities are thus not only of interest from the point of view of characterising the physical conditions of a given cluster, but also as an important observational input for cosmological studies. While the scaling relations of nearby clusters are fairly well known (e.g. Pratt et al. 2009; Arnaud et al. 2005), the evolution of these relations is only starting to be explored at redshifts $z \gtrsim 0.5 - 0.7$ (Vikhlinin et al. 2009b; Pacaud et al. 2007). The $z > 1$ regime is still practically unexplored.

The redshift range $z = 1 - 2$ is a transition period also for the galaxy population of clusters. Local clusters exhibit typically well-defined red-sequences populated by passively evolving early-type galaxies. While similar red sequences are found also in some of the high redshift clusters, e.g. the very massive cluster XMMU J2235.3-2557 (Strazzullo et al. 2010; Rosati et al. 2009), we are finding more and more cases, where star-formation is still ongoing (Fassbender et al. 2011b; Hayashi et al. 2010; Hilton et al. 2010).

Sizable, well controlled cluster samples at high redshift are thus important to address many questions about the cluster population as a whole, but also about the underlying cosmology. In this paper we provide first details on two new, X-ray selected clusters at $z > 1$. In Sect. 7.2 we describe their detection and follow-up observations (imaging and spectroscopy). Optical properties are summarized in Sect. 7.2.2 and the X-ray analysis in Sect. 7.2.3. We discuss the results and draw conclusions in Sect. 7.3 and 7.4, respectively. The analysis of a third, intermediate redshift cluster ($z = 0.647$), serendipitously detected together with XMMU J0302.2-0001, is provided in Appendix 7.5.1.

Throughout the article, we adopt a ΛCDM cosmology with $(\Omega_\Lambda, \Omega_M, w, H_0) = (0.7, 0.3, -1, 70$ km s^{-1} Mpc^{-1}). Physical parameters are estimated within an aperture corresponding to a factor 500 overdensity with respect to the *critical* density of the Universe at the cluster redshift.

Table 7.1: Observation log of the X-ray coverage of XMMU J0302.2-0001 and XMMU J1532.2-0836. The quoted exposure times are net clean times. MOS1 and MOS2 exposure times are averaged. The off-axis angle for the XMM-*Newton* observations is an average angle from all three detectors.

Cluster	Instrument	OBSID	Exp. time (PN/MOS) [ks]	Off-axis angle
XMMU J0302.2-0001	XMM	0041170101	36.4/46.2	10.9′
XMMU J1532.2-0836	XMM	0100240701	13.2/17.4	5.0′
XMMU J1532.2-0836	XMM	0100240801	19.4/25.8[†]	6.1′

[†] This observation is heavily contaminated by quiescent proton flaring and used only for systematics check (Sect. 7.2.3 and Sect. 7.3.2).

7.2   Observations and data analysis

The analysis of the presented clusters is based on archival, medium-deep X-ray observations and optical/near-infrared data (both imaging and spectroscopic) collected in a follow-up campaign. All observations are summarized in Tables 7.1 and 7.2.

7.2.1   Initial X-ray detection with XMM-*Newton*

Both XMMU J0302.2-0001 and XMMU J1532.2-0836 were detected as extended sources as part of the XMM-*Newton* Distant Cluster Project (XDCP) sample. The XDCP consists of 470 XMM-*Newton* archival fields with a total non-overlapping area close to 80 deg^2. The data was obtained from the XMM data archive.[2] The initial cluster detection was performed with the XMM-*Newton* science analysis system SAS v6.5 utilising a sliding box detection and a maximum likelihood source fitting.[3] Details of the source detection pipeline can be found in Fassbender (2008).

For the purposes of this paper we re-analyzed the observations containing both sources with the current updated version of SAS (v10.0). The details of the observations are summarized in Table 7.1.

XMMU J0302.2-0001

XMMU J0302.2-0001 was detected in the XMM-*Newton* observation OBSID: 0041170101 with 39.3 ks PN exposure time and 50.4 ks in either MOS camera. We identified and excised a time period strongly affected by soft proton flaring in a two-step cleaning process yielding 36.4 ks PN and 46.2 ks MOS clean exposures. We find no residual quiescent soft proton contamination in any of the detectors.

The source is detected at the coordinates $(\alpha, \delta) = (03^h\,02^m\,11.9^s, -00°\,01'\,34.3'')$ (J2000) at a relatively high off-axis angle of 11′ with very high detection and extent significance (both

---

[2]`xmm.esac.esa.int/xsa/`
[3]SAS tasks `eboxdetect` and `emldetect`.

$\gtrsim 10\sigma$). The beta model core radius is $r_C = 14.4''$, based on a fit with a fixed $\beta = 2/3$. In an aperture of $1'$ we detected 130 source counts in PN and 80 in the combined MOS detectors.

XMMU J1532.2-0836

The second X-ray source, XMMU J1532.2-0836, is found in two XMM-*Newton* observations (OBSID: 0100240701 and 0100240801) at coordinates $(\alpha, \delta) = (15^h 32^m 13.0^s\ -08° 36'\ 56.9'')$. The off-axis angles are in both observations similar, $\sim 5' - 6'$. Pointing 0100240801 is slightly deeper with 19.4/25.7 ks clean time in PN/MOS compared to 13.2/17.3 ks of 0100240701. Unfortunately, after inspecting the light curve of observation 0100240801 we find a steady decline of the count rate along the whole duration of the observation - a clear indication of a residual quiescent (i.e. non-flaring) soft proton contamination. To confirm this suspicion we use a diagnostic test suggested by De Luca and Molendi (2004). By looking at the count rate ratio inside and outside the field of view of each detector in the $8 - 10$ keV band, we find a $\sim 50\%$ soft background enhancement compared to the normal level in PN and more than 90% enhancement in both MOS cameras. Observation 0100240701 is found to be completely uncontaminated. In both observations we detect below 50 source counts, which is reflected in the uncertainty of derived parameters.

The system was detected at a $\sim 5\sigma$ significance level, however it was classified as a point source in observation 0100240701. It is only in the slightly deeper (but contaminated) observation, where the source is flagged as extended with a 2σ significance and beta model core radius of $r_C \simeq 8''$. Therefore, in the source detection step the extent is established only tentatively. We describe an in-depth investigation of the extent significance in Sect. 7.3.2, where we conclude that the currently available data is not sufficient to confirm the extended nature of the source with any statistical significance. All quoted values for XMMU J1532.2-0836 unless noted otherwise will come from the analysis of the uncontaminated field 0100240701.

XMMU J0302.1-0000

We also identified an additional cluster candidate in the first XMM-*Newton* observation (OBSID: 0041170101) roughly $2'$ from XMMU J0302.2-0001. We obtained spectroscopy for member galaxies for both clusters simultaneously in the same FORS2 pointing. This allowed us to confirm also this second source, XMMU J0302.1-0000, as a genuine cluster of galaxies at intermediate redshift $z \approx 0.65$. In the following we will focus on the two $z > 1$ clusters and we provide details for XMMU J0302.1-0000 in Appendix 7.5.1.

7.2.2 Optical/Near-infrared observations

In addition to the archival X-ray data, we have obtained optical/near-infrared imaging and deep optical spectroscopy for the clusters. In this section we provide the details of the available data and its analysis.

Follow-up imaging and optical properties

The optical/near-infrared imaging data used in this work is summarized in Table 7.2. This data was obtained prior to spectroscopy to allow pre-selection of the cluster candidates. Here we use it to investigate the basic optical properties of the cluster galaxy populations.

XMMU J0302.2-0001

In order to identify the optical counterparts of XMMU J0302.2-0001, we carried out medium deep H and z-band imaging data with the prime-focus wide-field (field-of-view of 15.4′ on the side) near-infrared OMEGA2000 camera (Bailer-Jones et al. 2000) at the 3.5m Calar Alto telescope. The observations were performed on 3rd and 4th January (H and z band respectively) 2006 under clear conditions (calibration with on-chip 2MASS stars was done in photometric conditions). We reduced the data with the designated OMEGA2000 NIR pipeline (Fassbender 2008). The individually reduced frames are visually checked and co-added. The total exposure time of the final stacked images is 50 min in H band (75 co-added frames) and 23 min in z band (23 frames). We reach a 50% completeness limit (Vega) of $H_{lim} = 21.0$ mag and $z_{lim} = 23.0$ mag with FWHM(H)= 1.34″ and FWHM(z)= 1.49″.

The photometry catalog was obtained by running `SExtractor` (Bertin and Arnouts 1996) in dual image mode with the unsmoothed H-band image used as the detection image. We then cross-checked the catalog with available SDSS photometry.

The VLT/FORS2 imaging (Prog. ID: 079.A-0119(A)) was carried out in the R-band at a fairly good seeing of ∼ 0.7″ and photometric conditions. With total clean exposure time of 20 min, it is a valuable complement to the Calar Alto imaging data. For the reduction of the pre-imaging data we followed the same procedure as Schwope et al. (2010) and Fassbender et al. (2011a).

In Fig. 7.1 (top left) we display a pseudo-color image of XMMU J0302.2-0001 in the H/z/R bands (red/green/blue). A population of red galaxies ($2.3 < z−H \leq 3.0$) is found to be coincident with the X-ray source. We show the z−H vs. H color-magnitude diagram (CMD) of XMMU J0302.2-0001 in Fig. 7.2 (left). We also overplot the synthetic z−H color of a Simple Stellar Population (SSP) model (formation redshift z_f=5, solar metallicity) for the cluster's redshift (red dashed line). We find around 10 red galaxies within 30″ from the X-ray center with colors well matching the model prediction. The overdensity of red galaxies compared to the field is at a ∼ 25σ significance level - one of the largest known overdensities at $z > 1$.

The brightest cluster galaxy (BCG) is coincident with the X-ray emission peak and seems to be undergoing merging activity (see Fig. 7.1, bottom left). The very bright blue object (H ≈ 17 mag) at the cluster redshift (but beyond 30″ from its center) is an AGN with redshift from SDSS (Sect. 7.3.4). Galaxy ID: 6 (in Table 7.3) also has a bluer color, which is consistent with the presence of a very strong [O ɪɪ] emission line (see Fig. 7.3).

XMMU J1532.2-0836

The imaging in the case of XMMU J1532.2-0836 consists of R and z band imaging obtained with the VLT/FORS2 instrument (Prog. ID: 078.A-0265) and seeing of 0.6″ and 0.8″, respectively.

The total exposure time is 16 min in R band and 8 min in z. The final R-z vs. z color-magnitude diagram of XMMU J1532.2-0836 is displayed in Fig. 7.2 (right). The dashed red line shows the R$-$z color of a spectro-photometric sequence (SSP model, z_f=5, solar metallicity) at the redshift of the cluster. Two spectroscopic members have colors consistent with this simple model.

As can be noted from the figure, these two galaxies are very close to the completeness limit of our data and we can thus see only the very brightest end of the galaxy population. The third galaxy (ID: 3) has bluer colors and a strong [O II] emission line. We also detect [Ne III]λ3869 Å and [Ne v]λ3426 Å emission lines. It is therefore likely that this galaxy harbours an obscured AGN (see Sect. 7.3.2).

We have designated the brightest spectroscopic member as the cluster candidate's BCG (ID: 1), with $\sim$ 5.5$''$ distance from the cluster center. This galaxy is relatively faint ($z^* - 0.4$). The brightest galaxy lying exactly at the predicted SSP color is a spectroscopically confirmed foreground galaxy. However, there is one galaxy slightly brighter than the marked BCG within 30$''$ from the X-ray center - which could also be a BCG candidate. Unfortunately, we do not have spectroscopy for this source. Compared to galaxy ID: 1 it has a slightly bluer color than the SSP prediction and a slightly larger cluster-centric distance, i.e. ID: 1 still remains the better BCG candidate.

Table 7.2: Summary of the optical/near-infrared observations of XMMU J0302.2-0001 and XMMU J1532.2-0836 analysed in this work. The grism column applies for spectroscopic observations, the band for imaging. Exposure times and seeing are reported for each band individually.

Cluster	Data	Exposure Time	Prog. ID	Date	Grism/Band	Seeing
XMMU J0302.2-0001	VLT/FORS2/ MXU spec.	3h (8×1308 sec)	080.A-0659	2008 Jun 6	300 I	$1.03'' - 1.26''$
XMMU J1532.2-0836	VLT/FORS2/ MXU spec.	3h (8×1308 sec)	081.A-0312	2008 Apr 4, 7	300 I	$0.79'' - 1.36''$
XMMU J0302.2-0001	CAHA 3.6m[†]/Omega2000 imag.	50 min/23 min		2006 Jan 3, 4	H/z	$1.34''/1.49''$
XMMU J0302.2-0001	VLT/FORS2 imag.	20 min	079.A-0119	2007 Feb 23	R	$0.7''$
XMMU J1532.2-0836	VLT/FORS2 imag.	16 min/8 min	078.A-0265	2008 Apr 4, 7	R/z	$0.6''/0.8''$

[†] Calar Alto Observatory.
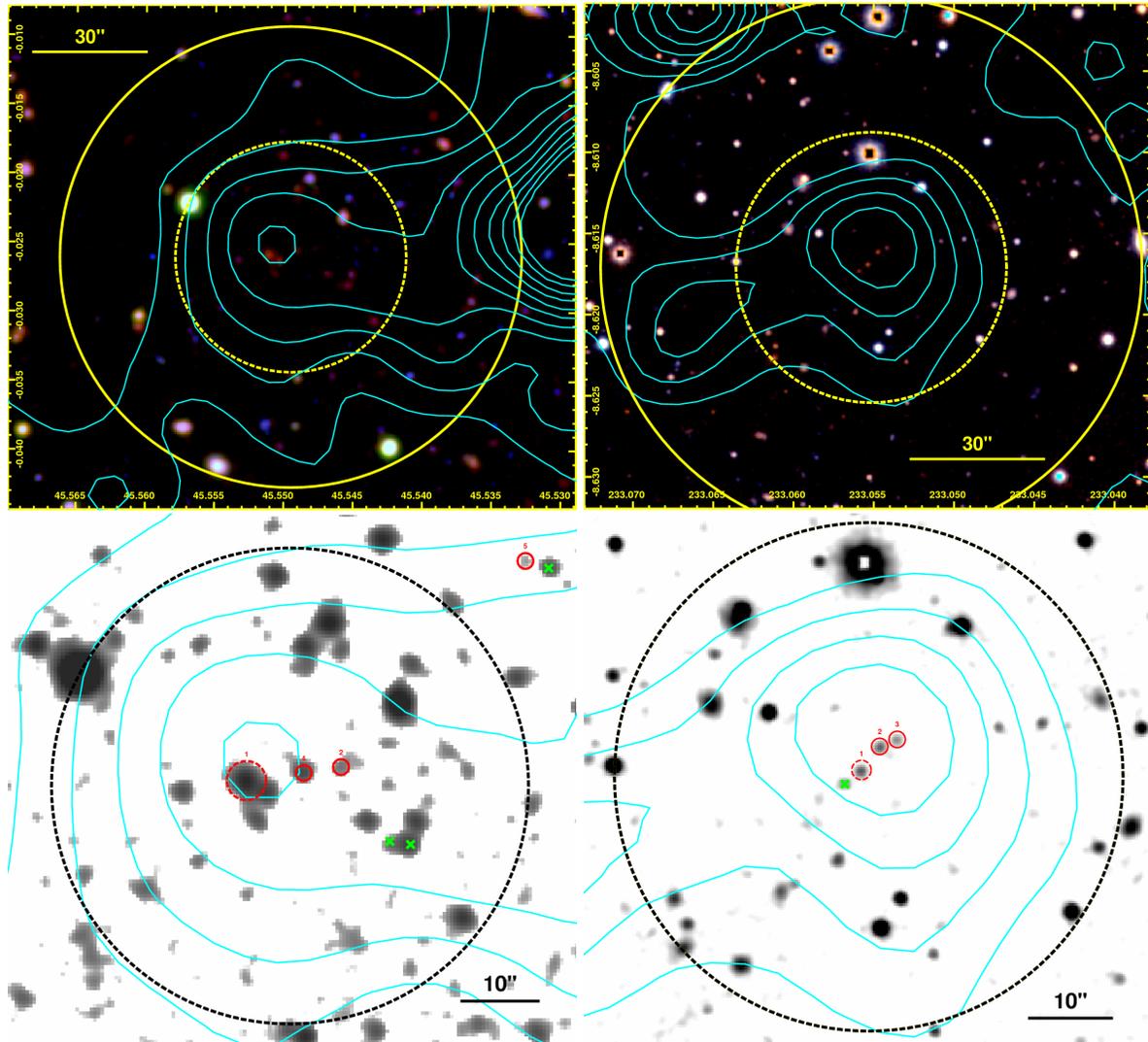
Figure 7.1: Optical/Near-Infrared images of the clusters. **Top:** Pseudo-color image of the clusters XMMU J0302.2-0001 (left, red channel: H band, green: z, blue: R) XMMU J1532.2-0836 (right, red channel: z, green: z+R, blue: R). Adaptively smoothed X-ray contours are overlaid in cyan. Solid/dashed circles mark a 60″/30″ radius region centered on the X-ray detection. An associated overdensity of red galaxies is apparent in both cases. **Bottom:** A high contrast zoom on the central regions of the clusters (dashed circle has a 30″ radius). XMMU J0302.2-0001 is displayed in the H band whereas XMMU J1532.2-0836 in the z band. Red circles mark the confirmed spectroscopic members with properties listed in Table 7.3 and spectra displayed in Fig. 7.3. The BCG is marked with a dashed red circle (ID 1 for both clusters). Spectroscopically confirmed foreground galaxies are indicated by green crosses.

Table 7.3: Spectroscopic redshifts of cluster member galaxies. The last column lists the main detected spectral features. Forbidden lines are detected in emission, the rest in absorption. The distance from the X-ray center in arcseconds is given as the d_X parameter.

ID	α (J2000)	δ (J2000)	z_{spec}	d_X [$''$]	Features
XMMU J0302.2-0001					
1 (BCG)	03:02:12.260	-00:01:33.87	1.1848 ± 0.0007	5.4	[O II]†, Ca-K, 4 000 Å break
2	03:02:11.462	-00:01:32.01	1.1735 ± 0.0007	7.0	Mg II, Ca-H/K, 4 000 Å break
3	03:02:16.181	-00:03:32.28	1.1806 ± 0.0004	134.3	[O II], Ca-H/K†
4	03:02:11.774	-00:01:32.61	1.1968 ± 0.0007	2.5	Mg II, [O II], Ca-H, G band
5	03:02:09.930	-00:01:05.91	1.2042 ± 0.0004	41.0	[O II]†
6	03:02:15.228	-00:01:49.87	1.1596 ± 0.0004	52.3	[O II]
XMMU J1532.2-0836					
1 (BCG)	15:32:13.294	-08:37:00.75	1.3592 ± 0.0016	5.5	Mg II, Ca-H/K
2	15:32:13.149	-08:36:57.97	1.3580 ± 0.0007	2.1	Fe II, Mg II, Ca-H/K
3	15:32:13.010	-08:36:57.14	1.3568 ± 0.0005	0.4	Fe II, [O II], [Ne III], [Ne V]

† The feature is faint.

Spectroscopic confirmation

In order to increase the efficiency of spectroscopic follow-up, we submit the X-ray identified candidates to a pre-screening process based on optical/near-infrared imaging. This allows us to compile a candidate shortlist with very low contamination rate (Fassbender 2008).

XMMU J0302.2-0001 was classified as a good high redshift cluster candidate based on its solid X-ray detection and a very prominent ($\sim 25\sigma$) overdensity of red galaxies. This system was therefore selected as a prime candidate for spectroscopic follow-up.

For XMMU J1532.2-0836, the depth of the available X-ray observations allowed us to establish it only as tentative high-z cluster candidate. However, the optical images revealed four very red galaxies exactly coincident with the X-ray emission peak and thus also this system was included among the cluster candidates for the purpose of spectroscopic confirmation with the VLT/FORS2 instrument.

For each cluster we carried out an observation in the MXU-mode (Mask eXchange Unit), whose $6.8' \times 6.8'$ field-of-view allows us to obtain a sufficient number of galaxy spectra with a single slit mask centered on the cluster.

We reduced the observations with a new FORS 2 adaptation of the VIMOS *Interactive Pipeline and Graphical Interface* (VIPGI, Scodeggio et al. 2005) which includes all the standard analysis steps - bias subtraction, flat field corrections, image stacking and extraction of background subtracted 1D galaxy spectra. The wavelength calibration is carried out using a Helium-Argon lamp reference line spectrum (calibration uncertainty $< 1\text{Å}$). Details of the spectroscopy reduction pipeline will be given in Nastasi et al., in prep. The final stacked spectra are corrected for the sensitivity function of the FORS 2 instrument. We obtain the galaxy redshifts by cross-correlating their spectra with a galaxy template library using the IRAF[4] package RVSAO and the EZ software (Kurtz and Mink 1998; Garilli et al. 2010, respectively).

XMMU J0302.2-0001

As can be seen in Fig. 7.3 (bottom, left), there is a peak of six concordant redshifts in the galaxy redshift distribution around the X-ray center of XMMU J0302.2-0001 at $z \approx 1.19$. The measured redshifts, the most dominant spectral features and cluster centric distances are listed in Table 7.3. Five of the galaxies are within $55''$ from the X-ray center. This includes also the BCG and two additional red galaxies in the immediate vicinity of the X-ray centroid ($< 10''$ offset, see Fig. 7.1), which allows us to establish the redshift of the system with good confidence. The spectra of galaxies ID: 4 and ID: 5 have low signal-to-noise ratios, but we still are able to measure their redshifts rather safely and keep them therefore in the member list. Galaxy ID: 6 is not passive - it exhibits an extremely strong [O II] emission line.

In order to estimate the final cluster redshift we apply a selection criterion adopted from Milvang-Jensen et al. (2008): we require the galaxy redshifts to be in a 0.015 wide redshift slice around the iteratively established cluster redshift. This selection includes galaxies ID: $1 - 5$ and yields a median cluster redshift of $z = 1.185 \pm 0.016$ (error is the interquartile range).

---

[4]`iraf.noao.edu`
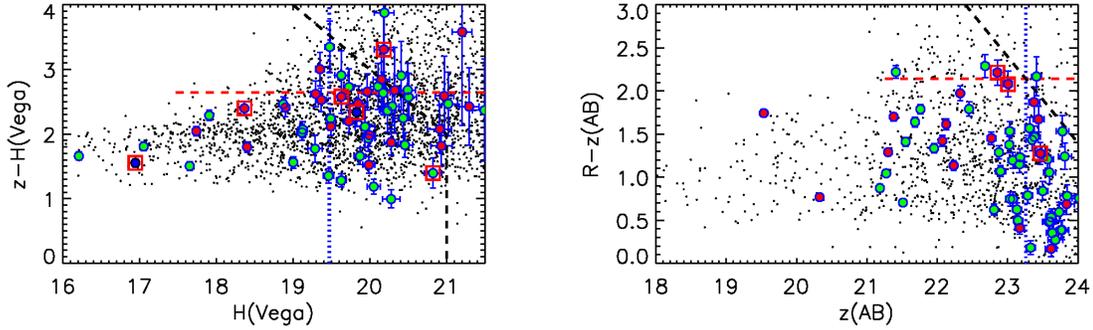
Figure 7.2: **Left:** The z-H vs. H color-magnitude diagram (CMD) for XMMU J0302.2-0001. Square boxes mark secure spectroscopic cluster members. Galaxies with projected cluster-centric distances less than 30″ are shown as red circles, those with distances between 30″ − 60″ as green circles. Galaxies with concordant redshift at > 60″ distances have blue circles. The dashed black line marks the magnitude limits. The apparent H band magnitude of a L^* galaxy at the cluster redshift is shown with a vertical blue dotted line. To help to guide the eye we over-plot the color of a solar metallicity SSP model for the clusters' redshifts with formation redshift $z_f = 5$ (red dashed line). **Right:** The R-z vs. z CMD of XMMU J1532.2-0836. The symbols and colors have the same meaning as in the above plot. Note that the R and z magnitudes here are in the AB system. Two of the spectroscopic members lay on the model prediction for a red sequence at this redshift, the third member has a significantly bluer color.

We conclude the discussion of the spectroscopy of XMMU J0302.2-0001 by remarking that there is an additional spectroscopic galaxy redshift from the Sloan Digital Sky Survey which is concordant with the cluster redshift. We discuss this source in Sect. 7.3.4.

XMMU J1532.2-0836

For XMMU J1532.2-0836 we were able to obtain three galaxy spectra (Fig. 7.1, top right). All three spectra have good signal-to-noise ratios and the redshifts can be anchored by several prominent spectral features (Table 7.3). They yield a redshift of the system equal to 1.358±0.001. The three spectroscopic members are within ∼ 6″ from the X-ray center (Fig. 7.1, bottom right). The fourth red galaxy close to the center was found to be a foreground object.

Galaxy ID: 3 has a very prominent [O ii] emission line and [Ne iii] and [Ne v] lines were detected as well. These features are characteristic for the population of obscured AGN (e.g. Groves et al. 2006). The implications of the presence of an AGN for the X-ray analysis of the source is discussed in Sect. 7.3.1.

Finally, we note that the four galaxies at $z \approx 1.1$ in Fig. 7.1 (bottom right) would constitute a system given our selection criterion (Sect. 7.2.2). However, these galaxies are spatially unrelated and thus do not form a genuine galaxy overdensity.
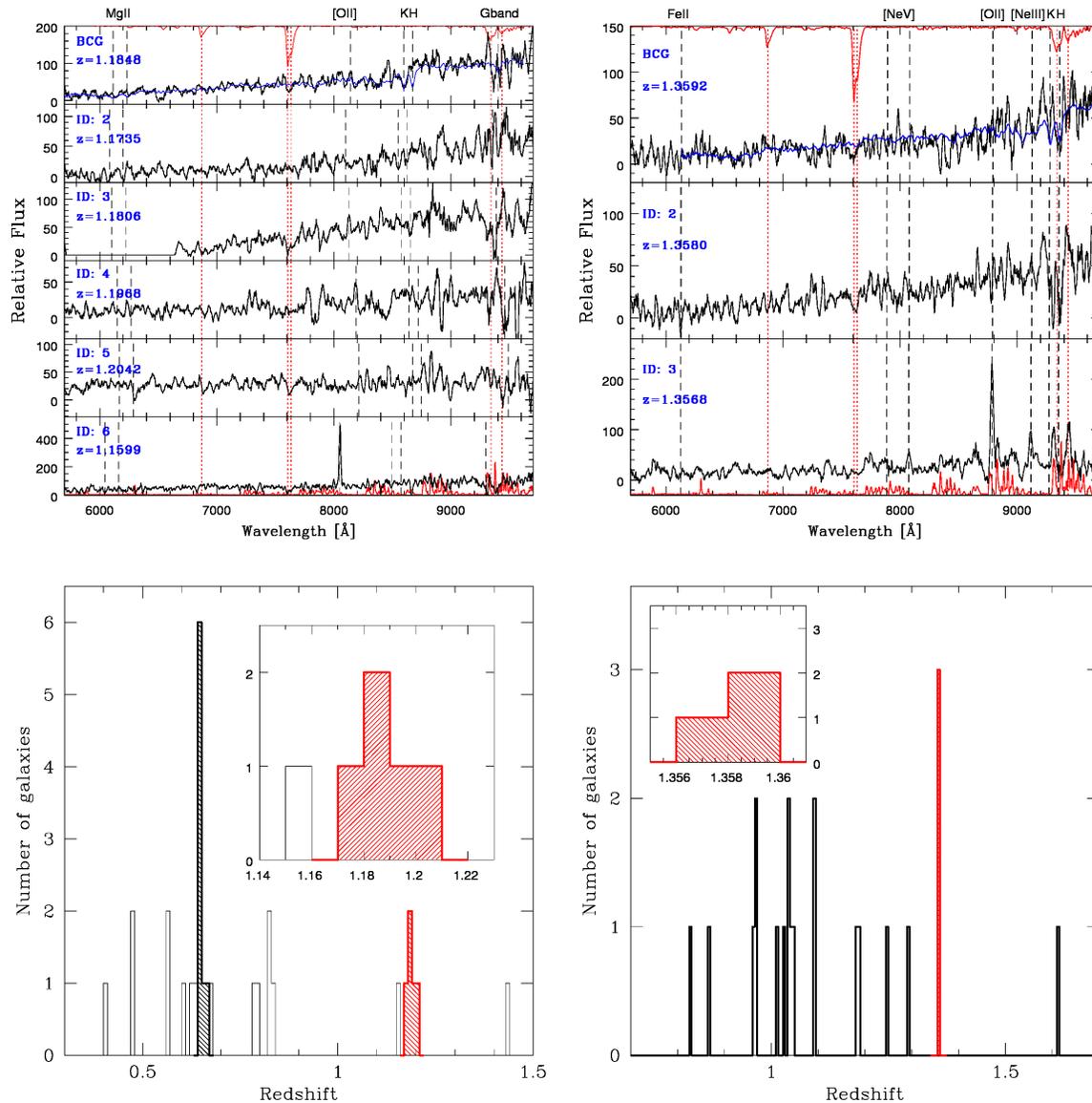
Figure 7.3: **Top:** Spectra of secure cluster members for XMMU J0302.2-0001 (left, $z = 1.185$) and XMMU J1532.2-0836 (right, $z = 1.358$) smoothed with a 7 pixel boxcar filter. The expected observed positions of prominent spectral features at the median redshift are indicated by black dashed lines. The sky spectrum (bottom) and telluric features (top) are overplotted in red. For the BCGs (top panels) we display an overlaid LRG template spectrum in blue. **Bottom:** Distribution of VLT/FORS2 galaxy spectra for the two clusters. The red hashed parts show the distribution of the red galaxies for both clusters (also shown in the insets), selected by requiring the redshift to be within $z_{CL} \pm 0.015$. The black hashed peak corresponds to cluster XMMU J0302.1-0000 (see Appendix 7.5.1). See Sect. 7.2.2 for discussion.

7.2.3   Growth curve analysis of the X-ray imaging data
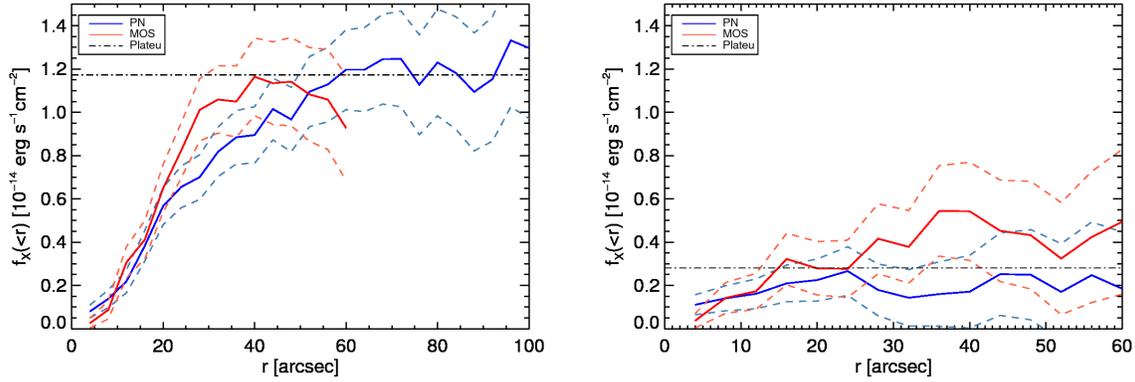
Figure 7.4: Growth curve analysis of XMMU J0302.2-0001 (z=1.185, left) and XMMU J1532.2-0836 (z=1.358, right). The curves show the encircled cumulative flux as a function of radius (PN: blue curve, combined MOS: red). Dashed lines mark the flux measurement error bars which include the Poisson noise and an additional 5% systematic error from the background estimation. The dashed horizontal lines mark the plateau levels. See Sect. 7.2.3 for details.

We utilize an improved version of the *growth curve method* (Böhringer et al. 2000), in order to trace the emission to an as high cluster-centric distance as possible and obtain a reliable measurement of the flux. The cumulative source flux (i.e. background-subtracted) as a function of radius, the growth curves, for the two systems are displayed in Fig. 7.4. The total source flux was determined iteratively by fitting a line to the flat part of the background-subtracted growth curve. We define the *plateau radius* (r_{plat}) as the aperture where the growth curve levels off into a flat plateau. The flux at this radius is the total detected flux of the source.

XMMU J0302.2-0001

For XMMU J0302.2-0001 we found $r_{plat} = 55''$, $F_{plat}(0.5 - 2.0 \, keV) = (11.73 \pm 1.36) \times 10^{-15}$ erg s^{-1} cm^{-2} and a total luminosity $L_{plat}(0.5 - 2.0 \, keV) = (8.56 \pm 0.99) \times 10^{43}$ erg s^{-1} (Fig. 7.4). Errors of the flux and luminosity include the Poisson errors and a 5% systematic error in the background estimation.

The analysis of this cluster is complicated by the presence of an extremely bright point source $80''$ away from the cluster center. At this high off-axis angle the point-spread function (PSF) is already significantly broadened with respect to its on-axis shape and therefore the emission of the point source is spread out in the PSF wings inside the cluster region. Before the background estimation we manually removed a circular region with a conservative radius centered on the point source. The flux estimation described above is based on images with the point source masked out in the same way. We have mitigated this contamination of the cluster emission by

Table 7.4: Basic X-ray parameters of XMMU J0302.2-0001 and XMMU J1532.2-0836. Flux and luminosity errors include the Poisson errors and a 5% systematic error in the background estimation. Errors of parameters obtained from scaling relations include the measurement errors of the luminosity and temperature, respectively, and the intrinsic scatter of the scaling relations. The first set of parameters uses the self-similar $L-T$ and $L-M$ relations from Pratt et al. (2009) for the bolometric luminosity. The second set of parameters (the no-evolution case) follows the prescription of Fassbender et al. (2011a) by removing one $E(z)$ factor from the bolometric luminosity scaling relations of Pratt et al. (2009). In both scenarios, scaling relations are obtained by the BCES orthogonal fit algorithm (Akritas and Bershady 1996) and the input luminosities include the core regions. Parameters for XMMU J1532.2-0836 are upper limits. See Sect. 7.3.1 for more discussion.

Parameter	XMMU J0302.2-0001	XMMU J1532.2-0836[a]	Units
α (J2000)[b]	03$^{\rm h}$ 02$^{\rm m}$ 11.9$^{\rm s}$	15$^{\rm h}$ 32$^{\rm m}$ 13.0$^{\rm s}$	
δ (J2000)[b]	$-00°$ 01$'$ 34.3$''$	$-08°$ 36$'$ 56.9$''$	
redshift	1.185 ± 0.016	1.358 ± 0.001	
$E(z)$	1.96	2.15	
Ang. scale	8.28	8.41	kpc s^{-1}
$n_{\rm H}^a$	7.07	8.13	10^{20} cm^{-2}
L-M, L-T self-similar evol.			
F_{500} [$0.5 - 2.0$ keV]	11.44 ± 1.28	3.02 ± 0.96	10^{-15} erg cm^{-2} s^{-1}
L_{500} [$0.5 - 2.0$ keV]	8.35 ± 0.93	3.81 ± 1.21	10^{43} erg s^{-1}
F_{500} [bolometric]	13.62 ± 2.96	3.52 ± 2.46	10^{-15} erg cm^{-2} s^{-1}
L_{500} [bolometric]	21.08 ± 2.36	8.63 ± 2.75	10^{43} erg s^{-1}
T_{500}	2.8 ± 0.7	2.1 ± 0.6	keV
M_{500}	1.2 ± 0.2	0.7 ± 0.2	10^{14} M$_\odot$
r_{500}	0.47	0.37	Mpc
M_{200}	1.7 ± 0.4	1.0 ± 0.3	10^{14} M$_\odot$
L-M, L-T no evol.			
F_{500} [$0.5 - 2.0$ keV]	11.59 ± 1.33	2.89 ± 1.14	10^{-15} erg cm^{-2} s^{-1}
L_{500} [$0.5 - 2.0$ keV]	7.80 ± 0.90	3.23 ± 1.27	10^{43} erg s^{-1}
F_{500} [bolometric]	12.93 ± 3.14	3.51 ± 2.72	10^{-15} erg cm^{-2} s^{-1}
L_{500} [bolometric]	21.62 ± 2.50	7.82 ± 3.03	10^{43} erg s^{-1}
T_{500}	3.5 ± 0.9	2.6 ± 0.7	keV
M_{500}	1.6 ± 0.3	0.9 ± 0.3	10^{14} M$_\odot$
r_{500}	0.53	0.42	Mpc
M_{200}	2.5 ± 0.5	1.4 ± 0.4	10^{14} M$_\odot$

[a] All values are upper limits; [b] X-ray coordinates based on a maximum-likelihood fit of a PSF-folded beta model to the surface brightness distribution; [c] Values from the LAB HI survey (Kalberla et al. 2005).

excluding these regions and extrapolating the cluster emission as measured at the same cluster-centric radius but from the uncontaminated parts.

XMMU J1532.2-0836

We display the growth curve for XMMU J1532.2-0836 in Fig. 7.4 (right) extracted from the uncontaminated field (OBSID: 0100240701, see Sect. 7.2.1). We detected the source emission out to $r_{plat} = 22''$, with a total source flux of $F_{plat}(0.5 - 2.0 \text{ keV}) = (2.82 \pm 1.11) \times 10^{-15}$ erg s^{-1} cm^{-2}, i.e. four times fainter than XMMU J0302.2-0001. This flux at the cluster's redshift corresponds to a total luminosity $L_{plat}(0.5 - 2.0 \text{ keV}) = (3.59 \pm 1.41) \times 10^{43}$ erg s^{-1}. We note that the source is very faint and thus the flux could be established only with a $\sim 40\%$ error. A systematic shift between the MOS and PN is also apparent in Fig. 7.4 (the MOS flux being higher). Note however, that the growth curves are cumulative flux distributions and thus the radial bins are not independent. All subsequent physical parameters are thus only tentative and will require a dedicated deeper (on-axis) X-ray observation for corroboration.

Except for pointing 0100240701 there is an additional XMM-*Newton* observation available of similar depth and at similar off-axis angle, but this one is heavily contaminated by soft-protons. There is some evidence that the soft protons undergo reflection on the telescopes mirror and are thus vignetted across the field of view. The vignetting function for MOS was tentatively established by Kuntz and Snowden (2008b) to be shallower than the vignetting of genuine X-ray photons. For PN a systematic study has not yet been carried out but a preliminary analysis suggests a similar shape to the MOS vignetting. Given this, our two-component background model should be able to capture the enhanced background to the first order. We have therefore extracted growth curves also from the second observation. We find that while there is a relatively large scatter between the curves, they typically agree within the error bars. The measured total flux (the plateau level of the curves) agree very well, the difference between them being much smaller than their errors: $F_{plat}(0100240701) = 2.82 \pm 1.11$ and $F_{plat}(0100240801) = 2.95 \pm 0.94$ in 10^{-15} erg s^{-1} cm^{-2} units in the $0.5 - 2.0$ keV band. This is a reassuring indication that indeed the plateau fitting algorithm and the procedure of combining the growth curves from PN and MOS yields very stable results, even for observations with non-standard backgrounds.

7.3   Results and discussion

7.3.1   Physical properties of the clusters

The number of counts for both clusters is insufficient for a spectroscopic analysis and therefore we can estimate additional physical parameters only through luminosity based scaling relations. In the following analysis, we will assume that the entire X-ray emission detected and character-ized by the growth curve analysis (Sect. 7.2.3) originates in the ICM (after removing the detected point sources). For XMMU J0302.2-0001 we find no indication that there is any further contam-ination, but in the case of XMMU J1532.2-0836 this assumption is likely not valid due to the

presence of an obscured AGN (Sect. 7.2.2). We discuss this possibility in Sect. 7.3.2. The physical parameters for this system should therefore be considered as upper limits.

Due to the high redshift of the clusters and the limited resolution of XMM-*Newton* we can not excise the core regions of the clusters. We therefore use the scaling relations that include cores. We use the growth curve (Böhringer et al. 2000) to iteratively obtain a self-consistent set of parameters utilizing luminosity based scaling relations. The iterative procedure is described in Šuhada et al. (2010), with the difference that we extrapolate the $0.5 - 2$ keV luminosity to obtain its bolometric value. We estimate the remaining physical parameters using the bolometric L−T and L−M relations from Pratt et al. (2009) (orthogonal fit, no Malmquist bias correction).

First, we assume a self-similar evolution of the scaling relations. Under this assumption, we estimate the objects to be intermediate mass systems with $M_{500} \simeq 1.2 \times 10^{14}$ $M_{\odot}$ for XMMU J0302.2-0001 and $M_{500} \simeq 7 \times 10^{13}$ $M_{\odot}$ for XMMU J1532.2-0836. This corresponds to temperatures T$\simeq$ 3 keV and T$\simeq$ 2 keV respectively. The results for both systems are summarized in Table 7.4.

The major uncertainty on the estimated physical parameters at these high redshifts stems from the fact that the evolution of the scaling relations is not yet well established. Self-similar evolution is a common assumption and a direct prediction of the simple, purely gravitation driven growth. However there are several indications that the evolution of luminosity scaling relations is slower than the self-similar prediction - see discussion in Fassbender et al. (2011a) and references therein, e.g. Stanek et al. (2010) and Reichert et al. (submitted).

We therefore adopt the simplified approach of Fassbender et al. (2011a) and remove a factor of $E(z)$ from the self-similar evolution factor ($E(z)^{-7/3}$) in the bolometric luminosity based scaling relations. This modified evolution factor, $E(z)^{-4/3}$, is consistent with preliminary results of Reichert et al. (submitted) based on a fit to a large sample of high redshift clusters compiled from the literature. Since our algorithm iteratively estimates a self-consistent set of parameters, the change of scaling relations impacts slightly the estimated flux and luminosity (mainly through the temperature dependence of the energy-conversion-factor). This change is minuscule, but for consistency we display the full sets of the estimated parameters for both calculations (i.e. the self-similar and no-evolution scenarios) in Table 7.4.

However, the impact of the different evolution models on temperatures and masses is serious. The non-evolving case approach yields roughly 30% higher cluster masses and $\sim$ 25% higher temperatures (Table 7.4, bottom). Given the precision of the scaling relations (and their intrinsic scatter) and the error of the luminosity measurement, the estimates are still in agreement within their 1σ error bars (albeit for the masses only barely). However, this uncertainty is systematic and very important for studies of cluster samples (and naturally the eventual cosmological constraints derived from them). This clearly demonstrates the importance of establishing a well controlled high-redshift calibration cluster sample.

For both the self-similar and no-evolution scenarios we also include our estimates of the mass M_{200} (mass inside the aperture where the mean density is 200 times the critical density of the Universe). The masses have been obtained by extrapolating M_{500} assuming an NFW profile (Navarro et al. 1997) and using the relations of Hu and Kravtsov (2003) and the DM profile concentration mass/redshift dependence of Bullock et al. (2001). The parameters are obtained iteratively using the M_{500} values as inputs. For both clusters the conversion factor $M_{500} \mapsto M_{200}$

is ≈ 1.5 and M_{200} is $\sim 90\%$ of the virial mass.

While at their observed redshifts the clusters would rank among intermediate and low mass systems, respectively, they still have $\sim 8 - 9$ Gyr of potential mass accretion ahead, before reaching the current epoch. In order to predict the final mass of the clusters at $z = 0$, we use the mean mass growth rate relations of Fakhouri et al. (2010), based on the mass assembly histories of halos in the Millennium and Millennium-II simulations. We estimate the $z = 0$ mass of XMMU J0302.2-0001 to be 1×10^{15} $M_{\odot}$ and 7×10^{14} $M_{\odot}$ for XMMU J1532.2-0836. Thus at the present epoch, XMMU J0302.2-0001 would be a very massive clusters with a mass similar to the Coma cluster. If we use the definition of formation time as the redshift at which the cluster acquired 50% of its $z = 0$ mass (e.g. see the appendix of Giocoli et al. 2007), the formation redshift of XMMU J0302.2-0001 would be around $z \approx 0.5$, while XMMU J1532.2-0836 would be assembled slightly earlier, at $z \approx 0.6$.

7.3.2 The nature of the X-ray emission of XMMU J1532.2-0836

XMMU J1532.2-0836 with its flux $F_{\mathrm{X}} \approx 3 \times 10^{-15}$ erg cm^{-2} s^{-1} is one of the faintest cluster candidates discovered in a serendipitous X-ray survey. Given the estimated upper limits, we are indeed entering here the low-mass cluster/group regime at high redshifts. Probing the feasibility limits of this kind of cluster surveys, however also means that we have to deal with increasing uncertainty in the sources' classification and characterization.

In this case, the initial detection revealed the presence of an extended source at $\sim 2\sigma$ significance level (but only in one of the two observations). Optical/near-infrared imaging confirmed the presence of red galaxies coincident with the X-ray detection and spectroscopic data confirmed the presence of a dynamically bound galaxy system.

Optical spectroscopy, however, also revealed the likely presence of an obscured AGN in the core of the cluster (Sect. 7.2.2). The X-ray spectral distribution of an AGN can in first approximation be described as a power-law (with average index $\Gamma \approx 1.8$) intrinsically absorbed with hydrogen column densities from $\sim 10^{22}$ cm^{-2} to over 10^{25} cm^{-2} (for Compton thick sources) depending on the structure and orientation of the circumnuclear absorber (e.g. Antonucci and Miller 1985). This local absorption introduces a photoelectric absorption cut-off removing most of the soft X-ray emission. Unfortunately, for an AGN at redshift $z = 1.358$ a significant fraction of photons are redshifted from unabsorbed parts of the spectrum into our detection band ($0.5 - 2$ keV). Intrinsic absorption column densities equal to a few times 10^{23} cm^{-2} are enough to remove a significant fraction of the soft emission even after redshifting and thus for these cases the AGN contamination of the observed X-ray emission should be small or even negligible. However, for lower column densities the AGN emission would give a significant contribution and indeed possibly be even the dominant source of the detected photons.

Since the observations are not deep enough to constrain the source spectrum, we have checked the hardness ratios (ratio of the difference of counts in two adjacent bands) of the source in our detection bands ($0.3 - 0.5$, $0.5 - 2$ and $2 - 4.5$ keV). Due to the faintness of the source the ratios are highly uncertain, but are consistent with ICM emission. Given the uncertainties, however, AGN contamination (assuming moderate absorption) can also not be ruled out this way.

Apart from the spectral distribution, a safe detection of source extent would constitute a

strong piece of evidence that the observed emission originates from the thermal bremsstrahlung of the ICM. As discussed in Sect. 7.2.1 source extent was detected only in the slightly deeper, but contaminated field. We re-examine the shallower, clean observation 0100240702 looking for instrumental effects that could mask the source's true extent. In this observation the source lies partially in a very prominent out-of-time (OoT) event stripe (in the PN detector) caused by the very bright star system (UZ Lib) which was the actual target of the observation. Originally, we removed the OoT stripe in the observation in a standard, statistical way.[5] We then try an alternative approach, by keeping the OoT events in the detection images and modelling them in the background estimation step. This method also does not yield an extent detection.

The area around the system is strongly affected by chip gaps in the MOS detectors. In the next run we therefore applied a much less conservative criterion for including low exposure areas in the vicinity of chip gaps, gaining thus more geometric area for source detection. With this modification the source is still detected without a significant extent.

As a final test, we carry out a joint source detection on both fields simultaneously (i.e. two times three detectors, each in three bands). The joint detection is carried out in two different ways. First we stack the data from the same detectors/bands and run source detection simultaneously on the nine merged data sets. XMMU J1532.2-0836 is detected in the merged data set with a higher detection significance as in either of the single observations, but its extent is not confirmed.

Merging observations has the disadvantage that the exact information on the shape of the point-spread-function (PSF) is lost (the two observations have slightly different off-axis and position angles. While the effect is expected to be small, it could be a deciding factor in this case, since the potentially extended emission is so weak. Therefore we also attempt to carry out source detections on all 18 images[6] simultaneously without stacking them. There is currently no SAS task that can carry out extended source detection in two pointings simultaneously, but we modified the source code of the `emosaicproc` task (experimental task in SAS v10.0.0, originally developed for point source detection in mosaic observations) to fit our purposes. However, also this approach does not yield a detection of extent at a statistically significant level. We repeated the procedures for several possible combinations of detectors with no extent detections in most of the cases. Extent was detected exclusively in runs where the two MOS detectors from the contaminated observations were used along with either of the PN cameras. Given that these MOS detectors have the highest contamination ($\sim$ 90% compared to 50% of the PN from this same observation) it leads us to the conclusion that the extent is likely due to an unaccounted background fluctuations caused by the soft-proton contamination. We estimate that for a fully conclusive confirmation of AGN presence a 25 ks *Chandra* observation will be sufficient (gathering $\sim$ 25 source counts). Time for this follow-up observation has been allocated.

In summary, the extent of the source was not confirmed by deeper analysis. While XMMU J1532.2-0836 clearly constitutes a dynamically bound system, the detected X-ray emission can not be unambiguously attributed to the ICM from the available data. Note however, that we have below 100 source counts (after background subtraction) even if we combine both available

---

[5]See e.g. the XMM-*Newton* user handbook, `xmm.esac.esa.int/sas/current/doc/`.
[6]Two observations times three detectors times three bands.

observations. Given our findings we can not exclude the possibility that the detected AGN is the dominant (possibly only) source of X-ray emission detected from this system. This source is thus an example of systems that even with availability of multi-wavelength data are hard to properly classify. For large upcoming surveys such systems will be presumably numerous (e.g. *eRosita*, which in addition has a slightly worse PSF) and therefore additional studies will be needed to establish how can we explore the cluster-group transition regime at high redshifts with good confidence and effective use of follow-up observing time.

7.3.3   The galaxy population of the clusters

It is interesting to note that in the cluster XMMU J0302.2-0001 we detect [O II] line emission in four out five spectroscopic members (excluding the galaxy ID: 6). This feature, an indicator of sustained star-formation, is detected along with other features which are typical for mature systems. Similar activity is observed also in other high redshift X-ray selected clusters: XMMU J1007.4+1237 (at $z = 1.56$ Fassbender et al. 2011b), XMMU J0338.8-0030 (Pierini et al., submitted) and XMMU J2235.3-2557 (Lidman et al. 2008) at $z = 1.39$. While some of these [O II] emitters are bluer than the cluster red sequence, many of them have colors in full agreement with the old, passive galaxies and in some cases are even redder (e.g. in XMMU J2235.3-2557). These galaxies can also span a large range in magnitudes, up to the very bright end of the cluster luminosity function. An increase in star formation activity in red sequence galaxies is also apparent in optically selected cluster sample of Finn et al. (2010) (mostly intermediate redshift systems) and in dense galaxy environments at redshifts ~ 1 seen in GOODS and DEEP2 galaxy surveys (Elbaz et al. 2007; Gerke et al. 2007; Cooper et al. 2008).

We are thus very likely observing residual stochastic star-formation in probably bulge dominated disc galaxies. This effect can be expected to be more important as we move to higher redshifts and enter lower-mass regimes. As we have remarked in Sect. 7.3.1, based on cluster mass growth rates from simulations, XMMU J0302.2-0001 is still in its assembly phase and is expected to be experiencing significant mass accretion and merging activity. These processes lead to large variations in the cluster/group tidal field. Based on numerical simulations Martig and Bournaud (2008) show that tidal field fluctuation can enhance the star formation activity of galaxies (beyond the expectations from purely galaxy-galaxy interaction driven activity). This effect should be particularly efficient at high redshifts and in low mass systems, before quenching processes take place. The XDCP project has the X-ray sensitivity and sky area to be able to effectively study this transition regime and the relevant environmental effects. We leave further discussion to an upcoming dedicated study based on available data. However, we note that in order to completely disentangle the ongoing processes, information on the spectral energy distribution at $\lambda > 4\,000$ Å (rest frame) is necessary as well as high-spatial resolution imaging in order to be able to assess the galaxy morphologies.

7.3.4 Cross-correlation with known sources

We queried the NASA/IPAC Extragalactic Database[7] and the SIMBAD Astronomical Database,[8] in search for potentially interesting known sources.

We find that XMMU J0302.2-0001 has been previously detected by the BLOX survey (Bonn lensing, optical, and X-ray selected galaxy clusters Dietrich et al. 2007) as the object BLOX J0302.2-0001.5. The cluster was selected in X-rays, but not by the optical and weak lensing detection algorithms. Their estimates of the X-ray parameters (r_C = 12.8″ ± 1.2″ and flux F_X = (12.1 ± 1.3) × 10^{-15} erg cm^{-2} s^{-1} in the $0.5 - 2$ KeV band) are in good agreement with our values. The cluster does not have a redshift measurement from the BLOX survey.

At a cluster centric distance of ∼ 185″ we find the source SDSS J030214.82+000125.3 identified in the Sloan Digital Sky Survey (SDSS) as a quasar (Véron-Cetty and Véron 2006). The object has a known spectroscopic redshift, z = 1.179 (Schneider et al. 2007; Cristiani et al. 1996), which is in concordance with our redshift for XMMU J0302.2-0001. At ∼ 185″ offset (corresponding to ∼ 1.5 Mpc at this redshift) it could be associated with the cluster's outskirt region. We also detect this quasar as a high significance X-ray point sources in our XMM-*Newton* observation (see Fig. 7.7).

For the cluster XMMU J1532.2-0836 we do not find any complementary redshifts in the databases. Neither do we find any known radio source within a 2′ radius from either system.

Both sources are also part of the The Second XMM-*Newton* serendipitous source catalog[9] (Watson et al. 2009). Their detection parameters are in agreement with our estimates, however since our pipeline is optimized for high redshift cluster detection, we detect both systems with slightly higher detection likelihoods.

7.4 Conclusions

1. We have detected two high redshift systems, XMMU J0302.2-0001 at z = 1.185 and XMMU J1532.2-0836 at z = 1.358. The objects were X-ray selected in the framework of the XMM-*Newton* Distant Cluster Project.

2. We have obtained and analysed medium deep optical/near-infrared imaging and deep optical spectroscopy with VLT/FORS2 and measured spectroscopic redshifts for both systems. We have confirmed XMMU J0302.2-0001 as a bona fide galaxy cluster. Among its spectroscopically confirmed members we find several luminous [O II] emitters. These giant galaxies are likely experiencing residual stochastic star formation activity, possibly triggered by galaxy-galaxy interactions and fluctuations in the overall tidal field.

3. Based on the obtained optical/near-infrared imaging we established that XMMU J0302.2-0001 has a well populated red sequence. In fact, XMMU J0302.2-0001 corresponds to one of the most prominent overdensities of red galaxies ($2.3 < z - H \leq 3.0$) among the known

---

[7]`nedwww.ipac.caltech.edu`
[8]`simbad.u-strasbg.fr/simbad/`
[9]`amwdb.u-strasbg.fr/2xmmidr3/catentries`

X-ray selected $z > 1$ clusters. Given the currently limited depth of the data for XMMU J1532.2-0836, we can see the bright end of the red sequence (finding two spectroscopical members to have colors consistent with a SSP spectro-photometric sequence for the cluster redshift), but deeper observations will be required to study the galaxy population of the cluster in more detail.

4. From archival XMM-*Newton* data we have estimated the basic physical parameters of XMMU J0302.2-0001. Within the r_{500} aperture we measured the luminosity (0.5-2 keV band) of cluster to be $L_{500} = (8.35 \pm 0.93) \times 10^{43}$ erg s^{-1}. Assuming a self-similar evolution of the L$-$M scaling relation this value correspond to $M_{500} = (1.2 \pm 0.2) \times 10^{14}$ M$_\odot$. This ranks XMMU J0302.2-0001 among intermediate mass clusters at its redshift.

5. We confirm the presence of a dynamically bound galaxy system with three concordant redshifts and coincident with XMMU J0302.2-0001. We also find [O II], [Ne III] and [Ne V] emission lines in the optical spectrum of one of the member galaxies making it a likely obscured AGN candidate.

6. We carried out an in-depth X-ray analysis of XMMU J1532.2-0836, showing that its original tentative detection as an extended source can not be confirmed by currently available data. While the nature of the X-ray emission as originating from faint ICM emission can not be ruled out, we conclude that it is likely that the emission is dominated (or possibly even fully caused) by the central AGN. Notwithstanding this, we estimate upper limits on the X-ray properties for the case that the AGN emission is negligible. We estimate the upper limit for the $0.5 - 2$ keV band luminosity to be $L_{500} = (3.81 \pm 1.21) \times 10^{43}$ erg s^{-1} and the corresponding mass $M_{500} = (0.7 \pm 0.2) \times 10^{14}$ M$_\odot$.

7. We have discussed the effect of non-self similar evolution of the scaling relations on our mass estimates. We find that a no-evolution scenario yields up to 30% higher masses and $\sim 25\%$ higher temperatures at these redshifts. This strongly underscores the importance of the efforts to properly calibrate these relationships in the redshift regime $z \gtrsim 0.8$.

8. We detected and analysed a third cluster, XMMU J0302.1-0000, which was serendipitously detected together with cluster XMMU J0302.2-0001. This cluster is established to be an intermediate mass system at an intermediate redshift, $z = 0.647$.

We are experiencing a time period when many crucial questions about the cluster population and its evolution can start to be addressed by analysing cluster samples at high redshifts. This is also the objective of the XDCP project, with the main aim to address the evolution of scaling relations and obtain cosmological constraints. The present paper extends the XDCP sample and provides the first analysis of the clusters in preparation for planned deeper studies based on additional optical/near-infrared data. XMMU J1532.2-0836 is scheduled for deep J and Ks imaging by the Hawk-I instrument on the VLT. A *Chandra* observation to investigate the nature of the X-ray emission from this system has also been allocated. For XMMU J0302.2-0001, K band imaging has already been obtained by the Large Binocular Telescope. A joint, multi-wavelength analysis of these (and other XDCP) targets will be discussed in up-coming studies.

Acknowledgements

7.5 Appendix

7.5.1 XMMU J0302.1-0000

The cluster XMMU J0302.1-0000 was detected in the observation OBSID: 0041170102 only $\sim 2'$ from XMMU J0302.2-0001 at an off-axis angle of $11'$, with a high confidence extent significance ($\sim 10\sigma$).

We measured the redshift of the cluster (z=0.647 ± 0.003) from the same VLT/FORS2 data taken for XMMU J0302.2-0001. The redshift is based on the Milvang-Jensen et al. (2008) criterion (Sect. 7.2.2), identifying 8 cluster members (black hashed peak in Fig. 7.3, bottom left).

This redshift places the cluster below the formal XDCP distant cluster sample limit (z≥ 0.8). The galaxy distribution of the cluster well matches the X-ray surface brightness distribution (see Fig. 7.5), with the BCG close to the X-ray peak.

We carry out the X-ray analysis as delineated in Sect. 7.2.1 and Sect. 7.2.3. In a $1'$ aperture we detect 140 source counts in PN and 114 in MOS. The estimated beta model core radius is $r_C = 30.9''$. The growth curves are displayed in Fig. 7.8. Both PN and MOS curves are in good agreement and have well established plateau levels with $F_{plat} = (19.83 \pm 2.16) \times 10^{-15}$ erg cm^{-2} s^{-1}.

We estimate the cluster's mass to be $M_{500} = (1.0 \pm 0.2) \times 10^{14}$ M$_\odot$ from its measured luminosity $L_{500} = (3.26 \pm 0.33) \times 10^{43}$ erg s^{-1} $(0.5 - 2$ keV). This corresponds to a 2.3 keV temperature. The effect of the evolution uncertainty described in Sect. 7.3.1 is slightly smaller than for the $z > 1$ cases - the no-evolution scenario yields a $\sim 20\%$ higher M_{500} and $\sim 13\%$ higher temperature. The physical parameters are summarized in Table 7.5.

In Fig. 7.5 we display the pseudo-color image of XMMU J0302.1-0000 and in Fig. 7.6. The individual frames and photometry are the same as for XMMU J0302.2-0001 and described in Sect. 7.2.2.
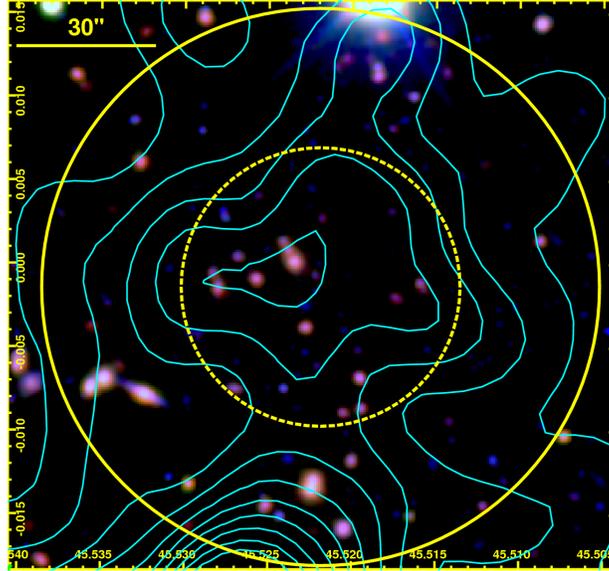
Figure 7.5: Pseudo-color image of the clusters XMMU J0302.1-0000 (left, red channel: H band, green: z, blue: R). Adaptively smoothed X-ray contours are overlaid in cyan. Solid/dashed circles mark a 60″/30″ radius region centered on the X-ray detection.

The CMD can be found in Fig. 7.6. The cluster has a rich red sequence with a BCG coincident with the X-ray centroid. Although the BCG seems to experience a merging activity, its color is in agreement with the SSP model prediction for the cluster redshift (red dashed line in Fig. 7.6).

We have obtained spectroscopy also for the very bright X-ray AGN ∼ 75″ from the cluster center (see Fig. 7.7) and find that its redshift is concordant with XMMU J0302.1-0000. At the cluster redshift this is equivalent to ∼ 0.5 Mpc, i.e. the AGN is associated with the cluster. This source is also contained in the SDSS catalog (Schneider et al. 2007) (quasar SDSS J030206.76-000121.3 at redshift $z = 0.641$).

Similarly to XMMU J0302.2-0001, the cluster XMMU J0302.1-0000 is also part of the BLOX survey catalog (see Sect. 7.3.4 and Dietrich et al. 2007), detected independently in the X-ray data and through an optical matched filter cluster finder (object ID: BLOX J0302.0-0000.0). The estimated X-ray extent of $r_C = 27.8″ \pm 1.9″$ is fully consistent with our value. The $0.5 - 2$ keV flux estimated by the BLOX survey is $F_X = (29.4 \pm 2.6) \times 10^{-15}$ erg cm^{-2} s^{-1}, i.e. significantly higher than our value. We note however, that their estimate is based on the direct output of the detection pipeline, whereas ours is from a dedicated growth curve analysis which includes several improvements: 1) a visual screening and manual adjustment of masks for contaminating sources (indeed there is a bright point source detected only 20″ from the cluster's core); 2) the redshift and temperature dependence of the energy conversion factor (which is needed to convert the detected counts to flux) is implemented in an iterative fashion and 3) we use the proper response file calculated locally for the clusters position. Finally, the largest part of the difference comes from the fact that the Dietrich et al. (2007) flux is extrapolated to infinity (assuming a
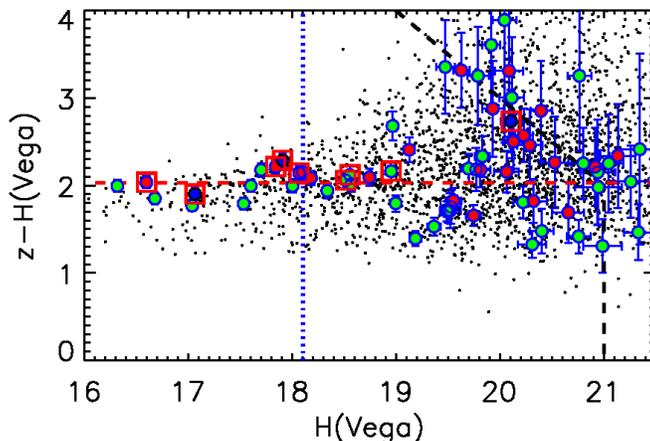
Figure 7.6: The z−H vs. H color-magnitude diagram of the XMMU J0302.1-0000 cluster's field. Red boxes mark secure spectroscopic cluster members. Galaxies with projected cluster centric distance less than $30''$ are shown as red circles, with distances between $30'' - 60''$ as green. Galaxies with concordant redshift at $> 60''$ distances have blue circles. The dashed black line marks the 50% completeness limit. The apparent H band magnitude of a L^* galaxy at cluster redshift ($z = 0.647$) is shown with a vertical blue dotted line. We overplot the z− H color of a solar metallicity SSP model with formation redshift $z_f = 5$ and age ~ 6.3 Gyr (corresponding to the cluster redshift) as a reference (red dashed line). The presence of a red sequence with analogous colors is evident.

beta-model), while our estimate corresponds to a (finite) aperture and is model independent. For a cluster with a large core radius ($\sim 31''$), there is a comparatively larger fraction of the total flux (extrapolated to infinity) outside r_{500} than for a cluster with smaller core radius (such as XMMU J0302.2-0001 ($r_C = 14''$), where the agreement with the BLOX survey value is much better).

The BLOX survey significantly underestimates the cluster redshift (their value is 0.4). They estimate a cluster richness of $\lambda_{CL} = 65.9$, where λ_{CL} is the equivalent number of L^* galaxies with the same total optical luminosity as the cluster galaxies (for the exact definition see Postman et al. 1996).

The cluster is also part of the Second XMM-*Newton* serendipitous source catalog (Watson et al. 2009). The source parameters in this catalog are in good agreement with our values.

In the NED database we find within a $4'$ query radius four galaxies with photometric redshifts in agreement with the cluster redshift (i.e. in the range $0.6 - 0.7$) from Waskett et al. (2004). This includes the already mentioned SDSS J030206.76-000121.3.

In summary, XMMU J0302.1-0000 is confirmed as an intermediate mass system at intermediate redshift. While it is below the redshift threshold of the XDCP distant cluster sample, owing to its proximity to XMMU J0302.2-0001 it will benefit from upcoming deeper multi-wavelength follow-up data and will be thus an interesting object in its own right.

Table 7.5: Basic X-ray parameters of XMMU J0302.1-0000. See Table 7.4 for explanations.

Parameter		Units
α (J2000)[a]	$03^h\ 02^m\ 05.3^s$	
δ (J2000)[a]	$-00°\ 00'\ 05.0''$	
redshift	0.647 ± 0.003	
E(z)	1.43	
Ang. scale	6.92	kpc s^{-1}
n_H^b	7.05	10^{20} cm^{-2}
L-M, L-T self-similar evol.		
F_{500} [0.5 − 2.0 keV]	19.20 ± 1.95	10^{-15} erg cm^{-2} s^{-1}
L_{500} [0.5 − 2.0 keV]	3.26 ± 0.33	10^{43} erg s^{-1}
F_{500} [bolometric]	22.78 ± 4.33	10^{-15} erg cm^{-2} s^{-1}
L_{500} [bolometric]	7.71 ± 0.78	10^{43} erg s^{-1}
T_{500}	2.3 ± 0.7	keV
M_{500}	1.0 ± 0.2	10^{14} M$_{\odot}$
r_{500}	0.56	Mpc/arcsec
M_{200}	1.4 ± 0.3	10^{14} M$_{\odot}$
L-M, L-T no evol.		
F_{500} [0.5 − 2.0 keV]	18.88 ± 2.01	10^{-15} erg cm^{-2} s^{-1}
L_{500} [0.5 − 2.0 keV]	3.14 ± 0.33	10^{43} erg s^{-1}
F_{500} [bolometric]	21.19 ± 4.56	10^{-15} erg cm^{-2} s^{-1}
L_{500} [bolometric]	7.73 ± 0.82	10^{43} erg s^{-1}
T_{500}	2.6 ± 0.6	keV
M_{500}	1.2 ± 0.3	10^{14} M$_{\odot}$
r_{500}	0.59	Mpc
M_{200}	1.7 ± 0.4	10^{14} M$_{\odot}$

[a] X-ray coordinates based on a maximum-likelihood fit of a PSF-folded beta model to the surface brightness distribution; [b] Values from the LAB HI survey (Kalberla et al. 2005).
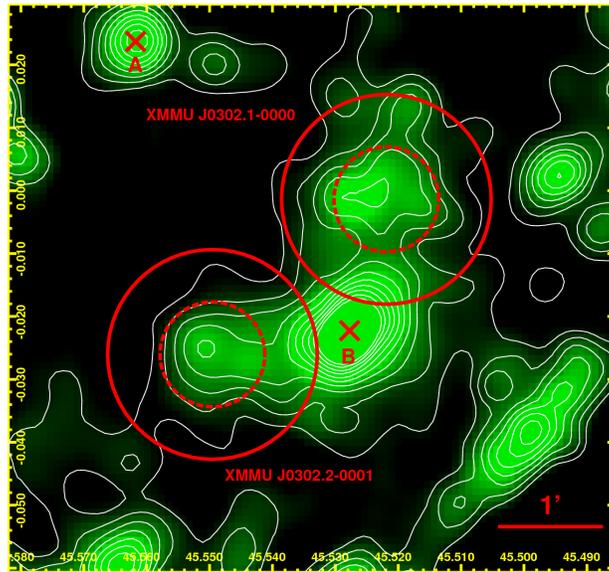
Figure 7.7: Adaptively smoothed $0.5 - 2$ keV X-ray image of the wider neighborhood of XMMU J0302.2-0001 and XMMU J0302.1-0000. The red circles have $60''$ radii, while the dashed circles $30''$. X-ray contours are overlaid in white. Point A marks the AGN at the redshift of XMMU J0302.2-0001 (SDSS J030214.82+000125.3) and point B the very X-ray bright AGN SDSS J030206.76-000121.3, that has a concordant redshift with the cluster XMMU J0302.1-0000.
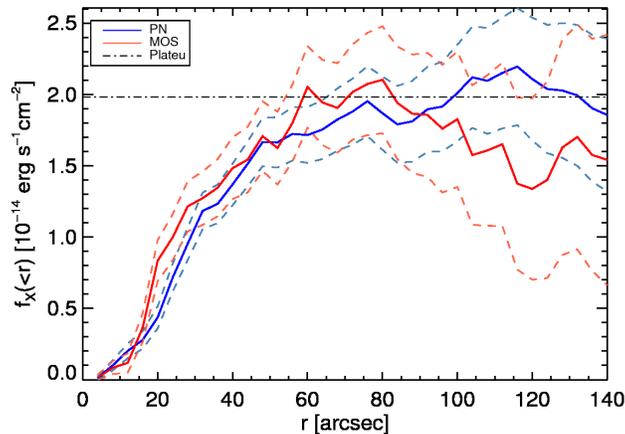
Figure 7.8: Growth curve analysis of XMMU J0302.1-0000. The curves show the encircled cumulative flux as a function of radius (PN: blue curve, combined MOS: red). Dashed line marks the flux measurement error bars which include the Poisson noise and an additional 5% systematic error from the background estimation. The dashed horizontal line marks the plateau level.

7.5.2   High redshift cluster detections in the past decade

We have argued in Sect. 7.1, that in the recent years much important progress has been made in the gradual construction of statistically large, high redshift cluster samples. These samples will allow us to calibrate the scaling relations to redshift ≈ 1 and beyond and constrain evolutionary models for the ICM and the cluster galaxy populations.

Reichert et al. (submitted) compiled a list of known clusters published up to year 2010 (including), which have secure spectroscopic redshifts and an X-ray luminosity measurement. We select from this catalog a high redshift subsample based on the XDCP project's criterion, i.e. clusters with redshifts $z > 0.8$. While the aim of this catalog is to compile clusters from larger samples, care was taken to include also individually reported high redshift objects. The catalog utilises the latest analysis of each cluster if several are available and therefore whenever it is possible we replace this reference with the year of first analysis (understood here as the discovery year). We aim here just for a simple qualitative analysis and therefore these minor effects do not influence our conclusions. The cumulative histogram of the compiled catalog of $z > 0.8$ clusters is shown in Fig. 7.9. As we can see the progress made in the past decade (2001 - 2010) is truly impressive. The total number of clusters given our criteria is 58. Only three of these clusters were known before the year 2001.

In the right panel of Fig. 7.9 we check whether the total number of clusters grows linearly with time (green line). While the fit is acceptable, there is an indication that the last few years the detection rate has been even larger. An exponential relation[10] yields only a slightly inferior fit (in the sense of the R^2 statistic[11]). An exponential growth might be also preferred if we relax the criteria and would include also clusters with only photometric redshift estimates and not having X-ray luminosity measurements. Especially the Sunyaev-Zel'dovich surveys are currently (e.g. since 2009) the main purveyors of cluster samples with high median redshifts (e.g. ~ 0.6 from the South Pole Telescope survey, Vanderlinde et al. 2010). We also overplot a second order polynomial in Fig. 7.9 (blue line) which well describes the observed detection counts (and confirms the preference for accelerating detection rates). The prediction of this model is 69 clusters given our selection criteria by the end of year 2011.

Upcoming large area X-ray surveys (with XMM-*Newton* and eventually *eRosita*) along with other cluster selection approaches (SZE, optical) and the new near-infrared spectrographs will enable us to further increase our high-z cluster samples. Independently of the exact shape of the growth of our cluster catalogs, the future of high redshift cluster studies certainly seems very promising.

---

[10]An exponential growth is motivated as a potential instance of Moore's law. A similar growth is observed not only in improvement of computing hardware (and other digital electronic devices), but given a suitable figure-of-merit also in several scientific subfields, e.g. the total number of particles in cosmological N-body simulations or the number of DNA base pairs sequenced per year. Naturally, this growth in cluster detections can not be sustained indefinitely, at the very least due to the finite number of clusters in the observable Universe.

[11]This fit is, however, mildly preferred by both the Bayesian and Akaike information criteria. It is also a clearly better description of observed trends up to years 2008-2009.
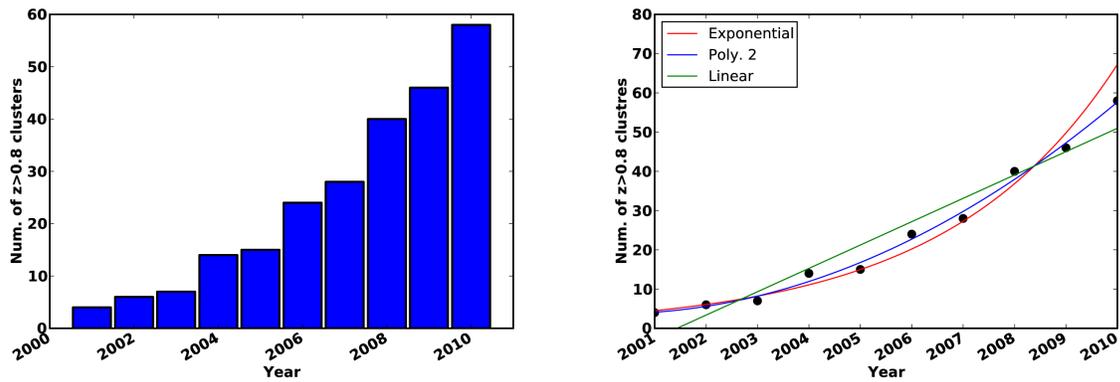
Figure 7.9: **Left:** Cumulative histogram of the known clusters with spectroscopic redshift > 0.8 and an X-ray luminosity measurement compiled by Reichert et al. (submitted). **Right:** A linear (green line), exponential (red) and second order polynomial fits to the data in the left panel. See the text for discussion.

Chapter 8

Summary and outlook

The studies performed in this thesis are all part of large ongoing projects - the XMM-BCS survey and the XMM-*Newton* Distant Cluster Project (XDCP). In this final chapter, I provide summaries and conclusions of the work presented here. Since the XMM-BCS survey constitutes the majority of the thesis (Chapters 4 and 5), I dedicate it the two final sections and begin with providing conclusions of the study carried out in the framework of the XDCP survey (Chapter 6).

8.1 Conclusions of the analysis of two $z > 1$ systems

The main aim of the XDCP project is the detection and study of very distant clusters ($z > 0.8$), with a focus on extending the calibration of X-ray scaling relations beyond the redshift of unity and the investigation of high redshift cluster galaxy populations (Böhringer et al. 2005; Fassbender 2008). In the scope of this project, we have carried out a multi-wavelength analysis of two distant, X-ray selected cluster candidates. The study consists of the X-ray analysis of the sources, measurement of their spectroscopic redshifts and characterization of their galactic population based on optical/near-infrared imaging data.

The first system, XMMU J0302.2-0001 at redshift $z = 1.185$, was confirmed as a genuine cluster with an estimated X-ray mass of $M_{500} = (1.6 \pm 0.3) \times 10^{14} \, M_{\odot}$. Its galaxy population was found to be both impressive and puzzling. Impressive, because the cluster was confirmed to have a $\sim 25\sigma$ overdensity of red galaxies compared to the field - one of the richest galaxy populations found at $z > 1$. Interestingly, optical spectroscopy of most of the analysed member galaxies revealed an [O $\textsc{ii}$] emission line - a marker of ongoing star formation activity. This is at variance with the typical picture of a cluster galaxy as an old, red, passively evolving object. As we approach the high redshift, low mass regime, an increase of star-formation can be expected. In this regime, the star formation is likely triggered not only by galaxy-galaxy interactions, but also by large-scale fluctuations of the global tidal field of the systems caused by ongoing formation processes (Martig and Bournaud 2008). The observed star formation is therefore probably the stochastic residual activity in bulge dominated disc galaxies due to this kind of events. We estimated that statistically the system has indeed still a long period of mass accretion and mergers ahead of itself.

The second system, XMMU J1532.2-0836 ($z = 1.358$), demonstrates the challenges we have to deal with when we are entering the cluster-group transition regime at these high redshifts. This very faint X-ray detection is spectroscopically confirmed to be coincident with a dynamically bound system of galaxies. However, optical spectroscopy also reveals that one of the member galaxies harbours an active galactic nucleus (AGN). Additionally, an in-depth analysis of the available X-ray data showed that the initial characterization of this system as an extended source (an attribute of cluster emission) is very likely spurious. We thus conclude that the X-ray emission of this system, while being consistent with originating from the intracluster medium, could be heavily contaminated (or even fully caused) by the central AGN. A snapshot observation with the Chandra X-ray telescope has been granted and will allow us to assess the true nature of this system.

A third, intermediate redshift ($z = 0.647$) cluster was serendipitously detected in the field of XMMU J0302.2-0001 and we provide its analysis as well.

8.2 Summary of the X-ray of the XMM-BCS survey

The main project of this thesis was to carry out initial studies in the framework of the XMM-BCS survey. This survey consists of a 14 deg^2 X-ray field (PI: H. Böhringer) observed by XMM-*Newton* and roughly the same area is also covered by the *Spitzer* Space Telescope in the mid-infrared (PI: A. Stanford). This test field lies in the heart of one of the two 50 deg^2 fields imaged in the *griz* optical bands by the Blanco Cosmology Survey (BCS, PI: J. Mohr). The field is also covered by the two major SZE experiments: the South Pole Telescope (PI: J. Carlstrom) and the Atacama Cosmology Telescope (PI: L. Page).

The survey's aim is not only to study the cluster population in this field, but also to investigate the selection functions of the different multi-wavelength approaches and compare and cross-calibrate the scaling relations between cluster observables and their total mass. In the scope of this work we made a first step towards this goal by analyzing the initial 6 deg^2 of the survey area and providing an X-ray selected cluster catalog comprising 46 systems (Chapter 4). These cluster candidates have been confirmed as being coincident with overdensities of red galaxies based on optical imaging provided by the Blanco Cosmology Survey. From four band optical photometry we were able to estimate with good precision the photometric redshifts of the clusters. For a low redshift subsample ($z < 0.4$), we have also obtained spectroscopic redshifts and found a good agreement with the photometric values. Using this distance information we measured the luminosities of the clusters and estimated their most important physical parameters from scaling relations, e.g. mass, temperature and the y_X parameter. The cluster sample is also characterized by its $\log N - \log S$ relation based on a simplified calculation of the survey sky coverage, but already shows a good agreement with measurements from other surveys. We also carried out first comparisons with optical studies available from literature (Menanteau et al. 2009, 2010; McInnes et al. 2009). In this preliminary study we find a significant discrepancy between the X-ray and optical mass estimates (with optical masses being higher). The cause of this discrepancy lays probably in the optical mass assignment, but we have no full access to the details of this process at the moment. This question will, however, be investigated further in a future study.

After the South Pole Telescope started its search for clusters via their Sunyav-Zel'dovich Effect (SZE) signature, it was soon realized that the current generation of instruments is only sensitive to the very massive end of the cluster population ($M \gtrsim 5 \times 10^{14}$ $M_{\odot}$). Since such massive clusters are relatively rare, it motivated our effort to extend the X-ray survey to a larger area (and thus increase the survey volume). The extension was made possible by the introduction of a novel XMM-*Newton* observation mode - the mosaic mode (it is indeed very rare that a new operation mode is added to a long-time operating mission in orbit). This mode brings great improvement in the observing efficiency of large sky areas compared to standard pointing observations, which allowed us to extend the X-ray field by 8 $\deg^2$ to a total area of 14 $\deg^2$. This was the first scientific application of mosaic mode observations. We have developed a data-reduction pipeline that allowed us to carry out source detection analogously to standard observations. As first results, we provided the detection and analysis of two massive clusters, SPT-CL J2332-5358 (at photometric redshift $z = 0.32$) and SPT-CL J2342-5411 (at $z = 1.08$). Both clusters were among the first clusters detected through their Sunyav-Zel'dovich effect signature by the South Pole Telescope (Vanderlinde et al. 2010). The cluster SPT-CL J2332-5358 was also blindly selected by optical cluster search in the BCS data (Menanteau et al. 2010). These clusters are thus the first systems detected independently by all three major surveying approaches.

Although, the X-ray data has shallow exposures ($\sim$ 3 ks) we were still able to find and characterize the cluster SPT-CL J2342-5411 at redshift $\sim$ 1 and provide a spectroscopic temperature measurement for SPT-CL J2332-5358. We found a good agreement between the SZE and X-ray masses, supporting the expectation, that the SZE provides a robust mass-proxy (here via the SZE detection significance and eventually via the integrated Compton Y parameter).

8.3 Outlooks for the XMM-BCS survey

After the first steps made in this thesis, there are still many scientific questions to be explored using the XMM-BCS multi-wavelength data. Here we summarize the main lines of upcoming investigations, several of which have been already initiated:

- A preliminary X-ray source catalog from the survey's extension is already available. In the next step, we will screen this preliminary catalog using the optical imaging data in order to construct a catalog of galaxy clusters and groups in a similar fashion as in the initial 6 $\deg^2$ region. We will measure the redshifts of these systems and determine their physical properties. The full 14 $\deg^2$ catalog is expected to have $\sim$ 100 clusters.

- The realistic selection function of the survey is a prerequisite for cosmological and scaling relation studies. We will provide its calculation based on Monte Carlo simulations using the software developed by Mühlegger (2010).

- The full cluster sample will be sizable enough that it can provide interesting cosmological constraints, although not as stringent as the current leading cosmological probes (cosmic microwave background studies, supernovae, etc.). The sample can, however, be combined with other, larger samples to gain extra leverage, e.g. with the REFLEX II sample

(Böhringer et al., in prep.) for which it constitutes a natural extension towards higher redshifts and lower mass systems.

- The cluster sample will be compared to the catalog of optically selected clusters from the BCS field (Song et al., in prep.). The comparison can address two important questions: 1) it can give us a direct view on the selection function of both surveying approaches; 2) by obtaining our own estimates of the optical masses from observables such as L_{200}, L_{BCG} and N_{200} [1] we can carry out a comparison with the X-ray mass estimates. Although the intrinsic scatter of the optical mass estimators is generally large, it is important that an unbiased link to the total cluster mass is established. This can in the future be utilized by large optical surveys such as Pan-STARRS and the Dark Energy Survey.

- The available *Spitzer* mid-infrared data can be used in conjunction with the optical imaging to improve the photometric redshifts, particularly for distant clusters with $z > 0.8$. Based on these data-sets we will also get a comprehensive look at the galaxy population of clusters and groups out to redshift ~ 1.

- We have initiated further X-ray-SZE studies based on a cooperation with the SPT collaboration. The current SPT cluster samples of Williamson et al. (2011) and Vanderlinde et al. (2010) include only sources with minimal detection significance of 4.5σ. The purity of the SPT sample is expected to drop under $\sim 50\%$ below the 4.5σ threshold. However, using our X-ray selected cluster catalog also lower significance SPT detections can be safely studied. As a first example, the most massive cluster from our sample (cluster XBCS 231653.1-545413) was found to have a direct SPT detection at the 4.2σ level (B. Benson, private communication).

  Another line of investigation concerns stacking analysis of the SZE data for the X-ray selected clusters. Here, from the X-ray masses we have calculated the expectation of the SPT detection significance for our sample. In a preliminary analysis, the top eleven clusters ranked by this parameter yield a $\sim 6\sigma$ detection significance in the stacked SZE data (there are indications in at least one of the clusters for point source contamination, this value should be thus considered as a lower limit, B. Benson, private communication). Nine of these systems have SPT individual detection significances $> 1.5\sigma$, with three clusters detected at $> 3\sigma$ levels. All these preliminary results show that with a joint SZE and X-ray analysis we are able to explore a completely new mass regime for SZE studies.

- Finally, as an example of ancillary science coming from the survey field, we add that we have detected a total of 3065 X-ray point sources in the survey (1639 in the core region and 1426 in the extension). Most of these point sources are AGN and using the available multi-wavelength data we will be able to carry out a study with a focus on the obscured AGN population.

---

[1]Total integrated optical luminosity, BCG luminosity and galaxy counts as a measure of cluster richness (Reyes et al. 2008, see also Sect. 5.5.6).

This thesis shows different aspects of multi-wavelength cluster surveys, with a focus on the X-ray band. The future of this kind of surveys looks very promising. Large SZE experiments, the South Pole Telescope, the Atacama Cosmology Telescope and the *Planck* mission, are all in operation and delivering their cluster detections. In the optical band, there are also several ambitious projects - both ongoing (Pan-STARRS) and future ones such as the Dark Energy Survey and the survey with the Large Synoptic Survey Telescope. The largest cluster catalog will be, however, provided by the *eRosita* instrument in X-rays. Up to hundred thousand systems are expected to be found with a few hundreds of clusters above redshift $z = 1$. Each of this surveying approaches comes with its own strengths and challenges, but ultimately by combining them, we will be able to utilize their synergies to get an unprecedented view of the cluster population and their place in the hierarchy of the cosmic large-scale structure.

Bibliography

Abell, G. O. (1958). The Distribution of Rich Clusters of Galaxies. *ApJS*, 3:211–+.

Afshordi, N., Lin, Y., Nagai, D., and Sanderson, A. J. R. (2007). Missing thermal energy of the intracluster medium. *MNRAS*, 378:293–300.

Akritas, M. G. and Bershady, M. A. (1996). Linear Regression for Astronomical Data with Measurement Errors and Intrinsic Scatter. *ApJ*, 470:706–+.

Allen, S. W. (1998). Resolving the discrepancy between X-ray and gravitational lensing mass measurements for clusters of galaxies. *MNRAS*, 296:392–406.

Allen, S. W., Rapetti, D. A., Schmidt, R. W., Ebeling, H., Morris, R. G., and Fabian, A. C. (2008). Improved constraints on dark energy from Chandra X-ray observations of the largest relaxed galaxy clusters. *MNRAS*, 383:879–896.

Allen, S. W., Schmidt, R. W., Ebeling, H., Fabian, A. C., and van Speybroeck, L. (2004). Constraints on dark energy from Chandra observations of the largest relaxed galaxy clusters. *MNRAS*, 353:457–467.

Andersson, K., Benson, B. A., Ade, P. A. R., Aird, K. A., Armstrong, B., Bautz, M., Bleem, L. E., Brodwin, M., Carlstrom, J. E., Chang, C. L., Crawford, T. M., Crites, A. T., de Haan, T., Desai, S., Dobbs, M. A., Dudley, J. P., Foley, R. J., Forman, W. R., Garmire, G., George, E. M., Gladders, M. D., Halverson, N. W., High, F. W., Holder, G. P., Holzapfel, W. L., Hrubes, J. D., Jones, C., Joy, M., Keisler, R., Knox, L., Lee, A. T., Leitch, E. M., Lueker, M., Marrone, D. P., McMahon, J. J., Mehl, J., Meyer, S. S., Mohr, J. J., Montroy, T. E., Murray, S. S., Padin, S., Plagge, T., Pryke, C., Reichardt, C. L., Rest, A., Ruel, J., Ruhl, J. E., Schaffer, K. K., Shaw, L., Shirokoff, E., Song, J., Spieler, H. G., Stalder, B., Staniszewski, Z., Stark, A. A., Stubbs, C. W., Vanderlinde, K., Vieira, J. D., Vikhlinin, A., Williamson, R., Yang, Y., and Zahn, O. (2010). X-ray Properties of the First SZE-selected Galaxy Cluster Sample from the South Pole Telescope. *arXiv: 1006.3068*.

Andreon, S., Garilli, B., and Maccagni, D. (1995). Multicolor surface photometry of brightest cluster galaxies. II. Enlarging the sample and improving the analysis. *A&A*, 300:711–+.

Andreon, S., Maughan, B., Trinchieri, G., and Kurk, J. (2009). JKCS 041: a colour-detected galaxy cluster at $z_{phot} \sim 1.9$ with deep potential well as confirmed by X-ray data. *A&A*, 507:147–157.

Antonucci, R. R. J. and Miller, J. S. (1985). Spectropolarimetry and the nature of NGC 1068. *ApJ*, 297:621–632.

Arnaud, M. (2005). X-ray observations of clusters of galaxies. In Melchiorri, F. and Rephaeli, Y., editors, *Background Microwave Radiation and Intracluster Cosmology*, pages 77–+.

Arnaud, M., Pointecouteau, E., and Pratt, G. W. (2005). The structural and scaling properties of nearby galaxy clusters. II. The M-T relation. *A&A*, 441:893–903.

Arnaud, M., Pointecouteau, E., and Pratt, G. W. (2007). Calibration of the galaxy cluster M{500}-Y{X} relation with XMM-Newton. *A&A*, 474:L37–L40.

Arnaud, M., Pratt, G. W., Piffaretti, R., Böhringer, H., Croston, J. H., and Pointecouteau, E. (2010). The universal galaxy cluster pressure profile from a representative sample of nearby systems (REXCESS) and the $Y_{SZ} - M_{500}$ relation. *A&A*, 517:A92+.

Aschenbach, B. (1985). X-ray telescopes. *Reports on Progress in Physics*, 48:579–629.

Bahcall, N. A., McKay, T. A., Annis, J., Kim, R. S. J., Dong, F., Hansen, S., Goto, T., Gunn, J. E., Miller, C., Nichol, R. C., Postman, M., Schneider, D., Schroeder, J., Voges, W., Brinkmann, J., and Fukugita, M. (2003). A Merged Catalog of Clusters of Galaxies from Early Sloan Digital Sky Survey Data. *ApJS*, 148:243–274.

Bailer-Jones, C. A., Bizenberger, P., and Storz, C. (2000). Achieving a wide-field near-infrared camera for the Calar Alto 3.5-m telescope. In M. Iye & A. F. Moorwood, editor, *Society of Photo-Optical Instrumentation Engineers (SPIE) Conference Series*, volume 4008 of *Society of Photo-Optical Instrumentation Engineers (SPIE) Conference Series*, pages 1305–1316.

Balaguera-Antolínez, A., Sánchez, A. G., Böhringer, H., Collins, C., Guzzo, L., and Phleps, S. (2011). The REFLEX II galaxy cluster survey: power spectrum analysis. *MNRAS*, pages 139–+.

Bardeen, J. M., Bond, J. R., Kaiser, N., and Szalay, A. S. (1986). The statistics of peaks of Gaussian random fields. *ApJ*, 304:15–61.

Baum, W. A. (1959). Population Inferences from Star Counts, Surface Brightness and Colors. *PASP*, 71:106–117.

Bekefi, G. (1966). *Radiation Processes in Plasmas, Wiley, New York, 1966*.

Bell, E. F., Naab, T., McIntosh, D. H., Somerville, R. S., Caldwell, J. A. R., Barden, M., Wolf, C., Rix, H., Beckwith, S. V., Borch, A., Häussler, B., Heymans, C., Jahnke, K., Jogee, S., Koposov, S., Meisenheimer, K., Peng, C. Y., Sanchez, S. F., and Wisotzki, L. (2006). Dry Mergers in GEMS: The Dynamical Evolution of Massive Early-Type Galaxies. *ApJ*, 640:241–251.

Benítez, N. (2000). Bayesian Photometric Redshift Estimation. *ApJ*, 536:571–583.

Berlind, A. A., Frieman, J., Weinberg, D. H., Blanton, M. R., Warren, M. S., Abazajian, K., Scranton, R., Hogg, D. W., Scoccimarro, R., Bahcall, N. A., Brinkmann, J., Gott, III, J. R., Kleinman, S. J., Krzesinski, J., Lee, B. C., Miller, C. J., Nitta, A., Schneider, D. P., Tucker, D. L., and Zehavi, I. (2006). Percolation Galaxy Groups and Clusters in the SDSS Redshift Survey: Identification, Catalogs, and the Multiplicity Function. *ApJS*, 167:1–25.

Bertin, E. and Arnouts, S. (1996). SExtractor: Software for source extraction. *A&AS*, 117:393–404.

Bielby, R. M., Finoguenov, A., Tanaka, M., McCracken, H. J., Daddi, E., Hudelot, P., Ilbert, O., Kneib, J. P., Le Fèvre, O., Mellier, Y., Nandra, K., Petitjean, P., Srianand, R., Stalin, C. S., and Willott, C. J. (2010). The WIRCAM Deep Infrared Cluster Survey. I. Groups and clusters at z=1.1. *A&A*, 523:A66+.

Binney, J. and Tabor, G. (1995). Evolving Cooling Flows. *MNRAS*, 276:663–+.

Birkinshaw, M. (1999). The Sunyaev-Zel'dovich effect. *Phys. Rep.*, 310:97–195.

Bîrzan, L., Rafferty, D. A., McNamara, B. R., Wise, M. W., and Nulsen, P. E. J. (2004). A Systematic Study of Radio-induced X-Ray Cavities in Clusters, Groups, and Galaxies. *ApJ*, 607:800–809.

Biviano, A. (2008). Galaxy systems in the optical and infrared. *arXiv: 0811.3535*.

Böhringer, H. and Morfill, G. E. (1988). On the dynamical role of cosmic rays in cooling flows in clusters of galaxies. *ApJ*, 330:609–619.

Böhringer, H., Mullis, C., Rosati, P., Lamer, G., Fassbender, R., Schwope, A., and Schuecker, P. (2005). Galaxy Cluster Archaeology. *The Messenger*, 120:33–36.

Böhringer, H., Pratt, G. W., Arnaud, M., Borgani, S., Croston, J. H., Ponman, T. J., Ameglio, S., Temple, R. F., and Dolag, K. (2010). Substructure of the galaxy clusters in the REXCESS sample: observed statistics and comparison to numerical simulations. *A&A*, 514:A32+.

Böhringer, H., Schuecker, P., Guzzo, L., Collins, C. A., Voges, W., Schindler, S., Neumann, D. M., Cruddace, R. G., De Grandi, S., Chincarini, G., Edge, A. C., MacGillivray, H. T., and Shaver, P. (2001). The ROSAT-ESO flux limited X-ray (REFLEX) galaxy cluster survey. I. The construction of the cluster sample. *A&A*, 369:826–850.

Böhringer, H., Schuecker, P., Pratt, G. W., Arnaud, M., Ponman, T. J., Croston, J. H., Borgani, S., Bower, R. G., Briel, U. G., Collins, C. A., Donahue, M., Forman, W. R., Finoguenov, A., Geller, M. J., Guzzo, L., Henry, J. P., Kneissl, R., Mohr, J. J., Matsushita, K., Mullis, C. R., Ohashi, T., Pedersen, K., Pierini, D., Quintana, H., Raychaudhury, S., Reiprich, T. H., Romer, A. K., Rosati, P., Sabirli, K., Temple, R. F., Viana, P. T. P., Vikhlinin, A., Voit, G. M., and Zhang, Y. (2007). The representative XMM-Newton cluster structure survey (REXCESS) of an X-ray luminosity selected galaxy cluster sample. *A&A*, 469:363–377.

Böhringer, H., Voges, W., Huchra, J. P., McLean, B., Giacconi, R., Rosati, P., Burg, R., Mader, J., Schuecker, P., Simiç, D., Komossa, S., Reiprich, T. H., Retzlaff, J., and Trümper, J. (2000). The Northern ROSAT All-Sky (NORAS) Galaxy Cluster Survey. I. X-Ray Properties of Clusters Detected as Extended X-Ray Sources. *ApJS*, 129:435–474.

Böhringer, H. and Werner, N. (2010). X-ray spectroscopy of galaxy clusters: studying astrophysical processes in the largest celestial laboratories. *A&A Rev.*, 18:127–196.

Bonamente, M., Joy, M., LaRoque, S. J., Carlstrom, J. E., Nagai, D., and Marrone, D. P. (2008). Scaling Relations from Sunyaev-Zel'dovich Effect and Chandra X-Ray Measurements of High-Redshift Galaxy Clusters. *ApJ*, 675:106–114.

Bonamente, M., Joy, M. K., LaRoque, S. J., Carlstrom, J. E., Reese, E. D., and Dawson, K. S. (2006). Determination of the Cosmic Distance Scale from Sunyaev-Zel'dovich Effect and Chandra X-Ray Measurements of High-Redshift Galaxy Clusters. *ApJ*, 647:25–54.

Bond, J. R., Cole, S., Efstathiou, G., and Kaiser, N. (1991). Excursion set mass functions for hierarchical Gaussian fluctuations. *ApJ*, 379:440–460.

Borgani, S., Diaferio, A., Dolag, K., and Schindler, S. (2008a). Thermodynamical Properties of the ICM from Hydrodynamical Simulations. *Space Sci. Rev.*, 134:269–293.

Borgani, S., Fabjan, D., Tornatore, L., Schindler, S., Dolag, K., and Diaferio, A. (2008b). The Chemical Enrichment of the ICM from Hydrodynamical Simulations. *Space Sci. Rev.*, 134:379–403.

Borgani, S. and Kravtsov, A. (2009). Cosmological simulations of galaxy clusters. *arXiv: 0906.4370*.

Boselli, A. and Gavazzi, G. (2006). Environmental Effects on Late-Type Galaxies in Nearby Clusters. *PASP*, 118:517–559.

Brough, S., Proctor, R., Forbes, D. A., Couch, W. J., Collins, C. A., Burke, D. J., and Mann, R. G. (2007). Spatially resolved kinematics and stellar populations of brightest cluster and group galaxies. *MNRAS*, 378:1507–1530.

Bullock, J. S., Kolatt, T. S., Sigad, Y., Somerville, R. S., Kravtsov, A. V., Klypin, A. A., Primack, J. R., and Dekel, A. (2001). Profiles of dark haloes: evolution, scatter and environment. *MNRAS*, 321:559–575.

Buote, D. A. and Tsai, J. C. (1996). Quantifying the Morphologies and Dynamical Evolution of Galaxy Clusters. II. Application to a Sample of ROSAT Clusters. *ApJ*, 458:27–+.

Burenin, R. A., Vikhlinin, A., Hornstrup, A., Ebeling, H., Quintana, H., and Mescheryakov, A. (2007). The 400 Square Degree ROSAT PSPC Galaxy Cluster Survey: Catalog and Statistical Calibration. *ApJS*, 172:561–582.

Burns, J. O. (1990). The radio properties of cD galaxies in Abell clusters. I - an X-ray selected sample. *AJ*, 99:14–30.

Butcher, H. and Oemler, Jr., A. (1978). The evolution of galaxies in clusters. II - The galaxy content of nearby clusters. *ApJ*, 226:559–565.

Carlstrom, J. E., Holder, G. P., and Reese, E. D. (2002). Cosmology with the Sunyaev-Zel'dovich Effect. *ARA&A*, 40:643–680.

Carroll, S. M., Press, W. H., and Turner, E. L. (1992). The cosmological constant. *ARA&A*, 30:499–542.

Cash, W. (1979). Parameter estimation in astronomy through application of the likelihood ratio. *ApJ*, 228:939–947.

Cavagnolo, K. W., Donahue, M., Voit, G. M., and Sun, M. (2008). An Entropy Threshold for Strong Hα and Radio Emission in the Cores of Galaxy Clusters. *ApJ*, 683:L107–L110.

Cavaliere, A., Danese, L., and de Zotti, G. (1977). Unborn clusters. *ApJ*, 217:6–15.

Cavaliere, A. and Fusco-Femiano, R. (1976). X-rays from hot plasma in clusters of galaxies. *A&A*, 49:137–144.

Cavaliere, A. and Fusco-Femiano, R. (1978). The Distribution of Hot Gas in Clusters of Galaxies. *A&A*, 70:677–+.

Chandrasekhar, S. (1950). *Radiative transfer, New York: Dover, 1950.*

Churazov, E., Brüggen, M., Kaiser, C. R., Böhringer, H., and Forman, W. (2001). Evolution of Buoyant Bubbles in M87. *ApJ*, 554:261–273.

Clowe, D., Bradač, M., Gonzalez, A. H., Markevitch, M., Randall, S. W., Jones, C., and Zaritsky, D. (2006). A Direct Empirical Proof of the Existence of Dark Matter. *ApJ*, 648:L109–L113.

Cole, S., Percival, W. J., Peacock, J. A., Norberg, P., Baugh, C. M., Frenk, C. S., Baldry, I., Bland-Hawthorn, J., Bridges, T., Cannon, R., Colless, M., Collins, C., Couch, W., Cross, N. J. G., Dalton, G., Eke, V. R., De Propris, R., Driver, S. P., Efstathiou, G., Ellis, R. S., Glazebrook, K., Jackson, C., Jenkins, A., Lahav, O., Lewis, I., Lumsden, S., Maddox, S., Madgwick, D., Peterson, B. A., Sutherland, W., and Taylor, K. (2005). The 2dF Galaxy Redshift Survey: power-spectrum analysis of the final data set and cosmological implications. *MNRAS*, 362:505–534.

Collins, C. A., Guzzo, L., Böhringer, H., Schuecker, P., Chincarini, G., Cruddace, R., De Grandi, S., MacGillivray, H. T., Neumann, D. M., Schindler, S., Shaver, P., and Voges, W. (2000). The ROSAT-ESO Flux-Limited X-ray (REFLEX) galaxy cluster survey - II. The spatial correlation function. *MNRAS*, 319:939–948.

Cooper, M. C., Newman, J. A., Weiner, B. J., Yan, R., Willmer, C. N. A., Bundy, K., Coil, A. L., Conselice, C. J., Davis, M., Faber, S. M., Gerke, B. F., Guhathakurta, P., Koo, D. C., and Noeske, K. G. (2008). The DEEP2 Galaxy Redshift Survey: the role of galaxy environment in the cosmic star formation history. *MNRAS*, 383:1058–1078.

Crain, R. A., Eke, V. R., Frenk, C. S., Jenkins, A., McCarthy, I. G., Navarro, J. F., and Pearce, F. R. (2007). The baryon fraction of ΛCDM haloes. *MNRAS*, 377:41–49.

Cristiani, S., Trentini, S., La Franca, F., Aretxaga, I., Andreani, P., Vio, R., and Gemmo, A. (1996). The optical variability of QSOs. *A&A*, 306:395–+.

Crook, A. C., Huchra, J. P., Martimbeau, N., Masters, K. L., Jarrett, T., and Macri, L. M. (2007). Groups of Galaxies in the Two Micron All Sky Redshift Survey. *ApJ*, 655:790–813.

Da Rocha, C., Ziegler, B. L., and Mendes de Oliveira, C. (2008). Intragroup diffuse light in compact groups of galaxies - II. HCG 15, 35 and 51. *MNRAS*, 388:1433–1443.

da Silva, A. C., Kay, S. T., Liddle, A. R., and Thomas, P. A. (2004). Hydrodynamical simulations of the Sunyaev-Zel'dovich effect: cluster scaling relations and X-ray properties. *MNRAS*, 348:1401–1408.

Davis, J. E. (2001). The Formal Underpinnings of the Response Functions Used in X-Ray Spectral Analysis. *ApJ*, 548:1010–1019.

De Luca, A. and Molendi, S. (2004). The 2-8 keV cosmic X-ray background spectrum as observed with XMM-Newton. *A&A*, 419:837–848.

De Lucia, G. and Blaizot, J. (2007). The hierarchical formation of the brightest cluster galaxies. *MNRAS*, 375:2–14.

de Plaa, J., Werner, N., Bleeker, J. A. M., Vink, J., Kaastra, J. S., and Méndez, M. (2007). Constraining supernova models using the hot gas in clusters of galaxies. *A&A*, 465:345–355.

den Herder, J. W., Brinkman, A. C., Kahn, S. M., Branduardi-Raymont, G., Thomsen, K., Aarts, H., Audard, M., Bixler, J. V., den Boggende, A. J., Cottam, J., Decker, T., Dubbeldam, L., Erd, C., Goulooze, H., Güdel, M., Guttridge, P., Hailey, C. J., Janabi, K. A., Kaastra, J. S., de Korte, P. A. J., van Leeuwen, B. J., Mauche, C., McCalden, A. J., Mewe, R., Naber, A., Paerels, F. B., Peterson, J. R., Rasmussen, A. P., Rees, K., Sakelliou, I., Sako, M., Spodek, J., Stern, M., Tamura, T., Tandy, J., de Vries, C. P., Welch, S., and Zehnder, A. (2001). The Reflection Grating Spectrometer on board XMM-Newton. *A&A*, 365:L7–L17.

Diaferio, A., Schindler, S., and Dolag, K. (2008). Clusters of Galaxies: Setting the Stage. *Space Sci. Rev.*, 134:7–24.

Dickey, J. M. and Lockman, F. J. (1990). H I in the Galaxy. *ARA&A*, 28:215–261.

Dietrich, J. P., Erben, T., Lamer, G., Schneider, P., Schwope, A., Hartlap, J., and Maturi, M. (2007). BLOX: the Bonn lensing, optical, and X-ray selected galaxy clusters. I. Cluster catalog construction. *A&A*, 470:821–834.

Dodelson, S. (2003). *Modern Cosmology, Academy Press, 2003*.

Dolag, K., Borgani, S., Schindler, S., Diaferio, A., and Bykov, A. M. (2008a). Simulation Techniques for Cosmological Simulations. *Space Sci. Rev.*, 134:229–268.

Dolag, K., Bykov, A. M., and Diaferio, A. (2008b). Non-Thermal Processes in Cosmological Simulations. *Space Sci. Rev.*, 134:311–335.

Dressler, A. (1980). Galaxy morphology in rich clusters - Implications for the formation and evolution of galaxies. *ApJ*, 236:351–365.

Dressler, A., Smail, I., Poggianti, B. M., Butcher, H., Couch, W. J., Ellis, R. S., and Oemler, Jr., A. (1999). A Spectroscopic Catalog of 10 Distant Rich Clusters of Galaxies. *ApJS*, 122:51–80.

Dubinski, J. (1998). The Origin of the Brightest Cluster Galaxies. *ApJ*, 502:141–+.

Egami, E., Misselt, K. A., Rieke, G. H., Wise, M. W., Neugebauer, G., Kneib, J., Le Floc'h, E., Smith, G. P., Blaylock, M., Dole, H., Frayer, D. T., Huang, J., Krause, O., Papovich, C., Pérez-González, P. G., and Rigby, J. R. (2006a). Spitzer Observations of the Brightest Galaxies in X-Ray-Luminous Clusters. *ApJ*, 647:922–933.

Egami, E., Rieke, G. H., Fadda, D., and Hines, D. C. (2006b). A Large Mass of H_2 in the Brightest Cluster Galaxy in Zwicky 3146. *ApJ*, 652:L21–L24.

Einasto, J. (1965). Influence of the atmospheric and instrumental dispersion on the brightness distribution in a galaxy. *Trudy Inst. Astrofiz. Alma-Ata 51, 87*.

Einasto, J. (2009). Dark Matter. *arXiv: 0901.0632*.

Eke, V. R., Baugh, C. M., Cole, S., Frenk, C. S., Norberg, P., Peacock, J. A., Baldry, I. K., Bland-Hawthorn, J., Bridges, T., Cannon, R., Colless, M., Collins, C., Couch, W., Dalton, G., de Propris, R., Driver, S. P., Efstathiou, G., Ellis, R. S., Glazebrook, K., Jackson, C., Lahav, O., Lewis, I., Lumsden, S., Maddox, S., Madgwick, D., Peterson, B. A., Sutherland, W., and Taylor, K. (2004). Galaxy groups in the 2dFGRS: the group-finding algorithm and the 2PIGG catalogue. *MNRAS*, 348:866–878.

Eke, V. R., Navarro, J. F., and Frenk, C. S. (1998). The Evolution of X-Ray Clusters in a Low-Density Universe. *ApJ*, 503:569–+.

Elbaz, D., Daddi, E., Le Borgne, D., Dickinson, M., Alexander, D. M., Chary, R., Starck, J., Brandt, W. N., Kitzbichler, M., MacDonald, E., Nonino, M., Popesso, P., Stern, D., and Vanzella, E. (2007). The reversal of the star formation-density relation in the distant universe. *A&A*, 468:33–48.

Ettori, S. (2000). Note on a polytropic β-model to fit the X-ray surface brightness of clusters of galaxies. *MNRAS*, 311:313–316.

Evrard, A. E. (1990). Formation and evolution of X-ray clusters - A hydrodynamic simulation of the intracluster medium. *ApJ*, 363:349–366.

Fabian, A. C. and Nulsen, P. E. J. (1977). Subsonic accretion of cooling gas in clusters of galaxies. *MNRAS*, 180:479–484.

Fabian, A. C., Sanders, J. S., Allen, S. W., Crawford, C. S., Iwasawa, K., Johnstone, R. M., Schmidt, R. W., and Taylor, G. B. (2003a). A deep Chandra observation of the Perseus cluster: shocks and ripples. *MNRAS*, 344:L43–L47.

Fabian, A. C., Sanders, J. S., Crawford, C. S., Conselice, C. J., Gallagher, J. S., and Wyse, R. F. G. (2003b). The relationship between the optical Hα filaments and the X-ray emission in the core of the Perseus cluster. *MNRAS*, 344:L48–L52.

Fabian, A. C., Sanders, J. S., Taylor, G. B., Allen, S. W., Crawford, C. S., Johnstone, R. M., and Iwasawa, K. (2006). A very deep Chandra observation of the Perseus cluster: shocks, ripples and conduction. *MNRAS*, 366:417–428.

Fakhouri, O., Ma, C., and Boylan-Kolchin, M. (2010). The merger rates and mass assembly histories of dark matter haloes in the two Millennium simulations. *MNRAS*, 406:2267–2278.

Fassbender, R. (2008). Studying Cosmic Evolution with the XMM-Newton Distant Cluster Project: X-ray Luminous Galaxy Clusters at $z >\sim 1$ and their Galaxy Populations. *arXiv: 0806.0861*.

Fassbender, R., Böhringer, H., Santos, J. S., Pratt, G. W., Šuhada, R., Kohnert, J., Lerchster, M., Rovilos, E., Pierini, D., Chon, G., Schwope, A. D., Lamer, G., Mühlegger, M., Rosati, P., Quintana, H., Nastasi, A., de Hoon, A., Seitz, S., and Mohr, J. J. (2011a). A pan-chromatic view of the galaxy cluster XMMU J1230.3+1339 at z = 0.975. Observing the assembly of a massive system. *A&A*, 527:A78+.

Fassbender, R., Nastasi, A., Böhringer, H., Šuhada, R., Santos, J. S., Rosati, P., Pierini, D., Mühlegger, M., Quintana, H., Schwope, A. D., Lamer, G., de Hoon, A., Kohnert, J., Pratt, G. W., and Mohr, J. J. (2011b). The X-ray luminous galaxy cluster XMMU J1007.4+1237 at z = 1.56. The dawn of starburst activity in cluster cores. *A&A*, 527:L10+.

Feldmeier, J. J., Ciardullo, R., Jacoby, G. H., and Durrell, P. R. (2004a). Intracluster Planetary Nebulae in the Virgo Cluster. III. Luminosity of the Intracluster Light and Tests of the Spatial Distribution. *ApJ*, 615:196–208.

Feldmeier, J. J., Mihos, J. C., Morrison, H. L., Harding, P., Kaib, N., and Dubinski, J. (2004b). Deep CCD Surface Photometry of Galaxy Clusters. II. Searching for Intracluster Starlight in Non-cD clusters. *ApJ*, 609:617–637.

Finn, R. A., Desai, V., Rudnick, G., Poggianti, B., Bell, E. F., Hinz, J., Jablonka, P., Milvang-Jensen, B., Moustakas, J., Rines, K., and Zaritsky, D. (2010). Dust-obscured Star Formation in Intermediate Redshift Galaxy Clusters. *ApJ*, 720:87–98.

Finoguenov, A., Guzzo, L., Hasinger, G., Scoville, N. Z., Aussel, H., Böhringer, H., Brusa, M., Capak, P., Cappelluti, N., Comastri, A., Giodini, S., Griffiths, R. E., Impey, C., Koekemoer, A. M., Kneib, J., Leauthaud, A., Le Fèvre, O., Lilly, S., Mainieri, V., Massey, R., McCracken, H. J., Mobasher, B., Murayama, T., Peacock, J. A., Sakelliou, I., Schinnerer, E., Silverman, J. D., Smolčić, V., Taniguchi, Y., Tasca, L., Taylor, J. E., Trump, J. R., and Zamorani, G. (2007). The XMM-Newton Wide-Field Survey in the COSMOS Field: Statistical Properties of Clusters of Galaxies. *ApJS*, 172:182–195.

Finoguenov, A., Watson, M. G., Tanaka, M., Simpson, C., Cirasuolo, M., Dunlop, J. S., Peacock, J. A., Farrah, D., Akiyama, M., Ueda, Y., Smolčić, V., Stewart, G., Rawlings, S., van Breukelen, C., Almaini, O., Clewley, L., Bonfield, D. G., Jarvis, M. J., Barr, J. M., Foucaud, S., McLure, R. J., Sekiguchi, K., and Egami, E. (2010). X-ray groups and clusters of galaxies in the Subaru-XMM Deep Field. *MNRAS*, 403:2063–2076.

Foley, R. J., Andersson, K., Bazin, G., de Haan, T., Ruel, J., Ade, P. A. R., Aird, K. A., Armstrong, R., Ashby, M. L. N., Bautz, M., Benson, B. A., Bleem, L. E., Bonamente, M., Brodwin, M., Carlstrom, J. E., Chang, C. L., Clocchiatti, A., Crawford, T. M., Crites, A. T., Desai, S., Dobbs, M. A., Dudley, J. P., Fazio, G. G., Forman, W. R., Garmire, G., George, E. M., Gladders, M. D., Gonzalez, A. H., Halverson, N. W., High, F. W., Holder, G. P., Holzapfel, W. L., Hoover, S., Hrubes, J. D., Jones, C., Joy, M., Keisler, R., Knox, L., Lee, A. T., Leitch, E. M., Lueker, M., Luong-Van, D., Marrone, D. P., McMahon, J. J., Mehl, J., Meyer, S. S., Mohr, J. J., Montroy, T. E., Murray, S. S., Padin, S., Plagge, T., Pryke, C., Reichardt, C. L., Rest, A., Ruhl, J. E., Saliwanchik, B. R., Saro, A., Schaffer, K. K., Shaw, L., Shirokoff, E., Song, J., Spieler, H. G., Stalder, B., Stanford, S. A., Staniszewski, Z., Stark, A. A., Story, K., Stubbs, C. W., Vanderlinde, K., Vieira, J. D., Vikhlinin, A., Williamson, R., and Zenteno, A. (2011). Discovery and Cosmological Implications of SPT-CL J2106-5844, the Most Massive Known Cluster at $z > 1$. *arXiv: 1101.1286*.

Forman, W., Jones, C., Churazov, E., Markevitch, M., Nulsen, P., Vikhlinin, A., Begelman, M., Böhringer, H., Eilek, J., Heinz, S., Kraft, R., Owen, F., and Pahre, M. (2007). Filaments, Bubbles, and Weak Shocks in the Gaseous Atmosphere of M87. *ApJ*, 665:1057–1066.

Friedrich, P., Bräuninger, H., Budau, B., Burkert, W., Eder, J., Freyberg, M. J., Hartner, G., Mühlegger, M., Predehl, P., Erhard, M., Gutruf, S., Jugler, D., Kampf, D., Borghi, G., Citterio, O., Rossi, M., Valsecchi, G., Vernani, D., and Zimmermann, M. (2008). Design and development of the eROSITA x-ray mirrors. In *Society of Photo-Optical Instrumentation Engineers (SPIE) Conference Series*, volume 7011 of *Presented at the Society of Photo-Optical Instrumentation Engineers (SPIE) Conference*.

Garilli, B., Fumana, M., Franzetti, P., Paioro, L., Scodeggio, M., Le Fèvre, O., Paltani, S., and

Scaramella, R. (2010). EZ: A Tool For Automatic Redshift Measurement. *PASP*, 122:827–838.

Geller, M. J. and Huchra, J. P. (1983). Groups of galaxies. III - The CfA survey. *ApJS*, 52:61–87.

Gerke, B. F., Newman, J. A., Faber, S. M., Cooper, M. C., Croton, D. J., Davis, M., Willmer, C. N. A., Yan, R., Coil, A. L., Guhathakurta, P., Koo, D. C., and Weiner, B. J. (2007). The DEEP2 galaxy redshift survey: the evolution of the blue fraction in groups and the field. *MNRAS*, 376:1425–1444.

Giocoli, C., Moreno, J., Sheth, R. K., and Tormen, G. (2007). An improved model for the formation times of dark matter haloes. *MNRAS*, 376:977–983.

Giodini, S., Pierini, D., Finoguenov, A., Pratt, G. W., Böhringer, H., Leauthaud, A., Guzzo, L., Aussel, H., Bolzonella, M., Capak, P., Elvis, M., Hasinger, G., Ilbert, O., Kartaltepe, J. S., Koekemoer, A. M., Lilly, S. J., Massey, R., McCracken, H. J., Rhodes, J., Salvato, M., Sanders, D. B., Scoville, N. Z., Sasaki, S., Smolcic, V., Taniguchi, Y., Thompson, D., and the COSMOS Collaboration (2009). Stellar and Total Baryon Mass Fractions in Groups and Clusters Since Redshift 1. *ApJ*, 703:982–993.

Gladders, M. D. and Yee, H. K. C. (2000). A New Method For Galaxy Cluster Detection. I. The Algorithm. *AJ*, 120:2148–2162.

Gladders, M. D. and Yee, H. K. C. (2005). The Red-Sequence Cluster Survey. I. The Survey and Cluster Catalogs for Patches RCS 0926+37 and RCS 1327+29. *ApJS*, 157:1–29.

Gobat, R., Daddi, E., Onodera, M., Finoguenov, A., Renzini, A., Arimoto, N., Bouwens, R., Brusa, M., Chary, R., Cimatti, A., Dickinson, M., Kong, X., and Mignoli, M. (2011). A mature cluster with X-ray emission at z = 2.07. *A&A*, 526:A133+.

Gregory, P. C., Vavasour, J. D., Scott, W. K., and Condon, J. J. (1994). The Parkes-MIT-NRAO (PMN) map catalog of radio sources covering -88 deg less than delta less than -37 deg at 4.85GHz. *ApJS*, 90:173–177.

Groves, B. A., Heckman, T. M., and Kauffmann, G. (2006). Emission-line diagnostics of low-metallicity active galactic nuclei. *MNRAS*, 371:1559–1569.

Guzzo, L., Schuecker, P., Böhringer, H., Collins, C. A., Ortiz-Gil, A., de Grandi, S., Edge, A. C., Neumann, D. M., Schindler, S., Altucci, C., and Shaver, P. A. (2009). The REFLEX galaxy cluster survey. VIII. Spectroscopic observations and optical atlas,. *A&A*, 499:357–369.

Haiman, Z., Allen, S., Bahcall, N., Bautz, M., Böhringer, H., Borgani, S., Bryan, G., Cabrera, B., Canizares, C., Citterio, O., Evrard, A., Finoguenov, A., Griffiths, R., Hasinger, G., Henry, P., Jahoda, K., Jernigan, G., Kahn, S., Lamb, D., Majumdar, S., Mohr, J., Molendi, S., Mushotzky, R., Pareschi, G., Peterson, J., Petre, R., Predehl, P., Rasmussen, A., Ricker, G., Ricker, P., Rosati, P., Sanderson, A., Stanford, A., Voit, M., Wang, S., White, N., and White, S. (2005). An X-ray Galaxy Cluster Survey for Investigations of Dark Energy. *arXiv: 0507013*.

Haiman, Z., Mohr, J. J., and Holder, G. P. (2001). Constraints on Cosmological Parameters from Future Galaxy Cluster Surveys. *ApJ*, 553:545–561.

Hayashi, M., Kodama, T., Koyama, Y., Tanaka, I., Shimasaku, K., and Okamura, S. (2010). High star formation activity in the central region of a distant cluster at z = 1.46. *MNRAS*, 402:1980–1990.

Henry, J. P., Salvato, M., Finoguenov, A., Bouche, N., Brunner, H., Burwitz, V., Buschkamp, P., Egami, E., Förster-Schreiber, N., Fotopoulou, S., Genzel, R., Hasinger, G., Mainieri, V., Rovilos, M., and Szokoly, G. (2010). An X-ray-selected Galaxy Cluster in the Lockman Hole at Redshift 1.753. *ApJ*, 725:615–624.

High, F. W., Stalder, B., Song, J., Ade, P. A. R., Aird, K. A., Allam, S. S., Armstrong, R., Barkhouse, W. A., Benson, B. A., Bertin, E., Bhattacharya, S., Bleem, L. E., Brodwin, M., Buckley-Geer, E. J., Carlstrom, J. E., Challis, P., Chang, C. L., Crawford, T. M., Crites, A. T., de Haan, T., Desai, S., Dobbs, M. A., Dudley, J. P., Foley, R. J., George, E. M., Gladders, M., Halverson, N. W., Hamuy, M., Hansen, S. M., Holder, G. P., Holzapfel, W. L., Hrubes, J. D., Joy, M., Keisler, R., Lee, A. T., Leitch, E. M., Lin, H., Lin, Y., Loehr, A., Lueker, M., Marrone, D., McMahon, J. J., Mehl, J., Meyer, S. S., Mohr, J. J., Montroy, T. E., Morell, N., Ngeow, C., Padin, S., Plagge, T., Pryke, C., Reichardt, C. L., Rest, A., Ruel, J., Ruhl, J. E., Schaffer, K. K., Shaw, L., Shirokoff, E., Smith, R. C., Spieler, H. G., Staniszewski, Z., Stark, A. A., Stubbs, C. W., Tucker, D. L., Vanderlinde, K., Vieira, J. D., Williamson, R., Wood-Vasey, W. M., Yang, Y., Zahn, O., and Zenteno, A. (2010). Optical Redshift and Richness Estimates for Galaxy Clusters Selected with the Sunyaev-Zel'dovich Effect from 2008 South Pole Telescope Observations. *ApJ*, 723:1736–1747.

Hilton, M., Lloyd-Davies, E., Stanford, S. A., Stott, J. P., Collins, C. A., Romer, A. K., Hosmer, M., Hoyle, B., Kay, S. T., Liddle, A. R., Mehrtens, N., Miller, C. J., Sahlén, M., and Viana, P. T. P. (2010). The XMM Cluster Survey: Active Galactic Nuclei and Starburst Galaxies in XMMXCS J2215.9-1738 at z = 1.46. *ApJ*, 718:133–147.

Hincks, A. D., Acquaviva, V., Ade, P. A. R., Aguirre, P., Amiri, M., Appel, J. W., Barrientos, L. F., Battistelli, E. S., Bond, J. R., Brown, B., Burger, B., Chervenak, J., Das, S., Devlin, M. J., Dicker, S. R., Doriese, W. B., Dunkley, J., Dünner, R., Essinger-Hileman, T., Fisher, R. P., Fowler, J. W., Hajian, A., Halpern, M., Hasselfield, M., Hernández-Monteagudo, C., Hilton, G. C., Hilton, M., Hlozek, R., Huffenberger, K. M., Hughes, D. H., Hughes, J. P., Infante, L., Irwin, K. D., Jimenez, R., Juin, J. B., Kaul, M., Klein, J., Kosowsky, A., Lau, J. M., Limon, M., Lin, Y., Lupton, R. H., Marriage, T. A., Marsden, D., Martocci, K., Mauskopf, P., Menanteau, F., Moodley, K., Moseley, H., Netterfield, C. B., Niemack, M. D., Nolta, M. R., Page, L. A., Parker, L., Partridge, B., Quintana, H., Reid, B., Sehgal, N., Sievers, J., Spergel, D. N., Staggs, S. T., Stryzak, O., Swetz, D. S., Switzer, E. R., Thornton, R., Trac, H., Tucker, C., Verde, L., Warne, R., Wilson, G., Wollack, E., and Zhao, Y. (2010). The Atacama Cosmology Telescope (ACT): Beam Profiles and First SZ Cluster Maps. *ApJS*, 191:423–438.

Hogg, D. W. (1999). Distance measures in cosmology. *arXiv: 9905116*.

Hu, W. and Kravtsov, A. V. (2003). Sample Variance Considerations for Cluster Surveys. *ApJ*, 584:702–715.

Huchra, J. P. and Geller, M. J. (1982). Groups of galaxies. I - Nearby groups. *ApJ*, 257:423–437.

Jarosik, N., Bennett, C. L., Dunkley, J., Gold, B., Greason, M. R., Halpern, M., Hill, R. S., Hinshaw, G., Kogut, A., Komatsu, E., Larson, D., Limon, M., Meyer, S. S., Nolta, M. R., Odegard, N., Page, L., Smith, K. M., Spergel, D. N., Tucker, G. S., Weiland, J. L., Wollack, E., and Wright, E. L. (2011). Seven-year Wilkinson Microwave Anisotropy Probe (WMAP) Observations: Sky Maps, Systematic Errors, and Basic Results. *ApJS*, 192:14–+.

Jeltema, T. E., Canizares, C. R., Bautz, M. W., and Buote, D. A. (2005). The Evolution of Structure in X-Ray Clusters of Galaxies. *ApJ*, 624:606–629.

Jeltema, T. E., Hallman, E. J., Burns, J. O., and Motl, P. M. (2008). Cluster Structure in Cosmological Simulations. I. Correlation to Observables, Mass Estimates, and Evolution. *ApJ*, 681:167–186.

Jenkins, A., Frenk, C. S., White, S. D. M., Colberg, J. M., Cole, S., Evrard, A. E., Couchman, H. M. P., and Yoshida, N. (2001). The mass function of dark matter haloes. *MNRAS*, 321:372–384.

Johnston, D. E., Sheldon, E. S., Wechsler, R. H., Rozo, E., Koester, B. P., Frieman, J. A., McKay, T. A., Evrard, A. E., Becker, M. R., and Annis, J. (2007). Cross-correlation Weak Lensing of SDSS galaxy Clusters II: Cluster Density Profiles and the Mass–Richness Relation. *arXiv: 0709.1159*.

Jones, C. and Forman, W. (1984). The structure of clusters of galaxies observed with Einstein. *ApJ*, 276:38–55.

Jones, D. H., Saunders, W., Colless, M., Read, M. A., Parker, Q. A., Watson, F. G., Campbell, L. A., Burkey, D., Mauch, T., Moore, L., Hartley, M., Cass, P., James, D., Russell, K., Fiegert, K., Dawe, J., Huchra, J., Jarrett, T., Lahav, O., Lucey, J., Mamon, G. A., Proust, D., Sadler, E. M., and Wakamatsu, K. (2004). The 6dF Galaxy Survey: samples, observational techniques and the first data release. *MNRAS*, 355:747–763.

Kaastra, J. S. (1992). An X-ray Spectral Code for Optically Thin Plasmas. *Internal SRON-Leiden Report, Updated Version 2.0*, 1.

Kaastra, J. S., Bykov, A. M., Schindler, S., Bleeker, J. A. M., Borgani, S., Diaferio, A., Dolag, K., Durret, F., Nevalainen, J., Ohashi, T., Paerels, F. B. S., Petrosian, V., Rephaeli, Y., Richter, P., Schaye, J., and Werner, N. (2008a). Clusters of Galaxies: Beyond the Thermal View. *Space Sci. Rev.*, 134:1–6.

Kaastra, J. S., Paerels, F. B. S., Durret, F., Schindler, S., and Richter, P. (2008b). Thermal Radiation Processes. *Space Sci. Rev.*, 134:155–190.

Kaiser, N. (1986). Evolution and clustering of rich clusters. *MNRAS*, 222:323–345.

Kalberla, P. M. W., Burton, W. B., Hartmann, D., Arnal, E. M., Bajaja, E., Morras, R., and Pöppel, W. G. L. (2005). The Leiden/Argentine/Bonn (LAB) Survey of Galactic HI. Final data release of the combined LDS and IAR surveys with improved stray-radiation corrections. *A&A*, 440:775–782.

Khedekar, S. and Majumdar, S. (2010). Using clusters in Sunyaev-Zel'dovich effect plus x-ray surveys as an ensemble of rulers to constrain cosmology. *Phys. Rev. D*, 82(8):081301–+.

King, I. R. (1966). The structure of star clusters. IV. Photoelectric surface photometry in nine globular clusters. *AJ*, 71:276–+.

Kitayama, T. and Suto, Y. (1996). Semianalytic Predictions for Statistical Properties of X-Ray Clusters of Galaxies in Cold Dark Matter Universes. *ApJ*, 469:480–+.

Kodama, T. and Arimoto, N. (1997). Origin of the colour-magnitude relation of elliptical galaxies. *A&A*, 320:41–53.

Kompaneets, A. A. (1956). . *Zh.E.F.T.*, 31:876–+.

Kravtsov, A. V., Vikhlinin, A., and Nagai, D. (2006). A New Robust Low-Scatter X-Ray Mass Indicator for Clusters of Galaxies. *ApJ*, 650:128–136.

Krick, J. E. and Bernstein, R. A. (2007). Diffuse Optical Light in Galaxy Clusters. II. Correlations with Cluster Properties. *AJ*, 134:466–493.

Kuntz, K. D. and Snowden, S. L. (2008a). The EPIC-MOS particle-induced background spectra. *A&A*, 478:575–596.

Kuntz, K. D. and Snowden, S. L. (2008b). The EPIC-MOS particle-induced background spectra. *A&A*, 478:575–596.

Kurtz, M. J. and Mink, D. J. (1998). RVSAO 2.0: Digital Redshifts and Radial Velocities. *PASP*, 110:934–977.

Lau, E. T., Kravtsov, A. V., and Nagai, D. (2009). Residual Gas Motions in the Intracluster Medium and Bias in Hydrostatic Measurements of Mass Profiles of Clusters. *ApJ*, 705:1129–1138.

Lewis, G. F., Babul, A., Katz, N., Quinn, T., Hernquist, L., and Weinberg, D. H. (2000). The Effects of Gasdynamics, Cooling, Star Formation, and Numerical Resolution in Simulations of Cluster Formation. *ApJ*, 536:623–644.

Lidman, C., Rosati, P., Tanaka, M., Strazzullo, V., Demarco, R., Mullis, C., Ageorges, N., Kissler-Patig, M., Petr-Gotzens, M. G., and Selman, F. (2008). HAWK-I imaging of the X-ray luminous galaxy cluster XMMU J2235.3-2557. The red sequence at z = 1.39. *A&A*, 489:981–988.

Liedahl, D. A., Osterheld, A. L., and Goldstein, W. H. (1995). New calculations of Fe L-shell X-ray spectra in high-temperature plasmas. *ApJ*, 438:L115–L118.

Loh, Y. and Strauss, M. A. (2006). The bright end of the luminosity function of red sequence galaxies. *MNRAS*, 366:373–386.

Lovisari, L., Schindler, S., and Kapferer, W. (2011). Inhomogeneous Metal Distribution in the Intra-Cluster Medium. *arXiv: 1101.2807*.

Lynden-Bell, D. (1967). Statistical mechanics of violent relaxation in stellar systems. *MNRAS*, 136:101–+.

Mackie, G. (1992). The stellar content of central dominant galaxies. II - Colors of cD envelopes. *ApJ*, 400:65–73.

Maddox, S. J., Efstathiou, G., Sutherland, W. J., and Loveday, J. (1990). The APM galaxy survey. I - APM measurements and star-galaxy separation. *MNRAS*, 243:692–712.

Mahdavi, A., Hoekstra, H., Babul, A., and Henry, J. P. (2008). Evidence for non-hydrostatic gas from the cluster X-ray to lensing mass ratio. *MNRAS*, 384:1567–1574.

Majumdar, S. and Mohr, J. J. (2003). Importance of Cluster Structural Evolution in Using X-Ray and Sunyaev-Zeldovich Effect Galaxy Cluster Surveys to Study Dark Energy. *ApJ*, 585:603–610.

Mantz, A., Allen, S. W., Ebeling, H., Rapetti, D., and Drlica-Wagner, A. (2010a). The observed growth of massive galaxy clusters - II. X-ray scaling relations. *MNRAS*, 406:1773–1795.

Mantz, A., Allen, S. W., Rapetti, D., and Ebeling, H. (2010b). The observed growth of massive galaxy clusters - I. Statistical methods and cosmological constraints. *MNRAS*, 406:1759–1772.

Markevitch, M. (1998). The L X-T Relation and Temperature Function for Nearby Clusters Revisited. *ApJ*, 504:27–+.

Markevitch, M., Gonzalez, A. H., David, L., Vikhlinin, A., Murray, S., Forman, W., Jones, C., and Tucker, W. (2002). A Textbook Example of a Bow Shock in the Merging Galaxy Cluster 1E 0657-56. *ApJ*, 567:L27–L31.

Markevitch, M. and Vikhlinin, A. (2007). Shocks and cold fronts in galaxy clusters. *Phys. Rep.*, 443:1–53.

Marriage, T. A., Acquaviva, V., Ade, P. A. R., Aguirre, P., Amiri, M., Appel, J. W., Barrientos, L. F., Battistelli, E. S., Bond, J. R., Brown, B., Burger, B., Chervenak, J., Das, S., Devlin, M. J., Dicker, S. R., Doriese, W. B., Dunkley, J., Dunner, R., Essinger-Hileman, T., Fisher, R. P., Fowler, J. W., Hajian, A., Halpern, M., Hasselfield, M., Hern'andez-Monteagudo, C., Hilton, G. C., Hilton, M., Hincks, A. D., Hlozek, R., Huffenberger, K. M., Hughes, D. H., Hughes, J. P., Infante, L., Irwin, K. D., Juin, J. B., Kaul, M., Klein, J., Kosowsky, A., Lau,

J. M., Limon, M., Lin, Y., Lupton, R. H., Marsden, D., Martocci, K., Mauskopf, P., Menanteau, F., Moodley, K., Moseley, H., Netterfield, C. B., Niemack, M. D., Nolta, M. R., Page, L. A., Parker, L., Partridge, B., Quintana, H., Reese, E. D., Reid, B., Sehgal, N., Sherwin, B. D., Sievers, J., Spergel, D. N., Staggs, S. T., Swetz, D. S., Switzer, E. R., Thornton, R., Trac, H., Tucker, C., Warne, R., Wilson, G., Wollack, E., and Zhao, Y. (2010). The Atacama Cosmology Telescope: Sunyaev Zel'dovich Selected Galaxy Clusters at 148 GHz in the 2008 Survey. *arXiv: 1010.1065*.

Marrone, D. P., Smith, G. P., Richard, J., Joy, M., Bonamente, M., Hasler, N., Hamilton-Morris, V., Kneib, J., Culverhouse, T., Carlstrom, J. E., Greer, C., Hawkins, D., Hennessy, R., Lamb, J. W., Leitch, E. M., Loh, M., Miller, A., Mroczkowski, T., Muchovej, S., Pryke, C., Sharp, M. K., and Woody, D. (2009). LoCuSS: A Comparison of Sunyaev-Zel'dovich Effect and Gravitational-Lensing Measurements of Galaxy Clusters. *ApJ*, 701:L114–L118.

Martig, M. and Bournaud, F. (2008). Triggering of merger-induced starbursts by the tidal field of galaxy groups and clusters. *MNRAS*, 385:L38–L42.

Mason, B. S., Myers, S. T., and Readhead, A. C. S. (2001). A Measurement of H_0 from the Sunyaev-Zeldovich Effect. *ApJ*, 555:L11–L15.

Matarrese, S., Coles, P., Lucchin, F., and Moscardini, L. (1997). Redshift evolution of clustering. *MNRAS*, 286:115–132.

Mathews, W. G. and Bregman, J. N. (1978). Radiative accretion flow onto giant galaxies in clusters. *ApJ*, 224:308–319.

Matsushita, K., Fukazawa, Y., Hughes, J. P., Kitaguchi, T., Makishima, K., Nakazawa, K., Ohashi, T., Ota, N., Tamura, T., Tozuka, M., Tsuru, T. G., Urata, Y., and Yamasaki, N. Y. (2007). Suzaku Observation of the Metallicity Distribution in the Intracluster Medium of the Fornax Cluster. *PASJ*, 59:327–338.

Mauch, T., Murphy, T., Buttery, H. J., Curran, J., Hunstead, R. W., Piestrzynski, B., Robertson, J. G., and Sadler, E. M. (2003). SUMSS: a wide-field radio imaging survey of the southern sky - II. The source catalogue. *MNRAS*, 342:1117–1130.

McInnes, R. N., Menanteau, F., Heavens, A. F., Hughes, J. P., Jimenez, R., Massey, R., Simon, P., and Taylor, A. (2009). First lensing measurements of SZ-detected clusters. *MNRAS*, 399:L84–L88.

McNamara, B. R. and Nulsen, P. E. J. (2007). Heating Hot Atmospheres with Active Galactic Nuclei. *ARA&A*, 45:117–175.

McNamara, B. R., Nulsen, P. E. J., Wise, M. W., Rafferty, D. A., Carilli, C., Sarazin, C. L., and Blanton, E. L. (2005). The heating of gas in a galaxy cluster by X-ray cavities and large-scale shock fronts. *Nature*, 433:45–47.

McNamara, B. R. and O'Connell, R. W. (1989). Star formation in cooling flows in clusters of galaxies. *AJ*, 98:2018–2043.

McNamara, B. R., Wise, M., Nulsen, P. E. J., David, L. P., Sarazin, C. L., Bautz, M., Markevitch, M., Vikhlinin, A., Forman, W. R., Jones, C., and Harris, D. E. (2000). Chandra X-Ray Observations of the Hydra A Cluster: An Interaction between the Radio Source and the X-Ray-emitting Gas. *ApJ*, 534:L135–L138.

Melin, J., Bartlett, J. G., Delabrouille, J., Arnaud, M., Piffaretti, R., and Pratt, G. W. (2011). The galaxy cluster Y_{SZ} - L_X and Y_{SZ} - M relations from the WMAP 5-yr data. *A&A*, 525:A139+.

Menanteau, F., Hughes, J. P., Barrientos, L. F., Deshpande, A. J., Hilton, M., Infante, L., Jimenez, R., Kosowsky, A., Moodley, K., Spergel, D., and Verde, L. (2010). Southern Cosmology Survey. II. Massive Optically Selected Clusters from 70 Square Degrees of the Sunyaev-Zel'dovich Effect Common Survey Area. *ApJS*, 191:340–351.

Menanteau, F., Hughes, J. P., Jimenez, R., Hernandez-Monteagudo, C., Verde, L., Kosowsky, A., Moodley, K., Infante, L., and Roche, N. (2009). Southern Cosmology Survey. I. Optical Cluster Detections and Predictions for the Southern Common-Area Millimeter-Wave Experiments. *ApJ*, 698:1221–1231.

Merritt, D., Graham, A. W., Moore, B., Diemand, J., and Terzić, B. (2006). Empirical Models for Dark Matter Halos. I. Nonparametric Construction of Density Profiles and Comparison with Parametric Models. *AJ*, 132:2685–2700.

Merritt, D., Navarro, J. F., Ludlow, A., and Jenkins, A. (2005). A Universal Density Profile for Dark and Luminous Matter? *ApJ*, 624:L85–L88.

Mewe, R., Gronenschild, E. H. B. M., and van den Oord, G. H. J. (1985). Calculated X-radiation from optically thin plasmas. V. *A&AS*, 62:197–254.

Milvang-Jensen, B., Noll, S., Halliday, C., Poggianti, B. M., Jablonka, P., Aragón-Salamanca, A., Saglia, R. P., Nowak, N., von der Linden, A., De Lucia, G., Pelló, R., Moustakas, J., Poirier, S., Bamford, S. P., Clowe, D. I., Dalcanton, J. J., Rudnick, G. H., Simard, L., White, S. D. M., and Zaritsky, D. (2008). Spectroscopy of clusters in the ESO distant cluster survey (EDisCS). II.. Redshifts, velocity dispersions, and substructure for clusters in the last 15 fields. *A&A*, 482:419–449.

Mohr, J. J., Fabricant, D. G., and Geller, M. J. (1993). An X-ray method for detecting substructure in galaxy clusters - Application to Perseus, A2256, Centaurus, Coma, and Sersic 40/6. *ApJ*, 413:492–505.

Molendi, S. and Pizzolato, F. (2001). Is the Gas in Cooling Flows Multiphase? *ApJ*, 560:194–200.

Molnar, S. M., Haiman, Z., Birkinshaw, M., and Mushotzky, R. F. (2004). Constraints on the Energy Content of the Universe from a Combination of Galaxy Cluster Observables. *ApJ*, 601:22–27.

Motl, P. M., Hallman, E. J., Burns, J. O., and Norman, M. L. (2005). The Integrated Sunyaev-Zeldovich Effect as a Superior Method for Measuring the Mass of Clusters of Galaxies. *ApJ*, 623:L63–L66.

Mühlegger, M. (2010). Simulated Observations of Galaxy Clusters for Current and Future X-ray Surveys. *PhD thesis, Technische Universität München*.

Mullis, C. R., McNamara, B. R., Quintana, H., Vikhlinin, A., Henry, J. P., Gioia, I. M., Hornstrup, A., Forman, W., and Jones, C. (2003). The 160 Square Degree ROSAT Survey: The Revised Catalog of 201 Clusters with Spectroscopic Redshifts. *ApJ*, 594:154–171.

Mullis, C. R., Rosati, P., Lamer, G., Böhringer, H., Schwope, A., Schuecker, P., and Fassbender, R. (2005). Discovery of an X-Ray-luminous Galaxy Cluster at z=1.4. *ApJ*, 623:L85–L88.

Murante, G., Arnaboldi, M., Gerhard, O., Borgani, S., Cheng, L. M., Diaferio, A., Dolag, K., Moscardini, L., Tormen, G., Tornatore, L., and Tozzi, P. (2004). The Diffuse Light in Simulations of Galaxy Clusters. *ApJ*, 607:L83–L86.

Nagai, D. (2006). The Impact of Galaxy Formation on the Sunyaev-Zel'dovich Effect of Galaxy Clusters. *ApJ*, 650:538–549.

Nagai, D., Vikhlinin, A., and Kravtsov, A. V. (2007). Testing X-Ray Measurements of Galaxy Clusters with Cosmological Simulations. *ApJ*, 655:98–108.

Navarro, J. F., Frenk, C. S., and White, S. D. M. (1997). A Universal Density Profile from Hierarchical Clustering. *ApJ*, 490:493–+.

Ness, J. U., with the XMM-Newton Community Support Team, and the XMM-Newton Science Operations Centre Team (2010). XMM-Newton Users' Handbook. 1.

Nevalainen, J., David, L., and Guainazzi, M. (2010). Cross-calibrating X-ray detectors with clusters of galaxies: an IACHEC study. *arXiv:1008.2102*.

Ngeow, C. C., Mohr, J. J., Barkhouse, W., Alam, T., Beldica, C., Cai, D., Daues, G., Duda, P., Annis, J., Lin, H., Tucker, D., Rest, A., Smith, C., Lin, Y., High, W., Hansen, S., Brodwin, M., Allam, S., and BCS Collaboration (2006). Application of the Dark Energy Survey Data Management System to the Blanco Cosmology Survey Data. In *American Astronomical Society Meeting Abstracts*, volume 38 of *Bulletin of the American Astronomical Society*, pages 929–+.

Norman, M. L. (2010). Simulating Galaxy Clusters. *arXiv: 1005.1100*.

Nulsen, P. E. J., David, L. P., McNamara, B. R., Jones, C., Forman, W. R., and Wise, M. (2002). Interaction of Radio Lobes with the Hot Intracluster Medium: Driving Convective Outflow in Hydra A. *ApJ*, 568:163–173.

Nulsen, P. E. J., McNamara, B. R., Wise, M. W., and David, L. P. (2005). The Cluster-Scale AGN Outburst in Hydra A. *ApJ*, 628:629–636.

Oemler, Jr., A. (1974). The Systematic Properties of Clusters of Galaxies. Photometry of 15 Clusters. *ApJ*, 194:1–20.

O'Hara, T. B., Mohr, J. J., Bialek, J. J., and Evrard, A. E. (2006). Effects of Mergers and Core Structure on the Bulk Properties of Nearby Galaxy Clusters. *ApJ*, 639:64–80.

Oort, J. H. (1932). The force exerted by the stellar system in the direction perpendicular to the galactic plane and some related problems. *Bull. Astron. Inst. Netherlands*, 6:249–+.

Ostriker, J. P. and Tremaine, S. D. (1975). Another evolutionary correction to the luminosity of giant galaxies. *ApJ*, 202:L113–L117.

Owen, F. N., Eilek, J. A., and Kassim, N. E. (2000). M87 at 90 Centimeters: A Different Picture. *ApJ*, 543:611–619.

Pacaud, F., Pierre, M., Adami, C., Altieri, B., Andreon, S., Chiappetti, L., Detal, A., Duc, P.-A., Galaz, G., Gueguen, A., Le Fèvre, J.-P., Hertling, G., Libbrecht, C., Melin, J.-B., Ponman, T. J., Quintana, H., Refregier, A., Sprimont, P.-G., Surdej, J., Valtchanov, I., Willis, J. P., Alloin, D., Birkinshaw, M., Bremer, M. N., Garcet, O., Jean, C., Jones, L. R., Le Fèvre, O., Maccagni, D., Mazure, A., Proust, D., Röttgering, H. J. A., and Trinchieri, G. (2007). The XMM-LSS survey: the Class 1 cluster sample over the initial 5 deg^2 and its cosmological modelling. *MNRAS*, 382:1289–1308.

Pacaud, F., Pierre, M., Refregier, A., Gueguen, A., Starck, J.-L., Valtchanov, I., Read, A. M., Altieri, B., Chiappetti, L., Gandhi, P., Garcet, O., Gosset, E., Ponman, T. J., and Surdej, J. (2006). The XMM Large-Scale Structure survey: the X-ray pipeline and survey selection function. *MNRAS*, 372:578–590.

Padmanabhan, T. (1999). Aspects of Gravitational Clustering. *arXiv: 9911374*.

Papovich, C., Momcheva, I., Willmer, C. N. A., Finkelstein, K. D., Finkelstein, S. L., Tran, K., Brodwin, M., Dunlop, J. S., Farrah, D., Khan, S. A., Lotz, J., McCarthy, P., McLure, R. J., Rieke, M., Rudnick, G., Sivanandam, S., Pacaud, F., and Pierre, M. (2010). A Spitzer-selected Galaxy Cluster at z = 1.62. *ApJ*, 716:1503–1513.

Peebles, P. J. E. (1993). *Principles Of Physical Cosmology, Princeton University Press, 1993*.

Penrose, R. (2005). *The Road To Reality, Vintage Books, 2005*.

Peterson, J. R. and Fabian, A. C. (2006). X-ray spectroscopy of cooling clusters. *Phys. Rep.*, 427:1–39.

Peterson, J. R., Kahn, S. M., Paerels, F. B. S., Kaastra, J. S., Tamura, T., Bleeker, J. A. M., Ferrigno, C., and Jernigan, J. G. (2003). High-Resolution X-Ray Spectroscopic Constraints on Cooling-Flow Models for Clusters of Galaxies. *ApJ*, 590:207–224.

Peterson, J. R., Paerels, F. B. S., Kaastra, J. S., Arnaud, M., Reiprich, T. H., Fabian, A. C., Mushotzky, R. F., Jernigan, J. G., and Sakelliou, I. (2001). X-ray imaging-spectroscopy of Abell 1835. *A&A*, 365:L104–L109.

Pierre, M., Chiappetti, L., Pacaud, F., Gueguen, A., Libbrecht, C., Altieri, B., Aussel, H., Gandhi, P., Garcet, O., Gosset, E., Paioro, L., Ponman, T. J., Read, A. M., Refregier, A., Starck, J.-L., Surdej, J., Valtchanov, I., Adami, C., Alloin, D., Alshino, A., Andreon, S., Birkinshaw, M., Bremer, M., Detal, A., Duc, P.-A., Galaz, G., Jones, L., Le Fèvre, J.-P., Le Fèvre, O., Maccagni, D., Mazure, A., Quintana, H., Röttgering, H. J. A., Sprimont, P.-G., Tasse, C., Trinchieri, G., and Willis, J. P. (2007). The XMM-Large Scale Structure catalogue: X-ray sources and associated optical data. Version I. *MNRAS*, 382:279–290.

Pierre, M., Pacaud, F., Juin, J. B., Melin, J. B., Clerc, N., and Corasaniti, P. S. (2010). Precision cosmology with a wide area XMM cluster survey. *arXiv: 1009.3182*.

Piffaretti, R. and Valdarnini, R. (2008). Total mass biases in X-ray galaxy clusters. *A&A*, 491:71–87.

Plagge, T., Benson, B. A., Ade, P. A. R., Aird, K. A., Bleem, L. E., Carlstrom, J. E., Chang, C. L., Cho, H., Crawford, T. M., Crites, A. T., de Haan, T., Dobbs, M. A., George, E. M., Hall, N. R., Halverson, N. W., Holder, G. P., Holzapfel, W. L., Hrubes, J. D., Joy, M., Keisler, R., Knox, L., Lee, A. T., Leitch, E. M., Lueker, M., Marrone, D., McMahon, J. J., Mehl, J., Meyer, S. S., Mohr, J. J., Montroy, T. E., Padin, S., Pryke, C., Reichardt, C. L., Ruhl, J. E., Schaffer, K. K., Shaw, L., Shirokoff, E., Spieler, H. G., Stalder, B., Staniszewski, Z., Stark, A. A., Vanderlinde, K., Vieira, J. D., Williamson, R., and Zahn, O. (2010). Sunyaev-Zel'dovich Cluster Profiles Measured with the South Pole Telescope. *ApJ*, 716:1118–1135.

Planck Collaboration, Ade, P. A. R., Aghanim, N., Arnaud, M., Ashdown, M., Aumont, J., Baccigalupi, C., Balbi, A., Banday, A. J., Barreiro, R. B., and et al. (2011a). Planck Early Results: The all-sky Early Sunyaev-Zeldovich cluster sample. *arXiv: 1101.2024*.

Planck Collaboration, Aghanim, N., Arnaud, M., Ashdown, M., Aumont, J., Baccigalupi, C., Balbi, A., Banday, A. J., Barreiro, R. B., Bartelmann, M., and et al. (2011b). Planck early results: Statistical analysis of Sunyaev-Zeldovich scaling relations for X-ray galaxy clusters. *arXiv: 1101.2043*.

Plionis, M., López-Cruz, O., and Hughes, D., editors (2008). *A Pan-Chromatic View of Clusters of Galaxies and the Large-Scale Structure*, volume 740 of *Lecture Notes in Physics, Berlin Springer Verlag*.

Poggianti, B. M., Smail, I., Dressler, A., Couch, W. J., Barger, A. J., Butcher, H., Ellis, R. S., and Oemler, Jr., A. (1999). The Star Formation Histories of Galaxies in Distant Clusters. *ApJ*, 518:576–593.

Poggianti, B. M., von der Linden, A., De Lucia, G., Desai, V., Simard, L., Halliday, C., Aragón-Salamanca, A., Bower, R., Varela, J., Best, P., Clowe, D. I., Dalcanton, J., Jablonka, P., Milvang-Jensen, B., Pello, R., Rudnick, G., Saglia, R., White, S. D. M., and Zaritsky, D. (2006). The Evolution of the Star Formation Activity in Galaxies and Its Dependence on Environment. *ApJ*, 642:188–215.

Postman, M., Lubin, L. M., Gunn, J. E., Oke, J. B., Hoessel, J. G., Schneider, D. P., and Christensen, J. A. (1996). The Palomar Distant Clusters Survey. I. The Cluster Catalog. *AJ*, 111:615–+.

Pratt, G. W. and Arnaud, M. (2003). Entropy scaling in galaxy clusters: Insights from an XMM-Newton observation of the poor cluster A1983. *A&A*, 408:1–16.

Pratt, G. W., Croston, J. H., Arnaud, M., and Böhringer, H. (2009). Galaxy cluster X-ray luminosity scaling relations from a representative local sample (REXCESS). *A&A*, 498:361–378.

Press, W. H. and Schechter, P. (1974). Formation of Galaxies and Clusters of Galaxies by Self-Similar Gravitational Condensation. *ApJ*, 187:425–438.

Puchwein, E., Springel, V., Sijacki, D., and Dolag, K. (2010). Intracluster stars in simulations with active galactic nucleus feedback. *MNRAS*, 406:936–951.

Rafferty, D. A., McNamara, B. R., Nulsen, P. E. J., and Wise, M. W. (2006). The Feedback-regulated Growth of Black Holes and Bulges through Gas Accretion and Starbursts in Cluster Central Dominant Galaxies. *ApJ*, 652:216–231.

Ramella, M., Boschin, W., Fadda, D., and Nonino, M. (2001). Finding galaxy clusters using Voronoi tessellations. *A&A*, 368:776–786.

Rasia, E., Ettori, S., Moscardini, L., Mazzotta, P., Borgani, S., Dolag, K., Tormen, G., Cheng, L. M., and Diaferio, A. (2006). Systematics in the X-ray cluster mass estimators. *MNRAS*, 369:2013–2024.

Reed, D., Gardner, J., Quinn, T., Stadel, J., Fardal, M., Lake, G., and Governato, F. (2003). Evolution of the mass function of dark matter haloes. *MNRAS*, 346:565–572.

Reed, D. S., Bower, R., Frenk, C. S., Jenkins, A., and Theuns, T. (2007). The halo mass function from the dark ages through the present day. *MNRAS*, 374:2–15.

Reiprich, T. H. (2001). *An X-Ray Flux-Limited Sample of Galaxy Clusters: Physical Properties and Cosmological Implications*. PhD thesis, Max-Planck-Institut für extraterrestrische Physik, P.O. Box 1312, 85741 Garching, Germany.

Reiprich, T. H. and Böhringer, H. (2002). The Mass Function of an X-Ray Flux-limited Sample of Galaxy Clusters. *ApJ*, 567:716–740.

Rephaeli, Y. (1995). Comptonization Of The Cosmic Microwave Background: The Sunyaev-Zeldovich Effect. *ARA&A*, 33:541–580.

Rephaeli, Y., Nevalainen, J., Ohashi, T., and Bykov, A. M. (2008). Nonthermal Phenomena in Clusters of Galaxies. *Space Sci. Rev.*, 134:71–92.

Reyes, R., Mandelbaum, R., Hirata, C., Bahcall, N., and Seljak, U. (2008). Improved optical mass tracer for galaxy clusters calibrated using weak lensing measurements. *MNRAS*, 390:1157–1169.

Richard, J., Smith, G. P., Kneib, J., Ellis, R. S., Sanderson, A. J. R., Pei, L., Targett, T. A., Sand, D. J., Swinbank, A. M., Dannerbauer, H., Mazzotta, P., Limousin, M., Egami, E., Jullo, E., Hamilton-Morris, V., and Moran, S. M. (2010). LoCuSS: first results from strong-lensing analysis of 20 massive galaxy clusters at z = 0.2. *MNRAS*, 404:325–349.

Roche, N., Bernardi, M., and Hyde, J. (2010). Colour gradients and the colour-magnitude relation: different properties of brightest cluster galaxies and E/S0 galaxies in the Sloan Digital Sky Survey. *MNRAS*, 407:1231–1244.

Rosati, P., della Ceca, R., Norman, C., and Giacconi, R. (1998). The ROSAT Deep Cluster Survey: The X-Ray Luminosity Function Out to z=0.8. *ApJ*, 492:L21+.

Sahlén, M., Viana, P. T. P., Liddle, A. R., Romer, A. K., Davidson, M., Hosmer, M., Lloyd-Davies, E., Sabirli, K., Collins, C. A., Freeman, P. E., Hilton, M., Hoyle, B., Kay, S. T., Mann, R. G., Mehrtens, N., Miller, C. J., Nichol, R. C., Stanford, S. A., and West, M. J. (2009). The XMM Cluster Survey: forecasting cosmological and cluster scaling-relation parameter constraints. *MNRAS*, 397:577–607.

Sanders, J. S. and Fabian, A. C. (2002). Spatially resolved X-ray spectroscopy of the core of the Centaurus cluster. *MNRAS*, 331:273–283.

Sanders, J. S. and Fabian, A. C. (2007). A deeper X-ray study of the core of the Perseus galaxy cluster: the power of sound waves and the distribution of metals and cosmic rays. *MNRAS*, 381:1381–1399.

Sarazin, C. L. (1988). *X-ray emission from clusters of galaxies, Cambridge Astrophysics Series, Cambridge: Cambridge University Press, 1988.*

Sarazin, C. L. (2002). The Physics of Cluster Mergers. In L. Feretti, I. M. Gioia, & G. Giovannini, editor, *Merging Processes in Galaxy Clusters*, volume 272 of *Astrophysics and Space Science Library*, pages 1–38.

Sato, K., Matsushita, K., Ishisaki, Y., Yamasaki, N. Y., Ishida, M., and Ohashi, T. (2009). Suzaku Observation of Group of Galaxies NGC 507: Temperature and Metal Distributions in the Intra-Cluster Medium. *PASJ*, 61:353–+.

Scharf, C. (2002). Optimal Chandra and XMM-Newton Bandpasses for Detecting Low-Temperature Groups and Clusters of Galaxies. *ApJ*, 572:157–159.

Schechter, P. (1976). An analytic expression for the luminosity function for galaxies. *ApJ*, 203:297–306.

Schindler, S. and Diaferio, A. (2008). Metal Enrichment Processes. *Space Sci. Rev.*, 134:363–377.

Schneider, D. P., Hall, P. B., Richards, G. T., Strauss, M. A., Vanden Berk, D. E., Anderson, S. F., Brandt, W. N., Fan, X., Jester, S., Gray, J., Gunn, J. E., SubbaRao, M. U., Thakar, A. R., Stoughton, C., Szalay, A. S., Yanny, B., York, D. G., Bahcall, N. A., Barentine, J., Blanton, M. R., Brewington, H., Brinkmann, J., Brunner, R. J., Castander, F. J., Csabai, I., Frieman, J. A., Fukugita, M., Harvanek, M., Hogg, D. W., Ivezić, Ž., Kent, S. M., Kleinman, S. J., Knapp, G. R., Kron, R. G., Krzesiński, J., Long, D. C., Lupton, R. H., Nitta, A., Pier, J. R., Saxe, D. H., Shen, Y., Snedden, S. A., Weinberg, D. H., and Wu, J. (2007). The Sloan Digital Sky Survey Quasar Catalog. IV. Fifth Data Release. *AJ*, 134:102–117.

Schneider, P. (2006). *Einführung in die extragalaktische Astronomie und Kosmologie*.

Schuecker, P., Böhringer, H., Collins, C. A., and Guzzo, L. (2003). The REFLEX galaxy cluster survey. VII. Ω_m and σ_8 from cluster abundance and large-scale clustering. *A&A*, 398:867–877.

Schuecker, P., Böhringer, H., Guzzo, L., Collins, C. A., Neumann, D. M., Schindler, S., Voges, W., De Grandi, S., Chincarini, G., Cruddace, R., Müller, V., Reiprich, T. H., Retzlaff, J., and Shaver, P. (2001). The ROSAT-ESO Flux-Limited X-Ray (REFLEX) galaxy cluster survey. III. The power spectrum. *A&A*, 368:86–106.

Schuecker, P., Böhringer, H., and Voges, W. (2004). Detection of X-ray clusters of galaxies by matching RASS photons and SDSS galaxies within GAVO. *A&A*, 420:61–74.

Schwope, A. D., Lamer, G., de Hoon, A., Kohnert, J., Böhringer, H., Dietrich, J. P., Fassbender, R., Mohr, J., Mühlegger, M., Pierini, D., Pratt, G. W., Quintana, H., Rosati, P., Santos, J., and Šuhada, R. (2010). XMMU J100750.5+125818: a strong lensing cluster at z = 1.082. *A&A*, 513:L10+.

Scodeggio, M., Franzetti, P., Garilli, B., Zanichelli, A., Paltani, S., Maccagni, D., Bottini, D., Le Brun, V., Contini, T., Scaramella, R., Adami, C., Bardelli, S., Zucca, E., Tresse, L., Ilbert, O., Foucaud, S., Iovino, A., Merighi, R., Zamorani, G., Gavignaud, I., Rizzo, D., McCracken, H. J., Le Fèvre, O., Picat, J. P., Vettolani, G., Arnaboldi, M., Arnouts, S., Bolzonella, M., Cappi, A., Charlot, S., Ciliegi, P., Guzzo, L., Marano, B., Marinoni, C., Mathez, G., Mazure, A., Meneux, B., Pellò, R., Pollo, A., Pozzetti, L., and Radovich, M. (2005). The VVDS

Data-Reduction Pipeline: Introducing VIPGI, the VIMOS Interactive Pipeline and Graphical Interface. *PASP*, 117:1284–1295.

Sérsic, J. L. (1963). Influence of the atmospheric and instrumental dispersion on the brightness distribution in a galaxy. *Boletin de la Asociacion Argentina de Astronomia La Plata Argentina*, 6:41–+.

Sheth, R. K., Mo, H. J., and Tormen, G. (2001). Ellipsoidal collapse and an improved model for the number and spatial distribution of dark matter haloes. *MNRAS*, 323:1–12.

Silk, J. (1976). Accretion By Galaxy Clusters and the Relationship Between X-Ray Luminosity and Velocity Dispersion. In *Bulletin of the American Astronomical Society*, volume 8 of *Bulletin of the American Astronomical Society*, pages 452–+.

Silk, J. and White, S. D. M. (1978). The determination of Q_0 using X-ray and microwave observations of galaxy clusters. *ApJ*, 226:L103–L106.

Simionescu, A., Böhringer, H., Brüggen, M., and Finoguenov, A. (2007). The gaseous atmosphere of M 87 seen with XMM-Newton. *A&A*, 465:749–758.

Simionescu, A., Roediger, E., Nulsen, P. E. J., Brüggen, M., Forman, W. R., Böhringer, H., Werner, N., and Finoguenov, A. (2009a). The large-scale shock in the cluster of galaxies Hydra A. *A&A*, 495:721–732.

Simionescu, A., Werner, N., Böhringer, H., Kaastra, J. S., Finoguenov, A., Brüggen, M., and Nulsen, P. E. J. (2009b). Chemical enrichment in the cluster of galaxies Hydra A. *A&A*, 493:409–424.

Simionescu, A., Werner, N., Finoguenov, A., Böhringer, H., and Brüggen, M. (2008). Metal-rich multi-phase gas in M 87. AGN-driven metal transport, magnetic-field supported multi-temperature gas, and constraints on non-thermal emission observed with XMM-Newton. *A&A*, 482:97–112.

Simionescu, A., Werner, N., Forman, W. R., Miller, E. D., Takei, Y., Böhringer, H., Churazov, E., and Nulsen, P. E. J. (2010). Metal transport by gas sloshing in M87. *MNRAS*, 405:91–99.

Skelton, R. E., Bell, E. F., and Somerville, R. S. (2009). The Effect of Dry Mergers on the Color-Magnitude Relation of Early-Type Galaxies. *ApJ*, 699:L9–L12.

Skrutskie, M. F., Cutri, R. M., Stiening, R., Weinberg, M. D., Schneider, S., Carpenter, J. M., Beichman, C., Capps, R., Chester, T., Elias, J., Huchra, J., Liebert, J., Lonsdale, C., Monet, D. G., Price, S., Seitzer, P., Jarrett, T., Kirkpatrick, J. D., Gizis, J. E., Howard, E., Evans, T., Fowler, J., Fullmer, L., Hurt, R., Light, R., Kopan, E. L., Marsh, K. A., McCallon, H. L., Tam, R., Van Dyk, S., and Wheelock, S. (2006). The Two Micron All Sky Survey (2MASS). *AJ*, 131:1163–1183.

Smith, R. K., Brickhouse, N. S., Liedahl, D. A., and Raymond, J. C. (2001). Collisional Plasma Models with APEC/APED: Emission-Line Diagnostics of Hydrogen-like and Helium-like Ions. *ApJ*, 556:L91–L95.

Spiga, D. (2011). Optics for X-ray telescopes: analytical treatment of the off-axis effective area of mirrors in optical modules. *arXiv: 1101.0629*.

Springel, V., White, S. D. M., Jenkins, A., Frenk, C. S., Yoshida, N., Gao, L., Navarro, J., Thacker, R., Croton, D., Helly, J., Peacock, J. A., Cole, S., Thomas, P., Couchman, H., Evrard, A., Colberg, J., and Pearce, F. (2005). Simulations of the formation, evolution and clustering of galaxies and quasars. *Nature*, 435:629–636.

Stanek, R., Evrard, A. E., Böhringer, H., Schuecker, P., and Nord, B. (2006). The X-Ray Luminosity-Mass Relation for Local Clusters of Galaxies. *ApJ*, 648:956–968.

Stanek, R., Rasia, E., Evrard, A. E., Pearce, F., and Gazzola, L. (2010). Massive Halos in Millennium Gas Simulations: Multivariate Scaling Relations. *ApJ*, 715:1508–1523.

Stanford, S. A., Eisenhardt, P. R., Brodwin, M., Gonzalez, A. H., Stern, D., Jannuzi, B. T., Dey, A., Brown, M. J. I., McKenzie, E., and Elston, R. (2005). An IR-selected Galaxy Cluster at z = 1.41. *ApJ*, 634:L129–L132.

Stanford, S. A., Romer, A. K., Sabirli, K., Davidson, M., Hilton, M., Viana, P. T. P., Collins, C. A., Kay, S. T., Liddle, A. R., Mann, R. G., Miller, C. J., Nichol, R. C., West, M. J., Conselice, C. J., Spinrad, H., Stern, D., and Bundy, K. (2006). The XMM Cluster Survey: A Massive Galaxy Cluster at z = 1.45. *ApJ*, 646:L13–L16.

Staniszewski, Z., Ade, P. A. R., Aird, K. A., Benson, B. A., Bleem, L. E., Carlstrom, J. E., Chang, C. L., Cho, H., Crawford, T. M., Crites, A. T., de Haan, T., Dobbs, M. A., Halverson, N. W., Holder, G. P., Holzapfel, W. L., Hrubes, J. D., Joy, M., Keisler, R., Lanting, T. M., Lee, A. T., Leitch, E. M., Loehr, A., Lueker, M., McMahon, J. J., Mehl, J., Meyer, S. S., Mohr, J. J., Montroy, T. E., Ngeow, C., Padin, S., Plagge, T., Pryke, C., Reichardt, C. L., Ruhl, J. E., Schaffer, K. K., Shaw, L., Shirokoff, E., Spieler, H. G., Stalder, B., Stark, A. A., Vanderlinde, K., Vieira, J. D., Zahn, O., and Zenteno, A. (2009). Galaxy Clusters Discovered with a Sunyaev-Zel'dovich Effect Survey. *ApJ*, 701:32–41.

Strazzullo, V., Rosati, P., Pannella, M., Gobat, R., Santos, J. S., Nonino, M., Demarco, R., Lidman, C., Tanaka, M., Mullis, C. R., Nuñez, C., Rettura, A., Jee, M. J., Böhringer, H., Bender, R., Bouwens, R. J., Dawson, K., Fassbender, R., Franx, M., Perlmutter, S., and Postman, M. (2010). Cluster galaxies in XMMU J2235-2557: galaxy population properties in most massive environments at z 1.4. *A&A*, 524:A17+.

Strüder, L., Briel, U., Dennerl, K., Hartmann, R., Kendziorra, E., Meidinger, N., Pfeffermann, E., Reppin, C., Aschenbach, B., Bornemann, W., Bräuninger, H., Burkert, W., Elender, M., Freyberg, M., Haberl, F., Hartner, G., Heuschmann, F., Hippmann, H., Kastelic, E., Kemmer,

S., Kettenring, G., Kink, W., Krause, N., Müller, S., Oppitz, A., Pietsch, W., Popp, M., Predehl, P., Read, A., Stephan, K. H., Stötter, D., Trümper, J., Holl, P., Kemmer, J., Soltau, H., Stötter, R., Weber, U., Weichert, U., von Zanthier, C., Carathanassis, D., Lutz, G., Richter, R. H., Solc, P., Böttcher, H., Kuster, M., Staubert, R., Abbey, A., Holland, A., Turner, M., Balasini, M., Bignami, G. F., La Palombara, N., Villa, G., Buttler, W., Gianini, F., Lainé, R., Lumb, D., and Dhez, P. (2001). The European Photon Imaging Camera on XMM-Newton: The pn-CCD camera. *A&A*, 365:L18–L26.

Sugiyama, N. (1995). Cosmic Background Anisotropies in Cold Dark Matter Cosmology. *ApJS*, 100:281–+.

Sunyaev, R. A. and Zel'dovich, I. B. (1980). Microwave background radiation as a probe of the contemporary structure and history of the universe. *ARA&A*, 18:537–560.

Sunyaev, R. A. and Zel'dovich, Y. B. (1970). The Spectrum of Primordial Radiation, its Distortions and their Significance. *Comments on Astrophysics and Space Physics*, 2:66–+.

Sunyaev, R. A. and Zel'dovich, Y. B. (1972). The Observations of Relic Radiation as a Test of the Nature of X-Ray Radiation from the Clusters of Galaxies. *Comments on Astrophysics and Space Physics*, 4:173–+.

Tanaka, M., Finoguenov, A., and Ueda, Y. (2010). A Spectroscopically Confirmed X-ray Cluster at z = 1.62 with a Possible Companion in the Subaru/XMM-Newton Deep Field. *ApJ*, 716:L152–L156.

Tinker, J., Kravtsov, A. V., Klypin, A., Abazajian, K., Warren, M., Yepes, G., Gottlöber, S., and Holz, D. E. (2008). Toward a Halo Mass Function for Precision Cosmology: The Limits of Universality. *ApJ*, 688:709–728.

Tinker, J. L., Robertson, B. E., Kravtsov, A. V., Klypin, A., Warren, M. S., Yepes, G., and Gottlöber, S. (2010). The Large-scale Bias of Dark Matter Halos: Numerical Calibration and Model Tests. *ApJ*, 724:878–886.

Tokoi, K., Sato, K., Ishisaki, Y., Ohashi, T., Yamasaki, N. Y., Nakazawa, K., Matsushita, K., Fukazawa, Y., Hoshino, A., Tamura, T., Egawa, C., Kawano, N., Ota, N., Isobe, N., Kawaharada, M., Awaki, H., and Hughes, J. P. (2008). Suzaku Observation of HCG 62: Temperature, Abundance, and Extended Hard X-Ray Emission Profiles. *PASJ*, 60:317–+.

Tonry, J. L. (1987). Properties of cD galaxies. In P. T. de Zeeuw, editor, *Structure and Dynamics of Elliptical Galaxies*, volume 127 of *IAU Symposium*, pages 89–96.

Tucker, D. L., Oemler, Jr., A., Hashimoto, Y., Shectman, S. A., Kirshner, R. P., Lin, H., Landy, S. D., Schechter, P. L., and Allam, S. S. (2000). Loose Groups of Galaxies in the Las Campanas Redshift Survey. *ApJS*, 130:237–265.

Turner, M. J. L., Abbey, A., Arnaud, M., Balasini, M., Barbera, M., Belsole, E., Bennie, P. J., Bernard, J. P., Bignami, G. F., Boer, M., Briel, U., Butler, I., Cara, C., Chabaud, C., Cole, R., Collura, A., Conte, M., Cros, A., Denby, M., Dhez, P., Di Coco, G., Dowson, J., Ferrando, P., Ghizzardi, S., Gianotti, F., Goodall, C. V., Gretton, L., Griffiths, R. G., Hainaut, O., Hochedez, J. F., Holland, A. D., Jourdain, E., Kendziorra, E., Lagostina, A., Laine, R., La Palombara, N., Lortholary, M., Lumb, D., Marty, P., Molendi, S., Pigot, C., Poindron, E., Pounds, K. A., Reeves, J. N., Reppin, C., Rothenflug, R., Salvetat, P., Sauvageot, J. L., Schmitt, D., Sembay, S., Short, A. D. T., Spragg, J., Stephen, J., Strüder, L., Tiengo, A., Trifoglio, M., Trümper, J., Vercellone, S., Vigroux, L., Villa, G., Ward, M. J., Whitehead, S., and Zonca, E. (2001). The European Photon Imaging Camera on XMM-Newton: The MOS cameras. *A&A*, 365:L27–L35.

Šuhada, R., Song, J., Böhringer, H., Benson, B. A., Mohr, J., Fassbender, R., Finoguenov, A., Pierini, D., Pratt, G. W., Andersson, K., Armstrong, R., and Desai, S. (2010). XMM-Newton detection of two clusters of galaxies with strong SPT Sunyaev-Zel'dovich effect signatures. *A&A*, 514:L3+.

Vanderlinde, K., Crawford, T. M., de Haan, T., Dudley, J. P., Shaw, L., Ade, P. A. R., Aird, K. A., Benson, B. A., Bleem, L. E., Brodwin, M., Carlstrom, J. E., Chang, C. L., Crites, A. T., Desai, S., Dobbs, M. A., Foley, R. J., George, E. M., Gladders, M. D., Hall, N. R., Halverson, N. W., High, F. W., Holder, G. P., Holzapfel, W. L., Hrubes, J. D., Joy, M., Keisler, R., Knox, L., Lee, A. T., Leitch, E. M., Loehr, A., Lueker, M., Marrone, D. P., McMahon, J. J., Mehl, J., Meyer, S. S., Mohr, J. J., Montroy, T. E., Ngeow, C., Padin, S., Plagge, T., Pryke, C., Reichardt, C. L., Rest, A., Ruel, J., Ruhl, J. E., Schaffer, K. K., Shirokoff, E., Song, J., Spieler, H. G., Stalder, B., Staniszewski, Z., Stark, A. A., Stubbs, C. W., van Engelen, A., Vieira, J. D., Williamson, R., Yang, Y., Zahn, O., and Zenteno, A. (2010). Galaxy Clusters Selected with the Sunyaev-Zel'dovich Effect from 2008 South Pole Telescope Observations. *ApJ*, 722:1180–1196.

Véron-Cetty, M. and Véron, P. (2006). A catalogue of quasars and active nuclei: 12th edition. *A&A*, 455:773–777.

Viana, P. T. P. and Liddle, A. R. (1996). The cluster abundance in flat and open cosmologies. *MNRAS*, 281:323–+.

Vikhlinin, A., Burenin, R. A., Ebeling, H., Forman, W. R., Hornstrup, A., Jones, C., Kravtsov, A. V., Murray, S. S., Nagai, D., Quintana, H., and Voevodkin, A. (2009a). Chandra Cluster Cosmology Project. II. Samples and X-Ray Data Reduction. *ApJ*, 692:1033–1059.

Vikhlinin, A., Kravtsov, A. V., Burenin, R. A., Ebeling, H., Forman, W. R., Hornstrup, A., Jones, C., Murray, S. S., Nagai, D., Quintana, H., and Voevodkin, A. (2009b). Chandra Cluster Cosmology Project III: Cosmological Parameter Constraints. *ApJ*, 692:1060–1074.

Vikhlinin, A., McNamara, B. R., Forman, W., Jones, C., Quintana, H., and Hornstrup, A. (1998a). A Catalog of 200 Galaxy Clusters Serendipitously Detected in the ROSAT PSPC Pointed Observations. *ApJ*, 502:558–+.

Vikhlinin, A., McNamara, B. R., Forman, W., Jones, C., Quintana, H., and Hornstrup, A. (1998b). A Catalog of 200 Galaxy Clusters Serendipitously Detected in the ROSAT PSPC Pointed Observations. *ApJ*, 502:558–+.

Voges, W., Aschenbach, B., Boller, T., Bräuninger, H., Briel, U., Burkert, W., Dennerl, K., Englhauser, J., Gruber, R., Haberl, F., Hartner, G., Hasinger, G., Kürster, M., Pfeffermann, E., Pietsch, W., Predehl, P., Rosso, C., Schmitt, J. H. M. M., Trümper, J., and Zimmermann, H. U. (1999). The ROSAT all-sky survey bright source catalogue. *A&A*, 349:389–405.

Voit, G. M. (2005). Tracing cosmic evolution with clusters of galaxies. *Reviews of Modern Physics*, 77:207–258.

von der Linden, A., Best, P. N., Kauffmann, G., and White, S. D. M. (2007). How special are brightest group and cluster galaxies? *MNRAS*, 379:867–893.

Warren, M. S., Abazajian, K., Holz, D. E., and Teodoro, L. (2006). Precision Determination of the Mass Function of Dark Matter Halos. *ApJ*, 646:881–885.

Waskett, T. J., Eales, S. A., Gear, W. K., McCracken, H. J., Brodwin, M., Nandra, K., Laird, E. S., and Lilly, S. (2004). XMM-Newton surveys of the Canada-France Redshift Survey fields - II. The X-ray catalogues, the properties of the host galaxies and the redshift distribution. *MNRAS*, 350:785–797.

Watson, M. G., Schröder, A. C., Fyfe, D., Page, C. G., Lamer, G., Mateos, S., Pye, J., Sakano, M., Rosen, S., Ballet, J., Barcons, X., Barret, D., Boller, T., Brunner, H., Brusa, M., Caccianiga, A., Carrera, F. J., Ceballos, M., Della Ceca, R., Denby, M., Denkinson, G., Dupuy, S., Farrell, S., Fraschetti, F., Freyberg, M. J., Guillout, P., Hambaryan, V., Maccacaro, T., Mathiesen, B., McMahon, R., Michel, L., Motch, C., Osborne, J. P., Page, M., Pakull, M. W., Pietsch, W., Saxton, R., Schwope, A., Severgnini, P., Simpson, M., Sironi, G., Stewart, G., Stewart, I. M., Stobbart, A., Tedds, J., Warwick, R., Webb, N., West, R., Worrall, D., and Yuan, W. (2009). The XMM-Newton serendipitous survey. V. The Second XMM-Newton serendipitous source catalogue. *A&A*, 493:339–373.

Werner, N., de Plaa, J., Kaastra, J. S., Vink, J., Bleeker, J. A. M., Tamura, T., Peterson, J. R., and Verbunt, F. (2006). XMM-Newton spectroscopy of the cluster of galaxies 2A 0335+096. *A&A*, 449:475–491.

Werner, N., Durret, F., Ohashi, T., Schindler, S., and Wiersma, R. P. C. (2008). Observations of Metals in the Intra-Cluster Medium. *Space Sci. Rev.*, 134:337–362.

Werner, N., Simionescu, A., Million, E. T., Allen, S. W., Nulsen, P. E. J., von der Linden, A., Hansen, S. M., Böhringer, H., Churazov, E., Fabian, A. C., Forman, W. R., Jones, C., Sanders, J. S., and Taylor, G. B. (2010). Feedback under the microscope-II. Heating, gas uplift and mixing in the nearest cluster core. *MNRAS*, 407:2063–2074.

Whiley, I. M., Aragón-Salamanca, A., De Lucia, G., von der Linden, A., Bamford, S. P., Best, P., Bremer, M. N., Jablonka, P., Johnson, O., Milvang-Jensen, B., Noll, S., Poggianti, B. M., Rudnick, G., Saglia, R., White, S., and Zaritsky, D. (2008). The evolution of the brightest cluster galaxies since z ˜ 1 from the ESO Distant Cluster Survey (EDisCS). *MNRAS*, 387:1253–1263.

Williamson, R., Benson, B. A., High, F. W., Vanderlinde, K., Ade, P. A. R., Aird, K. A., Andersson, K., Armstrong, R., Ashby, M. L. N., Bautz, M., Bazin, G., Bertin, E., Bleem, L. E., Bonamente, M., Brodwin, M., Carlstrom, J. E., Chang, C. L., Clocchiatti, A., Crawford, T. M., Crites, A. T., de Haan, T., Desai, S., Dobbs, M. A., Dudley, J. P., Fazio, G. G., Foley, R. J., Forman, W. R., Garmire, G., George, E. M., Gladders, M. D., Gonzalez, A. H., Halverson, N. W., Holder, G. P., Holzapfel, W. L., Hoover, S., Hrubes, J. D., Jones, C., Joy, M., Keisler, R., Knox, L., Lee, A. T., Leitch, E. M., Lueker, M., Luong-Van, D., Marrone, D. P., McMahon, J. J., Mehl, J., Meyer, S. S., Mohr, J. J., Montroy, T. E., Murray, S. S., Padin, S., Plagge, T., Pryke, C., Reichardt, C. L., Rest, A., Ruel, J., Ruhl, J. E., Saliwanchik, B. R., Saro, A., Schaffer, K. K., Shaw, L., Shirokoff, E., Song, J., Spieler, H. G., Stalder, B., Stanford, S. A., Staniszewski, Z., Stark, A. A., Story, K., Stubbs, C. W., Vieira, J. D., Vikhlinin, A., and Zenteno, A. (2011). An SZ-selected sample of the most massive galaxy clusters in the 2500-square-degree South Pole Telescope survey. *arXiv: 1101.1290*.

Wolter, A. (1952). Spiegelsysteme streifenden Einfalls als abbildende Optiken für Röntgenstrahlen (Grazing Incidence Mirror Systems as Imaging Optics for X-Rays). *Annalen der Physik*, 445:94–114.

Zhang, Y., Okabe, N., Finoguenov, A., Smith, G. P., Piffaretti, R., Valdarnini, R., Babul, A., Evrard, A. E., Mazzotta, P., Sanderson, A. J. R., and Marrone, D. P. (2010). LoCuSS: A Comparison of Cluster Mass Measurements from XMM-Newton and Subaru - Testing Deviation from Hydrostatic Equilibrium and Non-thermal Pressure Support. *ApJ*, 711:1033–1043.

Zibetti, S. (2008). Statistical Properties of the IntraCluster Light from SDSS Image Stacking. In J. Davies & M. Disney, editor, *IAU Symposium*, volume 244 of *IAU Symposium*, pages 176–185.

Zwicky, F. (1933). Die Rotverschiebung von extragalaktischen Nebeln. *Helvetica Physica Acta*, 6:110–127.

Zwicky, F. and Kowal, C. T. (1968). *"Catalogue of Galaxies and of Clusters of Galaxies", Volume VI*.

Acknowledgements

There are many people, without whom this work would not have been possible. I thank you all for your support, encouragement and friendship!

First of all, I would like to thank my supervisor Hans Böhringer. I am very grateful that you gave me this opportunity. I always knew that I can turn to you and find not only a great scientific and moral support, but also encouragement and inspiration for work. Thank you for all this!

Rene Fassbender, Daniele Pierini, Gabriel Pratt and Alexis Finoguenov - thank you for all your advices, help and patience. I learned a lot from you! These three years would not be so enjoyable without the friendly environment of the Cluster Group. In particular, I would like to thank for the nice chats to Gayoung Chon and Miguel Verdugo (also for helping me to plunder the La Silla canteen and for the comments on this thesis, respectively). I also thank Joe Mohr, Jeeseon Song, Joana Santos, Martin Mühlegger and Alessandro Nastasi for their great scientific input and friendly support all these years. Thanks Harald Baumgartner for the always quick and high spirited help with technical problems! Teta Soňa, you inspired me to choose this path and taught me so much about astronomy!

Norbi, thank you for everything! For your help, optimism and inspiration, I certainly would not be here without you. Dear Aurora, when I was the most troubled you always managed to give me the right advice and encouragement - thank you! Thank you Payel, Miro and Evka for making me feel here at home since day one. Tom, Paula, Umberto, Margarita, Julius for all the fun and balcony-paellas! Clemens, danke für deine Freundschaft, Krapfen und gute Gespräche! Ania, dzięki bardzo for all the really unforgettable, oosome fun we had! Dear colleague Maťo, thank you for your friendship, all the great discussions, fun, incredible train rides and so much more!

Alex, thanks for all the help and always cheering me up! Maťo, life has a way to bring us together. I'm so thankful for this, because I know I have such a great friend with me! Thank you both of you, Maťo and Alex, I have no idea how I would have gotten through the last months without you!

Köszöm Anyuka, mindenért, soha nem juthattam el ide drága szüleim nélkül! Ďakujem Ocko, za Tvoju podporu, a že ste mi toto s mamkou umožnili! Timik, ďakujem Ti, za všetko, bola si neuveriteľná podpora počas týchto rokov, nie len pre mňa, ale aj pre našich rodičov. Ivka, ďakujem, že si pri mne celý čas stála. Bez tvojej pomoci, trpezlivosti a podpory by som to nikdy nezvládol! Neviem ani vyjadriť ako som Vám všetkým vďačný!

Thank you! Ďakujem! Köszönöm!

Curriculum Vitae

Róbert Šuhada
born on 1st June, 1984
in Košice, Slovak Republic

Max-Planck-Institut
für Extraterrestrische Physik,
Giessenbachstrasse 1,
D-85748, Garching bei München
Email: rsuhada@mpe.mpg.de

EDUCATION:

2007 - 2011 Max Planck Institute for Extraterrestrial Physics,
Garching, Germany
PhD student, supervisor: Prof. Hans Böhringer

2002 - 2007 P. J. Šafárik University, Košice, Slovakia
MS (with distinctions) in Astronomy and Astrophysics, May 2007
BS (with distinctions) in Physics, June 2005

1998 - 2002 Secondary High School, Košice, Slovakia

PUBLICATION LIST:

- **Šuhada, R.**, Fassbender, R. , Nastasi, A., Böhringer, de Hoon, A., Pierini, D., Santos, J. S., H., Rosati, P., Mühlegger, M., Quintana, H., Schwope, A. D., Lamer, G., Kohnert, J., and Pratt, G. W., *Exploring the galaxy cluster-group transition regime at high redshifts: Physical properties of two newly detected* $z > 1$ *systems*, submitted to A&A

- Pierini, D., **Šuhada, R.**, Fassbender R., Nastasi, A., Böhringer, H., Salvato, M., Pratt, G. W., Lerchster, M., Rosati, P., Santos, J. S., de Hoon, A., Kohnert, J., Lamer, G., Mohr, J. J., Mühlegger, M., Quintana, H., Schwope, A., Biffi, V., Chon, G., Giodini, S., Koppenhoefer, J., Montalto, M., Verdugo, M., Ziparo, F., Afonso, P. M. J., Clemens, C., Greiner, J., Krühler, J., T., Küpcü Yoldaş, A., Olivares, F., Rossi, A., and Yoldaş, A., *First simultaneous optical/near-infrared imaging of an X-ray selected, high-redshift cluster of galaxies with GROND: The puzzling galaxy population of XMMU J0338.8+0030 at z=1.1*, submitted to A&A

- Fassbender, R., Böhringer, H., Santos, J. S., Pratt, G. W., **Šuhada, R.**, Kohnert, J., Lerchster, M., Rovilos, E., Pierini, D., Chon, G., Schwope, A. D., Lamer, G., Mühlegger, M.,

Rosati, P., Quintana, H., Nastasi, A., de Hoon, A., Seitz, S., and Mohr, J. J., (2011), *A pan-chromatic view of the galaxy cluster XMMU J1230.3+1339 at z=0.975. Observing the assembly of a massive system*, A&A, 527:A78+

- Fassbender, R., Nastasi, A., Böhringer, H., **Šuhada, R.**, Santos, J. S., Rosati, P., Pierini, D., Mühlegger, M., Quintana, H., Schwope, A. D., Lamer, G., de Hoon, A., Kohnert, J., Pratt, G. W., and Mohr, J. J., (2011), *The X-ray luminous galaxy cluster XMMU J1007.4+1237 at z=1.56 - The dawn of starburst activity in cluster cores*, A&A, 527:L10+

- **Šuhada, R.**, Song, J., Böhringer, H., Benson, B. A., Mohr, J., Fassbender, R., Finoguenov, A., Pierini, D., Pratt, G. W., Andersson, K., Armstrong, R., and Desai, S., (2010), *XMM-Newton detection of two clusters of galaxies with strong SPT Sunyaev-Zel'dovich effect signatures*, A&A, 514:L3+

- Schwope, A. D., Lamer, G., de Hoon, A., Kohnert, J., Böhringer, H., Dietrich, J. P., Fassbender, R., Mohr, J., Mühlegger, M., Pierini, D., Pratt, G. W., Quintana, H., Rosati, P., Santos, J., and **Šuhada, R.**, (2010), *XMMU J100750.5+125818: a strong lensing cluster at z=1.082*, A&A, 513:L10+

PRESENTATIONS:

- *The XMM-BCS Galaxy Cluster Survey*, with H. Böhringer et al., 2010, poster presented at Galaxy Clusters: Observations, Physics and Cosmology, in Garching, Germany

- *The XMM-BCS Galaxy Cluster Survey*, with H. Böhringer et al., 2009, talk presented at SZ at Bonn: Multiwavelength Look At Galaxy Clusters, in Bonn, Germany

- *Status of the XMM-BCS Galaxy Cluster Survey*, with H. Böhringer et al., 2009, talk presented at X-ray Distant Cluster Project Workshop 2008, in Garching, Germany

- *The X-ray-SZE-Optical-Near-Infrared Galaxy Cluster Survey*, with H. Böhringer et al., 2008, poster presented at X-ray Universe 2008, in Granda, Spain

- *The X-ray-SZE-Optical-Near-Infrared Galaxy Cluster Survey*, with H. Böhringer et al., 2008, talk presented at the XMM-XXL X-ray survey Workshop, in Paris, France

- *Long - term photometric behaviour of symbiotic system AG Dra*, with R. Gális et al., 2006, poster presented at IAU Symposium No. 240, XXVIth GA IAU, in Prague

- *XMM-Newton reveals the dynamical history of three nearby clusters of galaxies* with N. Werner et al., 2006, talk at SRON in Utrecht, The Netherlands

SUMMER SCHOOLS AND CONFERENCES:

- IMPRS Summer School: Statistical Inference from Astrophysical Data, 2009, Heidelberg, Germany

- Dark Energy 2008 conference, 2008, in Munich, Germany

- Galaxy Cluster Weighting Workshop, 2008, in Garching, Germany

- Enrico Fermi School 2008: Astrophysics of Galaxy Clusters, 2008, Varenna, Italy